

# **White Matter Degeneration in Huntington's Disease: A Study of Brain Structure and Cognition**

*Thesis submitted for the degree of Doctor of Philosophy*

**Helen Crawford**

Institute of Neurology

University College London

2016

## **Declaration**

I, Helen Crawford, confirm that the work presented in this thesis is my own. Where information has been derived from other sources, I confirm that this has been indicated in the thesis.

A handwritten signature in cursive script, appearing to read 'H. Crawford'.

## **Abstract**

Huntington's disease (HD) is a hereditary neurodegenerative disorder characterised by devastating physical, behavioural and mental dysfunction. Accumulating evidence indicates that abnormal white matter (WM) is a major hallmark of the disease, with both macro- and microstructural changes apparent before manifest diagnosis.

This thesis is an investigation of WM in HD and uses various imaging and cognitive techniques to address some key challenges. Firstly, the development of reliable structural measurement techniques sensitive to longitudinal change may aid characterisation of subtle abnormalities before disease onset. Secondly, optimised diffusion imaging techniques which incorporate superior image processing tools will further understanding as to why changes are harder to find in the premanifest stage and will increase sensitivity to detect them. Thirdly, the development of novel, hypothesis-driven neuropsychological tasks will help detect heterogeneous cognitive decline in individuals in the earliest disease stages.

To address these challenges, firstly, a novel corpus callosum (CC) segmentation technique is developed and applied to a large clinical cohort revealing disease-related reduction in baseline CC volume and elevated rates of change over 24 months in both premanifest and manifest HD participants. Secondly, an investigation of template effects in diffusion image analysis reveals consistency between analyses using three customised templates and evidence of the superiority of tensor-based registration over scalar-based registration is demonstrated. An exploratory investigation into the association between brain volume and WM diffusivity is also presented and disease-specific changes in HD gene-carriers are reported.

Lastly, two specially designed, pathology-targeted cognitive tasks are applied to a premanifest HD cohort. Abnormal interhemispheric transfer from the non-dominant to dominant hemisphere as well as altered attentional processing and impaired automaticity is revealed. By developing techniques to characterise WM pathology and explore cognitive deficits, this thesis improves our understanding of the role of WM degeneration in the premanifest and early stages of HD.

# Table of Contents

Declaration .....	2
Abstract .....	3
Table of Contents .....	4
Table of Figures .....	10
Table of Tables.....	19
List of Abbreviations .....	22
Aims of this Thesis .....	25
1. Background .....	26
1.1 Introduction to Huntington’s Disease.....	26
1.1.1 Genetics and Neuropathology .....	26
1.1.2 Prevalence and Clinical Presentation .....	27
1.1.3 Treatments.....	29
1.2 Neuroimaging Techniques .....	30
1.2.1 Structural MRI .....	31
1.2.2 Diffusion MRI.....	34
1.3 Cognition in HD .....	41
1.3.1 Cognitive Phenotype .....	42
1.3.2 Pathology and Cognition.....	43
1.3.3 Challenges in Premanifest HD .....	43
1.3.4 Summary of Cognition in HD .....	44
1.4 Summary .....	45
2. Methodology .....	46
2.1 Cohorts .....	46
2.1.1 Track-HD .....	46
2.1.2 TrackOn-HD .....	49
2.1.3 PADDINGTON .....	49

2.1.4	Additional Participants .....	50
2.2	Image Acquisition .....	50
2.2.1	Track-HD .....	50
2.2.2	TrackOn-HD .....	51
2.2.3	PADDINGTON .....	52
2.2.4	Individual MRI Scan .....	52
2.3	Image Analysis .....	52
2.3.1	Structural MR Image Analysis .....	52
2.3.2	Diffusion MR Image Analysis .....	61
2.4	Statistical Analysis .....	80
2.4.1	Sample Size Calculations .....	80
2.4.2	Regression .....	82
2.4.3	Correlation .....	83
2.4.4	Correction for Multiple Comparisons .....	83
	Development, Optimisation and Investigation of Neuroimaging Techniques .....	84
3.	Development of a Novel Segmentation Tool .....	84
3.1	Aims .....	85
3.2	Protocol Development .....	85
3.3	Reproducibility .....	86
3.4	Discussion .....	87
4.	Investigation of a Registration Tool .....	89
4.1	Aims .....	90
4.2	Methods .....	91
4.2.1	Participants .....	91
4.2.2	Image Analysis .....	91
4.2.3	Statistical Analysis .....	93
4.3	Results .....	94
4.4	Discussion .....	108

4.5	Conclusion.....	111
	Development of Novel Neuropsychological tasks.....	112
5.	Interhemispheric Transfer Task .....	112
5.1	Aims .....	114
5.2	Task Development.....	114
5.3	Pilot Study .....	116
5.4	Results .....	117
5.5	Discussion .....	117
6.	Interference Task.....	118
6.1	Aims .....	119
6.2	Task Development.....	119
6.3	Pilot Study .....	122
6.4	Results .....	123
6.5	Discussion .....	123
	Clinical Application: Imaging Tools.....	125
7.	Corpus Callosal Atrophy in Premanifest and Early HD .....	125
7.1	Aims .....	125
7.2	Materials and Methods .....	127
7.2.1	Participants.....	127
7.2.2	Image Analysis.....	128
7.2.3	Cognitive Measures.....	128
7.2.4	Statistical Analysis.....	129
7.3	Results .....	130
7.3.1	Group Demographics .....	130
7.3.2	Volumetric Group Differences.....	131
7.4	Discussion .....	135
7.5	Conclusion.....	138

8. Association between Brain Volume and White Matter Microstructure in Healthy Controls and HD Gene-Carriers .....	139
8.1 Aims .....	140
8.2 Methods .....	141
8.2.1 Participants .....	141
8.2.2 Image Analysis .....	141
8.2.3 Statistical Analysis .....	142
8.3 Results .....	143
8.3.1 TBSS Analysis .....	143
8.4 Discussion .....	153
8.4.1 Associations with White Matter .....	153
8.4.2 Associations with Grey Matter .....	155
8.4.3 Conclusions .....	157
9. White Matter Degeneration in HD: An Unbiased Tract-Based Spatial Statistics Study .....	159
9.1 Aims .....	161
9.2 Methods .....	162
9.2.1 Participants .....	162
9.2.2 Image Analysis .....	163
9.2.3 Statistical Analysis .....	164
9.3 Results .....	164
9.3.1 Tract-Based Between-Group Differences .....	165
9.3.2 Diffusion-Based Between-Group Differences .....	173
9.4 Discussion .....	176
9.4.1 Tract-Based Between-Group Differences .....	176
9.4.2 Diffusion-Based Between-Group Differences .....	180
9.5 Conclusions .....	180
Clinical Application: Cognitive Tools .....	181

10.	Interhemispheric Information Transfer Degeneration in Premanifest HD .....	181
10.1	Introduction.....	181
10.2	Aims.....	184
10.3	Methods .....	184
10.3.1	Participants.....	184
10.3.2	Task Administration.....	185
10.3.3	Behavioural Data Analysis.....	186
10.3.4	Clinical Correlations .....	188
10.3.5	Image Analysis.....	188
10.3.6	Volumetric Analysis .....	189
10.3.7	Regional Diffusion Analysis.....	189
10.3.8	ROI Tract-Based Spatial Statistics.....	189
10.3.9	Tractography of the Corpus Callosum .....	191
10.4	Results.....	193
10.4.1	Baseline Results .....	193
10.4.2	Clinical Correlations .....	195
10.4.3	Association between Whole CC Volume and CUD .....	198
10.4.4	Association between Whole CC Diffusion and CUD.....	198
10.4.5	ROI Tract-Based Spatial Statistics of the CC .....	201
10.4.6	Association between CC Tract Diffusion and CUD .....	202
10.4.7	Between-Group Differences in Imaging Metrics.....	205
10.4.8	Visit Two Results.....	205
10.4.9	Longitudinal Results .....	208
10.5	Discussion.....	211
10.6	Conclusion .....	221
11.	Susceptibility to Interference in Premanifest HD .....	222
11.1	Introduction.....	222
11.2	Aims.....	224



11.3	Methods .....	224
11.3.1	Participants .....	224
11.3.2	Task Administration .....	225
11.3.3	Behavioural Data Analysis .....	227
11.3.4	Clinical Correlations .....	228
11.3.5	Image Analysis .....	229
11.3.6	Caudate Volume Analysis .....	229
11.3.7	Tractography Analysis .....	230
11.4	Results .....	233
11.4.1	Baseline Results .....	233
11.4.2	Visit Two Results .....	249
11.4.3	Longitudinal Results .....	250
11.5	Discussion .....	251
11.6	Conclusions .....	259
	Conclusions .....	260
	Publications .....	263
	Journal Articles .....	263
	Abstracts for Poster Presentations .....	265
	Acknowledgements .....	267
	Appendix 1: Volumetric Analysis .....	268
	Corpus Callosum Segmentation: Standard Operational Procedure .....	268
	Appendix 2: Sample Size Calculations .....	274
	Interhemispheric Transfer Task .....	274
	Interference Task .....	277
	References .....	281

## Table of Figures

Figure 1-1. Natural history of HD. Adapted from Bates et al. (2015). .....	29
Figure 1-2. Principles of DTI. Adapted from <a href="http://www.diffusion-imaging.com">www.diffusion-imaging.com</a> . .....	35
Figure 2-1. Example of a T1 scan before (left) and after (right) N3 bias correction. ....	54
Figure 2-2. Examples of regional segmentations of whole-brain (top left), TIV (top right) and CC (bottom). .....	56
Figure 2-3. Example segmentations from one control participant in the Track-HD study. Top row: GM (left) and WM (right) segmentations in native space. Middle and bottom row: Modulated normalised GM (left middle), WM (right middle) and CSF (bottom) segmentations. ....	59
Figure 2-4. BET examples. T1 image is of a control participant from the Track-HD study. Top row: Default BET. Lots of non-brain tissue still included. Middle row: BET with a more stringent threshold. Still some non-brain included on the edge of the cortex. Bottom row: Improved BET mask shown in green. It successfully excludes the non-brain that the original stringent BET left in. ....	61
Figure 2-5. Overview of the pre-processing pipeline of the diffusion-weighted images. ....	62
Figure 2-6. Examples of commonly seen artefacts in raw diffusion data. Examples taken from the PADDINGTON study. (A) Both images have geometric distortions. (B) “Venetian Blind” or interlace effect. (C) Hyper-intensities in region near sinuses. (D) “Checkers” artefact. (E) High intensity axial slice, highlighted by arrow. ....	64
Figure 2-7. BET examples. B0 image is of a control participant from the Track-HD study. (A) Default BET: Mask is too large and includes non-brain (yellow). (B) Improved BET: Mask is too tight (blue). (C) Original BET mask eroded by one voxel: Flat ‘chimney’ effect at top of mask (red). (D) Top slice zeroed (red) and	

removed from BET mask (white). (E) Improved fit using original BET mask eroded and top slice removed (green). .....	66
Figure 2-8. The major eigenvector direction indicated by colour (red: right-left; green: anterior-posterior; blue: superior-inferior) overlaid onto the FA map. Data taken from a control participant in the Track-HD study.....	67
Figure 2-9. Examples of the quantitative maps outputted using FSL's DTIFIT. Images are of a control participant from the Track-HD study. (A) FA. (B) MD. (C) AD. (D) RD (average of $\lambda_2$ and $\lambda_3$ ).....	68
Figure 2-10. Overview of the ROI analysis pipeline. These steps are applicable for outputting diffusion metrics across ROIs. The registration step can also be applied when preparing images for tractography, but is not required for tract-based spatial statistics. ....	69
Figure 2-11. Failed T1 to FA FLIRT registration. Example of what happens when the T1 image is not brain extracted. Example of a control participant from the Track-HD study.....	70
Figure 2-12. Examples of FLIRT (blue), ANTs (red) and NiftyReg (green) registration. A WM mask is shown overlaid on a control Track-HD participant's FA image. ....	71
Figure 2-13. Example of the warped WM (green) and GM (purple) eroded, thresholded and binarised masks overlaid on the FA image. Example is of a control Track-HD participant.....	72
Figure 2-14. Overview of the default TBSS and DTI-TK registration pipelines used for TBSS analysis. ....	75
Figure 3-1. CC segmentation. Seeded region where threshold has successfully segmented the structure with no over-spill. ....	87
Figure 3-2. Examples of obvious edits to the CC segmentation. Remove over-spill delineated by the purple line (left) and the fornix and rostral seepage,	

highlighted by red arrows (middle). Right: Example of a blood vessel that needs removing, highlighted by the green arrows. .... 87

Figure 4-1. Axial slices from each of the three customised tensor templates..... 94

Figure 4-2. Subtraction maps. (A) Template 1 minus template 2. (B) Template 1 minus template 3. (C) Template 2 minus template 3. Bright voxels indicate higher values for template 1 in A and B and for template 2 in C. Dark voxels indicate higher values in template 2 in A and for template 3 in B and C. Grey values are exactly equal to zero. .... 95

Figure 4-3. FA and RD maps computed from the high resolution whole group templates, created using each of the three customised templates, labelled 1, 2 and 3. .... 96

Figure 4-4. Subtraction maps of the FA and RD maps computed from the high resolution whole group templates, created using each of the three customised templates. (A) Template 1 minus template 2. (B) Template 1 minus template 3. (C) Template 2 minus template 3. Bright voxels indicate higher values for template 1 in A and B and for template 2 in C. Dark voxels indicate higher values in template 2 in A and for template 3 in B and C. Grey values are exactly equal to zero..... 97

Figure 4-5. Mean FA images and FA skeletons for template 1 (green), template 2 (blue) and template 3 (red). Skeletons are thresholded between 0.2 - 0.7..... 98

Figure 4-6. Common voxels (pink) to all three FA skeleton masks generated using each of the three templates, overlaid on the mean FA image for template one. .... 98

Figure 4-7. Scatter plots of agreement between the mean FA values extracted from the three different template-registered data. The line of equality (black) is also shown. .... 102

Figure 4-8. Scatter plots of agreement between the mean RD values extracted from the three different template-registered data. The line of equality (black) is also shown.  $\cdot 10^{-3} \text{mm}^2 \cdot \text{s}^{-1}$  ..... 103

Figure 4-9. TBSS results (FWE-corrected, $p < 0.05$ ) for between-group differences in FA from analyses using each of the three templates. Skeletonised results are displayed on the total mean FA image. (A) Controls > Premanifest HD (B) Controls > Early HD (C) Premanifest > Early HD. Results from analysis using template one are in red, template two in blue and template three in green.....	105
Figure 4-10. TBSS results (FWE-corrected, $p < 0.05$ ) for FA contrast premanifest > early HD. These slices highlight the more pronounced differences between the analyses using each of the three templates. Results using template one are in red, template two in blue and template three in green. ....	105
Figure 4-11. TBSS results (FWE-corrected, $p < 0.05$ ) for between-group differences in RD from analyses using each of the three templates. Skeletonised results are displayed on the total mean FA image. (A) Premanifest > Controls (B) Early HD > Controls (C) Early HD > Premanifest. Results from analysis using template one are in red, template two in blue and template three in green.....	107
Figure 5-1. Schematic demonstrating the principles underlying the Poffenberger Paradigm. ....	113
Figure 5-2. Screenshots of the left and right lateralised stimuli and fixation cross in the interhemispheric transfer task. ....	115
Figure 5-3. Schematic diagram of the interhemispheric transfer task. ....	116
Figure 6-1. Examples of congruent (left) and incongruent (right) stimuli in the interference task. ....	120
Figure 6-2. Schematic diagram of the interference task. Conditions 2, 8 and 5 are shown. ....	122
Figure 7-1. (A) Boxplot of baseline CC volumes (% TIV). (B) Boxplot of annualised CC volume change (% baseline volume per year) measured over 24 months..	131
Figure 7-2. Scatter graphs depicting the association between baseline CC volume (% TIV) and performance on the three pre-defined cognitive measures. (A) Circle	

Tracing Indirect task, (B) Stroop Word Reading task, (C) Trail Making B task. .....	134
Figure 8-1. Harvard-Oxford Cortical Structural atlas (left) and JHU ICBM-DTI-81 White-Matter Labels atlas (right).....	142
Figure 8-2. TBSS results (FWE-corrected, $p < 0.05$ ) showing the positive correlation between WM volume (% TIV) and FA (red) in the premanifest HD group (A) and the early HD group (B). Skeletonised results are overlaid on the mean FA skeleton mask (green) on the mean FA image. ....	144
Figure 8-3. TBSS results (FWE-corrected, $p < 0.05$ ) showing the negative correlation between WM volume (% TIV) and AD (blue) in the premanifest HD group (A) and the early HD group (B). Skeletonised results are overlaid on the mean FA skeleton mask (green) on the mean FA image. ....	145
Figure 8-4. TBSS results (FWE-corrected, $p < 0.05$ ) showing the negative correlation between WM volume (% TIV) and RD (blue) in the premanifest HD group (A) and the early HD group (B). Skeletonised results are overlaid on the mean FA skeleton mask (green) on the mean FA image. ....	146
Figure 8-5. TBSS results (FWE-corrected, $p < 0.05$ ) in the control group. (A) Positive correlation between GM volume (% TIV) and FA (red). (B) Negative correlation between GM volume (% TIV) and RD (blue). Skeletonised results are overlaid on the mean FA skeleton mask (green) on the mean FA image. ....	150
Figure 8-6. TBSS results (FWE-corrected, $p < 0.05$ ) in the premanifest HD group. (A) Positive correlation between GM volume (% TIV) and AD (red). (B) Positive correlation between GM volume (% TIV) and RD (red). Skeletonised results are overlaid on the mean FA skeleton mask (green) on the mean FA image. ....	151
Figure 9-1. (A) FA. (B) MD. (C) AD. (D) RD. (E) Principle diffusion, directions are encoded in colours where red = right-left; green = anterior-posterior and blue = superior-inferior. (F) Mean FA skeleton overlaid onto the mean FA. ....	165

Figure 9-2. TBSS results (FWE-corrected, $p<0.05$ ) for between-group differences in FA. Skeletonised results (red) are overlaid on the mean FA skeleton mask (green) on the mean FA image. (A) Controls > Premanifest HD, (B) Controls > Early HD, (C) Premanifest > Early HD. ....	166
Figure 9-3. TBSS results (FWE-corrected, $p<0.05$ ) for between-group differences in FA. Skeletonised results (red) are overlaid on the mean FA skeleton mask (green) on the mean FA image. (A) Early HD > Controls, (B) Early HD > Premanifest. ....	167
Figure 9-4. TBSS results (FWE-corrected, $p<0.05$ ) for between-group differences in MD. Skeletonised results (dark blue) are overlaid on the mean FA skeleton mask (green) on the mean FA image. (A) Premanifest HD > Controls, (B) Early HD > Controls, (C) Early HD > Premanifest HD. ....	169
Figure 9-5. TBSS results (FWE-corrected, $p<0.05$ ) for between-group differences in AD. Skeletonised results (pink) are overlaid on the mean FA skeleton mask (green) on the mean FA image. (A) Premanifest HD > Controls, (B) Early HD > Controls, (C) Early HD > Premanifest HD. ....	171
Figure 9-6. TBSS results (FWE-corrected, $p<0.05$ ) for between-group differences in RD. Skeletonised results (light blue) are overlaid on the mean FA skeleton mask (green) on the mean FA image. (A) Premanifest HD > Controls, (B) Early HD > Controls, (C) Early HD > Premanifest HD. ....	171
Figure 9-7. Boxplots of WM diffusion metrics for each group. $\Delta 10^{-3}\text{mm}^2.\text{s}^{-1}$ . * $p<0.001$ ; ** $p<0.05$ . ....	175
Figure 10-1. The CC mask (blue) overlaid on the control groups' mean FA and mean FA skeleton (green). ....	190
Figure 10-2. The genu (red), body (green) and splenium (blue) of the CC overlaid on the MNI brain. The exclusion mask to prevent wayward fibre tracking for the genu and body is shown in pink. The exclusion mask for the splenium is shown in yellow. ....	192

Figure 10-3. Top row: Fibre tracts of the genu (red), body (green) and splenium (blue) overlaid on a T1 image. Bottom row: Fibre tracts of the genu (red), body (green) and splenium (blue) warped into diffusion space and overlaid on a FA image. ....	193
Figure 10-4. Mean RT (ms) for the premanifest HD group (left) and control group (right) as a function of responding hand at baseline. ....	197
Figure 10-5. Association between non-dominant hand CUD (ms) and CC volume (% TIV) in the premanifest HD group with adjusted regression line (red). ....	198
Figure 10-6. Association between non-dominant hand CUD (ms) and AD ( $(\text{mm}^2/\text{s}) \times 10^{-3}$ ) in the CC in the premanifest HD group, with adjusted regression line (red). ....	201
Figure 10-7. TBSS results for the positive association between AD and non-dominant hand CUD in the premanifest HD group. Skeletonised results are overlaid on the mean FA skeleton mask (green) on the mean FA image. Red-yellow voxels are thresholded at $p < 0.05$ (FWE-corrected). ....	203
Figure 10-8. Association between non-dominant hand CUD (ms) and FA within the genu of the CC in the premanifest HD group with adjusted regression line (red). ....	204
Figure 10-9. Association between genu tract FA and CPO in the premanifest HD group with the unadjusted fitted line (red). ....	204
Figure 10-10. Mean RT (ms) for the premanifest HD group (left) and control group (right) as a function of responding hand at visit two. ....	207
Figure 11-1. Top row: Left ACC (green) and right ACC (blue). Bottom row: Left DLPFC (pink), right DLPFC (light blue), left caudate (dark blue), right caudate (red), left prefrontal thalamus (yellow) and right prefrontal thalamus (green). All regions are overlaid on an individual T1-weighted image. ....	231



Figure 11-2. Top row: Midbrain, hemisphere and thalamic exclusion masks for tracts within the left hemisphere (yellow). Middle row: exclusion masks for ACC fibre tracking overlaid on the MNI brain. Bottom row: Example of wayward fibres from the right ACC (red) and the placement of the exclusion mask (blue) to prevent it.....	232
Figure 11-3. Box plot of median RTs (ms) for the control group (green) and the premanifest HD group (red) at baseline. ....	234
Figure 11-4. Association between the up/down interference effect and caudate volume (%TIV) in the premanifest HD group with adjusted regression line. ....	242
Figure 11-5. Association between the up/down congruent RT and caudate volume (%TIV) (top), and between the left/right congruent RT and caudate volume (%TIV) (bottom) in the premanifest HD group (red) and controls (green), along with adjusted regression lines. ....	242
Figure 11-6. Association between the up/down incongruent RT and caudate volume (%TIV) (top), and between the left/right incongruent RT and caudate volume (%TIV) (bottom) in the premanifest HD group (red) and controls (green), along with adjusted regression lines. ....	243
Figure 11-7. Top row: Left and right ACC tracts (red). Middle row: Left and right DLPFC – caudate tracts (green). Bottom row: Left and right DLPFC - thalamus tracts (blue). All tracts are overlaid on the FA image. ....	245
Figure 11-8. Association between the left/right (top) and the up/down (bottom) interference effect and FA in the right DLPFC–caudate tract in the premanifest HD group. Displayed with adjusted regression lines. ....	246
Figure 11-9. Association between the up/down interference effect and RD in the left DLPFC-thalamus tract (top), the right DLPFC – thalamus tract (middle) and the right DLPFC – caudate tract (bottom) in the premanifest HD group. Displayed with the adjusted regression lines. RD units are $(\text{mm}^2/\text{s}) \times 10^{-3}$ . ....	247

Figure 11-10. Correlation between FA in the right DLPFC–caudate tract and CPO in the premanifest HD group, along with the unadjusted fitted line. .... 248

Figure 11-11. Top: Correlation between RD ( $\text{mm}^2/\text{s} \times 10^{-3}$ ) in the right DLPFC–caudate tract and CPO in premanifest HD. Bottom: Correlation between RD ( $\text{mm}^2/\text{s} \times 10^{-3}$ ) in the right DLPFC–thalamus tract and CPO in premanifest HD. Both are shown with the unadjusted fitted lines. .... 249

## Table of Tables

Table 2-1. Demographics of the Track-HD Participants at Baseline.....	48
Table 4-1. Demographics and Clinical Characteristics of Participants.....	91
Table 4-2. Mean (SD) Diffusion Values from White Matter Skeleton.....	99
Table 4-3. Between-Template Differences in Diffusion Metrics by Group .....	99
Table 4-4. Between-Group Differences in Diffusion Metrics by Template .....	101
Table 4-5. Number of Significant Voxels (% of White Matter Skeleton) .....	108
Table 5-1. Table of Mean (SD) Reaction Times (ms) .....	117
Table 6-1. Interference Task Conditions.....	121
Table 6-2. Mean (SD) Reaction Time (ms) and Number of Errors .....	123
Table 7-1. Demographic, Clinical and Cognitive Characteristics of Participants .....	127
Table 7-2. Table of Mean (SD) Baseline CC Volumes (% of TIV) and Annualised rates of CC Volume Change (% of baseline) measured over 24 months .....	131
Table 7-3. Table of Adjusted Between-Group differences in Baseline CC Volume (% of TIV) and Annualised CC Volume Change (% of baseline volume) Over 24 months .....	132
Table 7-4. Relationship between Baseline CC Volume (% TIV) and Baseline Task Performance .....	133
Table 8-1. Peak Voxel Information for Associations with White Matter Volume .....	147
Table 8-2. Peak Voxel Information for Associations with Grey Matter Volume .....	152
Table 9-1. Demographic and Clinical Characteristics of Participants .....	162

Table 9-2. Peak Voxel Information for Between-Group Differences in FA .....	167
Table 9-3. Peak Voxel Information for Between-Group Differences in MD .....	170
Table 9-4. Peak Voxel Information for Between-Group Differences in AD .....	172
Table 9-5. Peak Voxel Information for Between-Group Differences in RD .....	173
Table 9-6. Mean Diffusion Metrics in White Matter by Group .....	174
Table 9-7. Adjusted Between-Group Differences in White Matter Diffusion .....	174
Table 10-1. Demographic and Clinical Characteristics of Participants .....	185
Table 10-2. Mean (SD) RT (ms) and Adjusted Between-Group Differences at Baseline .....	196
Table 10-3. Adjusted Within-Group Analysis of the Effects of Hand Dominance and Crossing on RT (ms) at Baseline .....	197
Table 10-4. Association Between CC Volume and Diffusion Metrics and Interhemispheric Transfer Time (ms) .....	199
Table 10-5. Peak Voxel Information for the Correlation Between AD and Non- Dominant Hand CUD in the Premanifest HD Group .....	202
Table 10-6. Mean (SD) RT (ms) and Adjusted Between-Group Differences at Visit Two .....	206
Table 10-7. Mean (SD) Annualised Change in RT (ms) and Adjusted Between-Group Differences in Annualised Change .....	209
Table 10-8. Adjusted Within-Group Analysis of Change in RT (ms) .....	210
Table 10-9. Adjusted Within-Group Analysis of the Effects of Hand Dominance and Crossing on Annualised Change in RT (ms) .....	210

Table 11-1. Demographic and Clinical Characteristics of Participants .....	225
Table 11-2. Task Conditions .....	226
Table 11-3. Mean (SD) RT (ms) and Adjusted Between-Group Differences at Baseline .....	235
Table 11-4. Mean (SD) Number of Errors and Adjusted Between-Group Differences at Baseline .....	236
Table 11-5. Adjusted Within-Group Analysis of the Effects of Arrow Direction and Congruence on RT (ms) and Number of Errors at Baseline .....	237
Table 11-6. Association Between Interference RT (ms) and Imaging Measures .....	239
Table 11-7. Adjusted Associations Between RT and Caudate Volume (% TIV) .....	244
Table 11-8. Adjusted Within-Group Analysis of Change in RT (ms) .....	251

## List of Abbreviations

3T	3 Tesla
ACC	Anterior cingulate cortex
AD	Axial diffusivity
ADC	Apparent diffusion coefficient
ANTs	Advanced Normalisation Tools
BEDPOSTX	Bayesian Estimation of Diffusion Parameters Obtained using Sampling Techniques
BET	Brain Extraction Tool
CAG	Cytosine-Adenosine-Guanine
CAP	CAG-Age Product
CC	Corpus callosum
CPO	Cumulative Probability to Onset
CSF	Cerebrospinal fluid
CUD	Crossed-uncrossed difference
DARTEL	Diffeomorphic Anatomical Registration Through Exponentiated Lie Algebra
DLPFC	Dorsolateral-prefrontal cortex
DTI	Diffusion tensor imaging
DTI-TK	Diffusion Tensor Imaging Toolkit
DWI	Diffusion weighted imaging
EPI	Echo planar imaging
FA	Fractional anisotropy
FDT	FMRIB Diffusion Toolbox
fMRI	Functional magnetic resonance imaging
FMRIB	Functional Magnetic Resonance Imaging of the Brain - Analysis Group, Oxford University, UK
FOV	Field of view
FSL	FMRIB Software Library
FWE	Family-Wise Error
GLM	General linear modelling
GLS	Generalised least squares (regression)
GM	Grey matter
H <sub>0</sub>	Null hypothesis
HD	Huntington's disease
HD1	Huntington's disease – stage 1

HD2	Huntington's disease – stage 2
<i>HTT</i>	Huntingtin protein
ICC	Intraclass correlation coefficient
IFOF	Inferior fronto-occipital fasciculus/fasciculi
ILF	Inferior longitudinal fasciculus/fasciculi
ISCED	International Standard Classification of Education
ITT	Interhemispheric transfer time
LVF	Left visual field
MBI	Mean brain intensity
MD	Mean diffusivity
MIDAS	Medical Image Display and Analysis Software
MNI	Montreal Neurological Institute
MP-RAGE	Magnetization prepared rapid gradient echo
MRI	Magnetic resonance imaging
N/n	Number
OLS	Ordinary least squares (regression)
PADDINGTON	Pharmacodynamic Approaches to Demonstration of Disease-modification in Huntington's disease by SEN0014196
PreHD-A	Premanifest Huntington's disease – further from predicted disease onset
PreHD-B	Premanifest Huntington's disease – closer to predicted disease onset
QC	Quality control
RD	Radial diffusivity
ROI	Region of interest
RT	Reaction time
RVF	Right visual field
SD	Standard deviation
SDMT	Symbol Digit Modalities Test
SLF	Superior longitudinal fasciculus/fasciculi
SPM	Statistical Parametric Mapping
TBSS	Tract-based spatial statistics
TE	Echo time
TFC	Total Functional Capacity
TFCE	Threshold-Free Cluster Enhancement
TIV	Total intracranial volume
TMS	Total Motor Score

TPM	Tissue probability map
TR	Repetition time
UCL	University College London
UF	Uncinate fasciculus/fasciculi
UHDRS	Unified Huntington's Disease Rating Scale
V1	Visit 1
V2	Visit 2
VBM	Voxel-based morphometry
WM	White matter



## **Aims of this Thesis**

The main aim of this thesis is to investigate white matter (WM) degeneration and its effects in Huntington's disease (HD). Using multi-modal image analysis, this thesis will further understanding of the underlying WM pathology of HD and by designing novel neuropsychological tests will measure the symptomatic effects of degeneration in this tissue. Specifically, this thesis will:

1. Assess and improve current imaging techniques to better ascertain structural brain changes and optimise technique sensitivity in premanifest and early HD by:
  - developing a novel structural segmentation technique for the corpus callosum (CC).
  - investigating the effects of template choice in tensor-based registration of diffusion images using an optimised technique.
2. Assess cognitive performance in the premanifest stage of HD using novel hypothesis-driven neuropsychological tasks by:
  - developing a novel cognitive task to measure interhemispheric information transfer and known degeneration of the CC.
  - developing a novel cognitive task to measure susceptibility to interference and known degeneration of associated WM tracts.
3. Apply the optimised neuroimaging techniques and cognitive tasks to a large clinical cohort in order to characterise WM abnormalities present in premanifest and early stage HD and their relation to clinically relevant behaviour.

# 1. Background

This introductory chapter firstly provides a background to HD, secondly presents the two imaging techniques applied in this thesis and describes some of the key cognitive deficits seen in HD, and then thirdly summarises the key themes and motivations of this thesis.

## 1.1 Introduction to Huntington's Disease

### 1.1.1 Genetics and Neuropathology

HD is a hereditary neurodegenerative disorder characterised by devastating physical, behavioural and mental dysfunction. First described by George Huntington in 1872, HD is today often regarded as a model neurodegenerative disease because of its known single cause, an expanded Cytosine-Adenosine-Guanine (CAG) trinucleotide repeat in the huntingtin gene (*HTT*) (MacDonald *et al.* 1993). This discovery 23 years ago has not only meant that predictive genetic screening is possible but also has enabled the study of the entire natural course of the disease.

The *HTT*-gene is located on chromosome 4, which codes for the protein huntingtin. The normal huntingtin protein, present throughout the body, is known to be critical in the development of the nervous system and has been found to influence brain-derived neurotrophic factor production and transport, as well as play a role in cell adhesion (Zuccato & Cattaneo 2014). The rest of its function however is not yet fully understood. The mutant form of huntingtin contains an abnormally long polyglutamine sequence, corresponding to the CAG expansion, which misfolds and aggregates within all cells that express the protein. The abnormally aggregated proteins exhibit toxic properties that build up, in turn causing neuronal dysfunction and death. This process is the reason that HD is described primarily as a toxic-gain-of-function disease, with numerous evidence of large huntingtin-rich inclusions from biochemical, cell, model organisms, such as mice, and patient studies (Davies *et al.* 1997; DiFiglia *et al.* 1997; Shao & Diamond 2007; Tobin & Signer 2000).

The age of motor onset of HD is strongly dependent on the length of the CAG repeat expansion, with longer expansions causing earlier onset. CAG repeats of up to 26 are a normal length, and extended CAG repeat lengths of 27-35 will not lead to the disease

but have the potential to expand within one or more generations (van den Bogaard *et al.* 2012). Reduced penetrance is seen with repeat lengths of 36-39, whilst  $\geq 40$  CAG repeats show full penetrance, meaning the carrier will definitely develop HD at some point during adulthood, with a mean age of onset about 45 years (Bates *et al.* 2015). The expected age of onset can be predicted using a commonly applied formula (Langbehn *et al.* 2004). The length of the CAG repeat only accounts for approximately 56% of the variation in age of disease onset (Gusella *et al.* 2014), therefore the remaining variation is explained by genetic and environmental modifiers, plus biological traits already present in the normal population may also influence HD pathogenesis.

The exact mechanisms of how the toxic process causes neurodegeneration in HD are not fully understood but have been the scrutiny of much research since the gene's discovery. As well as the direct neurotoxic effects of the mutant protein mentioned above, four other possible mechanisms have been described. One is mitochondrial disturbances leading to impaired energy metabolism, another is the transcriptional dysregulation of multiple genes. Additionally, disrupted intracellular processes including synaptic disruptions and also excitotoxicity causing overstimulation and cell death (Estrada Sanchez *et al.* 2008; Ross & Tabrizi 2011; Roze *et al.* 2008; Sturrock & Leavitt 2010) are suggested to play a role. It is most likely a combination of these processes rather than any one alone that causes the neurodegeneration seen in HD.

The neuropathological hallmark of HD is progressive striatal degeneration. Post mortem studies revealed the gradual loss of GABAergic medium spiny neurons, causing atrophy of the caudate nucleus and putamen (Vonsattel *et al.* 1985). Spiny neurons are projection neurons, which make up 90% of neostriatal neurons and receive tens of thousands of inputs from the cortex and thalamus (Vonsattel *et al.* 2011). As the disease progresses, atrophy spreads throughout the brain, affecting the cerebral white matter (WM), thalamus, cerebral cortex and cerebellum (Vonsattel *et al.* 2011).

### **1.1.2 Prevalence and Clinical Presentation**

HD is an autosomal dominant disease, meaning that only one parent needs to be carrying the abnormal gene for it to be inherited and a child of an affected parent has a 50% chance of being affected by the disorder themselves. Genetic testing is available for at-risk individuals (e.g. those with a parent with HD or a positive genetic test) over the age of 18 years. Prevalence of HD is 4-10 per 100,000 in the Western world, with

many more people potentially at risk (Ross & Tabrizi 2011). The global population prevalence has been found to show a more than tenfold variation across regions, with very low rates in South Africa and Zimbabwe (0.02 and 1.00 per 100,000 respectively), in contrast to higher rates in predominantly Caucasian populations (9.71 per 100,000) (Rawlins *et al.* 2016).

A recent systematic review found that despite the absence of any consistent change in the incidence of HD in the UK between 1990 and 2010, there has been a large increase in the prevalence of the disease over the same period (Wexler *et al.* 2016). A few possible reasons for this increase have been proposed, including general practitioners being more willing to report an HD diagnosis in the records of patients previously diagnosed due to a decrease in the stigma associated with HD, plus an increase in survival rates (Wexler *et al.* 2016).

HD is characterised by a triad of symptoms; motor dysfunction, most commonly chorea (jerky, involuntary movements), cognitive impairment (e.g. emotion recognition, attention), and neuropsychiatric problems (such as depression and apathy). It is the onset of motor symptoms, seen in someone at risk or tested genetically positive for the CAG expansion that forms the basis of a manifest HD diagnosis. These are assessed using the Unified Huntington's Disease Rating Scale (UHDRS) (Huntington Study Group 1996) motor examination, which ranges from 0 (no motor signs) to 124 (severe motor impairment). A diagnostic confidence score of 4 corresponds to 99% confidence that the motor signs are attributable to HD (Reilmann *et al.* 2014). Typically, a UHDRS Total Motor Score (TMS) of around 15 is usually strongly supportive of HD diagnosis (Bates *et al.* 2015). Total Functional Capacity (TFC) is also measured as part of the UHDRS on a scale from 0 (complete dependence) to 13 (full capacity) (Huntington Study Group 1996). A TFC score of 13-11 defines Stage I of the disease and a TFC score of 10-7 defines Stage II, also often called the early stages. Late stages III and IV are defined by TFC scores of 6-3 and 2-1 respectively (Shoulson & Fahn 1979).

Recent advances in the understanding of HD through neuroimaging and natural history studies have challenged the formal definition of HD and it is now well known that cognitive and behavioural changes are often seen many years before a motor diagnosis (Paulsen *et al.* 2006a; Tabrizi *et al.* 2009). Therefore, more-formal definitions have been proposed (Reilmann *et al.* 2014). Premanifest HD refers to the symptom-free period before diagnosis in someone with genetic confirmation of positive gene status, followed

by prodromal HD, which refers to when subtle signs and symptoms are present, and finally manifest HD. Figure 1-1 shows the natural course of HD.

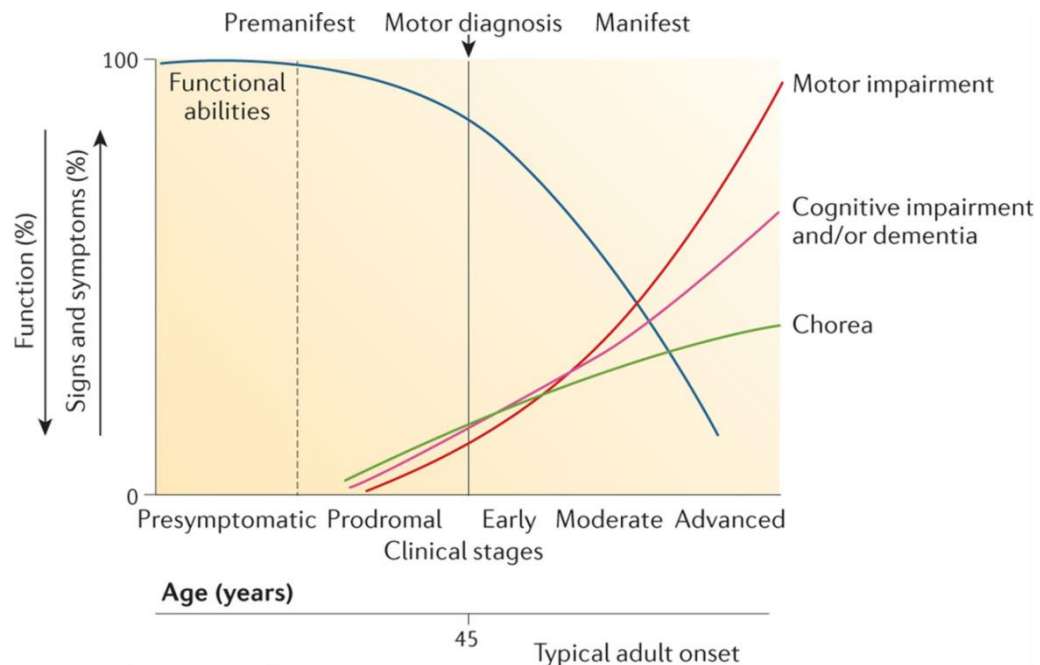


**Figure 1-1. Natural history of HD. Adapted from Bates *et al.* (2015).**

### 1.1.3 Treatments

There is currently no cure for HD but there are many symptomatic treatments available. To alleviate the symptoms of chorea, tetrabenazine, and more recently pridopidine (Dyhring *et al.* 2010) have been trialled and are commonly administered to HD patients (Zielonka *et al.* 2015). A common psychiatric feature of HD is depression, for which the standard treatment applies, i.e. selective serotonin reuptake inhibitors, or serotonin-norepinephrine reuptake inhibitors (Zielonka *et al.* 2015). If psychotic symptoms are present as well as depression, then antipsychotics should also be prescribed (Zielonka *et al.* 2015).

As well as symptomatic treatments, several disease-modifying drugs have been trialled, such as Baclofen, Lamotrigine, and Riluzole, including some more well-known substances, such as vitamin E and creatine, however, disappointingly none proved to be effective as a disease-modifying therapy (Mestre *et al.* 2009). Despite the current lack of disease-modifying treatments, the last 20 years of HD research has yielded an

increasing number of therapeutic targets (Wild & Tabrizi 2014). Future clinical trials of potential compounds are imminent, plus there are some very exciting and promising approaches emerging.

Reducing the expression of the mutant huntingtin protein using RNA interference, also referred to as ‘gene silencing’ or ‘huntingtin lowering’ is amongst the most promising therapeutic approaches (Wild 2016). Results in mice models have been very encouraging with not just an improvement in motor symptoms, but also a slowing of neuropathology (Harper *et al.* 2005). In September 2015 the first phase 1 human trial began at UCL (<http://www.bbc.co.uk/news/health-34552041>). An antisense oligonucleotide drug designed to suppress the production of huntingtin was successfully administered to a patient (<https://clinicaltrials.gov/ct2/show/NCT02519036>). The trial is still ongoing and HD researchers continue to be optimistic about its future use as a HD therapy.

## **1.2 Neuroimaging Techniques**

Neuroimaging techniques have been central to the current understanding of neurobiological changes in HD. Various brain imaging techniques have been used in the study of HD, from the assessment of brain structure and activation using magnetic resonance imaging (MRI) and functional MRI (fMRI), through to quantification of specific neural changes and metabolites using positron emission tomography and magnetic resonance spectroscopy. These techniques have previously been discussed in terms of both their cross-sectional and longitudinal applications in HD (Niccolini & Politis 2014; Rees *et al.* 2013), and MRI in particular has formerly been comprehensively reviewed (Kloppel *et al.* 2009).

The focus of this thesis, however, is structural T1-weighted and diffusion-weighted MRI, which are discussed below. In particular, this project has applied these imaging techniques to the investigation of white matter (WM) degeneration, therefore, after an introduction to the two imaging techniques the focus of this section will be the major research into WM and a discussion of the key results.

### 1.2.1 Structural MRI

Structural MRI is widely used in HD research because it is possible to visualise brain anatomy and quantify whole-brain and regional atrophy. This technique works by recording the radio signal emitted by protons when they are aligned in a magnetic field and exposed to a radio-frequency pulse. Different tissue types emit different signals and have different tissue relaxation properties, which contribute to the image contrast. T1-weighted images demonstrate the relaxation time of excited nuclei returning to their normal state.

The majority of HD research has focused on the most pathologically-affected structures, the caudate nucleus and putamen. MRI studies have showed pronounced volume loss of these regions in both premanifest and manifest HD gene-carriers compared with healthy controls (Aylward *et al.* 1996; Paulsen *et al.* 2006b; Rosas *et al.* 2001; Tabrizi *et al.* 2009; Wolf *et al.* 2013). Grey mater (GM) degeneration in premanifest and early stage HD is also increasingly well documented, with evidence of both regional volume loss (Tabrizi *et al.* 2009; 2011; 2012; 2013) and cortical thinning (Rosas *et al.* 2008).

WM degeneration in HD is now an established hallmark of the disease in both premanifest and manifest HD gene-carriers. The following sections will discuss the key structural MRI findings in WM in terms of the two approaches typically taken; hypothesis-driven region of interest (ROI) analysis and exploratory whole-brain analysis.

#### ***Region of Interest Analysis***

The majority of ROI studies in HD have focused on the most severely affected structures, such as the caudate and putamen, therefore, ROI analyses of WM structures are less common. That being said, a number of studies have looked at whole-WM as an ROI to measure atrophy between groups and over time.

Cerebral WM volume has been found to be significantly smaller in premanifest HD compared with healthy controls (Paulsen *et al.* 2006b; Paulsen *et al.* 2010), in particular the frontal WM volume was predominantly affected using ROI analyses within each of the four lobes (Aylward *et al.* 2011). Cerebral WM has also been found to be significantly associated with proximity to disease onset in premanifest HD (Paulsen *et al.* 2010). However, it has been argued that one limitation of characterising WM

atrophy in relation to disease onset is that imaging measures are correlated with predicted, not actual, proximity to diagnosis (Paulsen *et al.* 2010). This is an unavoidable issue due to the nature of the premanifest population, however, larger observational studies are beginning to follow up premanifest participants and are able to examine relationships with actual disease onset (Paulsen *et al.* 2014; Tabrizi *et al.* 2013).

Cerebral WM volume has also been found to be significantly smaller in early HD compared with controls (Rosas *et al.* 2003) and a recent study revealed longitudinal atrophy of WM over six, nine and 15-month intervals (Hobbs *et al.* 2015). Due to the nature of ROI studies, global volumes are measured and compared, therefore it is difficult to identify which particular parts of the cerebral WM are atrophying, therefore whole-brain mapping techniques may provide more information. Likewise, the technique with which the WM is defined will also influence volumetric results and may under or overestimate volume change.

The current gold-standard ROI measurement technique is manual segmentation whereby an expert traces the outline of a structure by hand on every slice of an MR image. Although highly accurate, this method is very time-consuming and is subject to inter- and intra-rater variability. Hence the development of automated techniques which may be more appropriate for use where large numbers of scans need to be processed in real time by several raters, for example in clinical trials. Both manual and automated methods, however, are hindered by poorly defined boundaries in smaller or complex structures, or particularly in WM analyses at the cortical boundary which can be highly variable across individuals (Smith *et al.* 2006), affecting both accuracy and reliability. The majority of WM ROI analysis using structural images, however, has been conducted using automated segmentation techniques or whole-brain methods, as below.

### ***Whole-Brain Approach***

Structural MRI studies can also take a more exploratory, whole-brain approach to the study of volumetric differences in HD and have revealed widespread atrophy in regions beyond the striatum and throughout the cortex. Voxel-based morphometry (VBM) has revealed many widespread volumetric differences without the restriction of *a priori* assumptions, including the cingulate, pre-central and pre-frontal cortices, occipital,



parietal, and temporal cortices in manifest HD (Henley *et al.* 2009; Hobbs *et al.* 2010; Tabrizi *et al.* 2009; 2011; 2012; 2013).

These particular studies have been very important in HD research and have highlighted the pronounced loss of WM in premanifest individuals (Aylward *et al.* 2011; Tabrizi *et al.* 2009; 2011; 2012; 2013) and in early HD (Hobbs *et al.* 2010; 2013; Tabrizi *et al.* 2011; 2012; 2013). In premanifest HD, WM atrophy has been localised to the frontal lobe (Aylward *et al.* 2011), around the striatum, and posterior-frontal regions (Tabrizi *et al.* 2009). In early HD volume loss has been found to be much more widespread affecting all lobes (Tabrizi *et al.* 2009), and significantly elevated rates of WM atrophy compared with controls are seen over time across all disease stages (Tabrizi *et al.* 2012). WM degeneration has also been associated with longer CAG length and decline in cognitive and motor performance (Hobbs *et al.* 2010; Paulsen *et al.* 2010; Scahill *et al.* 2013).

Despite the automation of the whole-brain approach, there are, however, many differences between studies in terms of the processing steps, software used and statistical models, amongst many other factors. The numerous methodological limitations associated with VBM analyses have previously been examined (Henley *et al.* 2010) and changes in data processing within VBM were found to produce findings that mimicked biological changes. Results, therefore, must always be interpreted with caution.

WM degeneration in manifest HD is well established, however, whole-brain studies have shown less consistent findings in premanifest stages. Some smaller studies, for example, did not find any differences in WM atrophy rates compared with controls (Hobbs *et al.* 2010; Kipps *et al.* 2005). This may have been due to the small sample sizes, but also the characteristics of the premanifest HD group. Participants were far from estimated motor onset with correspondingly low disease burden scores (Hobbs *et al.* 2010). The whole-brain analyses techniques may have been subject to the limitations mentioned above, or may not have been sensitive to the subtle differences in this group and ROI measures may have improved sensitivity to longitudinal change. Equally, techniques designed to assess microstructural changes, such as diffusion-weighted imaging (DWI), may be better able to detect abnormalities at this stage of the disease when more pronounced, macrostructural changes are not yet apparent.

### ***Summary of Structural MRI***

Overall, WM atrophy measures have been shown to be sensitive to both premanifest and manifest HD progression (Tabrizi *et al.* 2012) and are strongly associated with a range of clinical measures including UHDRS TFC (Rosas *et al.* 2011), motor function (Scahill *et al.* 2013), and estimated time to disease onset (Paulsen *et al.* 2010). Hypothesis-driven ROI studies allow the analysis of pathologically-affected structures, whereas whole-brain studies allow more exploratory analysis, without the need for *a priori* assumptions.

Cross-sectional differences measured using structural MRI are useful for making assumptions about disease progression, particularly in highlighting volume loss in individuals many years from disease onset. However, longitudinal studies are vital for determining whether imaging measures are sensitive to volume change over time and the assessment of their utility for clinical trials. Equally, the development of reliable measurement techniques that are sensitive to longitudinal change may provide better characterisation of subtle abnormalities before disease onset.

#### **1.2.2 Diffusion MRI**

DWI is an MR imaging technique that has become increasingly common in the study of HD over the last 20 years. DWI enables the characterisation of water diffusion throughout the brain and has yielded significant insights into the microstructural tissue properties of WM associated with HD pathogenesis. The most common approaches for analysing diffusion data are ROI studies, where diffusion metrics are averaged within *a priori* selected regions, whole-brain voxelwise techniques, such as tract-based spatial statistics (TBSS), and finally tractography, which investigates diffusivity within specific tracts.

### ***Principles of Diffusion Imaging***

Diffusion imaging works on the principle that in water, movement of water molecules is random, diffusing equally in all directions, however, becomes restricted when encountering barriers and obstacles such as cellular structures and axons. This can provide insight into the microstructural properties of the underlying fibres and possible changes in WM fibre organisation. Diffusion is largely isotropic (water movement in all directions) and unrestricted in cerebrospinal fluid (CSF), but largely anisotropic (water

movement is restricted) in WM due to the presence of cellular structures and axonal organisation (Figure 1-2). Diffusion imaging, therefore, focuses on WM microstructure. It is important to note, however, that diffusion imaging can only index diffusion and its displacement when encountering barriers or obstacles over a period of time and is not a direct measure of tissue integrity.

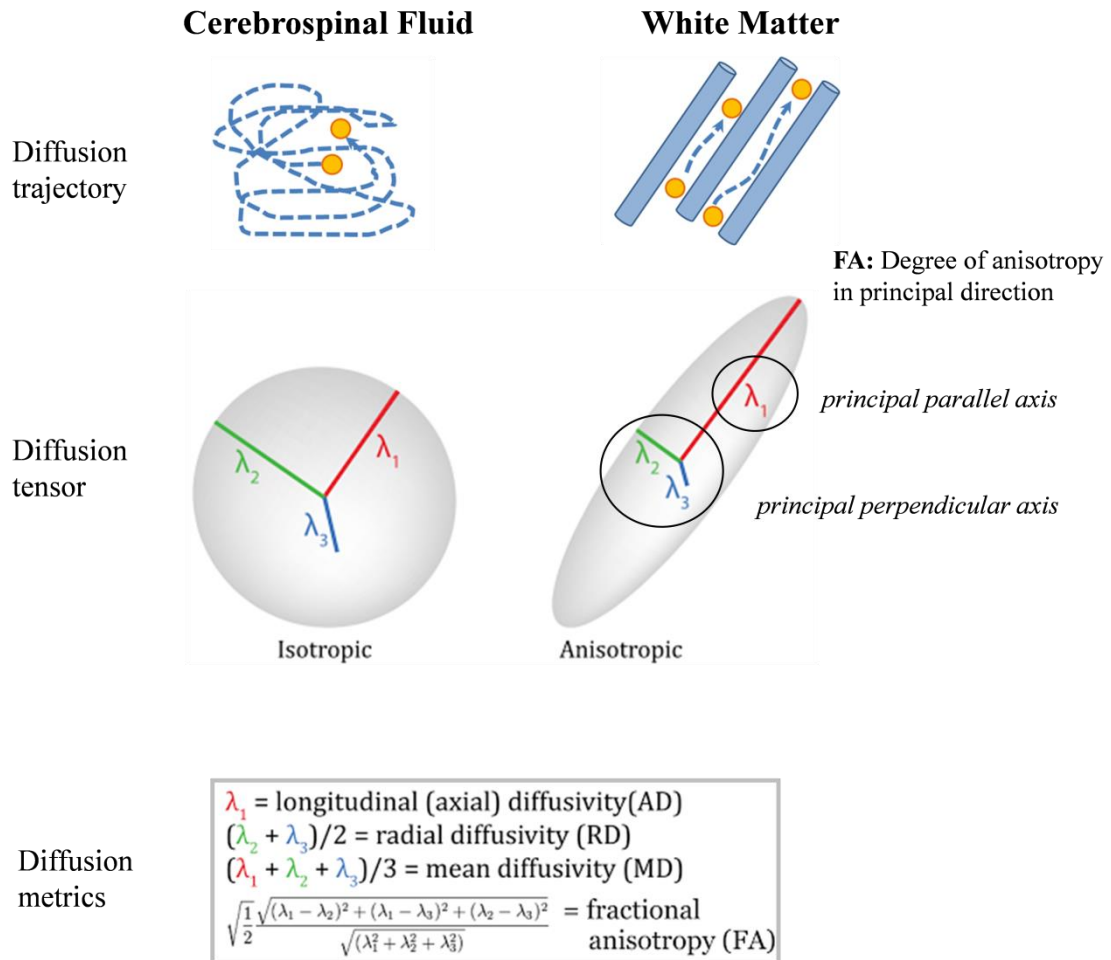


**Figure 1-2. Principles of DTI. Adapted from [www.diffusion-imaging.com](http://www.diffusion-imaging.com).**

Earlier studies using DWI focussed on measures which were rotationally variant and dependent on the direction of an applied gradient. Diffusion Tensor Imaging (DTI) can provide information on the direction and extent of diffusivity independent of the fibre direction (Basser *et al.* 1994). A diffusion tensor is fitted at each voxel, indexing diffusion displacement in a series of orientations, which correspond to the applied gradient directions. Each tensor is characterised by three orthogonal axes that represent diffusion in the direction of the principal parallel axis (nominally the main underlying fibre;  $\lambda_1$ ) and in the direction of the two principal perpendicular axes ( $\lambda_2$ ,  $\lambda_3$ ). For each

of the main axes, eigenvectors define the orientation and corresponding eigenvalues define the value of diffusion; together these give the tensor its shape which represents the diffusion probability (Figure 1-2). It is the relationship between motion in these parallel and perpendicular directions that form the basis of DTI and is used for the calculation of quantitative measures used in DTI analysis (Assaf & Pasternak 2008).

Scalar measures are derived following tensor estimation within each voxel. Fractional anisotropy (FA), perhaps the most commonly used metric, is a measure of the degree of anisotropy in the principal diffusion direction and is typically believed to reflect coherence or organisation of the underlying fibres. However, because it is a summary index of diffusivity along both the parallel and perpendicular axes, it can be influenced by these measures and their underlying biological causes, such as neuronal fibre density, intracellular structures and myelin (Beaulieu 2002). The apparent diffusion coefficient (ADC) reflects the total amount of diffusion in the three principal directions and the mean diffusivity (MD) simply quantifies average diffusion in these three directions. Axial diffusivity (AD) represents diffusion parallel to the main axis ( $\lambda_1$ ) and radial diffusivity (RD) is an average of diffusivity along the two main perpendicular axes ( $\lambda_2, \lambda_3$ ; Figure 1-2). Increases in AD have been purported to reflect axonal injury or degeneration, whilst increases in RD reflect demyelination (Song *et al.* 2002; 2003). However, this is a simplified interpretation and it is important to remember that the diffusion tensor is sensitive to a broad range of factors, including both technical, related to the image itself, and biological, such as crossing axonal fibres and therefore, interpretation should proceed with due caution (Alexander *et al.* 2007).

As previously mentioned, the main focus of diffusion imaging is WM microstructure. However, some studies have investigated the diffusion properties of the most severely affected GM structures, the caudate and putamen. Increases in FA in early manifest HD (Delmaire *et al.* 2013; Douaud *et al.* 2009; Hobbs *et al.* 2013; Muller *et al.* 2016) and premanifest HD (Sanchez-Castaneda *et al.* 2013), as well as elevated AD, RD (Hobbs *et al.* 2013; Muller *et al.* 2016) and MD (Odish *et al.* 2015; Sritharan *et al.* 2010) have been found in these structures compared with controls, however, diffusion metrics in GM are difficult to interpret and could reflect various intra- and extra-cellular processes.

### ***Region of Interest Analyses***

ROI approaches in diffusion studies are often used in conjunction with, and to complement tract-based techniques. Diffusion metrics are extracted from particular regions and mean values within the ROI compared across participants. Several studies have looked at whole-WM as an ROI to measure the overall magnitude of diffusion and compare this between groups. Abnormalities have recently been demonstrated in whole-WM in early manifest HD, evident from increased MD, AD and RD (Hobbs *et al.* 2013; Odish *et al.* 2015) and decreased FA (Hobbs *et al.* 2013) compared with healthy controls.

The corpus callosum (CC) is the largest WM fibre bundle within the brain and the major area of commissural information transfer. Altered diffusion characteristics in the CC may represent pathological changes across the cerebral cortex and, therefore, has frequently been the focus of ROI analysis in DTI studies. ROI analyses of the CC have revealed significant reductions in FA in manifest HD compared to matched control participants in the genu, body, and splenium (Rosas *et al.* 2006; Steventon *et al.* 2015) and reduced FA in premanifest HD in just the CC body (Rosas *et al.* 2006). MD has also been shown to be elevated in manifest HD compared with controls in the whole CC region (Steventon *et al.* 2015).

The internal capsule, another large WM fibre bundle, contains axons running to and from the cortex past the basal ganglia; increases and decreases in FA were found in the internal capsule in both premanifest and manifest HD participants compared with controls (Rosas *et al.* 2006).

ROI analyses have shown consistent findings overall, however, some discrepancies in the literature do exist. No differences were found in FA of whole-WM between manifest HD and control participants (Odish *et al.* 2015). The authors argue that diffusivity measures are more sensitive to microstructural changes compared with FA, which is in line with previous studies (Hobbs *et al.* 2013). Changes were equally more prominent in AD than RD, although not substantial enough to alter FA as well. Only AD in the premanifest HD group was found to significantly differ from both controls and manifest HD participants in whole-WM (Odish *et al.* 2015).

### ***Whole-Brain Analyses***

TBSS analysis is a whole-brain technique that uses voxelwise statistical analysis of diffusion data to localise changes in diffusion in WM tracts (Smith *et al.* 2006; full details of how this technique works are provided in section 2.3.2: Tract-Based Spatial Statistics).

Degeneration of WM in HD measured using TBSS analysis of diffusion data has been well documented. Studies reveal consistent findings of decreased FA and increased measures of diffusivity in widespread areas of WM in HD participants compared with healthy controls. Common regions showing abnormal microstructure are the CC (Bohanna *et al.* 2011; Della Nave *et al.* 2010; Di Paola *et al.* 2014; Novak *et al.* 2013), external capsules (Bohanna *et al.* 2011; Della Nave *et al.* 2010; Novak *et al.* 2013), corona radiata (Bohanna *et al.* 2011; Della Nave *et al.* 2010), superior longitudinal fasciculi (SLF; Bohanna *et al.* 2011; Novak *et al.* 2013), inferior longitudinal fasciculi (ILF; Della Nave *et al.* 2010; Novak *et al.* 2013), as well as parts of the corticospinal tracts (Della Nave *et al.* 2010) and cingulum (Novak *et al.* 2013). AD and RD have also been found to be increased in HD compared with controls (Bohanna *et al.* 2011; Della Nave *et al.* 2010; Di Paola *et al.* 2014). WM diffusion metrics were also shown to be significant predictors of disease burden score (Novak *et al.* 2013).

Degeneration of WM in premanifest individuals has also been revealed using TBSS analysis, although with some inconsistencies in findings. Compared with controls, premanifest participants had lower FA and higher RD in parts of the CC (Di Paola *et al.* 2014), and higher MD in the right CC, right SLF and ILF, and the left external capsule (Novak *et al.* 2013), however, no difference was found in FA between premanifest HD and controls (Novak *et al.* 2013).

A newly developed exploratory technique called cortical pattern matching measured superficial WM, late myelinating tissue situated at the juncture of cortical grey and WM, in premanifest and manifest HD. There were no differences in FA between premanifest HD participants and controls, despite increased AD in occipital and motor areas, but manifest HD patients showed reduced FA in the occipital, temporal and right frontal lobe and increased AD in widespread areas compared with controls (Phillips *et*

*al.* 2016). Superficial WM changes were also strongly correlated with CAG repeat length and disease burden (Phillips *et al.* 2016).

The majority of HD research using TBSS and other whole-brain methods has been cross-sectional but one recent longitudinal study over 18 months found reductions in FA localised to the CC and cingulum in manifest HD participants compared with controls (Poudel *et al.* 2015).

TBSS is also useful for investigating associations between clinical or cognitive variables and diffusion properties within the WM tracts. A recent study found an association between reduced FA and increased levels of depression in HD participants within parts of the splenium, and an association between reduced FA and increased levels of irritability in premanifest HD in parts of the left ILF and SLF (Gregory *et al.* 2015). Lower FA in the frontal cortex, anterior cingulate cortex (ACC), insula and cerebellum in HD participants with subthreshold depressive symptoms has also been found (Sprengelmeyer *et al.* 2014).

There are several limitations to consider when applying TBSS, however. Numerous methodological considerations have been suggested to improve the sensitivity, objectivity and interpretability of results (Bach *et al.* 2014), including incorporating tensor-based registration to prevent sub-optimal anatomical specificity in areas of merging fibres. The quality of image registration can greatly affect anatomical alignment and the registration of images acquired using diffusion MRI is particularly complicated by the fact that these images contain orientational information that can be impacted by spatial transformation (Alexander *et al.* 2001). Tensor-based registration, for example, has been shown to outperform other registration algorithms (Keihaninejad *et al.* 2012; Wang *et al.* 2011), producing more consistent mapping of tensor orientation and, therefore, more reliable results. The choice of FA-based or tensor-based registration, therefore, should be considered when embarking on whole-brain DTI analysis, but also when reviewing previous findings.

### ***Tractography Analyses***

Tractography is a technique applied to DTI data that enables the reconstruction of pre-specified (except in the case of whole-brain tractography) WM tracts within the brain and the investigation of their diffusion metrics. Tractography has been increasingly used

to study the microstructural properties of tracts especially vulnerable to degeneration in HD.

Fibre tracking analysis of the CC has consistently shown decreased FA (Phillips *et al.* 2013; Steventon *et al.* 2015) and increased MD (Steventon *et al.* 2015) and RD (Phillips *et al.* 2013) in both premanifest and manifest HD patients compared with controls. Callosal FA and RD were also found to be correlated with disease burden and CAG repeat length in premanifest and manifest HD (Phillips *et al.* 2013). Similarly, fibre tract analysis showed higher ADC in CC pathways in early HD (Dumas *et al.* 2012).

Higher ADC in early HD (Dumas *et al.* 2012) and increased MD, AD and RD in premanifest HD (Matsui *et al.* 2015) has been found in prefrontal WM tracts compared with controls. Decreased FA and increased MD, AD, and RD in the major tracts of the prefrontal cortex were also associated with increased CAG-Age Product (CAP) scores (Matsui *et al.* 2015).

Other tracts examined include pathways within the sensorimotor network, which have been found to have higher ADC in premanifest and manifest HD compared with controls (Dumas *et al.* 2012), and the corticospinal tract, which has been found to have decreased FA and increased AD and RD bilaterally in HD patients compared with controls (Phillips *et al.* 2014b). Increased AD and RD in the corticospinal tract was also found to be associated with motor impairment in early manifest HD (Muller *et al.* 2016; Phillips *et al.* 2014b) and in premanifest HD, along with decreased FA (Phillips *et al.* 2014b).

Thalamic pathways analysed using tractography have higher ADC (Dumas *et al.* 2012) and higher AD and RD (Muller *et al.* 2016) in early HD compared with controls, plus changes in diffusivity in thalamus-somatosensory cortex tracts were associated with motor deficits (Muller *et al.* 2016). Deep WM tracts have similarly been studied and demonstrated increased AD and RD in premanifest HD participants compared with controls (Phillips *et al.* 2014a). WM connectivity between frontal, parietal and striatal brain regions in both premanifest and manifest HD has also been found to be significantly reduced (measured by the number of streamlines) and associated with motor and cognitive performance (Poudel *et al.* 2014).



### *Summary of Diffusion MRI*

DTI has recently yielded significant insights into brain microstructure in both premanifest and manifest HD. Accumulating evidence indicates that abnormal WM is a hallmark of HD and microstructural changes are apparent before the onset of manifest disease.

Using DTI to examine WM microstructure could be valuable in assessing future therapeutic interventions in HD as it is possible that microstructural change occurs prior to macrostructural change. However, despite both micro- and macrostructural measures being sensitive to HD pathology, statistical comparison has shown no significant advantages between the highest performing measures (Hobbs *et al.* 2013).

It is important to also highlight the caution with which DTI findings must be interpreted. Diffusion imaging only measures diffusivity; it is an indirect measure of microstructure, plus the diffusion tensor is sensitive to a broad range of factors, including image artefacts and crossing axonal fibres. Changes in diffusivity could equally be caused by changes to oligodendrocytes and axonal membranes, or disrupted axonal transport due to the mutant huntingtin protein. Likewise, discrepancies in the literature, particularly in the premanifest stage could be due to the range of analysis techniques and measurements used, or may actually be a reflection of the differential involvement of fibre connections between different regions.

Further longitudinal research is needed to better ascertain whether DTI can provide improved sensitivity compared with macrostructural analysis, as well as the development and consistent use of optimised techniques which incorporate superior image processing techniques, such as tensor-based registration. Continued investigations are also required to further probe diffusivity of the WM in the premanifest stage to understand why changes here are harder to find despite known macrostructural degeneration.

### **1.3 Cognition in HD**

Typically, the most prominent sign of HD is the presence of involuntary motor movements, however, cognitive deficits are also apparent, often preceding the development of motor symptoms. There is little evidence of measurable cognitive

deterioration in individuals far from disease onset, despite the evidence that striatal atrophy and WM loss are apparent at this stage. The focus for current cognitive research in HD, therefore, is characterising the not well-understood link between underlying HD pathology and the cognitive phenotype, particularly in the earliest preclinical phase.

### **1.3.1 Cognitive Phenotype**

Many cognitive domains are affected in HD including the following broad categories; memory, psychomotor speed, emotion recognition and executive function. Language, attention, learning and visuospatial awareness are affected to a lesser extent.

In manifest HD there have been numerous reports of impaired memory functioning in both early and late stages of the disease (Hart *et al.* 2013; Tabrizi *et al.* 2009; Wolf *et al.* 2008). Premanifest HD patients have also demonstrated significantly lower scores on working memory tasks compared with controls (Kloppel *et al.* 2015; Stout *et al.* 2011; Tabrizi *et al.* 2009; You *et al.* 2013). The difficulty with interpreting memory functioning in HD, however, is the many sub-types within memory, e.g. short term, long term and working memory. Of the sub-domains, however, working memory seems to produce the clearest and most consistent findings of impairment in HD, even many years before onset (Dumas *et al.* 2013).

Measures of psychomotor speed, such as the Symbol Digit Modalities Test (SDMT), finger tapping and circle tracing tasks, have consistently been found to be impaired compared with controls in both manifest (Tabrizi *et al.* 2012; Unmack Larsen *et al.* 2015; Vaportzis *et al.* 2014) and premanifest HD (Stout *et al.* 2011; Unmack Larsen *et al.* 2015; Verny *et al.* 2007). SDMT also had the biggest effect size for measuring change in performance over 24 months in early HD patients compared with controls and showed a strong association with decline in TFC and TMS (Tabrizi *et al.* 2012). Indirect circle tracing also showed a strong association with decline in TFC and TMS in early HD (Tabrizi *et al.* 2012).

Emotion recognition, particularly of facial expressions is another domain where both early HD and premanifest HD patients have shown significant dysfunction (Tabrizi *et al.* 2009). Emotion recognition had the biggest effect size in measuring change in performance over 24 months in early HD compared with controls (Tabrizi *et al.* 2012). It has also shown the largest effect size for premanifest participants near to diagnosis

and accounted for the greatest degree of variance in proximity to disease onset (Stout *et al.* 2011). Recognition of negative emotions are especially affected, such as anger, disgust and fear, which have recently been found severely impaired in premanifest HD (Bora *et al.* 2015).

Executive function is a generic term for cognitive functions thought to be mediated by the prefrontal cortex and include tasks such planning, decision making and monitoring. Early and late stage HD patients performed worse compared with controls on problem solving accuracy and other executive function related tasks (Hart *et al.* 2013; Morkl *et al.* 2016; Unmack Larsen *et al.* 2015). Premanifest HD patients also perform worse than controls in measures of executive function (Hart *et al.* 2013; Unmack Larsen *et al.* 2015; Verny *et al.* 2007).

### **1.3.2 Pathology and Cognition**

Numerous studies have attempted to elucidate the complex link between brain structure and cognitive function in HD. Dysfunction of the fronto-striatal circuits has been increasingly investigated due to the known gradual degeneration of the striatum. An association between basal-ganglia cortical connectivity and performance on the SDMT and Stroop word reading test has recently been demonstrated in early manifest patients, suggesting that altered structural connectivity directly contributes to clinical phenotype in HD (Novak *et al.* 2015). Fronto-striatal circuitry in premanifest HD has also been investigated using a Stroop interference task (Beste *et al.* 2012). Response times were longer in premanifest HD participants compared with controls and were associated with the ACC–basal ganglia networks.

### **1.3.3 Challenges in Premanifest HD**

Comprehensive reviews of cognition in premanifest HD report that most studies reliably found declines in visuomotor performance and working memory in those closer to disease onset (Harrington *et al.* 2012; Papp *et al.* 2011; Stout *et al.* 2011). Greater variability in both the detection and cognitive domain affected, however, has been described in those farther from predicted disease onset, or those with less pathology (Papp *et al.* 2011).

Despite unequivocal evidence of striatal atrophy and WM loss in individuals far from predicted clinical diagnosis, evidence of cognitive decline is difficult to observe in those far from onset and, consequently, some discrepancies have arisen in the literature. One study failed to find differences between premanifest HD and controls in a memory task (van der Hiele *et al.* 2007), another, longitudinal changes in psychomotor speed and memory (Witjes-Ane *et al.* 2007). Similarly, change in cognitive performance over 24 months in a large battery of cognitive tests could not be identified in premanifest HD participants compared with controls (Tabrizi *et al.* 2012).

The PREDICT-HD study, a 31-site international study of cognitive, clinical and imaging biomarkers in HD gene-carriers not yet showing motor symptoms (Paulsen *et al.* 2006a), reported that tests assessing psychomotor speed, working memory and emotion recognition were the most sensitive to preclinical neurocognitive effects, however less evidence in individuals far from estimated diagnosis was detected, with the exception of the emotion recognition test (Stout *et al.* 2011). The lack of observed cognitive deficits in individuals far (>15 years) from estimated disease onset, however, does not mean that subtle decline has not already begun. It could be that they have not been detected yet because of effect sizes below detectable thresholds in the samples tested, or the tasks have not been able to adequately target the affected cognitive function (Stout *et al.* 2011).

The above findings suggest that cognitive decline in HD may develop gradually, perhaps over more than a decade. Therefore, cognitive tasks need to be developed to specifically target the underlying structural–functional relationships in order to better characterise deficits in individuals far from onset. Novel tasks designed to directly probe striatal pathways and areas of pathologically affected WM, both cross-sectionally and longitudinally may help to explain the structure-function relationship, as well as detect differences in individuals many years from onset.

#### **1.3.4 Summary of Cognition in HD**

Cognitive impairment is widespread across many cognitive domains in the later stages of HD, however, selectively impacts processing speed, executive function and the ability to multitask in premanifest and early stages (Papoutsis *et al.* 2014). Evidence of cognitive dysfunction in premanifest stages of HD has been inconsistent, however, further research using novel, pathology-targeted tasks may help to resolve this.

## 1.4 Summary

Structural and diffusion MRI have yielded significant insights into WM macro- and microstructure in both manifest and premanifest HD. WM atrophy is a robust marker of disease progression in early HD as well as a predictor of onset in the premanifest stage (Tabrizi *et al.* 2013).

The premanifest stage of HD naturally exhibits less pathology compared with early manifest stages and with reduced pathology comes greater variability both in terms of the cognitive function affected as well the ability to detect deficits. The same is true for imaging techniques and their sensitivity to group differences and change in WM over time. A thorough investigation of current imaging and cognitive tools, applied to a large clinical cohort comprising individuals at various disease stages is needed to address this problem.

The longitudinal multi-national studies Track-HD (Tabrizi *et al.* 2009; 2011; 2012; 2013) and TrackOn-HD (Kloppel *et al.* 2015), which involved well-characterised clinical cohorts, have already made substantial progress in tackling this issue. The work in this thesis aims to add to this progress through an investigation of novel structural and current diffusion imaging techniques, as well as novel neuropsychological tasks to help characterise WM abnormalities present in premanifest and early HD and their relation to clinically relevant behaviour.

## 2. Methodology

### 2.1 Cohorts

This thesis utilised structural MRI and diffusion data from three main studies: Track-HD, TrackOn-HD and PADDINGTON. Details of the studies and their respective cohorts are provided below, along with information regarding two additional participants recruited for the cognitive studies, described in chapters 10 and 11.

#### 2.1.1 Track-HD

Track-HD was a multi-centre, international prospective observational biomarker study designed with similar principles to a clinical trial. The aim of the study was to identify the changes that occur in gene-carriers from the earliest preclinical stages to early stage II disease by assessing a wide range of measurements, including MRI, clinical, quantitative motor, oculomotor, cognitive and neuropsychiatric measures over three years (Tabrizi *et al.* 2009).

The cohort comprised a total of 366 participants recruited from four study sites: Leiden (Netherlands), London (UK), Paris (France) and Vancouver (Canada) (Tabrizi *et al.* 2009). It consisted of 120 premanifest, 123 early HD participants and 123 age and sex-matched healthy controls. Premanifest gene-carriers were defined by having, at baseline, a:

- a. Positive genetic test with CAG repeat length  $\geq 40$
- b. Burden of pathology score  $(\text{CAG} - 35.5) \times \text{age} > 250$  (Penney *et al.* 1997)
- c. Unified Huntington's disease rating scale (UHDRS) (Huntington Study Group 1996) Total Motor Score (TMS)  $\leq 5$

The premanifest group were divided at the baseline group median (10.8) for time to predicted diagnosis (Langbehn *et al.* 2004) into those further from predicted onset (preHD-A, mean 14 years from onset) and those closer to disease onset (preHD-B, mean 8 years from onset). Early HD patients were separated according to their baseline UHDRS Total Functional Capacity (TFC) score (Huntington Study Group 1996) into Stage 1 (HD1, TFC 11-13) and Stage II (HD2, TFC 7-10).

Healthy control participants were spouses or partners of individuals with premanifest or early HD or gene-negative siblings, to ensure consistency of environments with carriers of the *HTT* gene expansion. All participants were required to be aged between 18-65 years, with an absence of any major psychiatric disorder or history of significant head injury at the time of enrolment. Participants were not excluded based on medication usage, unless actively part of an experimental therapeutic trial, to avoid novel, potentially disease-modifying drugs having unknown effects and confounding the results. Full participant demographics are detailed in Table 2-1.

All participants underwent neuroimaging and a large battery of assessments in the clinical, oculomotor, quantitative motor, cognitive, and neuropsychiatric domains. As this was a dynamic study, assessments varied slightly each year in response to new findings. Details are provided in the publications by Tabrizi *et al.* (2009; 2011; 2012; 2013).

Data was collected annually, comprising four time-points in total. 116 premanifest individuals, 114 early HD patients and 115 control participants completed the 12-month follow-up. At 24-months 117 premanifest HD, 116 early HD and 116 controls completed, and at 36-month follow up 97 controls, 104 premanifest and 97 early HD completed. Sample sizes were smaller than baseline and varied at subsequent time points due to participant withdrawal. A full description of data collection, storage and the procedures, including inclusion/exclusion criteria and reasons for participant withdrawal are provided in previous publications (Tabrizi *et al.* 2009; 2011; 2012; 2013).

**Table 2-1. Demographics of the Track-HD Participants at Baseline**

	Controls (n=123)	PreHD			HD		
		PreHD-A (n=62)	PreHD-B (n=58)	Combined (n=120)	HD1 (n=77)	HD2 (n=46)	Combined (n=123)
Age (years)	46.1 (10.2, 23.0–65.7)	41.1 (8.6, 18.6–59.4)	40.6 (9.2, 22.3–64.1)	40.8 (8.9, 18.6–64.1)	47.2 (10.3, 22.8–64.1)	51.4 (8.6, 33.3–63.3)	48.8 (9.9, 22.8–64.1)
Women	68 (55%)	33 (53%)	33 (57%)	66 (55%)	46 (60%)	21 (46%)	67 (55%)
Education (years)	4.0 (1.3)	4.1 (1.1)	3.8 (1.3)	3.9 (1.2)	3.8 (1.3)	3.2 (1.4)	3.6 (1.3)
Disease-burden score*	-	259.1 (30.1)	333.1 (30.0)	294.8 (47.7)	364.1 (74.3)	397.6 (67.5)	376.6 (73.3)
Centres							
Leiden	30	16	14	30	16	14	30
London	30	14	16	30	19	11	30
Paris	30	14	16	30	26	4	30
Vancouver	33	18	12	30	16	17	33

Data are mean (SD, range) or number (%). \*Disease-burden score=age×(CAG length–35.5)(Penney *et al.* 1997). Table adapted from Tabrizi *et al.* (2009).



### **2.1.2 TrackOn-HD**

The TrackOn-HD study followed up 79 controls and 102 premanifest HD participants from the Track-HD study, as well as 33 new controls and 30 new premanifest participants, and involved most of the same assessments, including structural and diffusion MRI, plus additional task and resting-state fMRI data acquisition at each of the three time points. This study aimed to explore the key finding from the Track-HD study; premanifest HD gene-carriers show relatively normal cognitive and motor task performance despite brain loss in areas associated with these tasks. Compensatory mechanisms, therefore, may be responsible for maintaining brain function in these individuals and the TrackOn-HD study aimed to model this compensation (Kloppel *et al.* 2015).

A full description of data collection, storage and the procedures, including inclusion/exclusion criteria in TrackOn-HD are provided in previous Track-HD publications (Tabrizi *et al.* 2009; 2011; 2012; 2013), as well as the recent TrackOn-HD paper (Kloppel *et al.* 2015).

Both Track-HD and the TrackOn-HD study were approved by the local ethics committees and all participants provided written informed consent.

### **2.1.3 PADDINGTON**

The PADDINGTON study (Pharmacodynamic Approaches to Demonstration of Disease-modification in Huntington's disease by SEN0014196) was a European Seventh Framework Programme Project and more information can be found here: <http://www.paddingtonproject.eu>. Part of the project was Work Package 2, an observational, imaging biomarker study that aimed to assess imaging techniques and parameters to support phase II and phase III studies of SEN0014196 in HD patients.

101 participants were recruited from four European sites: Leiden (Netherlands), London (UK), Paris (France) and Ulm (Germany). 61 were early manifest HD participants, classified as stage 1 of the disease (Shoulson & Fahn 1979) with a UHDRS TFC score of  $\geq 11$  (Huntington Study Group 1996). The remaining 40 participants were matched controls i.e. partners, spouses or gene-negative siblings of the early HD participants.

Assessments included structural and diffusion-weighted MRI, plus a battery of cognitive, motor and neuropsychiatric tests (similar to those used in Track-HD) conducted at baseline, six months and 15 months (Hobbs *et al.* 2013; 2015).

#### **2.1.4 Additional Participants**

Two additional participants, one premanifest HD and one control, not from the cohorts above were recruited into the cognitive studies; interhemispheric information transfer (chapter 10) and susceptibility to interference (chapter 11). These participants were recruited to try and reach the recruitment target. One individual was recruited during their routine visit to the HD clinic at The National Hospital for Neurology and Neurosurgery, London, UK. The final participant was recruited through a connection to the HD Research Centre.

## **2.2 Image Acquisition**

### **2.2.1 Track-HD**

Structural and diffusion-weighted MRI data were acquired using protocols designed specifically for the Track-HD study (Tabrizi *et al.* 2009). Structural data was acquired using the same acquisition protocol at each time point. Initially, diffusion data was not included in the core protocol and three sites (London, Leiden and Paris) collected diffusion imaging using their own acquisitions. The acquisition was then standardised with a generic protocol for the third visit onwards, as described below.

Data were acquired on two different scanner systems (3T Philips Achieva at Leiden and Vancouver and 3T Siemens TIM Trio at London and Paris). T1 images were acquired using a 3D magnetisation-prepared rapid gradient echo (MP-RAGE) acquisition sequence on 3T Siemens (London, Paris) and Phillips (Leiden, Vancouver) whole body scanners with the following parameters: Repetition Time (TR) = 2200ms (Siemens; S)/ 7.7ms (Philips; P), Echo Time (TE) = 2.2ms (S)/ 3.5ms (P), Flip Angle = 10° (S)/ 8° (P), Field of view (FOV) = 28cm (S)/ 24cm (P), matrix size 256x256 (S)/224x224 (P), yielding 208 (S)/164 (P) sagittal slices to cover the entire brain with a slice thickness of 1.0 mm with no inter-slice gap.

For the work included in this thesis, diffusion data were used from the 36 month visit (2011). This was because this visit had the most diffusion data available (including data acquired from the PADDINGTON study). No diffusion data were collected at the Vancouver site in the Track-HD study in 2011. For the remaining three sites (Leiden (Phillips), London and Paris (Siemens)) diffusion weighted images for DTI data were acquired using an echo planar imaging (EPI) protocol in 42 different encoding directions, with a diffusion weighting of  $b = 1000 \text{ sec/mm}^2$ . 1 (Phillips), or 7 (Siemens) additional reference images with no diffusion weighting ( $b = 0 \text{ sec/mm}^2$ ) were acquired. For scans collected in London dimensions were of  $128 \text{ pixels} \times 96 \text{ pixels} \times 65 \text{ slices}$  per volume, with  $TE = 84\text{ms}$  and  $TR = 7600\text{ms}$ ; for Paris, dimensions were of  $128 \text{ pixels} \times 128 \text{ pixels} \times 75 \text{ slices}$  per volume, with  $TE = 88\text{ms}$  and  $TR = 13100\text{ms}$  and for Leiden, dimensions were of  $112 \text{ pixels} \times 112 \text{ pixels} \times 55 \text{ slices}$  per volume, with  $TE = 56\text{ms}$  and  $TR = 8078\text{ms}$ . Voxel size for Siemens scans was  $2 \times 2 \times 2\text{mm}^3$  and for the Phillips scan  $1.96 \times 1.96 \times 2\text{mm}^3$ .

### **2.2.2 TrackOn-HD**

The 3T structural image data acquisition sequence for the TrackOn-HD study was the same as that used in the Track-HD study across the four sites. There were, however, some minor differences in the parameters used in the diffusion-weighted acquisition sequence (detailed below). For the work included in this thesis diffusion data were only used from the 24-month (2014) visit. Data from this visit were analysed along with task data collected in the cognitive studies (chapters 10 and 11), therefore was most suitable due to its proximity to the date of cognitive testing.

Diffusion-weighted images with 42 unique gradient directions ( $b = 1000 \text{ sec/mm}^2$ ) were acquired from both Siemens (London and Paris) and Phillips (Leiden and Vancouver) scanners. Seven images with no diffusion weighting ( $b = 0 \text{ sec/mm}^2$ ) and one image with no diffusion weighting ( $b = 0 \text{ sec/mm}^2$ ) were acquired from the Siemens and Philips scanners respectively. For the Siemens scanners,  $TE = 88\text{ms}$  and  $TR = 1300\text{ms}$ ; for the Phillips scanners,  $TE = 56\text{ms}$  and  $TR = 1100\text{ms}$ . Voxel size for the Siemens scanners was  $2 \times 2 \times 2 \text{ mm}$  and for the Phillips scanners  $1.96 \times 1.96 \times 2\text{mm}$ . 75 slices in total were collected for each diffusion-weighted and non-diffusion weighted volume.

### **2.2.3 PADDINGTON**

3T MRI data (T1- and diffusion-weighted) were acquired based on protocols previously standardised for multi-site use (Tabrizi *et al.* 2009).

T1-weighted MP-RAGE scans were acquired yielding contiguous sagittal slices with a slice thickness of 1mm (Leiden (Phillips), London (Siemens), Paris (Siemens)) or 1.1mm (Ulm (Siemens)), and no inter-slice gap. Diffusion weighted images for DTI data were acquired using an EPI protocol in 42 (Leiden, London, Paris) or 47 (Ulm) different encoding directions, with a diffusion weighting of  $b = 1000 \text{ sec/mm}^2$ . 1 (Leiden), 7 (London, Paris), or 3 (Ulm) additional reference images with no diffusion weighting ( $b = 0 \text{ sec/mm}^2$ ) were acquired. Contiguous axial slices were acquired with 2mm (Leiden, London, Paris) or 2.2mm (Ulm) slice thickness and corresponding in-plane resolution of  $2\text{mm}^3$  and  $2.2\text{mm}^3$  isotropic voxels respectively. For a full description of the protocol at each site please see Hobbs *et al.* (2013).

### **2.2.4 Individual MRI Scan**

A T1-weighted MRI scan was acquired for one of the additional participants recruited for the cognitive tasks (chapters 10 and 11) as part of another research study taking place at the UCL Institute of Neurology. Three T1 scans were collected using a 3T Siemens Trio. The best quality scan was selected for this thesis, acquired with TR = 2000ms, TE = 2.85ms, Flip Angle =  $8^\circ$ , FOV = 282ms, matrix size = 256x256, slice thickness = 1.10mm.

## **2.3 Image Analysis**

### **2.3.1 Structural MR Image Analysis**

The structural scans used in this thesis are all T1-weighted and the processing steps are described below.

### ***Pre-Processing***

Image pre-processing and quality control (QC) was carried out using in-house Medical Image Display and Analysis Software (MIDAS, version 5.10) (Freeborough *et al.* 1997).

Initial QC of all datasets collected in the Track-HD study was carried out in London by IXICO (<http://www.ixico.com/>) to ensure reliability and stability of scan acquisition over time, followed by a thorough visual check again at UCL. First QC of the structural T1 scans collected in the TrackOn-HD and PADDINGTON studies was carried out at UCL. Visual checks were performed for complete brain coverage, wrap, missing data, motion artefacts, noise, inhomogeneity, flow, susceptibility and anything else that compromised image quality. The most frequently seen artefacts were due to motion, common in a movement disorder like HD, and which caused ringing, ghosting and blurring in the images.

Two T1 scans were collected in the Track-HD study during each scan session to increase the likelihood of having one high quality scan. Both images were checked and rated against each other. The best quality T1 scan was then used for further analysis. If a T1 scan did not pass initial QC, e.g. because there was significant blurring or motion artefacts, then a rescan was requested at the earliest point possible. Only one T1 scan was acquired for the TrackOn-HD study but the same quality checks were applied.

After QC each image was bias corrected to ensure that any residual bias in the image intensities was corrected. T1-weighted images are susceptible to intensity non-uniformity, also known as illumination artefact, bias field and intensity inhomogeneity. This artefact has several possible causes, including a lack of uniform sensitivity of the radio-frequency emitting and receiving coils, static field ( $B_0$ ) inhomogeneities and eddy currents (Gispert *et al.* 2004). However it is largely determined by the interaction of the participant with the excitation field, the size of which depends on the pulse sequence and field strength (Sled & Pike 1998).

It is important that this bias is corrected for, particularly for multi-scanner and multi-site imaging studies, as well as for accurate brain segmentation because many segmentation algorithms rely on intensity levels for classification. The N3 correction is a commonly

used non-parametric non-uniform intensity normalization method, first proposed by Sled *et al.* (1998). This correction has been found to demonstrate a high degree of stability (Arnold *et al.* 2001), reduce coil-type and pulse-sequence differences and improve reproducibility (Leow *et al.* 2006), as well as reduce system dependency effects on brain volumetry (Goto *et al.* 2012). This method, with optimised parameters for 3T data (Boyes *et al.* 2008) was applied to all T1-weighted images used in this thesis. Figure 2-1 gives an example of a T1 scan before and after N3 bias correction.

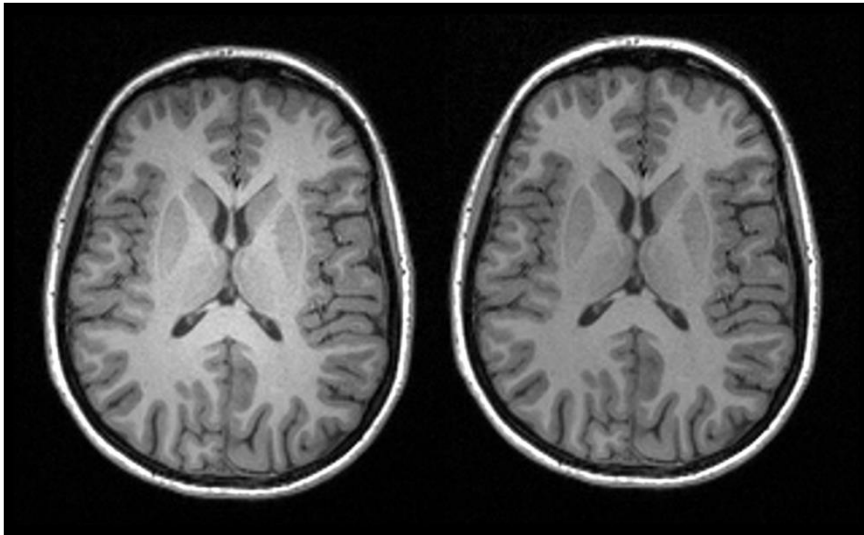


*Figure 2-1. Example of a T1 scan before (left) and after (right) N3 bias correction.*

### ***Volumetric Analysis: Manual Delineation***

Manual delineations were performed on the bias corrected T1 images in MIDAS (Freeborough *et al.* 1997). The manual segmentations are referred to as semi-automated because they use pre-defined intensity thresholds based upon the mean brain intensity (MBI) to help outline the structures. Expert raters then follow validated protocols to complete the segmentations.

### ***Whole-Brain***

The whole-brain region was segmented in native-space (the original position of the brain in the scanner FOV) using a semi-automated protocol at baseline, and a completely automated propagation for follow-ups. The whole-brain segmentation involved the application of erosions and dilations using a morphological segmentor to exclude as much non-brain tissue as possible and to separate the brain from the scalp

and CSF. Manual editing was used to tidy up the region and ensure that remaining non-brain tissue was not included. Re-thresholding was then used to restore any missing voxels in the brain. Individual brain segmentations took on average one hour to complete. See Figure 2-2 for an example segmentation.

The whole-brain region was then registered into a standard-space, Montreal Neurological Institute (MNI) 305 atlas space (Mazziotta *et al.* 1995), for subsequent ROI analysis. This was done to ensure consistent orientation and application of landmark-defined cut-offs. The images were warped into standard-space using a linear, rigid registration with nine degrees of freedom, which estimates the parameters required for the best image alignment and then discards the scaling parameters to reposition the image without altering the volume.

### ***Total-Intracranial Volume***

Total intracranial volume (TIV) refers to all tissues within the cranium, i.e. all grey matter (GM), white matter (WM) and CSF. TIV represents maximal brain growth during development and once full capacity is reached in adolescence does not usually change over time. TIV delineation was performed by outlining the dura using the MBI thresholds (Whitwell *et al.* 2001). These were set to 30% of the MBI with a maximum upper threshold. Starting at the most inferior slice of the cerebellum and finishing at the most superior slice containing cortex, every tenth slice was outlined. The volume between the delineated slices was interpolated and manual edits helped where the thresholds failed. Individual TIV segmentations took on average 20 minutes to complete. See Figure 2-2 for an example segmentation.

In this thesis TIV segmentation was also performed using an automated technique for data that did not have a manual segmentation (see section: Statistical Parametric Mapping below). TIV segmentations were used throughout to adjust for variation in head-size. Regional volumes have been shown to be strongly associated with TIV (Barnes *et al.* 2010) therefore volumes are reported as a percentage of TIV (Whitwell *et al.* 2001).

### *Corpus Callosum*

A manual delineation protocol for the corpus callosum (CC) was developed as part of this thesis (full details in chapter 3 and full protocol in Appendix 1: Volumetric Analysis). Briefly, the procedure involved consistently selecting the mid-sagittal slice, including this and four slices both left and right i.e. nine slices in total. Intensity constraints derived from the MBI of the scan, in this case 100% and 150%, automatically highlighted the CC. Borders of the region were manually edited where necessary. Individual CC segmentations took on average five minutes to complete. See Figure 2-2 for an example segmentation.

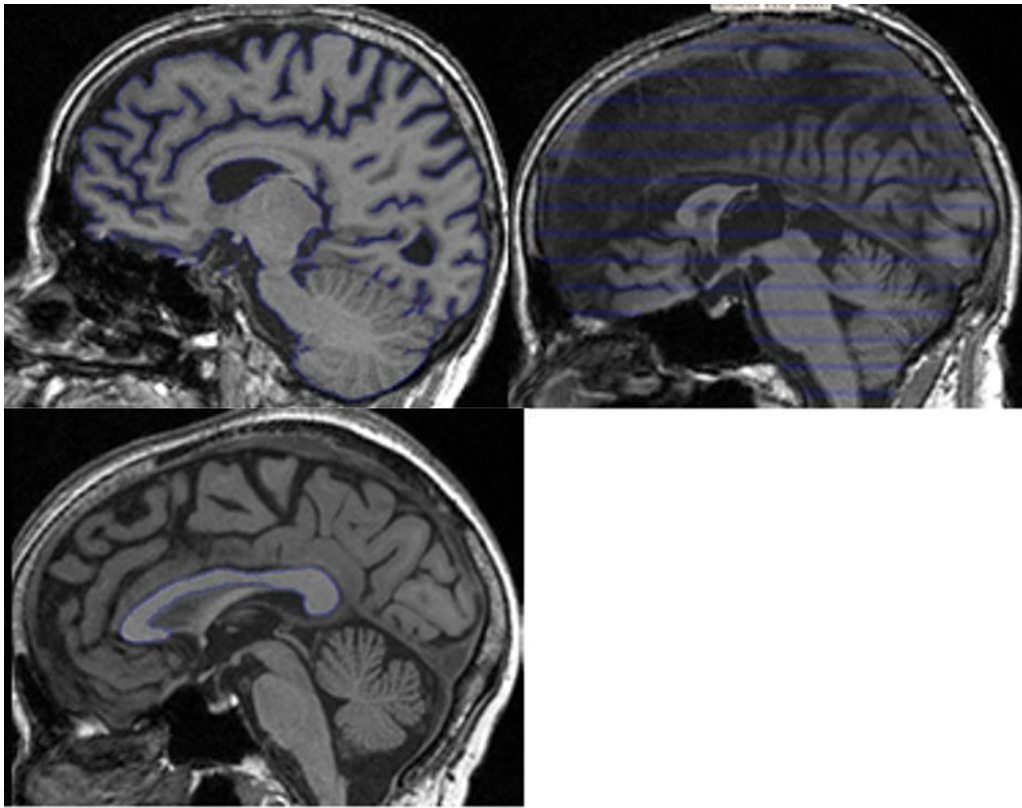


*Figure 2-2. Examples of regional segmentations of whole-brain (top left), TIV (top right) and CC (bottom).*

### *Volumetric Analysis: Automated Delineation*

Manual delineations, although seen as the ‘gold standard’, are time-consuming and rely upon expert raters who require training and validating, which may not be appropriate for use in clinical trials where large numbers of scans need to be processed in real time by several raters. This type of application is likely to increase the variability of



measures and possibly decrease the sensitivity. Therefore automated methods are now widely used and accepted for use in imaging studies.

### *Statistical Parametric Mapping*

Statistical Parametric Mapping (SPM; <http://www.fil.ion.ucl.ac.uk/spm/>) software is a tool for analysing brain imaging data from various modalities and uses a voxel-based approach. SPM software has mainly been applied in this thesis for tissue segmentation. All projects that used SPM used version 8 which was run on the Matlab R2012b platform (Mathworks, USA). Although SPM12 was released in October 2014, SPM8 had already been used to analyse various data in this thesis, therefore it was decided to continue using the same version throughout for consistency in analyses.

### *Segmentation*

Unless otherwise stated the *New Segment* tool was used for tissue segmentation with SPM in this thesis. This toolbox is an extension of the default *Unified Segmentation* tool (Ashburner & Friston 2005) which can segment the different tissue types, bias correct and spatially normalise images in one process. Alternating among classification, bias correction and registration in iterative steps provides better results than applying each part separately ([http://www.fil.ion.ucl.ac.uk/spm/doc/spm8\\_manual.pdf](http://www.fil.ion.ucl.ac.uk/spm/doc/spm8_manual.pdf)).

The bias correction models intensity variations in the images due to the excitation field and variations due to different tissue types using Gaussians and tissue probability maps (TPMs). The TPMs are modified versions of the International Consortium for Brain Mapping Tissue Probabilistic Atlases, derived from 452 T1-weighted scans (provided by the ICBM, John C. Mazziotta and Arthur W. Toga ([http://www.loni.ucla.edu/ICBM/ICBM\\_TissueProb.html](http://www.loni.ucla.edu/ICBM/ICBM_TissueProb.html))).

The segmentation step involves a non-linear deformation field being estimated according to the TPMs on an individual participant's image, and additional information is used based upon other participants' brain images. These priors are generated by aligning multiple participants' data, assigning voxels to different tissue types and then averaging the tissue classes across participants. These maps provide the probability of any given voxel in a registered image being any of the three tissue classes: GM, WM and CSF ([http://www.fil.ion.ucl.ac.uk/spm/doc/spm8\\_manual.pdf](http://www.fil.ion.ucl.ac.uk/spm/doc/spm8_manual.pdf)). The whole model is

further refined by allowing the TPMs to be deformed according to a set of estimated parameters, which means that segmentation and spatial normalisation can be combined. Normalisation then involves an initial affine alignment with the TPMs and warping regularisation. This last step determines how smooth the deformations are.

*New Segment* has various extensions to the default version including a larger set of TPMs (bone, other soft tissue and air, as well as GM, WM and CSF), which allows for a different treatment of voxels outside of the brain, an improved and more robust registration, as well as the ability to use multi-spectral data ([http://www.fil.ion.ucl.ac.uk/spm/software/spm8/SPM8\\_Release\\_Notes.pdf](http://www.fil.ion.ucl.ac.uk/spm/software/spm8/SPM8_Release_Notes.pdf)).

The images outputted from this tool are tissue class images in native space (i.e. aligned with the original image), spatially normalised images and/or spatially normalised images with modulation. Modulation multiplies the normalised image by its relative volume before and after warping to compensate for volume change during normalisation.

The native space GM and WM segmentations were used as ROI masks in chapters 8 and 9, and the modulated normalised GM, WM and CSF segmentations were used to estimate TIV in chapters 8, 10 and 11. Summing these three segmentations using the *New Segment* toolbox has been found to perform very well compared to manual or other automatic measurements of TIV and is the recommended method (Ridgway *et al.* 2011). See Figure 2-3 for example segmentations.

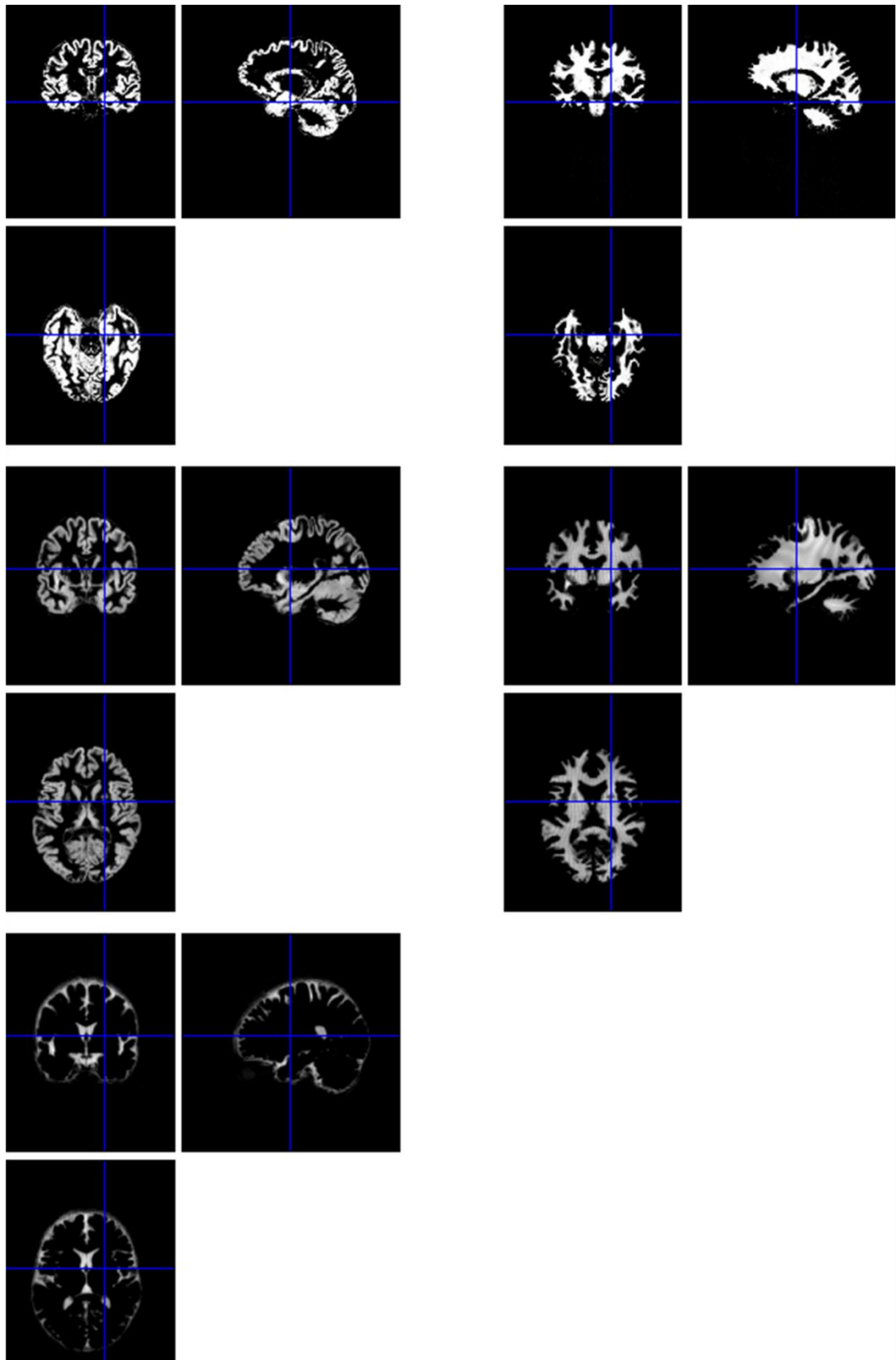


*Figure 2-3. Example segmentations from one control participant in the Track-HD study. Top row: GM (left) and WM (right) segmentations in native space. Middle and bottom row: Modulated normalised GM (left middle), WM (right middle) and CSF (bottom) segmentations.*

### ***Apply Deformations***

The *Apply Deformations* toolbox was used to apply the deformation field from an individual participant to an ROI in order to warp the region into the participant's structural native space. DARTEL (Diffeomorphic Anatomical Registration Through Exponentiated Lie Algebra) is a registration tool in SPM used for creating study-specific templates (Ashburner 2007) and had been applied to these images in a previous study. Although DARTEL was not applied directly in this thesis, the warping parameters generated previously were applied here in chapters 10 and 11.

### ***Brain Extraction***

The Brain Extraction Tool (BET) (Smith 2002) was run on T1 images to remove non-brain tissue in preparation for registration to diffusion space and to ensure good alignment. All brain-extracted T1 images were visually inspected. If parts of the eyes and/or neck were not completely removed, BET was rerun using a more stringent threshold. However, there were many cases where BET was still unsuccessful, therefore an improved pipeline was routinely applied. This pipeline applied a series of erosions and dilations to a segmented GM and WM mask (created using our structural image in SPM, see section: Segmentation above), which was then applied to the original BET image to create a much improved fit. See Figure 2-4 for examples of poor and successful brain extraction.

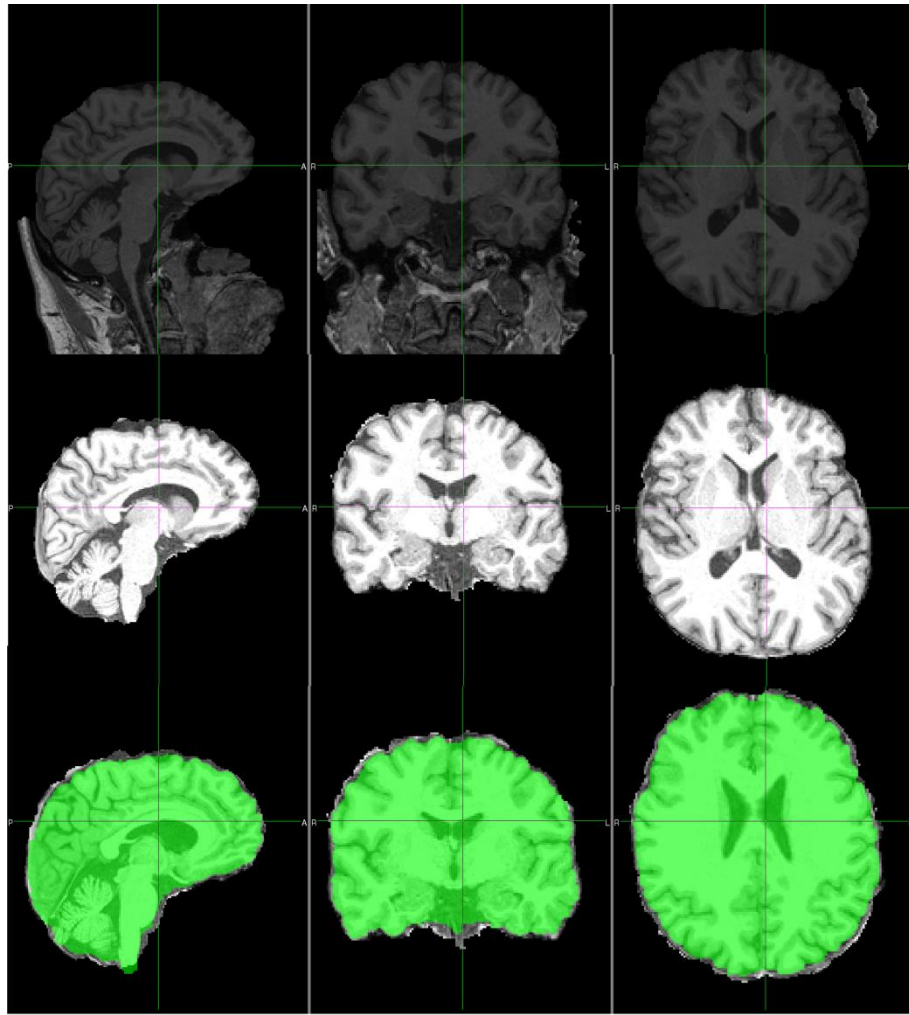


*Figure 2-4. BET examples. T1 image is of a control participant from the Track-HD study. Top row: Default BET. Lots of non-brain tissue still included. Middle row: BET with a more stringent threshold. Still some non-brain included on the edge of the cortex. Bottom row: Improved BET mask shown in green. It successfully excludes the non-brain that the original stringent BET left in.*

### 2.3.2 Diffusion MR Image Analysis

DWI is so called because it provides image contrast based upon the variation of diffusion of water molecules within the brain (explained in section 1.2.2: Principles of Diffusion Imaging). The raw DWI images used in this thesis were processed according to the steps outlined below (see Figure 2-5 for a schematic overview of the pre-processing steps).

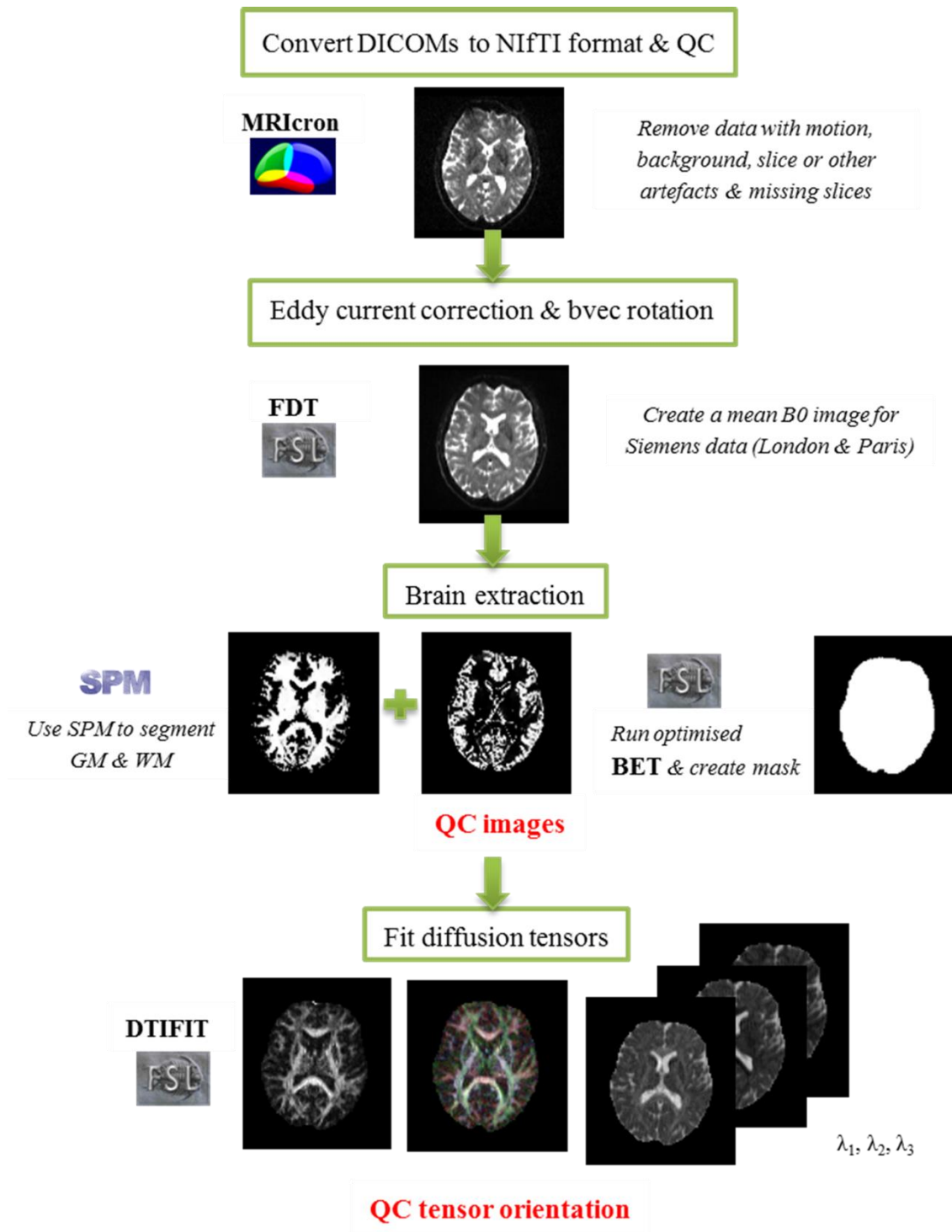


Figure 2-5. Overview of the pre-processing pipeline of the diffusion-weighted images.

## ***Pre-Processing***

### ***Image Conversion and Quality Control***

For this thesis all diffusion data were converted from raw DICOMs to 4D NIfTI image format using Chris Rorden's MRICron software (<http://people.cas.sc.edu/rorden/mricron/index.html>) and all volumes were individually visually inspected for quality. Images were viewed using FMRIB Software Library (FSL) version 5.0.2 (Smith *et al.* 2004). Common issues recorded were missing slices, background artefacts and slice artefacts. DWI can be highly sensitive to participant motion therefore rapid EPI is commonly used to maximise the image signal-to-noise-ratio (Alexander *et al.* 2007). The use of EPI for acquisition means that the volumes are prone to susceptibility artefacts from magnetic field inhomogeneities, causing warping that can be severe in regions near to where bone meets air e.g. prefrontal areas and the inferior temporal lobe near the auditory canal (Alexander *et al.* 2007). These types of artefacts were common in the dataset but any particularly severe cases were noted.

If more than three slices showed artefact within a gradient volume, or artefacts were present on more than three volumes within a dataset, the whole dataset was excluded. This approach was favoured over removal of just the corrupted volumes to avoid introducing disease-related bias caused by increased motion in the HD group compared with the control group and uneven sampling of gradient directions. Figure 2-6 shows some examples of artefacts commonly seen in diffusion data.

Further visual inspection followed each stage of the processing outlined below.

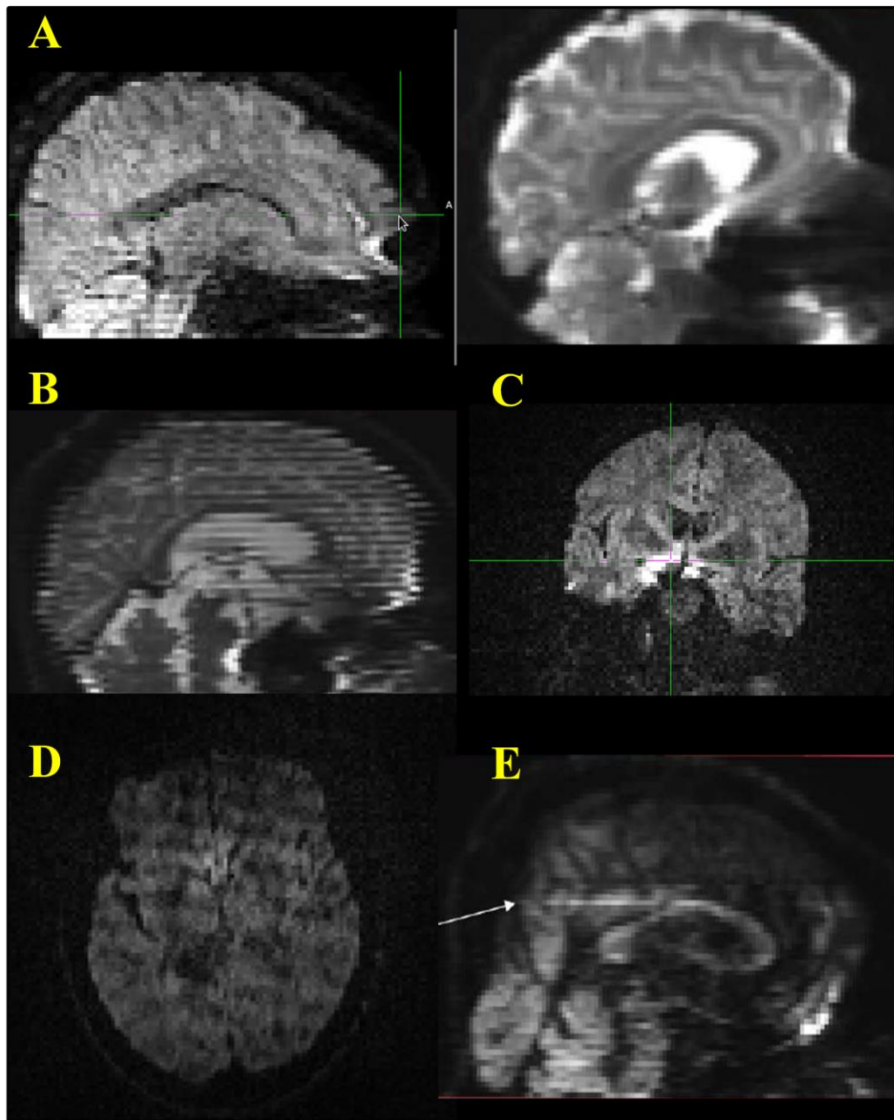


*Figure 2-6. Examples of commonly seen artefacts in raw diffusion data. Examples taken from the PADDINGTON study. (A) Both images have geometric distortions. (B) “Venetian Blind” or interlace effect. (C) Hyper-intensities in region near sinuses. (D) “Checkers” artefact. (E) High intensity axial slice, highlighted by arrow.*

### ***Eddy Current/Motion Correction***

Eddy current correction was carried out using FSL’s FMRIB Diffusion Toolbox (FDT). Localised electrical currents can cause stretches and shears in the diffusion weighted images which are different for the different gradient directions. Distortions and small head movements present in each volume are corrected using eddy current correction. This is done by affinely registering all volumes to a reference volume, in this case the first B0 (the constant, homogeneous magnetic field, non-diffusion weighted image)



reference image. After correction, the bvec files (text files containing the list of gradient directions) were updated.

### ***Brain Extraction***

BET (Smith 2002) was run on B0 images to remove non-brain tissue. For those sites where multiple B0 images were collected (London, Paris and Ulm), an average reference image was created by merging and then averaging across the seven interleaved B0 images. All brain-extracted B0 images were visually inspected. If parts of the eyes and/or neck were not completely removed, BET was rerun using a more stringent threshold. However, there were many cases where BET was still unsuccessful, therefore the improved pipeline was applied. This pipeline applied a series of erosions and dilations to a segmented GM and WM mask (created using our structural image in SPM, see section 2.3.1: Statistical Parametric Mapping), which was then applied to the original BET image.

The improved BET pipeline however was not as successful at creating an improved fit on the B0 images as it was when applied to the T1 images (section 2.3.1: Brain Extraction). The masks were frequently tight and many had holes in (see Figure 2-7, b). Therefore, the original BET masks were eroded by one voxel, which seemed to improve the fit by filling the holes in the improved masks without being so loose as to include the ‘halo’ of noise present in the FA maps.

There was incomplete brain coverage for some of the scans and sometimes the very top of the brain was cut off. For those participants the mask produced a flat ‘chimney’ effect at the top (see Figure 2-7, c). To reduce this, the top slice of the masks was zeroed using the bucket fill tool in *fslview*. FSL’s *fslmaths* was then used to subtract this top slice from the eroded mask and to binarise it. See Figure 2-7 for examples of poor and successful brain extraction.

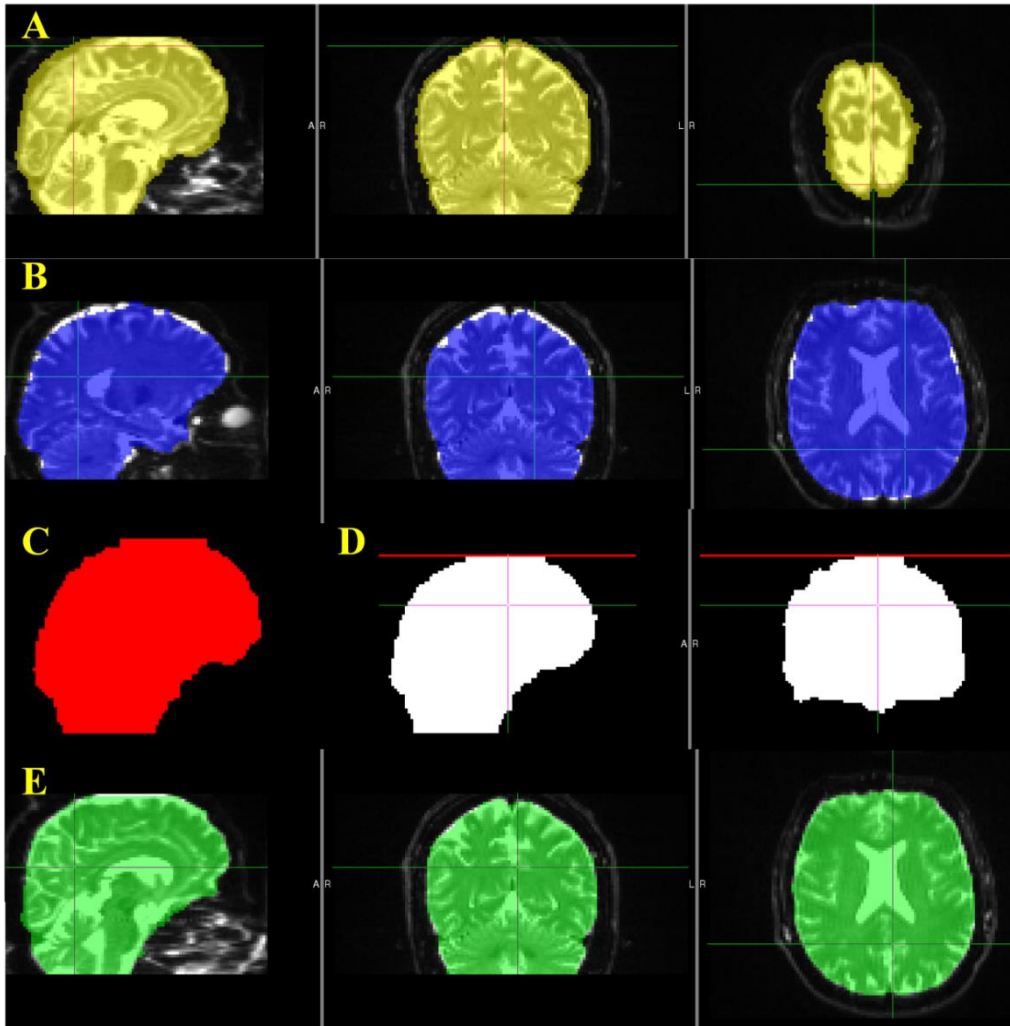


**Figure 2-7. BET examples.** *B0 image is of a control participant from the Track-HD study. (A) Default BET: Mask is too large and includes non-brain (yellow). (B) Improved BET: Mask is too tight (blue). (C) Original BET mask eroded by one voxel: Flat ‘chimney’ effect at top of mask (red). (D) Top slice zeroed (red) and removed from BET mask (white). (E) Improved fit using original BET mask eroded and top slice removed (green).*

### ***Fitting the Tensors***

FSL’s DTIFIT was used to fit a diffusion tensor model at each voxel in the corrected diffusion data. It uses the eddy-corrected B0 and gradient-direction volumes, the b-vector file (which details the gradient information) and the b-values file (which details the weighting of each volume).

The diffusion tensor is characterised by three eigenvalues ( $\lambda_1, \lambda_2, \lambda_3$ ) which describe the diffusivities along the principal axes of the tensor. Three corresponding orthogonal eigenvectors ( $\varepsilon_1, \varepsilon_2, \varepsilon_3$ ) define the orientation of principle axes. The principal

eigenvector is assumed to run parallel to the main underlying fibre direction, while the second and third eigenvectors are the two largest axes perpendicular to the main fibre direction (see section 1.2.2: Principles of Diffusion Imaging).

Tensor orientation for each participant was visually checked by viewing the red-green-blue colour map indicating the primary eigenvector orientations in each voxel, overlaid onto the fractional anisotropy (FA) map (see Figure 2-8). Mean diffusivity (MD), FA, and axial diffusivity (AD;  $\lambda_1$ ) maps are automatically outputted at this step (see Figure 2-9). Radial diffusivity (RD) – average diffusivity in the principal directions perpendicular to the main fibre - maps can be created by calculating the mean of eigenvalues  $\lambda_2$  and  $\lambda_3$  (see Figure 2-9).

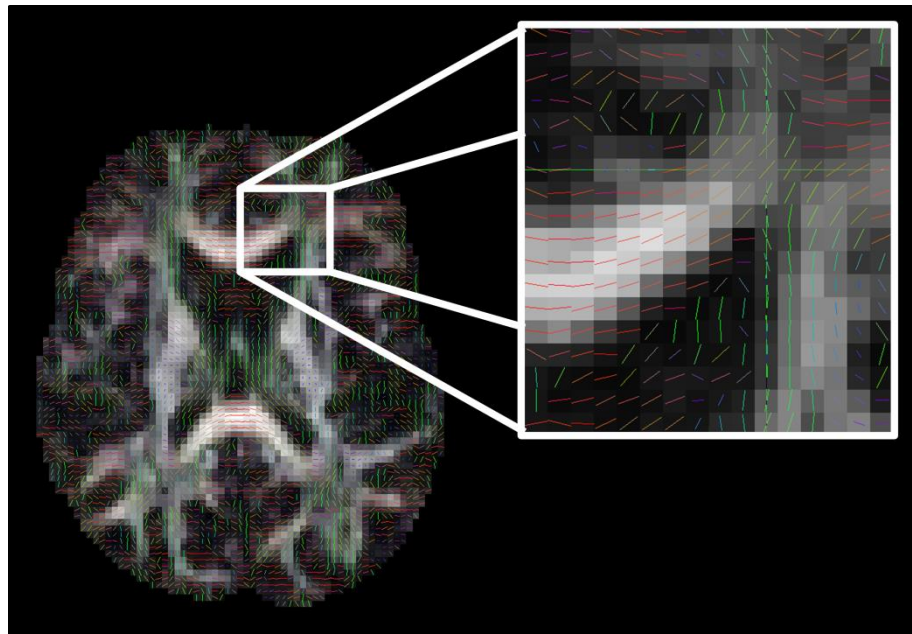


*Figure 2-8. The major eigenvector direction indicated by colour (red: right-left; green: anterior-posterior; blue: superior-inferior) overlaid onto the FA map. Data taken from a control participant in the Track-HD study.*

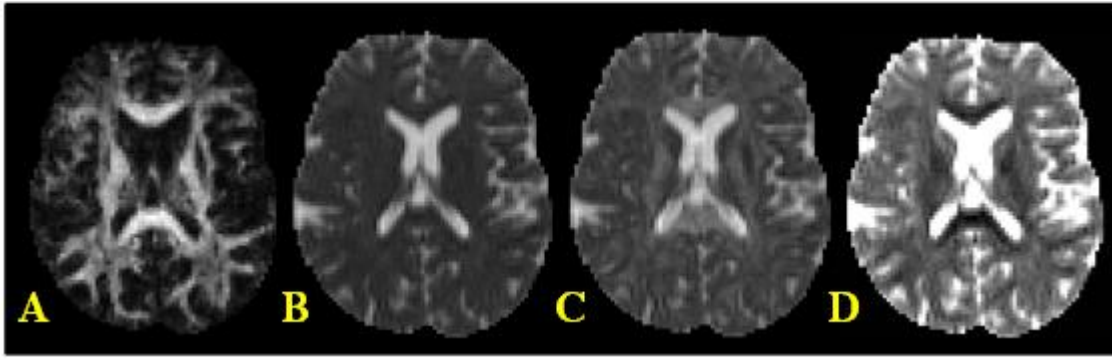


*Figure 2-9. Examples of the quantitative maps outputted using FSL's DTIFIT. Images are of a control participant from the Track-HD study. (A) FA. (B) MD. (C) AD. (D) RD (average of  $\lambda_2$  and  $\lambda_3$ ).*

### ***Region of Interest Analysis***

ROI analysis of DTI data is applied in chapters 8 and 9. Specific methods for computing diffusion metrics over the CC are reported in chapter 10 and the processing steps for acquiring metrics in GM and WM are outlined below. Unless explicitly stated, all analysis was performed in FSL. An overview of the analysis stages is provided in Figure 2-10.

Firstly, the brain extracted T1 image was registered to the FA map for each participant to acquire the deformation parameters necessary for the subsequent alignment of the ROIs to individual participants' diffusion space. The brain extracted T1 image was chosen over the original T1 image to ensure better registration and to avoid the type of poor registration seen in Figure 2-11.

Three registration techniques were visually compared to guarantee good registration of the ROIs to the FA images. In order to double check the T1 warping, the transformation parameters for each technique were initially applied to each participant's processed WM segmentation (described below). It was much easier to assess the anatomical alignment using the WM region as well as viewing the T1 image in diffusion space.

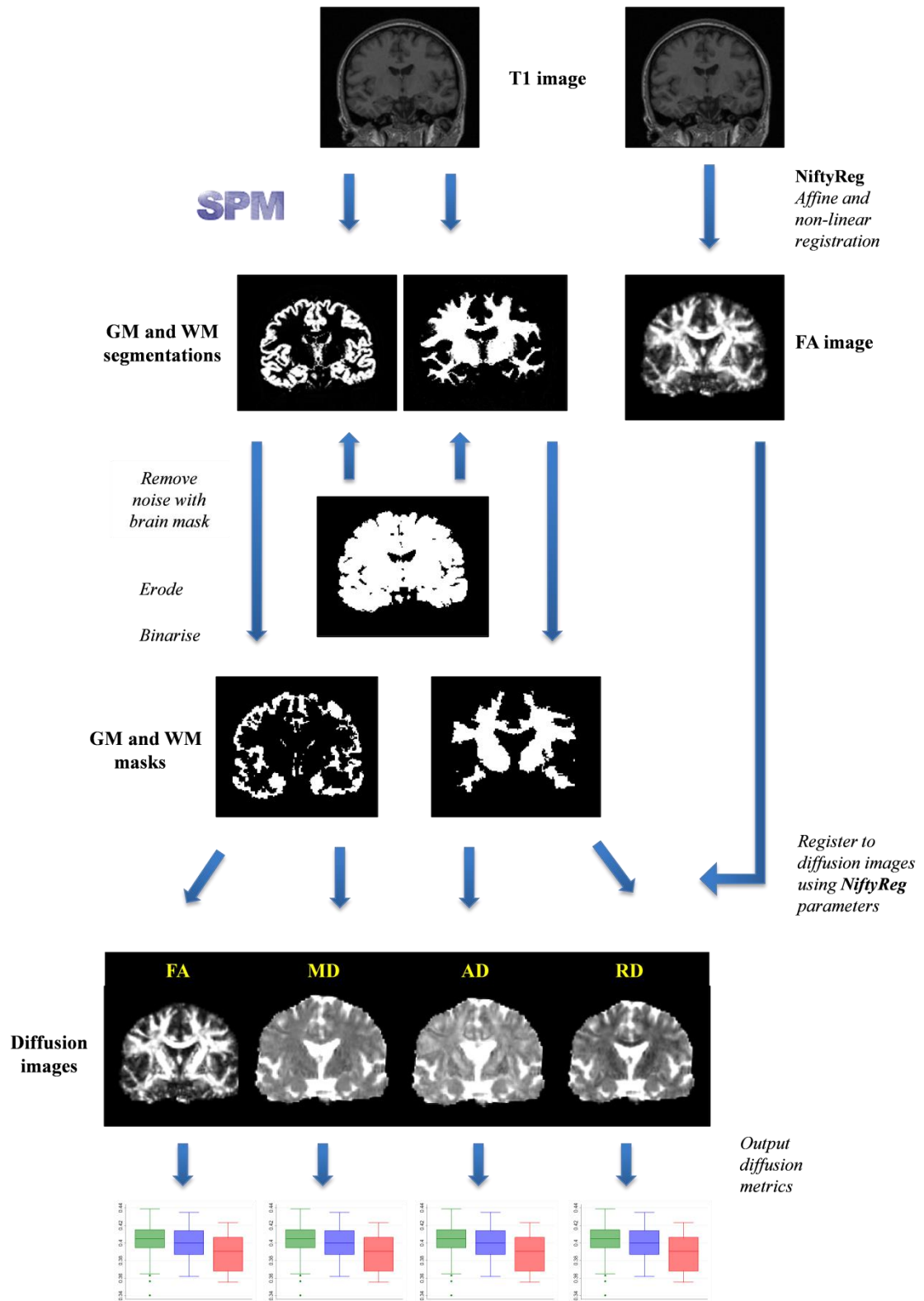


**Figure 2-10. Overview of the ROI analysis pipeline.** These steps are applicable for outputting diffusion metrics across ROIs. The registration step can also be applied when preparing images for tractography, but is not required for tract-based spatial statistics.

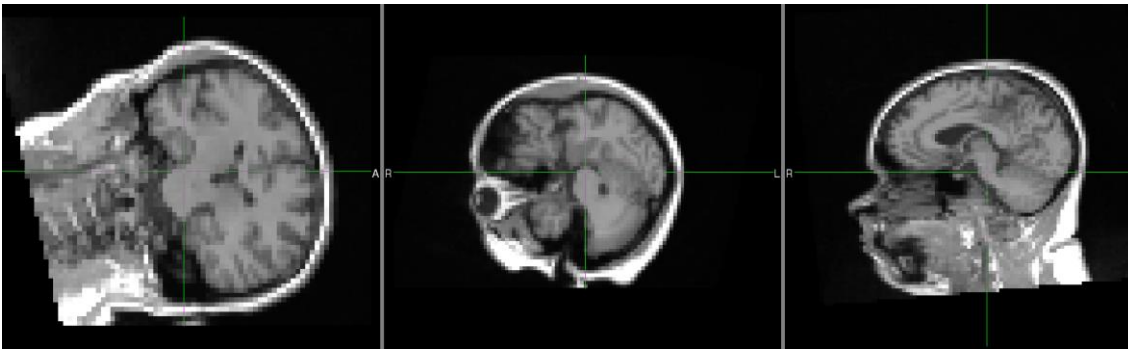


**Figure 2-11. Failed T1 to FA FLIRT registration. Example of what happens when the T1 image is not brain extracted. Example of a control participant from the Track-HD study.**

FLIRT is a fully automated linear, affine registration tool (Greve & Fischl 2009; Jenkinson & Smith 2001; Jenkinson *et al.* 2002). Linear registration matches one image to another through translation, rotation, zooming and shearing. Registration was performed with 12 degrees of freedom (affine), firstly using the B0 image as the target. As registration was of a poor quality, registration was then performed using the FA image, in line with the PADDINGTON study (Hobbs *et al.* 2013). This produced better anatomical correspondence, but was still quite poor overall. See Figure 2-12 (left) for an example of poor alignment of the WM region to the FA image using FLIRT.

The next registration technique used was ANTs (Advanced Normalisation Tools) - a freely available image registration, segmentation and statistical tool (<http://stnava.github.io/ANTs/>), which incorporates the Insight ToolKit (Avants *et al.* 2014). Klein *et al.* (2009) compared the ANTs registration algorithm to 14 other nonlinear algorithms and found ANTs to perform the best. For a decent, fast registration (as suggested in the ANTs documentation), the *antsRegistrationSyNQuick.sh* script was run using the default parameters with rigid, affine and deformable transform types. Overall the alignment with this technique was good, and appeared better than the FLIRT technique, however, there were several cases where the registration was poor (see Figure 2-12, middle).

NiftyReg was the third registration technique assessed. NiftyReg is an open-source software developed for rigid, affine and non-linear registration of MR images (<http://cmictig.cs.ucl.ac.uk/wiki/index.php/NiftyReg>). The T1 image was registered to the FA map using a global affine initialisation step (Ourselin *et al.* 2001) followed by a non-linear registration step (Modat *et al.* 2010). On visual inspection, this registration



was very good and the best of the three techniques used. However, it is beyond the scope of this project to compare the three registration algorithms fully. Such work has already been published (Klein *et al.* 2009). Therefore the method that demonstrated the best visual anatomical correspondence between images was selected, in this case NiftyReg. Having registered the T1 images to each participant's FA map, the next steps for ROI analysis could be completed. See Figure 2-12 (right) for an example of good alignment of the WM region to the FA image using NiftyReg.

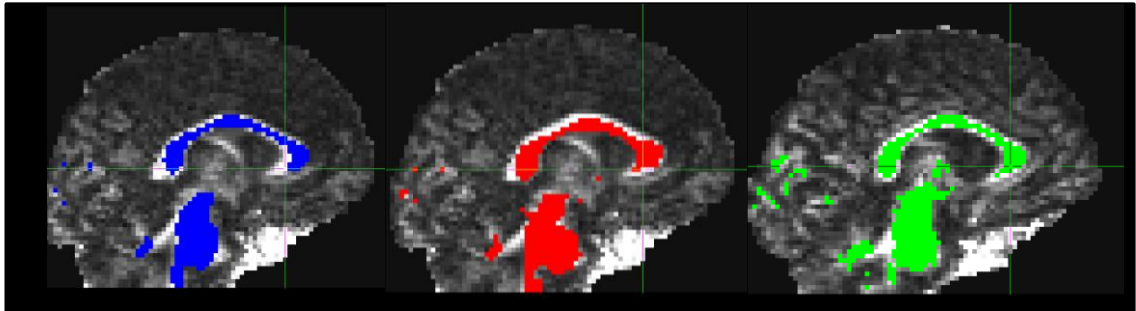


*Figure 2-12. Examples of FLIRT (blue), ANTs (red) and NiftyReg (green) registration. A WM mask is shown overlaid on a control Track-HD participant's FA image.*

Whole WM and GM regions were segmented in SPM using the T1 images. Noise around the regions was removed by multiplying the region by the whole brain mask, which was manually segmented in MIDAS (described in section 2.3.1: Volumetric Analysis: Manual Delineation). These were then eroded in T1 space in order to reduce partial volume effects when warping to diffusion space. The regions were then registered to individual participants' tensor maps using the parameters from the initial T1 image to FA map registration with trilinear interpolation (using NiftyReg), thresholded to 0.5 (to reduce partial volume effects) and binarised. Regions were multiplied together and overlapping regions subtracted from both masks. All masks were visually inspected and diffusion metrics (FA, MD, RD and AD) for whole WM and GM were extracted using FSL's *fslstats*. Figure 2-13 shows an example of one participant's GM and WM masks overlaid on their FA image.

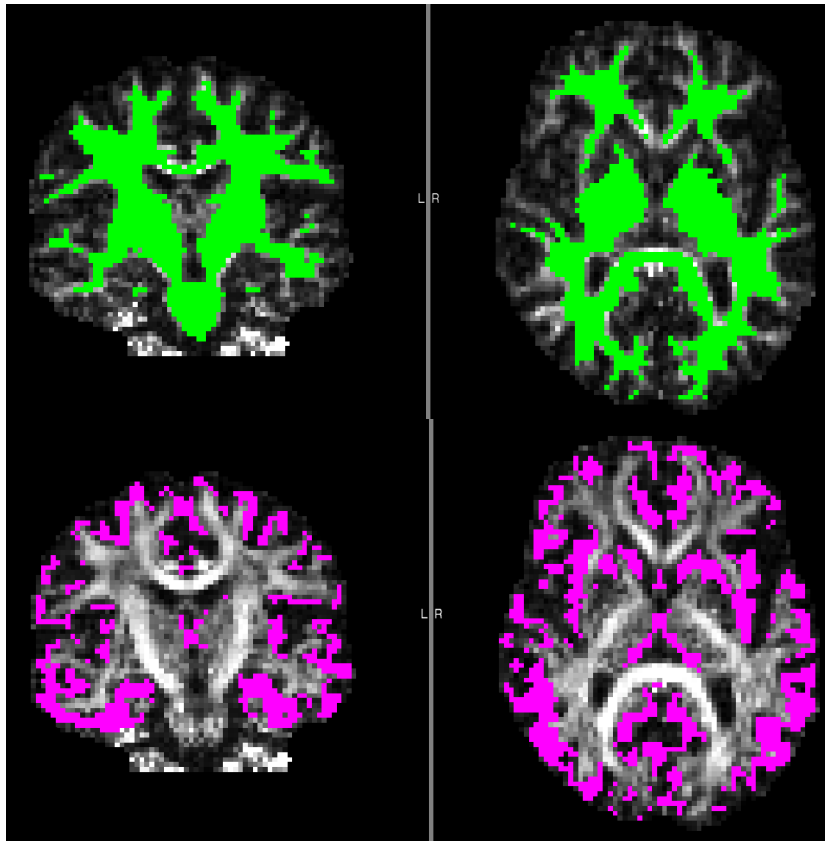


*Figure 2-13. Example of the warped WM (green) and GM (purple) eroded, thresholded and binarised masks overlaid on the FA image. Example is of a control Track-HD participant.*

### ***Tract-Based Spatial Statistics***

Voxelwise statistical analysis of diffusion data was carried out using both the entire default tract-based spatial statistics (TBSS) pipeline (Smith *et al.* 2006) and one which included an improved registration technique using DTI-TK. The processing steps for both pipelines are outlined in detail below and illustrated in Figure 2-14.

#### ***Default TBSS Pipeline***

TBSS (Smith *et al.* 2006), part of FSL (Smith *et al.* 2004) is a whole-brain, voxelwise statistical analysis technique for DTI data. First, FA maps (output from FSL's DTIFIT) for each participant were aligned using the nonlinear registration tool FNIRT (Andersson *et al.* 2007a, 2007b), which uses a b-spline representation of the registration warp field (Rueckert *et al.* 1999) to create a common space. This initial alignment was performed with intermediate degrees of freedom so that the data was aligned enough to



make local comparison possible, but with the overall structure topology remaining preserved (Smith *et al.* 2006).

Next, a target image was selected for alignment. The FMRIB58\_FA standard-space image is recommended in FSL. One non-linear registration per participant aligns the FA images to the target in a 1x1x1mm standard space. All aligned data were then affine-transformed into 1x1x1mm<sup>3</sup> MNI152 space. Subsequent processing and analysis was carried out in this space for convenience of interpretation and display, plus creation of the FA skeleton and projection of FA onto the skeleton works well at this higher resolution and limits partial voluming (Smith *et al.* 2006). Once complete, the non-linear transform to the target and the affine transform to MNI152 space was combined and applied to each participant's FA image. This resulted in all of the original FA images being transformed into MNI152 space.

The standard-space FA images were then merged into one 4D file and averaged to create the mean FA image. This mean image was locally relatively smooth because of averaging across participants as well as the resolution upsampling (Smith *et al.* 2006). The mean FA image was then used for tract skeleton generation, which aims to represent the tracts that are common to all participants in the sample. The creation of the skeleton is a complex process. Put simply, it is achieved by searching through all voxels in the local 'tract perpendicular direction', and identifying the voxel with the highest FA as the centre of the tract (Smith *et al.* 2006). The result should be a mean FA skeleton which represents the centres of all tracts common to the sample.

The skeleton was then thresholded to restrict analysis to points within WM which had been successfully aligned. A threshold of 0.2 successfully excluded GM (which typically has an FA value of <0.2) and CSF, and also prevented the skeleton reaching the outmost edges of the cortex where the tracts are less well aligned across participants. The mean FA skeleton was visually checked by overlaying it on the merged 4D file of all the data. Alignment of the FA images and the choice of threshold were also checked. All subsequent processing was carried out within the set of voxels defined in the resulting binary skeleton mask.

The next step involved projecting each participant's aligned FA image onto the mean FA skeleton in order to correct for any misalignments from the first non-linear

registration step. This was done by looking in the perpendicular tract direction (computed in the previous step) of each participant's FA to find the maximum FA value and assign it to the skeleton voxel. This resulted in alignment between the skeleton and the FA image. The perpendicular search was constrained by a distance map in which all the voxels were filled with a value representing the distance to the nearest skeleton point, thereby ensuring that any given voxel can only be mapped to a single section of skeleton. At this point each participant's FA data were aligned to the common FA skeleton and all data were represented as a skeletonised 4D image.

In order to run TBSS using other diffusion-derived data than FA (e.g. MD or AD), the *tbss\_non\_FA* script was run, which applied the original non-linear registration to the non-FA data, merged each participant's data into a 4D file and then projected this onto the original mean FA skeleton (using the original FA images to find the projection vectors). This resulted in skeletonised data for the non-FA measures which were used in the voxelwise statistics in the same way as the FA data.

Voxelwise cross-participant statistics were then performed using the FSL Randomise tool (Winkler *et al.* 2014), which uses general linear modelling (GLM) and thresholding to find correlating voxels and/or conduct group comparisons. In this thesis the Threshold-Free Cluster Enhancement (TFCE) (Smith & Nichols 2009) was used as recommended. This is similar to cluster-based thresholding but potentially more robust. All results were fully corrected for multiple comparisons across space with a p-value set to  $<0.05$ , unless otherwise stated. Significant clusters of 20 voxels or more were identified using FSL's *cluster* tool. In order to present the skeletonised results more clearly, results were 'thickened' using FSL's *tbss\_fill* tool so they filled out into the local tracts.

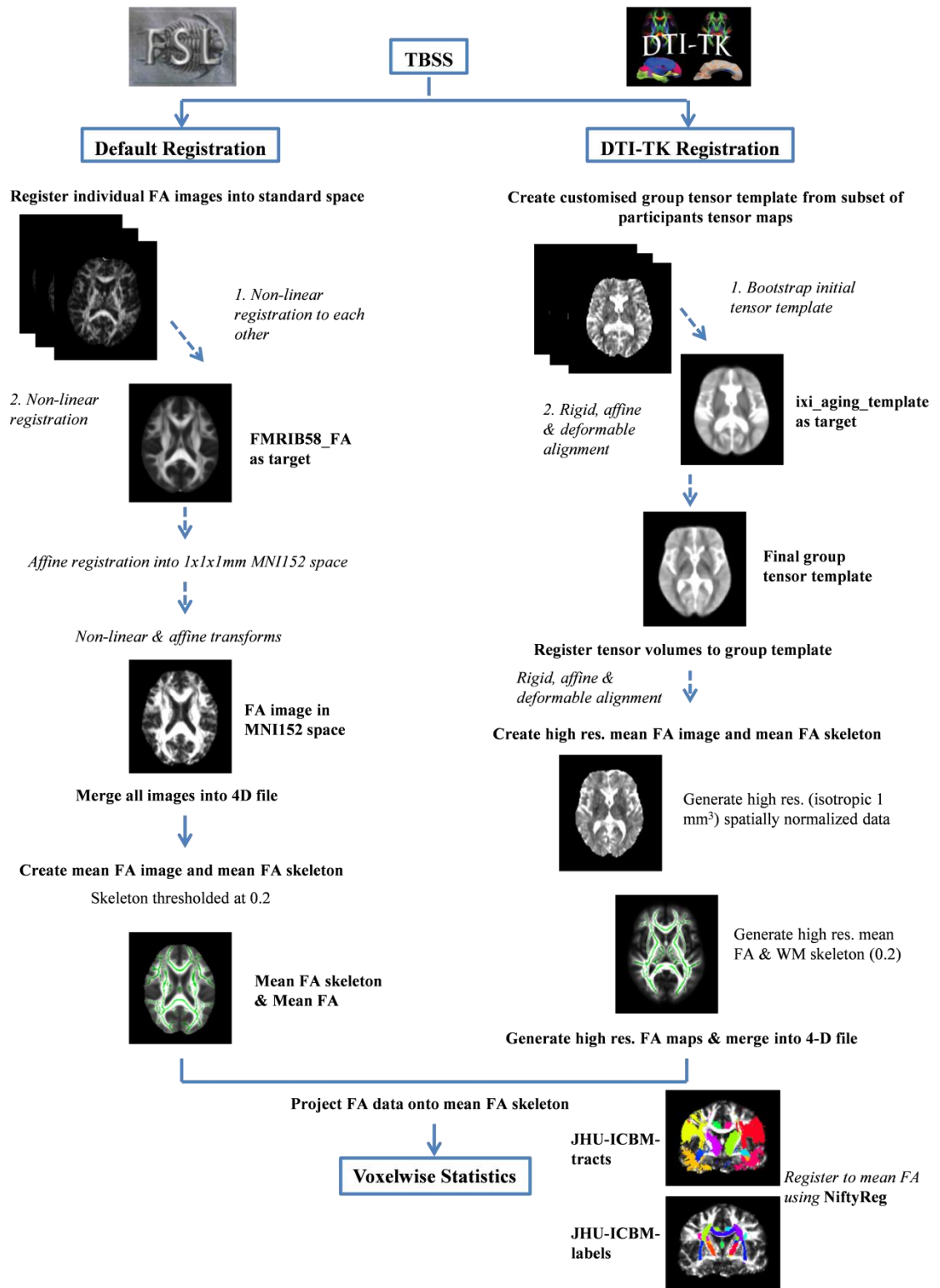


Figure 2-14. Overview of the default TBSS and DTI-TK registration pipelines used for TBSS analysis.

### ***TBSS with DTI-Toolkit***

Diffusion Tensor Imaging Toolkit (DTI-TK; Zhang *et al.* 2006) is a freely available spatial normalisation and atlas construction toolkit (<http://dti-tk.sourceforge.net/pmwiki/pmwiki.php>). It implements a registration algorithm to align WM tracts by matching the orientation of the underlying fibre bundle at each voxel (tensor-based registration). This technique is different to the FA-based registration implemented in the default TBSS pipeline and was developed to address one of the main limitations of DTI analysis; non-discernible fibre orientation when fibres cross within a voxel. This technique also replaces the initial nonlinear registrations of participant's FA maps into standard space in the default pipeline with the creation of a customised template to achieve better alignment of the images. DTI-TK has been used in the analysis reported in this thesis in chapters 4 and 9, the processing steps for which are outlined below and presented in Figure 2-14 (alongside the default TBSS registration steps for comparison).

After brain extraction (described in section 2.3.2), diffusion data were converted to a DTI-TK compatible format using the *fsl\_to\_dtiik* tool. All data were registered to a customised template using diffusion tensor maps from a selection of participants within the sample being analysed. The template should reflect the sample being studied and include an equal number of participants from each group i.e. controls and HD participants, and from each site i.e. Leiden, London and Paris to reduce bias. The effects of participant selection to create the tensor template are explored in chapter 4 and details of specific template composition are reported in the relevant chapter (9).

The initial tensor template was created using a bootstrapping process, with the IXI Aging DTI Template as a target template. This template, constructed from 51 normal elderly participants has been optimised for use with DTI-TK's pipeline. The subset of selected data used to create the customised template were firstly aligned using an affine registration algorithm (Zhang *et al.* 2004). The algorithm is analytic rather than algorithmic and conducts region-wise matching which improves the overall smoothness of the warp via smoothness constraints at the interfaces of each region (Zhang *et al.* 2006). Then the aligned images are registered to the template using a deformable algorithm, which uses a metric based upon the apparent diffusion coefficients (ADC),

i.e. what the diffusion tensor represents, but only focuses on the anisotropic component of the ADC profile (Zhang *et al.* 2006).

The tensor volume for each participant was then registered to the final template using rigid, affine and deformable alignment (Zhang *et al.* 2004; Zhang *et al.* 2006). DTI-TK was then used to generate a spatially normalised high-resolution ( $1\text{mm}^3$ ) template. From this population-specific template, the 4D mean FA map and mean FA skeleton were generated. The high-resolution mean FA map was created using DTI-TK's own *TVtool*, and the mean FA skeleton was generated using FSL's *tbss\_skeleton* tool. Next, the *TVtool* was used to generate an FA map of the spatially normalised high-resolution DTI data for each individual, and then FSL's *fslmerge* was used to merge all participants' data into a single 4D file. All FA maps were visually checked in FSL's visualisation tool, *fslview*.

The mean FA mask was then generated using FSL's *fslmaths* tool. From here all participants' diffusion data was projected onto the mean FA skeleton in FSL as above, again using a FA skeleton threshold of 0.2. Voxelwise statistics were run as described above.

In order to run analysis on non-FA data, maps were generated as above for each individual using DTI-TK's *TVtool*. The maps were then merged into a 4D file and the mean map of the high-resolution population-specific template was created as before. The mean map and the 4D file were masked by the mean FA mask using FSL's *fslstats*. All participant's maps were then projected to the WM skeleton using the *tbss\_skeleton* tool resulting in skeletonised data. Statistics were conducted on the non-FA data in the same way using FSL's Randomise command (Winkler *et al.* 2014).

Anatomical labels of significant voxels were obtained by warping the labels and tracts from the JHU-ICBM-labels-1mm and JHU-ICBM-tracts-maxprob-thr-0-1mm atlases (Mori *et al.* 2005) to the high resolution mean FA image using NiftyReg. This process was performed using a global affine registration followed by non-linear registration. This was in order to help identify the anatomic area of any significant findings without having to further register all images and results from DTI-TK space into standard-space.

## ***Tractography***

DTI tractography is a technique used to reconstruct the WM tracts in the brain and has been used in chapters 10 and 11 of this thesis. The following sections describe the processing steps required to perform tractography analysis on the pre-processed DTI data. To recap, pre-processed data is data that has been visually quality checked, eddy current and motion corrected, brain extracted and had a diffusion tensor model fitted at each voxel.

### ***BEDPOSTX***

There are many areas of WM in the brain where fibres cross or interleave and therefore multiple axon orientations are present within a voxel. This makes the estimation of a tensor within these types of voxels difficult and often results in incorrect low values of anisotropy. To avoid this problem, techniques are being developed that are capable of estimating multiple fibre orientations within a voxel.

Prior to running probabilistic tractography, crossing fibres were modelled using FSL's BEDPOSTX (Bayesian Estimation of Diffusion Parameters Obtained using Sampling Techniques; Behrens *et al.* 2007) which is an extension of a previously published probabilistic tractography routine (Behrens *et al.* 2003) applied to multiple fibre orientations in each voxel (Behrens *et al.* 2007).

It uses a partial volume model, which splits the diffusion signal into an anisotropic component for each fibre orientation, plus a single isotropic component. Bayesian estimation is used to fit the model to the signal at each voxel (Behrens *et al.* 2003). To ensure the model is only fitted in the case of multiple fibre bundles (and avoid applying a complex model to single fibre orientations, in the case of medial callosal voxels for example), automatic relevance determination (ARD) is used. ARD is a type of model selection technique that allows online selection of the number of fibre orientations supported by the data at each voxel, greatly simplifying fibre tracking through multiple orientations (Behrens *et al.* 2007).

## ***ROI Identification and Warping***

Before tractography was performed, the relevant ROIs for the analyses were identified. In this thesis tractography was performed within the CC (chapter 10), within the anterior cingulate cortex (ACC; chapter 11), and for tracts connecting the dorsolateral-prefrontal cortex (DLPFC) to the caudate and DLPFC to the thalamus (chapter 11). Specific methods are outlined in the relevant sections but the following is a summary.

ROIs in standard space were created using the Anatomy Toolbox (Eickhoff *et al.* 2005). Each mask was warped from standard space into structural space (using the T1 image) for each participant using the *Apply Deformation* in SPM. Exclusion masks to prevent wayward fibre tracking were also created in standard space using the MNI template (Mazziotta *et al.* 1995). They were created within *fslview* in FSL by flood filling slices in the MNI template with the bucket tool, or manually filling areas with the pen tool. The hemisphere masks, for example, had several filled slices either left or right of the midline to prevent fibre tracking across the hemispheres when tracking in specific left or right hemisphere regions. The masks were similarly warped to T1 space using SPM.

A WM termination mask (inverted SPM segmentation) was used to ensure that tracts did not extend beyond WM into GM, CSF or dura. All regions and masks were visually inspected to check that each warped ROI was in the correct anatomical location by overlaying them onto each participant's T1 image.

## ***Fibre Tracking***

FSL's PROBTRACKX conducts tractography that generates probabilistic streamlines from a region or between regions (Behrens *et al.* 2003). It repetitively samples from the distributions of principal diffusion directions at each voxel, generating a streamline, or connectivity distribution from pre-specified seed voxels. PROBTRACKX2 (the most recent version of PROBTRACKX) was used and pathways were only tracked through at least one of the seed points, i.e. the paths were only tracked if they passed through voxels in at least one of the ROIs.

Default parameters were used for the fibre tracking. Briefly, the number of samples was set to 5000; this determines the number of individual pathways that are reconstructed within the probability distribution of the principle fibre. Prior to running each full

tractography analyses, reconstruction was tested for anatomical correctness using a lower number of samples. The curvature threshold was 0.2 to limit pathways from turning too sharply within a voxel thus including implausible streamlines. The number of steps per sample was 2000 and the step length was 0.5mm. This means that at each step (every 0.5mm) the distribution of principle diffusion directions is assessed and a new fibre orientation is estimated. Streamlines were terminated once they had travelled 2000 steps, or a distance of 1m. The subsidiary fibre threshold was 0.01 and seed sphere sampling was set to 0 so that tracking ran from the seed (i.e. the ROI) centre.

The resulting tracts were then visually checked in *fslview* by overlaying the tracts on each participant's T1 image, along with the corresponding ROIs. The tracts were then warped into diffusion space using FSL's linear registration tool, FLIRT (Greve & Fischl 2009; Jenkinson & Smith 2001; Jenkinson *et al.* 2002). Despite having previously assessed this registration tool and found NiftyReg to be superior (section 2.3.2: Region of Interest Analysis), the FLIRT registration step was already established in the DTI tractography pipeline and was always visually checked for every participant to ensure correct alignment. Each warped tract was overlaid on each participant's FA map.

### ***Output Diffusion Metrics***

In order to output diffusion metrics (e.g. FA, AD, and RD), a script was run that produced a text file containing the diffusion values for each participant and each tract of interest. The script takes a mask of the warped pathways and then gives each streamline a weighting based on the weighted mean of the FA within that mask.

## **2.4 Statistical Analysis**

All statistical analyses in this thesis were performed using STATA (StataCorp LP).

### **2.4.1 Sample Size Calculations**

One of the first and most important things to consider when designing a study is determining the sample size required for answering the research question. Calculating the sample size for a study typically requires the following components (Noordzij *et al.* 2010):



1. Type I error ( $\alpha$ ). This measures the probability that, given the null hypothesis ( $H_0$ ) that participants in the sample come from the same population, any differences found are likely to happen. The  $\alpha$  is usually set at 0.05, which gives a <5% chance of getting a false-positive effect (Noordzij *et al.* 2010).
2. Power. Also called a type II error ( $\beta$ ). This component is usually set at 0.20, which gives a <20% chance of getting a false-negative effect. The corresponding power would be 80%, representing the probability of correctly rejecting the  $H_0$  (Noordzij *et al.* 2010).
3. Effect size. This is often the combination of two other components, variability and the smallest effect of interest, expressed as a multiple of the standard deviation of the observations. This is called the standardised difference (Noordzij *et al.* 2010).

For the majority of this thesis, data used has been previously acquired as part of the Track-HD, TrackOn-HD and PADDINGTON studies. The sample size calculations for these studies were therefore already conducted and are detailed in the relevant papers. For Track-HD, the primary study aim was to identify and quantify clinically meaningful longitudinal change in various measurements over two years, with a narrow confidence interval. Therefore, the sample size was determined according to projected uncertainty within sample size recommendations for future clinical trials, which advocate a larger sample than that required to detect cross-sectional differences (Tabrizi *et al.* 2009).

The two cognitive task studies investigating interhemispheric transfer (chapter 10) and susceptibility to interference (chapter 11) required sample size calculations for their respective outcomes and hypotheses and were conducted independently for each task. It is important to emphasise that both were pilot studies. Previous studies have used interhemispheric- and interference-style tasks in other populations, but these tasks have not been investigated thus far in a HD cohort. Therefore, the sample size calculations were based on studies using similar tasks used in non-HD patient groups, plus studies in HD groups which used a different set of cognitive tasks. Full information of the sample size calculations for both cognitive tasks is provided in Appendix 2: Sample Size Calculations.

## 2.4.2 Regression

Regression analysis is used to fit models to data in order to estimate the relationship between variables, typically an outcome and one or more predictors. Linear regression analysis was used multiple times in this thesis and full details are provided in the relevant sections.

Generalised least squares (GLS) regression was used to model between-group differences for continuous variables e.g. CC volume (chapter 7). In this case the GLS was appropriate because it allowed for differing variances between the groups, e.g. increasing variability in baseline CC volume with increasing disease stage. GLS regression was also used to examine longitudinal between-group differences in atrophy rates (% per year). In order to do this, change was converted to a percentage of baseline CC volume and annualised.

Ordinary least squares regression (OLS) was used to test for within- and between-group differences in the outcome variables for both the interhemispheric transfer (chapter 10) and interference task (chapter 11). Robust estimate of variance was used to help control for the effects of outliers and differing variance between the groups. In order to analyse any possible change in results over one year, a linear regression model was used to test for within- and between-group change in the outcome variables. The annual change in reaction time (RT) was calculated for each participant by subtracting the baseline RT (V1) from the visit two RT (V2), and then multiplying this by 365.25 divided by the actual time interval between visits:  $(V2 - V1) \times 365.25 / \text{interval}$ . Linear regression models were also used to investigate disease-related associations (i.e. in HD gene-carriers only) between imaging metrics and cognitive/clinical variables.

### *Covariates*

Potentially confounding covariates were controlled for where possible to prevent confounding or interacting effects on the results. All analyses in this thesis controlled for age and gender. Study site was added as a covariate when data were being analysed from more than one site. Where analyses included cognitive variables, education (measured using the International Standard Classification of Education; ISCED) was also controlled for. In longitudinal analyses, the testing interval was added as a covariate.

Investigations restricted to HD gene-carriers also included disease-burden score (Penney *et al.* 1997) as an adjustment variable to help ensure associations were not driven by general disease severity (e.g. in chapter 7). In chapters 10 and 11 the number of individual responses was also included in the regression models using weighted means in order to limit the effects of unequal responses between participants and groups.

In order to account for variation in head size, cross-sectional between-group analyses of regional volumes were adjusted for total TIV, either using the manual method (Whitwell *et al.* 2001, described in section 2.3.1: Total-Intracranial Volume), or the automated method using SPM (described in section 2.3.1: Statistical Parametric Mapping) if no manual region had previously been acquired. This was done by expressing each volume as a percentage of TIV (Barnes *et al.* 2010).

### **2.4.3 Correlation**

Correlation analysis, broadly speaking, is used to examine the relationship between two variables. Spearman's correlation analysis is a non-parametric correlation that measures the extent to which one variable tends to increase or decrease as the other variable increases. This type of analysis was used to assess the relationship between the cognitive outcome variables and disease status in the premanifest HD participants (chapters 10 and 11). The Spearman coefficient is more robust than the more commonly used Pearson, making it more appropriate for small sample sizes. Additionally, it is not overly influenced by outliers in the data.

### **2.4.4 Correction for Multiple Comparisons**

All statistical comparisons run the risk of detecting a false-positive result. In neuroimaging analyses, where thousands of statistical tests are performed simultaneously, this risk is considerably increased. The Family-Wise Error (FWE) rate is the probability of making a false-positive discovery (type I error) when performing multiple tests. FWE correction aims to reduce this probability by adjusting the p-value threshold (e.g.  $p < 0.05$ ) according to the number of tests being made. In this thesis, all results from the voxel-wise, TBSS analyses were FWE-corrected for multiple comparisons.

# Development, Optimisation and Investigation of Neuroimaging Techniques

Assessing and improving current imaging techniques will help better ascertain structural brain changes and optimise technique sensitivity at all disease stages. Fulfilling the first aim of this thesis, the next chapter describes the development of a macrostructural technique to segment the corpus callosum (CC) using T1-weighted images. This is followed by an investigation of a tensor-based registration technique for diffusion-weighted images, focusing on the effects of customised group template choice in a large clinical cohort.

## 3. Development of a Novel Segmentation Tool

Volumetric MR imaging studies have highlighted the pronounced loss of WM in premanifest individuals (Nopoulos *et al.* 2011; Novak *et al.* 2013; Tabrizi *et al.* 2009; 2011; 2012; 2013) and in early HD (Hobbs *et al.* 2010; 2013; Novak *et al.* 2013; Tabrizi *et al.* 2011; 2012; 2013). Driven by this abundance of evidence, the current study focussed on the largest and arguably one of the most important WM fibre bundles in the brain, the CC. It is situated beneath the cortex at the longitudinal fissure, connecting the left and right cerebral hemispheres. It provides vital connections to cortical areas known to be affected in HD and plays an integral role in interhemispheric communication.

The CC can be subdivided into three main sections. At the posterior is the splenium, anteriorly is the genu (or "knee") and between the two is the truncus, or "body". Topographical organization of the CC has been demonstrated with DTI-based tractography (Hofer & Frahm 2006) and fMRI studies (Fabri *et al.* 2011) and it is well-known that each region of the CC projects to distinct cortical areas (see Fabri *et al.* 2014 for a review). Thinner, slow-conducting fibres in the genu connect prefrontal higher-order processing areas and thicker, fast-conducting axons connect the visual, motor and somatosensory areas and are believed to be involved in mid-line fusion (Aboitiz *et al.* 1992a, 1992b).

Much of the recent increase in research has used DTI to illustrate loss of microstructural integrity in the CC of HD participants, implementing thickness measures, DTI metrics and DTI tractography for cross-sectional comparison with healthy controls (Bohanna *et al.* 2011; Di Paola *et al.* 2012; Dumas *et al.* 2012; Klöppel *et al.* 2008; Phillips *et al.* 2013; Rosas *et al.* 2006; Rosas *et al.* 2010; Steventon *et al.* 2015). T1-weighted MRI, however, is the most commonly used MR acquisition for measuring regions of interest (ROIs) in HD (Hobbs *et al.* 2013; Rosas *et al.* 2003; Tabrizi *et al.* 2009; 2011; 2012; 2013), and is used for studying both GM and WM at the voxel level (Hobbs *et al.* 2010; Klöppel *et al.* 2008; Scahill *et al.* 2013).

### **3.1 Aims**

This study aimed to develop a novel semi-automated technique for anatomically accurate delineation of the whole CC using structural 3T T1-weighted MRI scans. The long term objective was to apply this technique to a clinical cohort in order to investigate cross-sectional and longitudinal group differences in CC volume and hypothesis-driven associations with cognitive function (see chapter 7).

### **3.2 Protocol Development**

The CC segmentation protocol was developed and tested on the multi-site dataset from the PADDINGTON study (Hobbs *et al.* 2013) including both atrophied and healthy brains. Image processing was carried out using MIDAS (Freeborough *et al.* 1997). 3T MRI scans were registered into standard MNI 305 atlas space (Mazziotta *et al.* 1995) to ensure consistent orientation and landmark-defined cut-offs over time.

Firstly, the mid-sagittal slice was selected. One of the first studies to anatomically quantify and subdivide the CC acquired measurements on the mid-sagittal slice (Witelson 1989), and many subsequent studies also used the mid-sagittal slice as a delineation starting point or reference for tractography (Catani *et al.* 2002; Hofer & Frahm 2006; Karakas *et al.* 2011). This slice was chosen by firstly locating the anterior commissure sagittally, and then coronally placing the position bar in the centre of the two ventricles where they are at their closest. The slice where the least brain was evident surrounding the CC was consistently chosen, indicating the most middle point between the two brain hemispheres.

A ‘seed’ was placed manually within the CC and intensity constraints derived from the mean brain intensity (MBI) of the scan automatically highlighted the CC (Figure 3-1). These thresholds were derived empirically by adjusting the values of the MBI to optimise the delineation of the CC. 100% and 150% thresholds were chosen based on visual assessment. This first seed placement produced good delineation of the structure in the majority of cases (Figure 3-1). However, the borders of the region were manually edited where necessary. Common edits involved removal of region over-spill beyond the structure boundary or blood vessels running adjacent to the CC and moving away from it (Figure 3-2).

The segmentation was repeated four slices either side of the mid-sagittal slice, i.e. nine slices in total. The whole segmentation took approximately five minutes for each participant. Please see Appendix 1: Volumetric Analysis for the complete standard operating procedure.

### **3.3 Reproducibility**

Reliability of the technique was assessed using CC volume measurements of eight participants (from the dataset described above (Hobbs *et al.* 2013)); healthy and early HD participants from four study sites. Four raters performed the CC measurement twice, one week apart, enabling assessment of inter- and intra-rater reliability using the intraclass correlation coefficient (ICC). An ICC of less than 0.40 is thought to be poor and an ICC of between 0.75 – 1.00 is reported to be excellent (Cicchetti 1994). Inter-rater reliability of the current technique was very high: the ICC for both measurements were >0.999. Intra-rater reliability was also extremely good (ICCs >0.999 for all four raters).

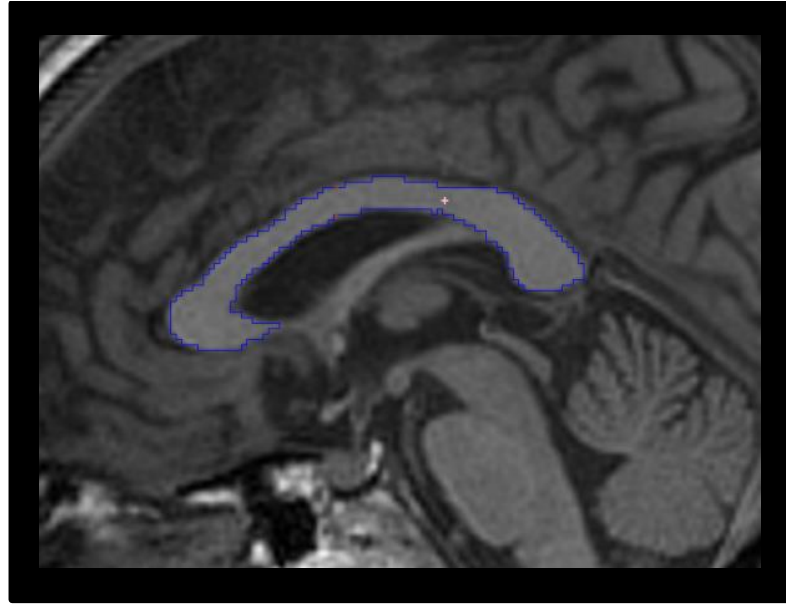


*Figure 3-1. CC segmentation. Seeded region where threshold has successfully segmented the structure with no over-spill.*

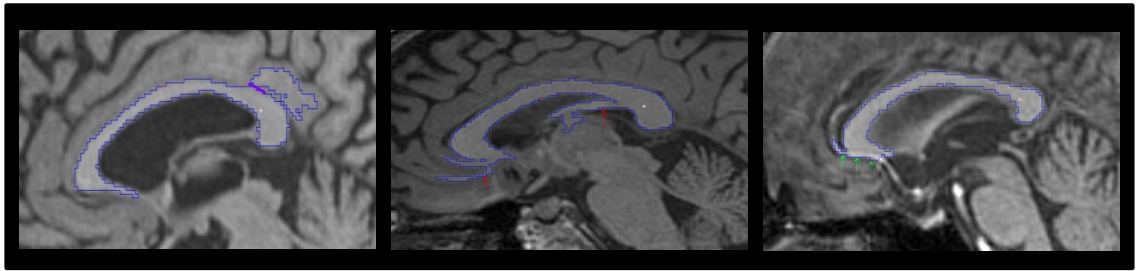


*Figure 3-2. Examples of obvious edits to the CC segmentation. Remove over-spill delineated by the purple line (left) and the fornix and rostral seepage, highlighted by red arrows (middle). Right: Example of a blood vessel that needs removing, highlighted by the green arrows.*

### 3.4 Discussion

A novel segmentation technique for the CC was successfully developed using conventional T1-weighted MRI scans. This technique was optimised for anatomical precision using the structures visible on these particular scans. The technique is semi-automated therefore has an advantage over automated techniques because the thresholds can be overridden where necessary. Strong reliability of the method is evidenced by the excellent inter- and intra-rater reliability, however it should be noted that the reproducibility test is limited by the reduced sample size of eight scans. It also worth noting that the technique has yet to be systematically compared with automated CC

delineation techniques. Nonetheless manual delineation of brain structures is often deemed the gold-standard methodology.

Additional segmentation of the structure's three main sub-regions was investigated (genu, body and splenium), however structural MRI scans do not reveal morphologically discernible structures and after numerous attempts further subdivision was abandoned. The lack of consistent anatomical landmarks introduced too much subjective bias into the procedure making it unreliable and subsequent results unreproducible.

Since development, the technique was applied to two clinical cohorts, one of which is the multi-centre PADDINGTON study (Hobbs *et al.* 2013; 2015), and findings have subsequently been published (Crawford *et al.* 2013). Full details of the clinical application of this procedure are provided in chapter 7.



## 4. Investigation of a Registration Tool

One of the issues with image registration of DTI data is the need to accurately align WM in a manner that is consistent with the inherent fibre orientation, a problem compounded in regions where two or more fibre bundles cross. Image warping is also more complex because transformations of the images can change the orientation of the diffusion tensors and cause errors in anatomical alignment. This is problematic for subsequent analysis and extraction of diffusion metrics if voxels sampled contain incorrect fibre orientation.

Likewise, structural changes, such as inter-individual variability and atrophy in neurodegenerative diseases like HD can cause difficulties in image alignment, especially to predefined atlases or standard templates. These templates are often created using the brain scans of young, healthy, and probably more homogeneous participants. The choice of a reference or target image for registration is therefore very important and several studies have shown that using a group-wise average atlas as the reference outperforms other reference targets, specifically for TBSS (Keihaninejad *et al.* 2012), and voxel-based morphometry (VBM) analysis (Shen *et al.* 2007).

As discussed previously (section 2.3.2: TBSS with DTI-Toolkit), the registration technique DTI-TK (Zhang *et al.* 2006) was developed to help achieve accurate alignment of diffusion images by employing a registration algorithm that matches the orientation of the underlying fibres at each voxel. There is much evidence to show that tensor-based registration outperforms other scalar or FA-based registration (Keihaninejad *et al.* 2013; Park *et al.* 2003; Wang *et al.* 2011).

In order to achieve optimal alignment of WM, DTI-TK creates a customised diffusion tensor template to which all other diffusion tensor images are registered, in preparation for next-level group analysis, such as TBSS analysis. The customised template should act as a good representation of the data in terms of the cohort being studied and the type of analysis being conducted, such as patient-control group comparisons. For example, if examining data from two groups acquired from different study sites, then balanced datasets from both groups and sites should be included in the template to reduce bias. It is not always computationally possible to use all participant data to create a template in

studies with large datasets, therefore the creation of a template from a small subset of data is necessary and customisation that best reduces bias is very important.

The original DTI-TK validation used only one arbitrary tensor image as a template (Zhang *et al.* 2006) and as yet, there are no established guidelines on template size or composition. Therefore, it is possible that data used in the creation of the template may cause bias or inaccurate alignment due to differences in image quality or study site, for example, or just individual variation in the tensors themselves. Due to the advantages of tensor-based registration using DTI-TK for DTI analysis (chapter 9), this issue was explored further in a small methodological study.

The aim of the study was to investigate the creation of the customised template and assess whether the selection of tensor data could affect DTI analysis, including whole-brain TBSS analysis. Focus here was on the diffusion measures fractional anisotropy (FA) and radial diffusivity (RD) (described in section 1.2.2: Principles of Diffusion Imaging). FA is a widely used metric in DTI research and it is well established that both FA and RD are affected in HD (Bohanna *et al.* 2011; Della Nave *et al.* 2010), with RD being particularly sensitive in premanifest HD (Di Paola *et al.* 2014). Data from four different study sites (Leiden, London, Paris and Ulm) and three different participant groups (premanifest HD, early HD and controls) were used for this study, reflecting the type of sample used in multi-site research and clinical trials.

## 4.1 Aims

This study aimed to assess template effects on diffusion imaging data analysis using an unbiased tensor-based registration approach, DTI-TK (Zhang *et al.* 2006), followed by whole-brain TBSS analysis. In particular, this study examined whether pseudo-randomisation of participants for inclusion in the creation of three independent templates would produce similar diffusion metrics across the three participant groups, similar between-group differences in metrics, and concordantly located between-group differences using TBSS.

## 4.2 Methods

### 4.2.1 Participants

Diffusion images from premanifest HD, early HD and healthy control participants were taken from the 36 month visit of the Track-HD study (Tabrizi *et al.* 2013) and the baseline visit of the PADDINGTON study (Hobbs *et al.* 2013). These particular visits were chosen from each of the studies because they produced the largest amount of diffusion data. The demographic and clinical characteristics of the participants and the distributions across study sites are presented in Table 4-1.

**Table 4-1. Demographics and Clinical Characteristics of Participants**

<b>Demographics and Clinical Characteristics of Participants</b>			
	<b>Control</b>	<b>Premanifest</b>	<b>Early HD</b>
<b>N = 153</b>	50	59	44
<b>Site (total N):</b>			
Leiden (29)	10	13	6
London (53)	17	22	14
Paris (52)	15	24	13
Ulm (19)	8	0	11
<b>Age, years*</b>	44.06 (6.05)	40.93 (6.39)	44.75 (8.18)
<b>Gender F/M</b>	29/21	30/29	23/21
<b>CAG repeat length</b>	-	43.36 (2.12)	44.32 (2.99)
<b>Disease-Burden Score**<math>\pm</math></b>	-	308.73 (66.27)	360.33 (69.12)

Values are represented as mean (SD), except gender where the numbers of males/females are given. \*In 2011 \*\*As measured at baseline  $\pm$ Disease-Burden Score = (CAG length – 35.5) x age (Penney *et al.* 1997).

### 4.2.2 Image Analysis

Diffusion data were visually checked for gross artefacts, motion and signal dropout. Data were then eddy current corrected and brain extraction was performed. The

diffusion tensor model was fitted at each voxel according to the pre-processing pipeline described in section 2.3.2: Pre-Processing. The DTI-TK protocol and TBSS analysis were then performed, as described in section 2.3.2: TBSS with DTI-Toolkit.

Three separate customised tensor templates were created, each comprising 24 different participants pseudo-randomly selected from the cohort. Two participants were chosen from each site and from each group, with the exception of the premanifest HD group where an extra participant from London and Paris were selected to ensure equal numbers across the three templates. This was because there was no premanifest HD data from Ulm in the cohort (only early stage HD and control participants were studied in the PADDINGTON study (Hobbs *et al.* 2013)).

The final tensor templates comprised eight control participants (two Leiden, two London, two Paris and two Ulm), eight premanifest HD participants (two Leiden, three London and three Paris), and eight early HD participants (two Leiden, two London, two Paris and two Ulm).

In order to make an initial visual comparison of the three templates, they were subtracted from one another in FSL using *fslmaths*. Each participant's tensor image was then registered to each of the three tensor templates and FA and RD maps were computed from the high resolution whole-group templates according to the DTI-TK pipeline. All registrations to the tensor templates were visually checked for accurate alignment. The FA and RD maps for each of the three template groups were also subtracted from one another and visually compared.

The WM skeletons generated in the TBSS pre-processing steps for each of the three template groups were compared by adding together each binary FA skeleton mask using *fslmaths* and viewing the overlapping voxels. In order to assess the correspondence between the three skeletons, images were thresholded to only show the voxels common to all three template skeletons.

Skeletonised FA results are automatically generated in TBSS analysis, however RD results were calculated separately, according to the TBSS pipeline (section 2.3.2: TBSS with DTI-Toolkit). Briefly, this was done by generating the RD maps for each participant, merging them into a 4D file to create the mean RD map and then projecting

this onto the WM skeleton to obtain the skeletonised data. The mean FA and RD values were then extracted from the skeletons for each participant group, for each of the separate template groups using *fslstats* and entered into the regression analyses.

Whole-brain voxelwise TBSS analysis was conducted separately with the data generated using the three different templates. Between-group comparisons were run using the FA and RD data. FA maps created from each of the three template groups were merged and a total mean FA map was created onto which the combined TBSS results were overlaid for comparison.

#### **4.2.3 Statistical Analysis**

Regression models were fitted to assess between-group differences within each template group, whilst controlling for age, gender and study site. Between-template differences in diffusion values output from the WM skeleton were assessed using paired t-tests, which were Bonferroni corrected for multiple comparisons. The Bonferroni correction is a conservative correction that reduces the rate of finding false-positive results by adjusting the alpha level by the number of tests being made, in this case 18, giving a corrected p-value of  $<0.003$ . Spearman's Rank correlation coefficients were also computed to examine agreement between the templates.

Scatter plots were used to illustrate agreement between the diffusion metrics output from the analyses with the three separate templates. The data points for each participant group were plotted separately to identify any potential disease-related bias.

Voxelwise cross-participant statistics were performed with the data generated using the three different templates using the FSL Randomise tool, which uses general linear modelling (GLM) and thresholding to find correlating voxels. Statistical contrasts between all participant groups for each template were performed on all voxels within the FA skeleton mask using non-parametric permutation tests ( $n=500$ ). Age, gender and study site were included in the models as regressors of no interest. All results were family-wise error (FWE) corrected for multiple comparisons using the threshold free cluster enhancement (TFCE) method and thresholded at  $p<0.05$ . In order to present the skeletonised results more clearly, results were 'thickened'. The number of significant voxels ( $p<0.05$ ) for each between-group contrast was also output using *fslmaths*.

### 4.3 Results

Figure 4-1 shows each of the three customised tensor templates and Figure 4-2 shows the difference once they were subtracted from one another. On visual inspection, the three templates did not look dissimilar, however the subtraction maps revealed some differences between the templates. Template one and template three appeared to be the most different, mainly due to the bright voxels around the edge of the brain which indicated higher tensor values for template one (Figure 4-2, B). Template one and template two were marginally less different but equally had differences at the edge of the cortex (Figure 4-2, A). Templates two and three appeared the most similar (Figure 4-2, C).

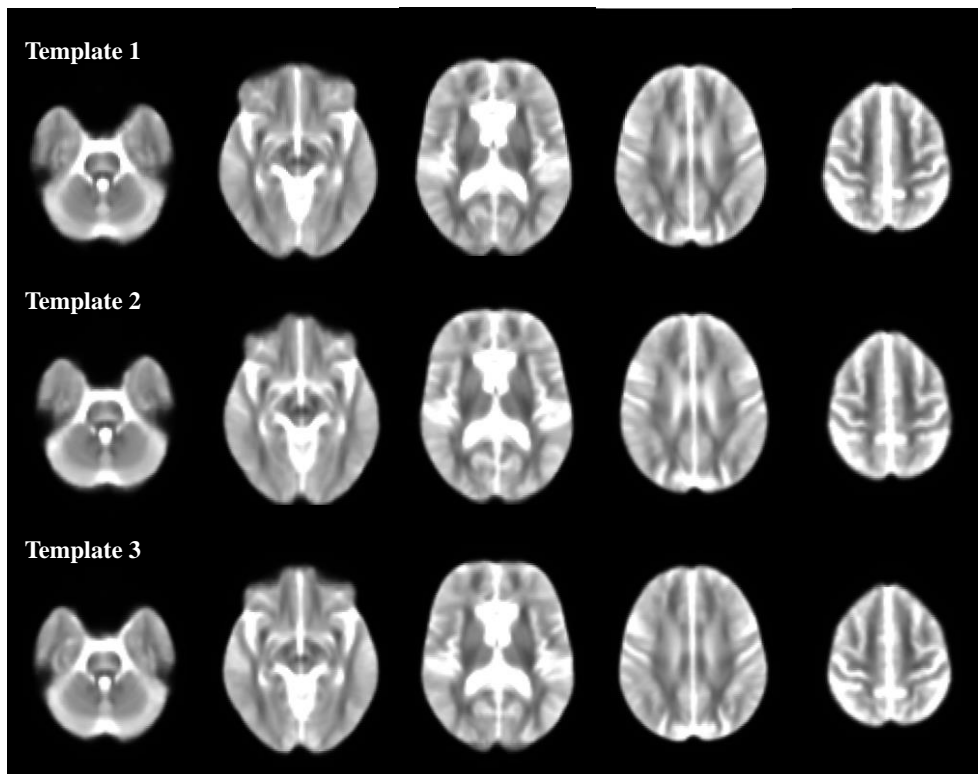


*Figure 4-1. Axial slices from each of the three customised tensor templates.*

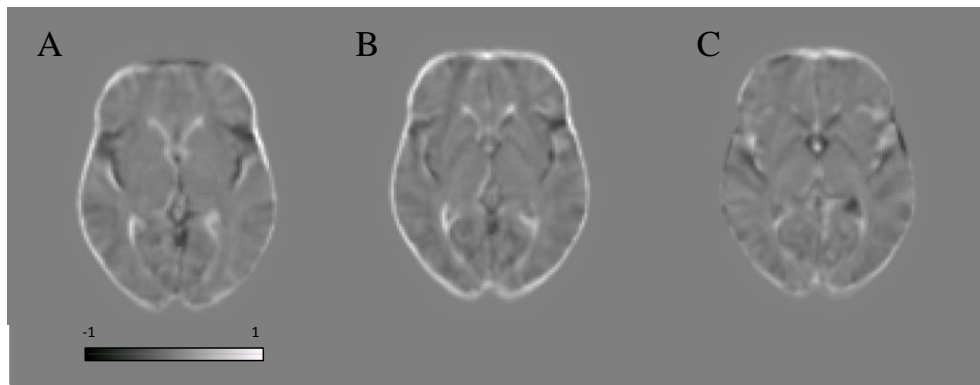


**Figure 4-2. Subtraction maps. (A) Template 1 minus template 2. (B) Template 1 minus template 3. (C) Template 2 minus template 3. Bright voxels indicate higher values for template 1 in A and B and for template 2 in C. Dark voxels indicate higher values in template 2 in A and for template 3 in B and C. Grey values are exactly equal to zero.**

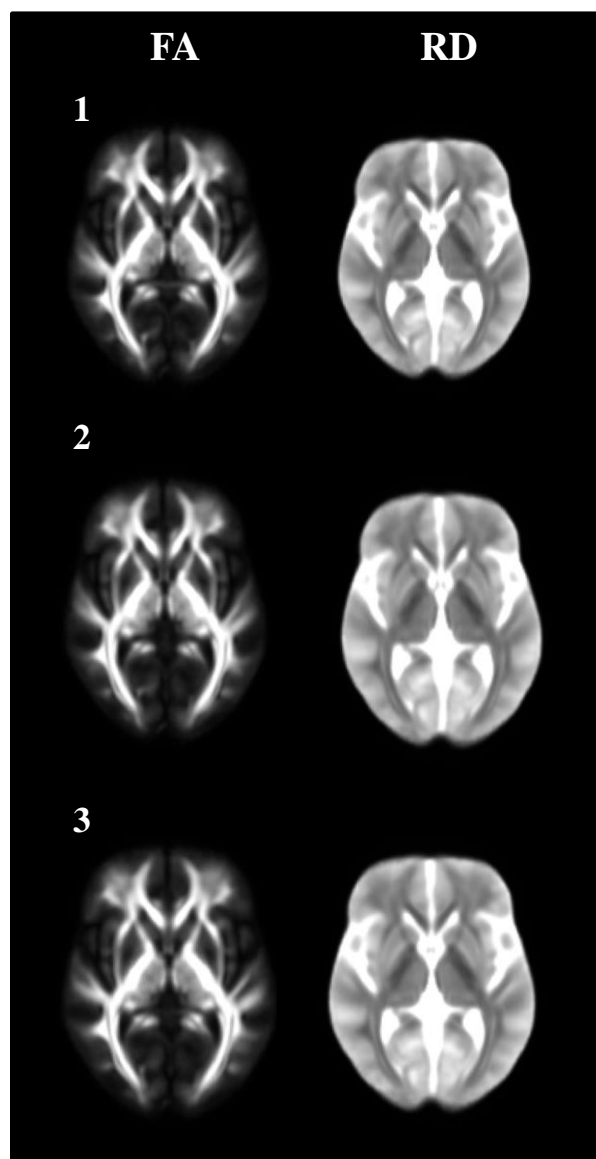
Each of the registrations between participants' tensor images to the final group tensor templates were visually checked and all passed QC. At this stage, there were no set parameters for differentiation between registration quality of the three datasets.

Figure 4-3 shows the mean FA and RD maps computed from the high resolution whole group templates using each of the three customised templates. Similarly, visual inspection was insufficient to detect any subtle differences in registration quality.

The subtraction images of the FA and RD maps in Figure 4-4 revealed some differences between the three different datasets. The largest differences appeared to be for the mean FA maps, particularly between template one and template three (Figure 4-4, B). The smallest difference appeared to be between the RD maps of template two and three (Figure 4-4, C). The mean FA skeletons for each of the datasets are provided in Figure 4-5 and voxels common to all three separate skeletons are identified in Figure 4-6.

Mean diffusion values extracted from each of the three separately generated WM skeletons are displayed in Table 4-2 and the between-template differences in each of the groups' metrics are given in Table 4-3. Although analyses using the three different templates reported relatively similar diffusion values for each group, the paired t-test analysis revealed that several of the mean differences between the three sets of values were significantly different from zero, indicating a difference in the values produced using each of the three templates.

The analysis using template one had lower FA and higher RD compared with template two. This difference was significant across all groups ( $p < 0.001$ , see Table 4-3). Metrics from the analyses using templates one and three did not differ for any of the participant groups. FA values in the control and early HD groups from the analyses using templates two and three were significantly different (both  $p < 0.001$ , see Table 4-3), with template two data reporting higher values. The control group was the only group to show significantly different RD between analyses for templates two and three ( $t(49) = -3.519$ ,  $p = 0.001$ ), in this case template two was smaller.



*Figure 4-3. FA and RD maps computed from the high resolution whole group templates, created using each of the three customised templates, labelled 1, 2 and 3.*



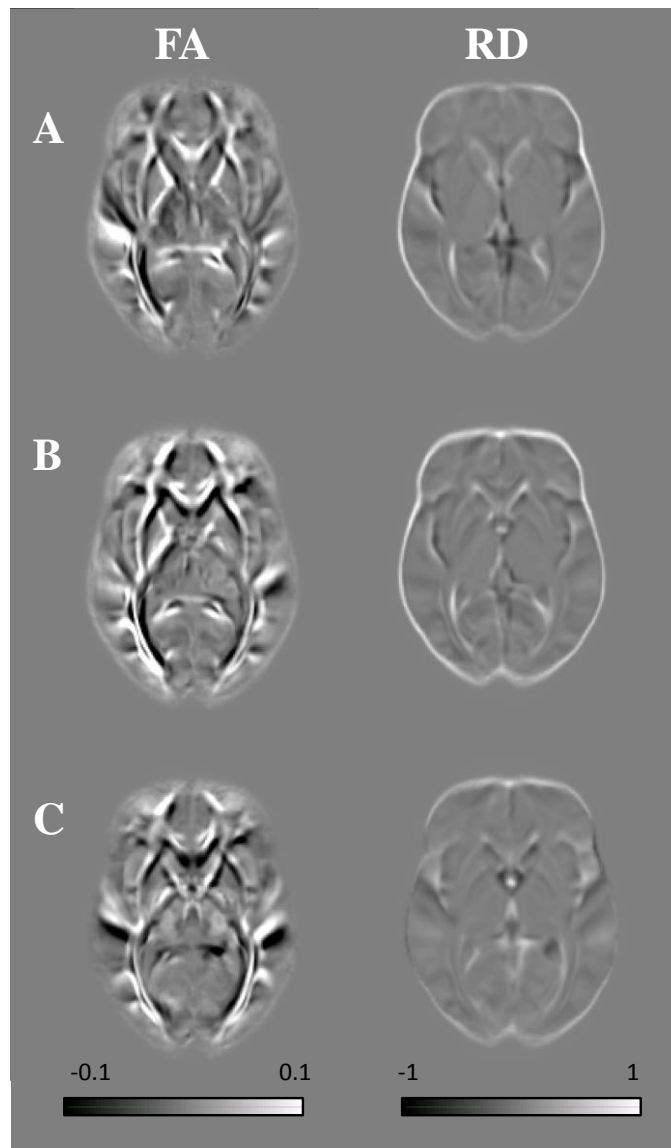


**Figure 4-4.** Subtraction maps of the FA and RD maps computed from the high resolution whole group templates, created using each of the three customised templates. (A) Template 1 minus template 2. (B) Template 1 minus template 3. (C) Template 2 minus template 3. Bright voxels indicate higher values for template 1 in A and B and for template 2 in C. Dark voxels indicate higher values in template 2 in A and for template 3 in B and C. Grey values are exactly equal to zero.

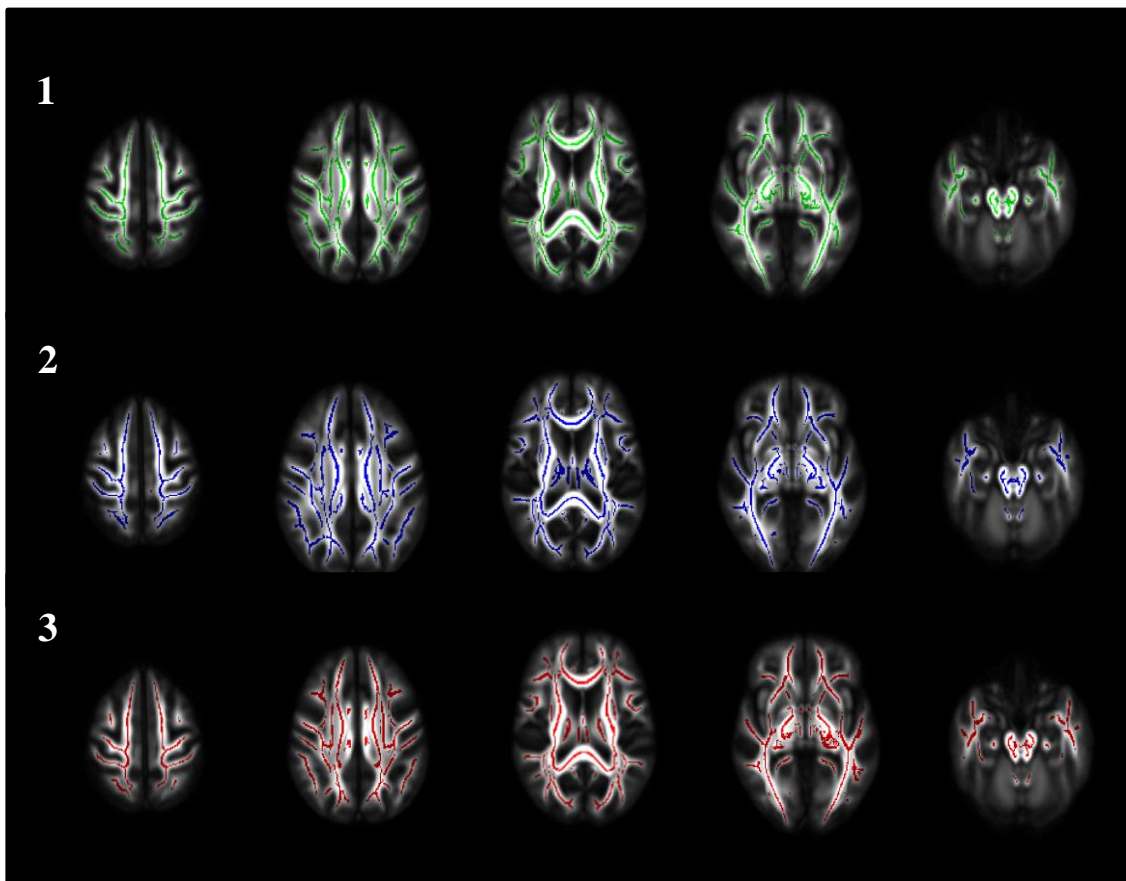


*Figure 4-5. Mean FA images and FA skeletons for template 1 (green), template 2 (blue) and template 3 (red). Skeletons are thresholded between 0.2 - 0.7.*

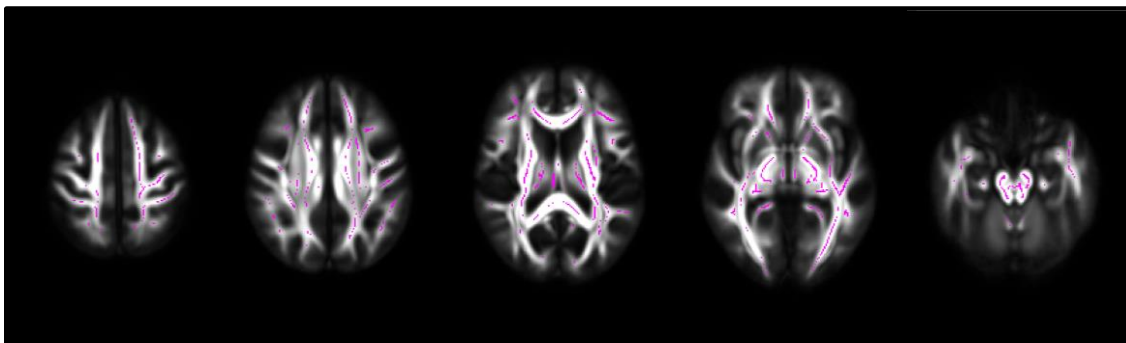


*Figure 4-6. Common voxels (pink) to all three FA skeleton masks generated using each of the three templates, overlaid on the mean FA image for template one.*

**Table 4-2. Mean (SD) Diffusion Values from White Matter Skeleton**

Metric	Group	Template 1	Template 2	Template 3
<b>FA</b>	Control	0.447 (0.017)	0.448 (0.018)	0.446 (0.017)
	Premanifest HD	0.444 (0.015)	0.445 (0.015)	0.442 (0.017)
	Early HD	0.430 (0.019)	0.431 (0.019)	0.430 (0.019)
<b>RD*</b>	Control	0.532 (0.030)	0.531 (0.029)	0.531 (0.029)
	Premanifest HD	0.535 (0.022)	0.534 (0.022)	0.536 (0.024)
	Early HD	0.577 (0.039)	0.575 (0.039)	0.575 (0.039)

\*10<sup>-3</sup>mm<sup>2</sup>.s<sup>-1</sup>

**Table 4-3. Between-Template Differences in Diffusion Metrics by Group**

Template Analysis	Controls	Premanifest HD	Early HD
<b>FA</b>			
1 vs. 2	-0.001 (0.001)	-0.001 (0.002)	-0.001 (0.002)
	-5.393 (49)	-4.244 (58)	-4.539 (43)
	0.000	0.000	0.000
1 vs. 3	0.000 (0.002)	0.002 (0.006)	0.000 (0.002)
	2.011 (49)	2.036 (58)	0.235 (43)
	0.050	0.046	0.816
2 vs. 3	0.002 (0.001)	0.003 (0.007)	0.001 (0.001)
	9.725 (49)	3.001 (58)	7.681 (43)
	0.000	0.004	0.000
<b>RD*</b>			
1 vs. 2	0.001 (0.002)	0.001 (0.002)	0.002 (0.003)
	5.201 (49)	4.720 (58)	4.288 (43)
	0.000	0.000	0.000
1 vs. 3	0.001 (0.002)	-0.001 (0.007)	0.001 (0.003)
	2.595 (49)	-0.920 (58)	3.006 (43)
	0.013	0.362	0.004
2 vs. 3	-0.001 (0.001)	-0.002 (0.008)	-0.000 (0.002)
	-3.519 (49)	-1.878 (58)	-0.812 (43)
	0.001	0.065	0.421

Values shown are the mean difference (SD), t-statistic (degrees of freedom) and two-tailed p-values. Results are Bonferroni corrected with alpha level p<0.003. Light grey shading indicates that the mean difference between templates is significantly different from zero at two-tailed p<0.003. Dark grey shading indicates that this difference is significant at two-tailed p<0.001. \*10<sup>-3</sup>mm<sup>2</sup>.s<sup>-1</sup>.

Table 4-4 contains the between-group differences in all diffusion metrics for the analyses using each of the three templates, adjusted for age, gender and study site. All three template analyses produced similar differences for both metrics (both  $p < 0.001$ ) in the early HD versus the control group analysis. The same was true for the early HD group when compared with the premanifest HD group (significant differences at  $p < 0.05$  for FA and  $p < 0.001$  for RD).

Using template three, FA was significantly lower in the premanifest HD group compared with controls ( $-0.008$ , 95% C.I.  $-0.014$ ,  $-0.001$ ,  $p = 0.023$ ), whereas this difference was only trend significant for analyses using templates one and two ( $p = 0.056$  and  $p = 0.050$  respectively).

Unsurprisingly, the Spearman's Rank analysis found a significant correlation between all measures, across all groups, for all templates ( $p < 0.05$ ). There was also strong agreement between the FA and RD values for analyses using all template groups as demonstrated in Figure 4-7 and Figure 4-8. There were, however, three premanifest HD outliers whose FA values were lower and RD values were higher for analysis using template three compared with that of the other templates. This can be seen from the cluster of three points above and below the line of equality in the scatter plots.

**Table 4-4. Between-Group Differences in Diffusion Metrics by Template**

Analysis	Template 1	Template 2	Template 3
<b>FA</b>			
Premanifest HD vs. Controls	-0.006 (-0.012, 0.000) 0.056	-0.006 (-0.013, -0.000) 0.050	-0.008 (-0.014, -0.001) 0.023
Early HD vs. Controls	-0.017 (-0.023, -0.010) 0.000	-0.016 (-0.023, -0.010) 0.000	-0.016 (-0.023, -0.009) 0.000
Early HD vs. Premanifest HD	-0.012 (-0.017, -0.004) 0.002	-0.010 (-0.017, -0.004) 0.003	-0.008 (-0.015, -0.002) 0.017
<b>RD*</b>			
Premanifest HD vs. Controls	0.011 (0.000, 0.021) 0.044	0.011 (0.001, 0.021) 0.038	0.012 (0.002, 0.023) 0.021
Early HD vs. Controls	0.042 (0.031, 0.053) 0.000	0.042 (0.031, 0.052) 0.000	0.041 (0.030, 0.052) 0.000
Early HD vs. Premanifest HD	0.031 (0.020, 0.042) 0.000	0.031 (0.020, 0.042) 0.000	0.028 (0.017, 0.040) 0.000

Values shown are regression coefficients (95% C.I.s) and p-values. Dark grey shading indicates a between-group difference at  $p < 0.001$  and light grey shading indicates  $p < 0.05$ , adjusted for age, gender and site.  $\ast 10^{-3} \text{mm}^2 \cdot \text{s}^{-1}$ .

The registration of the tensor data from these three outlying participants to tensor template three was reviewed and the alignment was visually satisfactory. It could be argued that the registration of these individuals to template three was marginally poorer than to that of the other two templates but this could not be quantified visually. In order to examine these three participants further, axial diffusivity (AD) maps were also generated and values extracted from the WM skeleton in the same way as for RD. AD was found to be slightly lower for all three participants in analysis using template three compared with templates one and two.

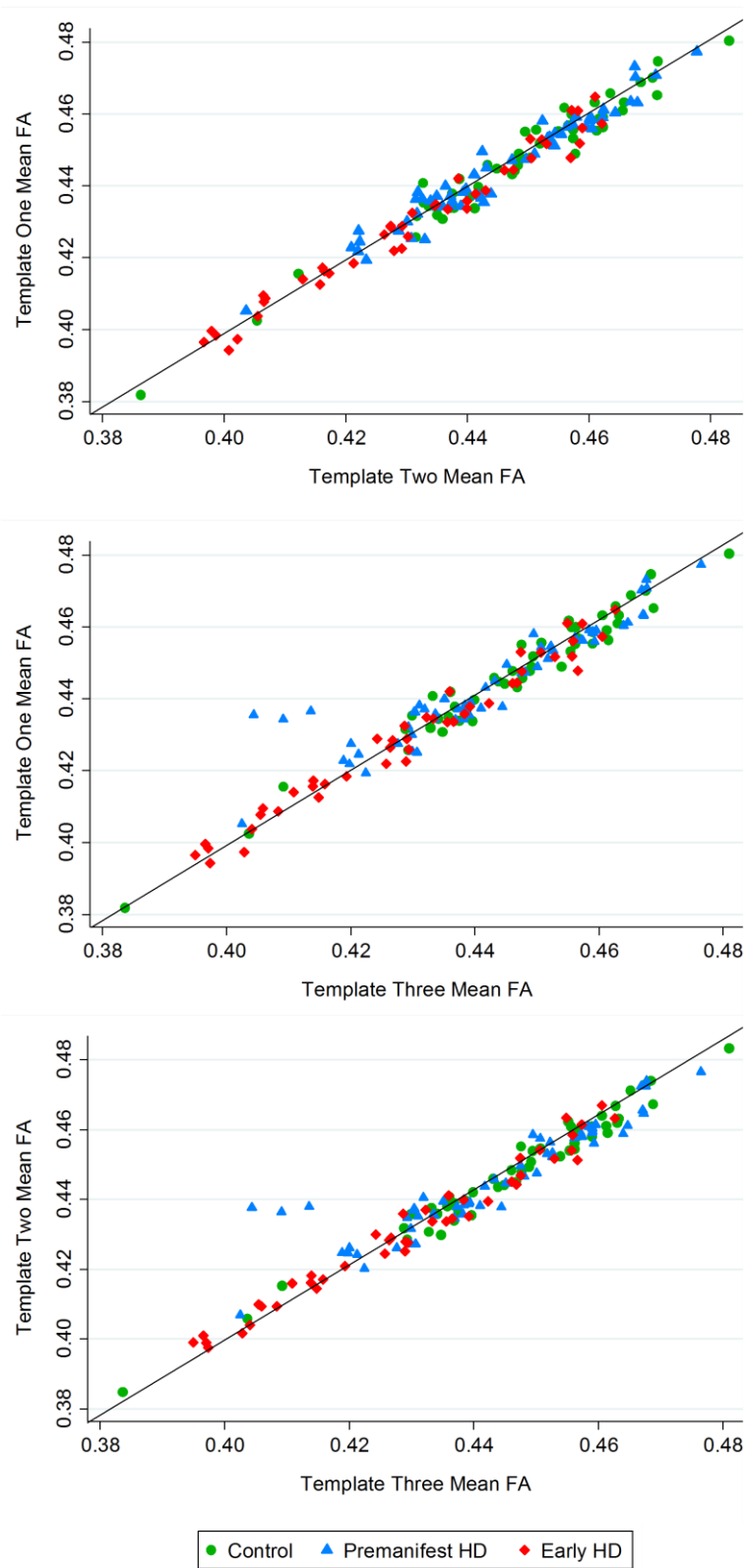


**Figure 4-7. Scatter plots of agreement between the mean FA values extracted from the three different template-registered data. The line of equality (black) is also shown.**

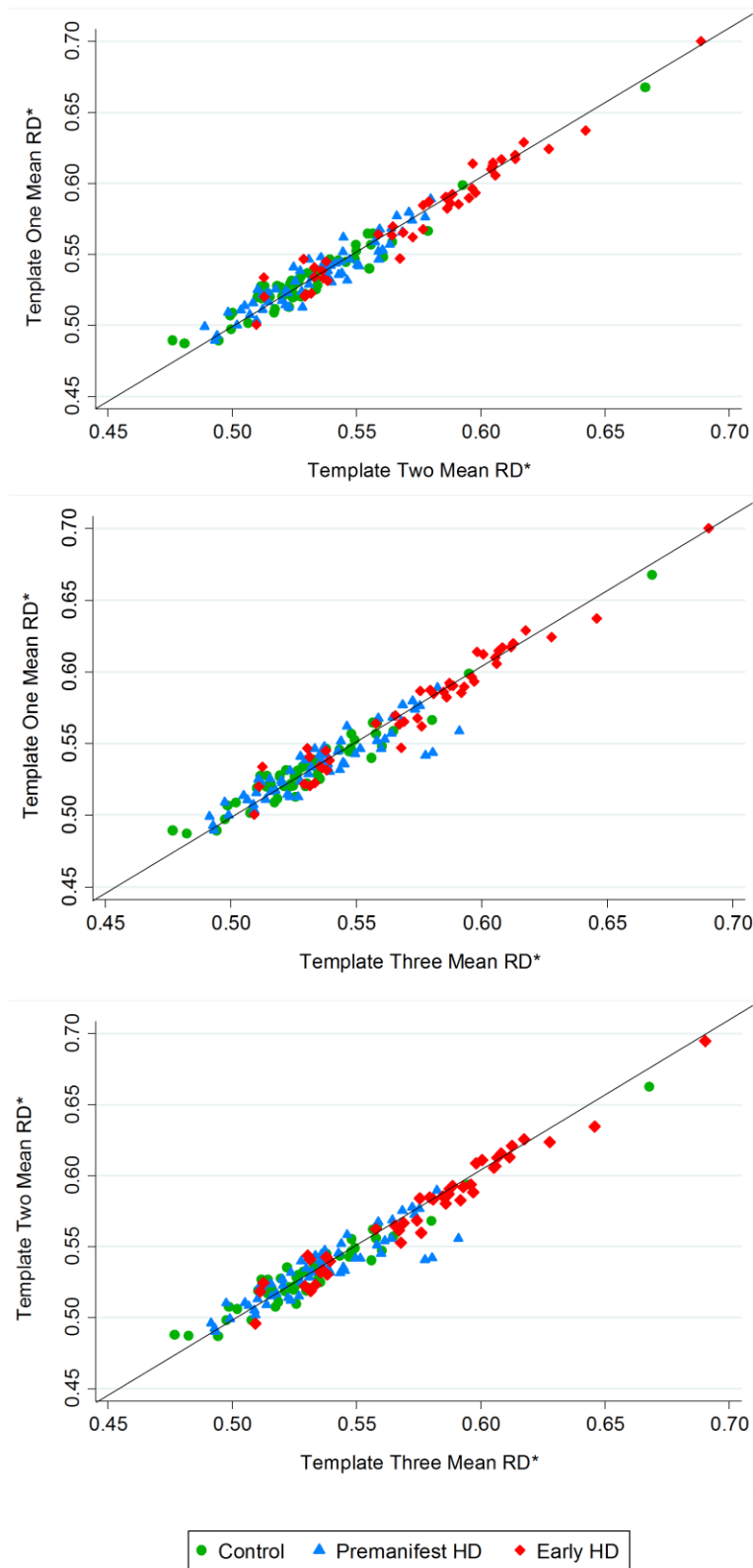


**Figure 4-8.** Scatter plots of agreement between the mean RD values extracted from the three different template-registered data. The line of equality (black) is also shown.  $\ast 10^{-3} \text{ mm}^2 \cdot \text{s}^{-1}$

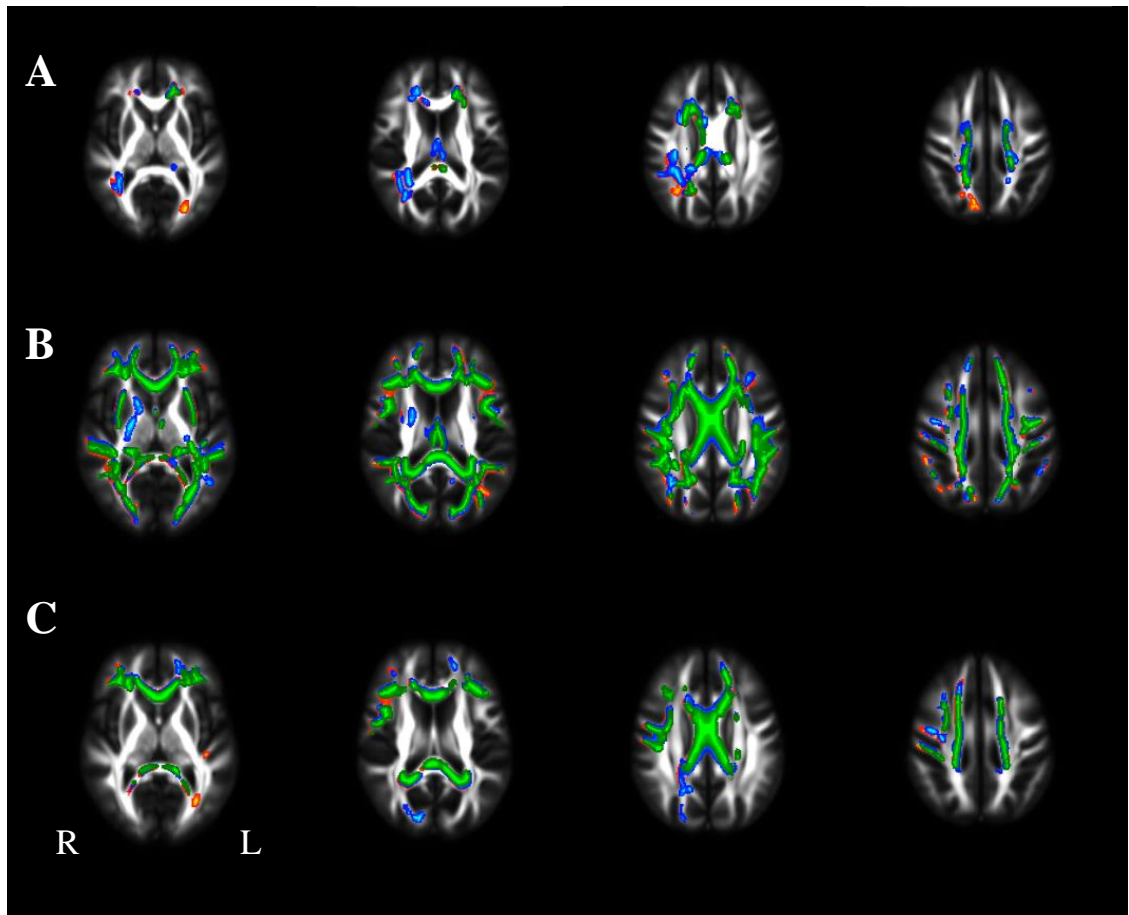
Overall, there was much consistency in the findings from the whole-brain TBSS analyses using each of the three templates. However, there were some parts of the WM skeleton where the three template analyses differed in terms of between-group differences in FA and RD. The location, direction and strength of whole-brain between-group differences found with TBSS analysis is described in detail elsewhere in this thesis (chapter 9); here the main focus is the potential differences in findings between analyses using each of the separate templates.

Figure 4-9 shows the TBSS results for between-group differences in FA. Data from analysis using template one produced a finding of higher FA in controls compared with premanifest HD participants in parts of the WM skeleton that analysis with the other two templates did not produce, including the left posterior thalamic radiation and the right inferior fronto-occipital fasciculus (IFOF; Figure 4-9, A). Conversely, findings from analysis with template three did not show significantly higher FA for controls compared with premanifest HD participants in the right anterior corona radiata, right anterior thalamic radiation, and fornix, which was found in the analysis with templates one and two (Figure 4-9, A). Again, this is reflected in the percentage of significant voxels found for this between-group comparison. Analysis with template three produced half the amount of significant voxels, just 4% of the skeleton, compared with 8% of the skeleton for analyses with the other two templates (Table 4-5).

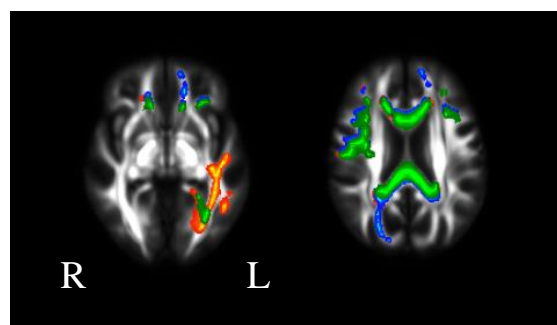
Independent analyses using the three template groups consistently found widespread areas of the WM skeleton where controls had higher FA compared with early HD participants (Figure 4-9, B). This was also reflected in a similar percentage of significant voxels (43% of the skeleton) where FA was higher in controls than premanifest HD for all three of the template analysis groups (Table 4-5).

Analysis using template one also produced a finding of higher FA in the premanifest HD group compared with the early HD group in the left posterior thalamic radiation, which was not found following analysis using the other two templates (Figure 4-9, C and more clearly seen in Figure 4-10, left). Analysis with template two also showed higher FA in premanifest HD participants compared with early HD participants in the right forceps major and right IFOF (Figure 4-9, C and Figure 4-10, right). The same percentage of the WM skeleton (14%) was, however, found to be significant for this participant group contrast across analyses using all three of the templates (Table 4-5).





*Figure 4-9. TBSS results (FWE-corrected,  $p < 0.05$ ) for between-group differences in FA from analyses using each of the three templates. Skeletonised results are displayed on the total mean FA image. (A) Controls > Premanifest HD (B) Controls > Early HD (C) Premanifest > Early HD. Results from analysis using template one are in red, template two in blue and template three in green.*



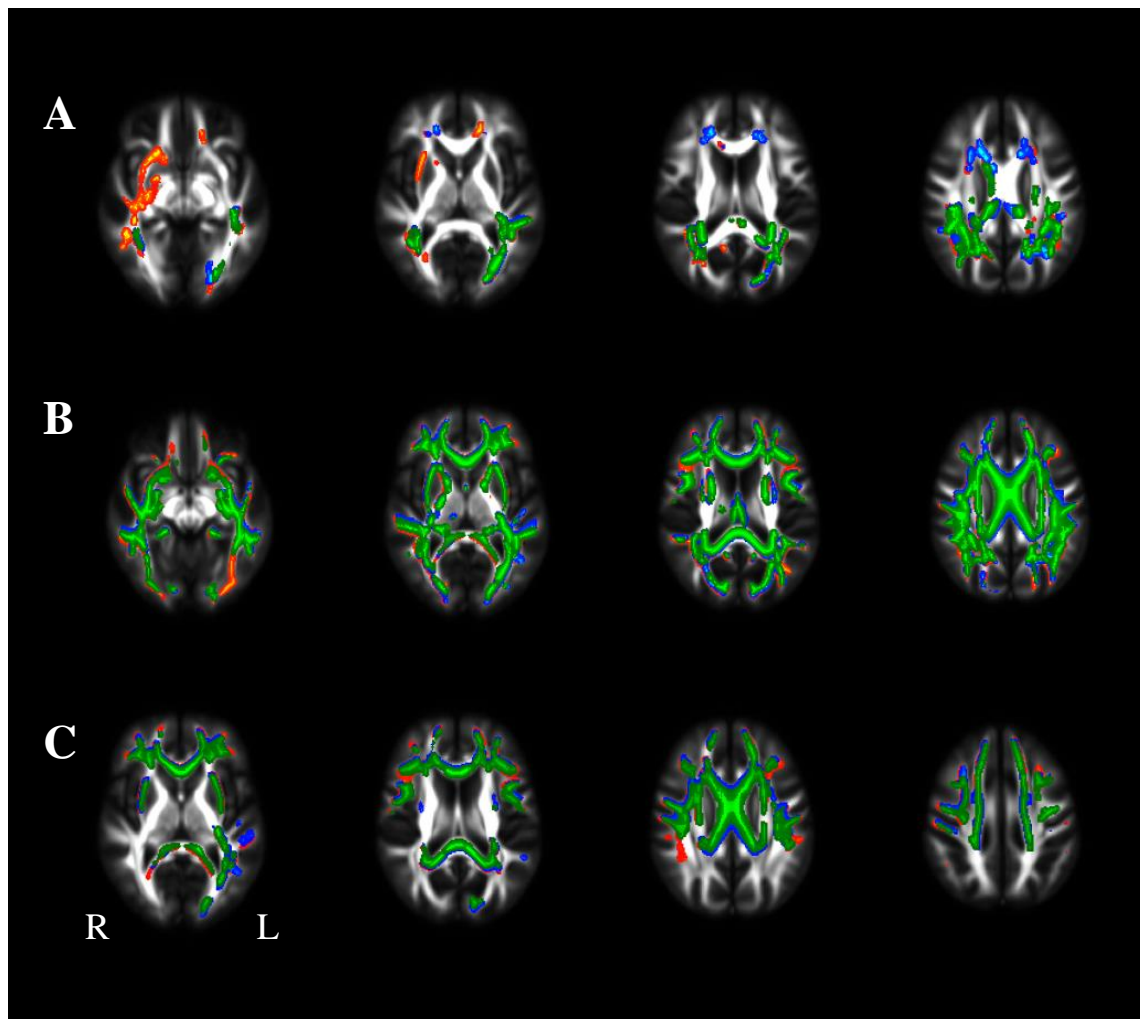
*Figure 4-10. TBSS results (FWE-corrected,  $p < 0.05$ ) for FA contrast premanifest > early HD. These slices highlight the more pronounced differences between the analyses using each of the three templates. Results using template one are in red, template two in blue and template three in green.*

Figure 4-11 shows the TBSS results for between-group differences in RD. TBSS analysis using template one revealed a greater number of significant voxels where

premanifest HD participants had higher RD compared with controls in the right external capsule, the right superior longitudinal fasciculus (SLF), and the left anterior corona radiata, which was not seen in the analysis using the other two templates (Figure 4-11, A). In addition, unlike analysis with templates one and two, analysis using template three did not find significant voxels for this between-group contrast in the bilateral corona radiata and body of the CC (Figure 4-11, A). Equally, analysis with template three only revealed the premanifest HD group to have higher RD compared with controls in 10% of the WM skeleton, compared with 14% in analysis using template one and 12% in analysis using template two (Table 4-5).

In line with the FA results, separate analysis using each of the three templates consistently found widespread areas of the WM skeleton where the early HD group had higher RD compared with the control group (Figure 4-11, B), with the exception of analysis using template one which found additional significant voxels in part of the left inferior longitudinal fasciculus (ILF; Figure 4-11, B). Slightly less significant voxels were found for this between-group contrast in analysis using template three, with 56% of the WM skeleton showing higher RD for early HD compared with controls, in contrast to 57% and 58% of the skeleton in the analysis using the other templates (Table 4-5).

Finally, analysis with each of the three templates showed consistently located, higher RD for the early HD group compared with the premanifest HD group, with the exception of analysis using template one which found some additional significant voxels in the right SLF (Figure 4-11, C). Analysis with the three templates equally found 31% of the WM skeleton where early HD RD was higher compared with premanifest HD RD (Table 4-5).



*Figure 4-11. TBSS results (FWE-corrected,  $p < 0.05$ ) for between-group differences in RD from analyses using each of the three templates. Skeletonised results are displayed on the total mean FA image. (A) Premanifest > Controls (B) Early HD > Controls (C) Early HD > Premanifest. Results from analysis using template one are in red, template two in blue and template three in green.*

**Table 4-5. Number of Significant Voxels (% of White Matter Skeleton)**

<b>Metric</b>	<b>Group Contrast</b>	<b>Template 1*</b>	<b>Template 2*</b>	<b>Template 3*</b>
<b>FA</b>	Controls > Premanifest	6049 (8.129)	5785 (8.077)	2620 (3.738)
	Controls > Early HD	32144 (43.197)	32144 (43.197)	30320 (43.260)
	Premanifest > Early HD	10717 (14.402)	10717 (14.402)	9862 (14.071)
<b>RD**</b>	Premanifest > Controls	10747 (14.442)	8538 (11.920)	6932 (9.890)
	Early HD > Controls	42566 (57.202)	41209 (57.533)	39475 (56.322)
	Early HD > Premanifest	23056 (30.984)	22423 (31.305)	21489 (30.660)

Values here are the number (%) of significant voxels from analysis using each of the three templates.

\*The white matter (WM) skeleton created from analysis using template one had a total of 74,413 voxels; template two had 71,627 voxels and template three had 70,088 voxels. \*\* $10^{-3}\text{mm}^2\cdot\text{s}^{-1}$

## 4.4 Discussion

The current study aimed to examine template effects on diffusion imaging data analysis using an unbiased tensor-based registration approach. In particular, the aim was to assess whether diffusion data registered using three independent tensor templates, created with data selected pseudo-randomly, would produce similar diffusion metrics both within and between three participant groups in the WM skeleton. In addition, whether analyses using these three different templates would find consistent between-group differences in FA and RD using whole-brain TBSS.

Overall, there was good agreement between analyses using each of three customised templates, both in terms of extracted diffusion metrics and TBSS between-group comparisons. The findings show that independent sets of individual tensor data selected for tensor template creation (provided data from each site and group is chosen in a multi-site, multi-group cohort), will yield consistent results in subsequent analyses. It is important, however, to highlight that there were some subtle differences between the three sets of analyses. Explanations of why this might be are discussed.

The WM skeleton was chosen as the region from which to extract FA and RD values because it is an easily identifiable region to explore the effects of using different templates and was automatically generated in the TBSS analysis. The Spearman's Rank correlation and scatter plot analysis showed that the analyses using all three templates were highly correlated and the majority of the data points were on, or close to, the line of equality.

Between-template comparisons of the extracted diffusion metrics indicated a difference in the values produced using each of the three templates. However, these differences were relatively small, ranging from just 0.001 to 0.002 e.g. analysis with template two reported a FA value of 0.431 in early HD compared with 0.430 with template three. Analyses using templates one and two, and analyses using templates two and three were found to be most discordant. Interestingly, FA caused more inconsistency than RD. This could be due to the fact that FA is a summary index of the directionality of the diffusion tensor, both perpendicular and parallel to the main fibre orientation, i.e. the RD and AD respectively. Therefore, underlying changes in the ratio between AD and RD will influence FA and subtle differences in alignment may cause an increase or decrease in FA. Differences in the diffusion metrics could also be explained by demographic differences of participants whose data were entered into each customised template. Although numbers were equal in terms of group and study site, the gender and age of participants selected were not necessarily equivalent. It is beyond the scope of this study to quantify the demographic effects here, however, similarity between the template used for normalisation and the study sample could have an effect on alignment. This in turn could cause subtle variations in metrics extracted from particular ROIs, including the WM skeleton.

Without clear empirically-based hypotheses of predicted group differences, choosing an optimal template for detecting between-group differences is challenging. To explore this issue, firstly, the extracted raw diffusion metrics were compared between-groups using analyses from each of the three templates. There was notable variability in the ability to detect differences between control and premanifest HD participants in FA according to the template used. This could be due to the fact that the two groups are relatively similar in terms of structure. Damage to WM is generally less extensive during the premanifest stage of HD and thus subtle between-group differences become harder to detect. Conversely, for early HD participants significant differences when compared to the

control group were found consistently in analyses using all three templates. Increasing evidence demonstrates that in the premanifest stage, measures of diffusivity, including RD, are more sensitive to WM microstructural change compared with FA (Matsui *et al.* 2015; Odish *et al.* 2015); this could explain the findings here.

There were, however, three premanifest HD participants who showed outlying diffusion metrics following analysis using template three. FA values were lower and RD slightly higher when plotted against the other template results (Figure 4-7 and Figure 4-8). Poor registration could explain the presence of these outliers, but when viewing the individual registrations visual assessment was insufficient to confirm this. Another possible explanation could be the influence of the relationship between the AD and RD. Decreasing AD, along with increasing RD, could in turn cause a decrease in FA because as mentioned above, FA is an index of both the parallel and perpendicular eigenvectors. The lower AD found using template three could therefore be driving the outlying decrease in FA, which appears more pronounced (Figure 4-7) than the RD (Figure 4-8) judging by the distance from the line of equality. Further scrutiny of the image alignment and AD metrics may shed more light on this issue but was beyond the scope of the current study. However, given that this was an issue in just three participants this suggests that it is not a systematic problem.

To further examine the issue of template choice and the ability to detect between-group differences, whole-brain TBSS was conducted. Results revealed that, in general, analyses using each of the three separate templates produced similar whole brain between-group differences in FA and RD. This was most pronounced between the control and early HD group, where differences were easier to detect. The comparisons with the premanifest HD group caused the most variation according to template used, particularly when comparing with the control group, and more so the metric FA. Differences in FA in the left posterior thalamic radiation and the right IFOF were inconsistent across the three sets of analyses. For example, FA was found to be lower than controls but higher than early HD in these areas in analysis with template one.

Differences between analyses using each of the three templates were also identified in the RD. Like FA, the majority of inconsistencies were found for the comparison between the premanifest HD group and controls, with the right SLF and bilateral anterior corona radiata in particular showing disagreement. One possible reason for a

discrepancy in these particular regions could be differences in registration, where subtle misalignments in prominent tracts such as these could have an impact. Regions towards the superior and posterior of the brain can be subject to more noise in DTI, possibly due to motion. However, anatomical alignment based on visual assessment was satisfactory for all registrations, although, it is possible that some alignment inaccuracies were below the threshold of visual detection.

An alternative explanation may relate more to subtle microstructural changes in the premanifest HD group. Minor atrophy or changes in diffusion may be occurring in these regions in different ways and at different rates at this premanifest stage of the disease and thus differences become harder to detect here. Correspondingly, when early HD participants were compared to the control group significant differences were found consistently within the WM tracts in analyses using all three templates. This also supports the above pattern of findings from the between-group comparisons of the extracted raw diffusion metrics.

## **4.5 Conclusion**

Following analysis using each of the three templates, it can be said that in general, there was considerable consistency for both extracted diffusivity metrics and between-group comparisons; the main exception being FA differences between control and premanifest HD participants, and the location of some WM tract differences. Therefore, given that it is computationally prohibitive to use data from all participants to create a tensor template, tensor-based registration using DTI-TK was used in further diffusion imaging analysis and customised, study-specific tensor templates were created with confidence (chapter 9).

## Development of Novel Neuropsychological tasks

At this stage of research development, it is important to focus our efforts on the premanifest stage and develop techniques sensitive to degenerating cognition, which may help us to further understand the underlying neuropathology and unravel the heterogeneous cognitive phenotype present many years before onset.

Fulfilling the second aim of this thesis, this section describes the development of two novel, hypothesis-driven cognitive tasks designed to study two basic cognitive processes, both linked to brain regions known to be affected in HD; interhemispheric information transfer and susceptibility to interference.

### 5. Interhemispheric Transfer Task

The CC plays a significant role in interhemispheric information transfer and is involved in many cognitive processes by way of its connectivity to numerous brain areas. Evidence from functional MRI studies confirms that the CC is the main structure involved in interhemispheric communication (Pellicano *et al.* 2013; Tettamanti *et al.* 2002). The transfer of information across the CC can be measured by different paradigms such as dichotic listening (Pellicano *et al.* 2013), event-related potentials (Westerhausen *et al.* 2006) and the most common behavioural measure, the Poffenberger Paradigm (Marzi 1999).

The Poffenberger Paradigm is a very simple, unimanual reaction time (RT) task designed by Poffenberger in 1912 (Poffenberger 1912). He was the first to devise a way of measuring interhemispheric transfer time (ITT), which is thought to reflect the time it takes for information to transmit between hemispheres across the CC. The task exploits the process of how a stimulus presented to the left visual field (LVF) is projected to the right hemisphere, and stimuli presented to the right visual field (RVF), the left hemisphere (see Figure 5-1). The paradigm requires participants to respond as quickly as possible with their left or right hand to lateralised visual stimuli. When stimuli are presented to the same side as the responding hand, the opposite hemisphere controls both the perception of it and motor response to it, therefore no interhemispheric transfer is required (uncrossed condition). When the stimuli and responding hand are on



opposite sides, however, the information must pass from the receiving hemisphere to the responding hemisphere, necessitating interhemispheric transfer (crossed condition) (Semprini *et al.* 2012), and should lead to longer RT than in the uncrossed condition, which has been reported in numerous publications (Chaumillon *et al.* 2014; Cherbuin & Brinkman 2006; Marzi *et al.* 1991; Pellicano *et al.* 2013; Schulte *et al.* 2013; Semprini *et al.* 2012). An estimate of ITT is obtained by simply calculating the difference in RT between crossed and uncrossed responses (CUD). The CUD has been widely used as an index of callosal function and dysfunction (see Zaidel & Iacoboni 2003 for a review).

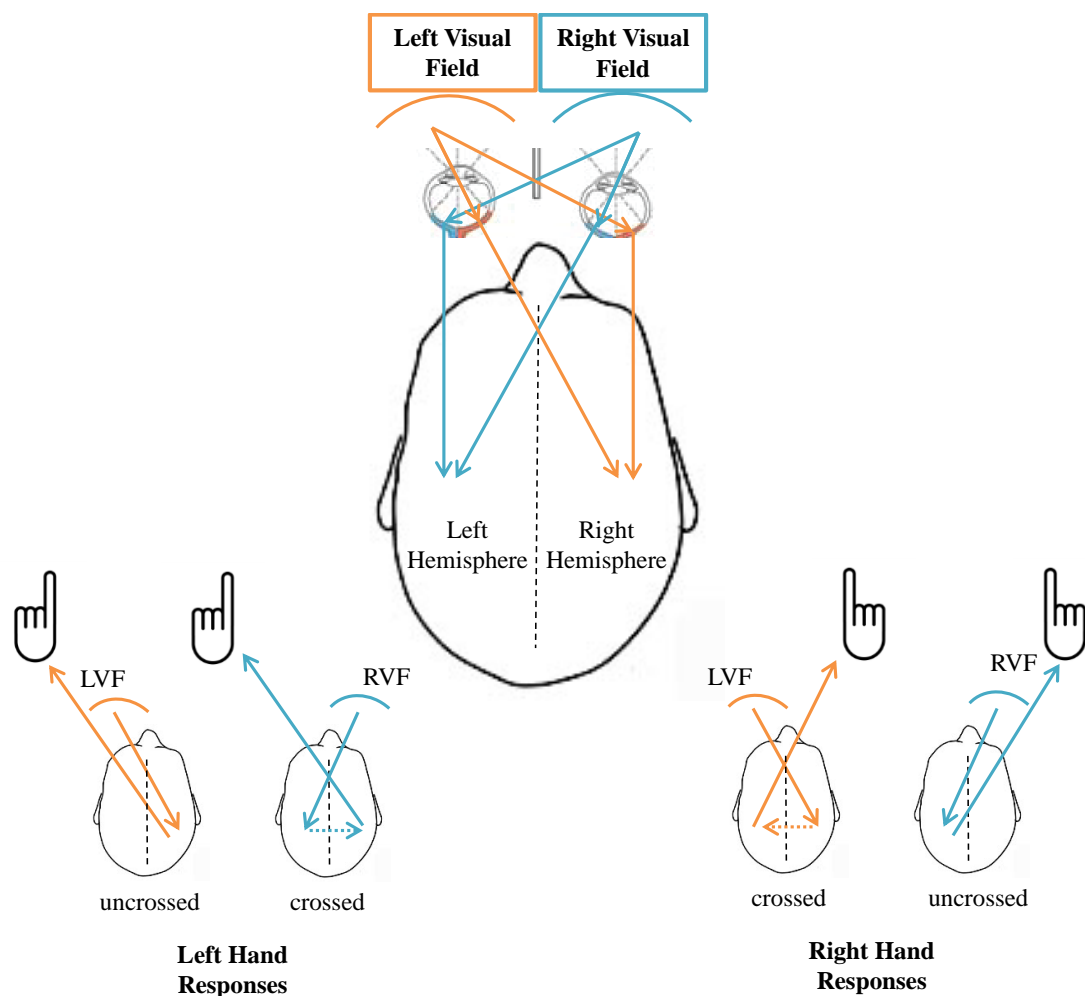


**Figure 5-1. Schematic demonstrating the principles underlying the Poffenberger Paradigm.**

Investigating the interhemispheric transfer of information across the CC is particularly relevant in HD because the CC is well-known to be significantly reduced and microstructurally abnormal in premanifest and early stages of HD compared with controls (Crawford *et al.* 2013; Di Paola *et al.* 2012; Dumas *et al.* 2012; Novak *et al.* 2013; Phillips *et al.* 2013).

## **5.1 Aims**

To develop an interhemispheric information transfer task and conduct a small pilot study. The long term objective was to administer this task to a clinical cohort of premanifest HD and healthy control participants in order to investigate cross-sectional and longitudinal group differences in interhemispheric transfer and associations with CC volume and microstructure (see chapter 10).

## **5.2 Task Development**

The task was created using the MATLAB (R2014a) Toolbox Cogent 2000 (freely available from [www.vislab.ucl.ac.uk](http://www.vislab.ucl.ac.uk)) and was developed based upon Poffenberger paradigms described in previous literature (Chaumillon *et al.* 2014; Schulte *et al.* 2005; Semprini *et al.* 2012; Westerhausen *et al.* 2006). Although the design of the task in the current study was not original, the application of this experiment to a premanifest HD cohort was entirely novel at the time of creation.

The task involved participants responding as quickly as possible to stimuli presented laterally to a small fixation cross in the centre of the laptop screen. Participants were positioned at arms-length from the laptop screen. The stimulus was a small white, filled circle presented on a black screen in either the LVF or RVF, at random. Screen resolution was 1024 by 768, and the stimulus was displayed at pixel positions -400 and +400, equidistant from the centre (pixel coordinate 0,0), where the fixation cross was positioned (see Figure 5-2). The participant's responding hand was alternated between blocks with the starting hand inter-individually balanced. Participants responded with the index finger of either their left or right hand using the left or right mouse buttons. Participants were instructed to have the hand they were not responding with down by their side.

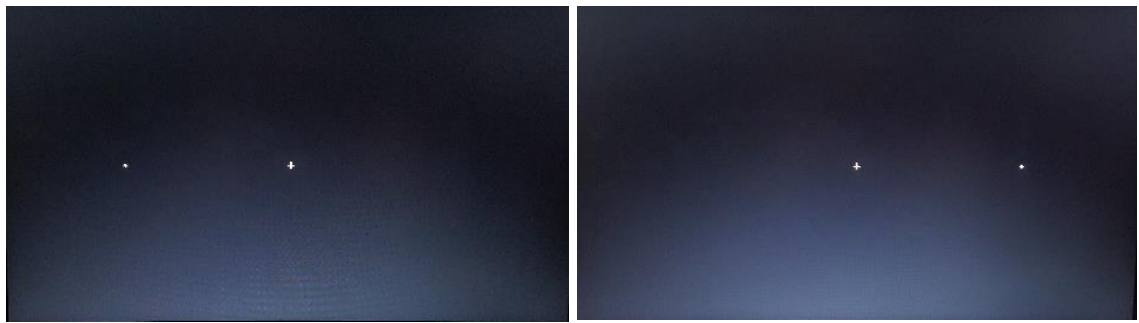


*Figure 5-2. Screenshots of the left and right lateralised stimuli and fixation cross in the interhemispheric transfer task.*

There were four conditions in total: LVF and left hand; RVF and right hand; LVF and right hand; RVF and left hand. The first two conditions were the uncrossed conditions and the latter two were the crossed conditions. The conditions were randomised within block. There were 80 trials for each condition, therefore 160 crossed/uncrossed trials. Every trial began with a fixation cross presented for varying amounts of time (900, 1650 or 2400ms) before the stimulus was presented (inter-stimulus interval) in order to prevent expectancy effects. The next trial was then initiated by the participant's response. Participants were able to rest, if needed, at the beginning of each block where an instruction screen showed which hand they were to respond with next.

Responses were recorded using a Corsair Raptor M40 gaming mouse, designed for performance gaming with a powerful optical sensor and 1000Hz report rate. The mouse was alternated on each side to coincide with responding hand. There were four blocks in total, with 80 trials per block, therefore 320 total trials. An additional dummy trial was included at the beginning of each block, which was not counted in the final analysis. This was in order to avoid including the first trial, which was subject to a slight millisecond delay on initiation of the script. The task was completed on a laptop in a dimly lit room and lasted approximately 15-20 minutes. A diagram of the task design is shown in Figure 5-3.

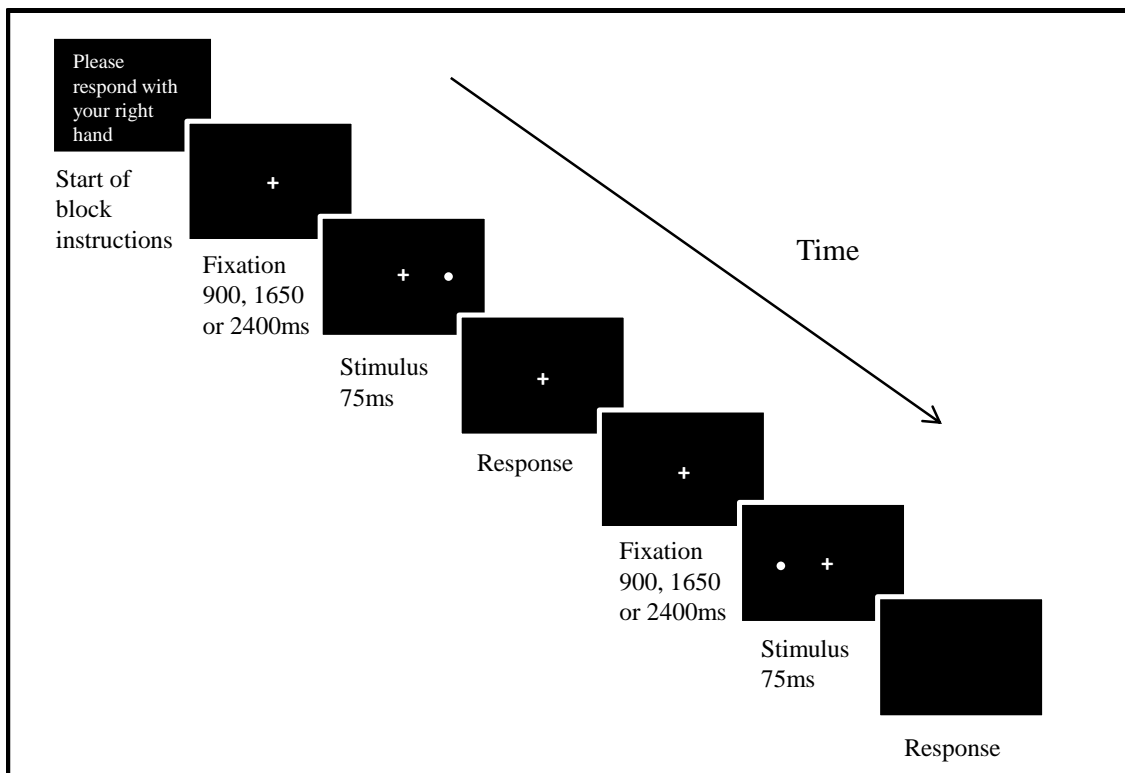


*Figure 5-3. Schematic diagram of the interhemispheric transfer task.*

Data generated for this task included:

1. RT in milliseconds under 'crossed' (stimulus and responding hand on opposite sides) and 'uncrossed' (same sides) conditions.
2. CUD: difference in milliseconds between RTs under the crossed and uncrossed conditions (also referred to as ITT).

### 5.3 Pilot Study

In order to check the task script was running properly and to assess whether the Poffenberger phenomenon was detectable, a small pilot study was conducted using ten healthy volunteers from the HD Research Group.

For analysis, the first 'dummy' trial of each block was excluded as well as any trials where responses were <100ms or >1000ms (These timings were later changed for analysis of the real task data, see chapter 10). These were deemed to be anticipation or

attentional errors. The mean crossed and uncrossed RTs were calculated, along with the CUD. (This was also later changed to median RTs, see chapter 10).

## 5.4 Results

Mean RTs are shown in Table 5-1. The difference between mean crossed and uncrossed responses was 3.69ms.

**Table 5-1. Table of Mean (SD) Reaction Times (ms)**

Condition	Reaction Time (ms)
Crossed	331.52 (62.55)
Uncrossed	327.83 (62.65)

## 5.5 Discussion

This small pilot study found that participants took longer to respond in trials where the stimuli and responding hand were on opposite sides compared with when they were on the same side. This finding is in line with the literature (Marzi 1999; Semprini *et al.* 2012; Zaidel & Iacoboni 2003) and successfully demonstrates the phenomenon that this task was originally designed to measure (Poffenberger 1912). The difference in RTs here is an indirect measure of interhemispheric transfer and represents the time taken for information to pass between hemispheres across the CC.

A CUD of 3.69ms is consistent with previous research, where a value of 3-4ms was reported in a meta-analysis of 16 studies using the Poffenberger paradigm (Marzi *et al.* 1991). Having successfully reproduced the CUD in a healthy sample, this interhemispheric transfer task was applied to a cohort of premanifest HD and healthy control participants (see chapter 10). Further analysis of RTs and the effect of responding hand, plus the association between ITT and CC volume and microstructure was conducted.

## 6. Interference Task

Psychomotor speed tasks have consistently been found to be sensitive in premanifest HD (Harrington *et al.* 2012; Unmack Larsen *et al.* 2015; Wolf *et al.* 2008), including tasks involving making attentional shifts and inhibiting inappropriate responses (Georgiou *et al.* 1995).

Beste *et al.* (2012) investigated the fronto-striatal circuits in premanifest HD participants by combining the Stroop (a commonly used interference paradigm) with task-switching (responding to the print-colour of the word and responding to the meaning of the word) in order to examine the parallel processing of conflict monitoring and adaptation of action. The authors found that anterior cingulate cortex (ACC)–basal ganglia networks seem to be the driving force in mediating parallel conflict monitoring and flexible adaptation of actions. RTs were longer in premanifest HD participants than controls and were most increased in the hardest trial type. The ACC is increasingly believed to be strongly associated with conflict monitoring (see Botvinick *et al.* 2004 for a review).

The Eriksen Flanker task is a commonly used interference task that incorporates various cognitive processes, including conflict monitoring and inhibition. Eriksen and Eriksen (Eriksen & Eriksen 1974) originally designed this simple search task to assess visual information processing. The task involves central target detection with varying levels of surrounding noise stimuli. The accuracy and speed of identifying the target depends on the similarity of the target and the noise. Studies in healthy participants have demonstrated that participants are slower to respond and make more errors when the target and flankers are incongruent, compared with when they are congruent (Kerns 2006; Mansfield *et al.* 2013), and have also shown an association with the ACC and prefrontal cortex (Kerns 2006).

Investigating susceptibility to interference using a flanker-style paradigm is particularly relevant in HD because of the well-known degeneration of the cingulate cortex and fronto-striatal connections (Hobbs *et al.* 2011; Marrakchi-Kacem *et al.* 2013), and previous findings of impairment in this task in manifest HD (Beste *et al.* 2008a; Beste *et al.* 2008b). Furthermore, developing a task that incorporates trials with increasing

cognitive load may prove more sensitive to between-group differences in performance in premanifest HD participants (Wolf *et al.* 2008).

## **6.1 Aims**

To develop an adapted version of the Eriksen Flanker task and conduct a small pilot study. The long term objective was to administer this task to a clinical cohort of premanifest HD and healthy control participants in order to investigate cross-sectional and longitudinal group differences in susceptibility to interference and associations with clinically relevant variables and imaging metrics of interest (see chapter 11).

## **6.2 Task Development**

The task was created using the MATLAB (R2014a) Toolbox Cogent 2000 (freely available from [www.vislab.ucl.ac.uk](http://www.vislab.ucl.ac.uk)) and was based upon Eriksen Flanker paradigms described in previous literature (Beste *et al.* 2008a; Mansfield *et al.* 2013). It involved participants responding as quickly as possible to the direction of a centrally presented arrow (target), whilst ignoring the direction of four surrounding arrows (flankers), positioned two on either side, which differs from the vertical arrangement of only two flanking arrows in previous studies (Beste *et al.* 2008a; Mansfield *et al.* 2013). Every trial began with a fixation cross presented in the centre of the screen (pixel coordinate 0,0) for varying amounts of time (900, 1650 or 2400ms) before the stimulus was presented. Similar to the above task, the jittered inter-stimulus interval was included to prevent expectancy effects.

The main variable being tested in the task was congruency. For this there were two conditions; the congruent condition, where the flanking arrows were pointing in the same direction as the target arrow, and the incongruent condition, where the flanking arrows were pointing in the opposite direction. Participants had to respond to the direction of the central arrow only, either using their left index finger to target arrows pointing left (left mouse button) and their right middle finger (right mouse button) to target arrows pointing right. Responses were recorded using a Corsair Raptor M40 gaming mouse, designed for performance gaming with a powerful optical sensor and 1000Hz report rate.

In order to examine the relationship between performance and cognitive demand, as well as increase the likelihood of detecting between-group differences, a second variable was investigated. The number of flanking arrows was varied and tested, however an initial pilot study revealed that increasing the number of flanking arrows did not cause an increase in RT or errors. Therefore, the use of upwards and downwards facing arrows was investigated. Trials of this type introduced a memory component into the task whereby participants not only had to try and ignore the flanking arrows but also had to remember which button (left or right) the arrow (up or down) was assigned to. This type of trial has also not been investigated in conjunction with horizontally displayed arrows in previous interference paradigms.

Figure 6-1 provides examples of the stimuli.



*Figure 6-1. Examples of congruent (left) and incongruent (right) stimuli in the interference task.*

The corresponding mouse buttons (left or right) were counterbalanced between participants to upwards and downwards facing arrows only. Arrows were presented facing left, right, up and down an equal number of times, therefore there were eight



conditions in total. Please see Table 6-1 for a list of the conditions. There were 52 trials per condition and the order was pseudo-randomized with each condition occurring equally frequently. Sequential effects were minimised by not having more than three target arrows facing the same direction in a row.

There were 104 trials per block, with four blocks, giving a total of 416 trials. As with the interhemispheric transfer task, an additional ‘dummy’ trial was included at the beginning of each block which was not counted in the final analysis. The task took approximately 20 minutes to complete, plus practice trials. The practice task presented participants with every trial type and displayed feedback of ‘correct’ or ‘incorrect’. Please see Figure 6-2 for a diagram of the task design.

**Table 6-1. Interference Task Conditions**

Condition	Congruency	Arrow direction
1	Congruent	<<<<<
2	Congruent	>>>>>
3	Congruent	^ ^ ^ ^ ^
4	Congruent	v v v v v
5	Incongruent	<<><<
6	Incongruent	>><>>
7	Incongruent	^ ^ v ^ ^
8	Incongruent	v v ^ v v

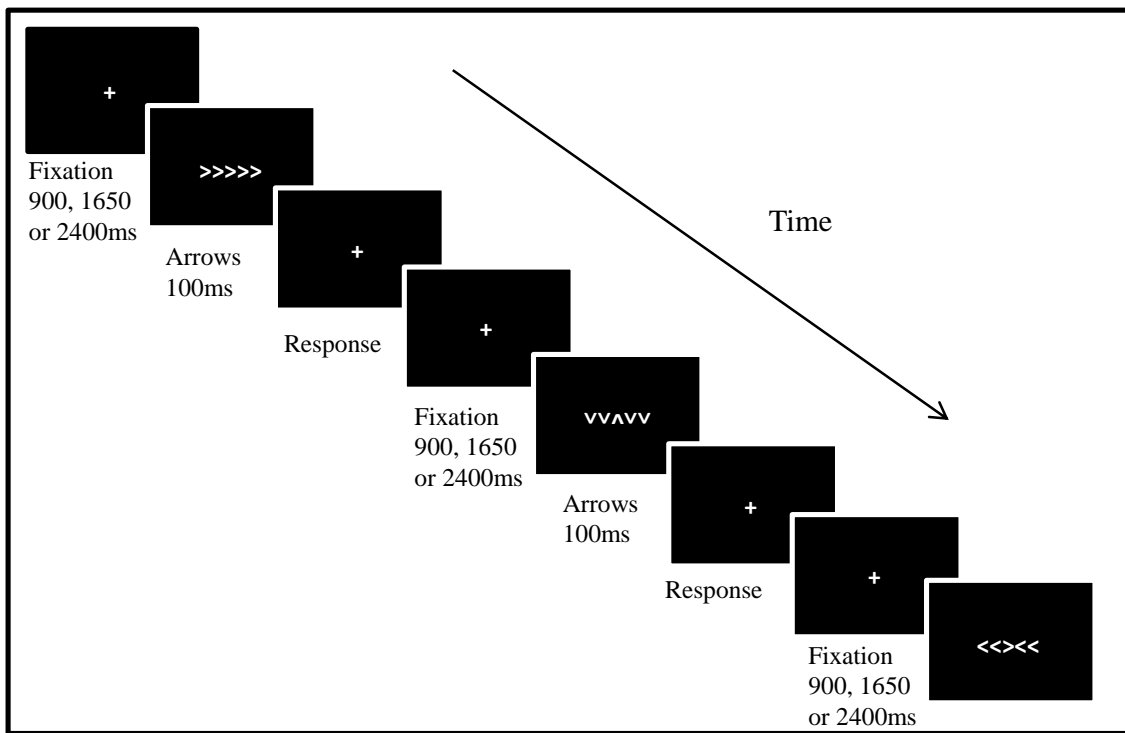


*Figure 6-2. Schematic diagram of the interference task. Conditions 2, 8 and 5 are shown.*

Data generated for this task included:

1. RT in milliseconds under 'congruent' (target and flankers pointing in same direction) and 'incongruent' (different directions) trials.
2. RT in milliseconds for left/right and up/down facing arrows.
3. Number of errors for each trial.

### 6.3 Pilot Study

In order to check that the task script was working properly and to assess whether the flanker effect was detectable, a small pilot study was conducted using ten healthy volunteers from the HD Research Group. Participants completed the task on a laptop in a dimly lit room.

For analysis, the first ‘dummy’ trial of each block was excluded, as well as any trials where responses were <100ms or >1300ms. These were deemed to be anticipation or attentional errors. The mean congruent and incongruent reaction times were calculated, as well as the number of errors for each trial type and they were statistically compared using one sample t-tests. Behavioural analysis, however, was later changed for the real task data, as described in chapter 11.

## 6.4 Results

Mean RTs and the number of errors are shown in Table 6-2. Participants took 48.37ms longer to respond to incongruent trials compared with congruent trials ( $p<0.001$ ). This effect was greater for trials where arrows were facing left and right (58.10ms) compared with arrows facing up and down (37.18ms). Responses, however, were on average slower in the up/down trials compared with left/right trials (569.77ms and 504.56ms respectively). More mistakes were made in the incongruent trials overall, with the most errors being made in the up/down arrow trials.

**Table 6-2. Mean (SD) Reaction Time (ms) and Number of Errors**

Condition	Reaction Time (ms)	Errors
Congruent – All	510.94 (127.55)	34
Incongruent – All	559.31 (118.25)	44
Congruent >>	475.51 (96.82)	1
Incongruent ><	533.61 (97.97)	8
Congruent <sup>vv</sup>	551.18 (145.18)	33
Incongruent <sup>^v</sup>	588.36 (131.39)	36

## 6.5 Discussion

Overall, participants took longer and made more errors in response to incongruent trials compared with congruent trials. This is in line with previous research where congruency effects on RT were 60ms (Mansfield *et al.* 2013) and 27ms (Cagigas *et al.* 2007) in

healthy control participants. As expected, RT was longer and more errors were made in the more difficult trials where arrows were facing up and down. This could be due to the additional cognitive load of having to remember which button was assigned to which arrow. The flanker effect, however, was not greater than in trials with left/right facing arrows. This could be because the concept of left and right is innate to humans and making left and right responses is very practiced and automatic. Therefore, the left and right facing flanking arrows caused more interference, meaning participants had to try harder to inhibit the incorrect response.

Having successfully demonstrated the flanker effect in a healthy sample this interference task was applied to a cohort of premanifest HD and healthy control participants (see chapter 11). Further analysis of the effects of congruence and arrow direction, on both RT and accuracy, plus the association with imaging metrics of interest was conducted.

## **Clinical Application: Imaging Tools**

Having developed and tested imaging techniques as described in chapters 3 and 4, the aim was to apply these to a clinical cohort to determine their sensitivity to disease pathology. The Track-HD, TrackOn-HD and PADDINGTON studies provide large well-characterised cohorts with not only high quality imaging but extensive supporting clinical and behavioural data, allowing structure-function relationships to be explored.

## **7. Corpus Callosal Atrophy in Premanifest and Early HD**

The CC is a highly variable and complex structure. There is extensive evidence of microstructural integrity loss in HD, as well as evidence suggesting the structural degeneration of interhemispheric connections may contribute to cognitive deficits. Rosas *et al.* (2006) demonstrated an association between fractional anisotropy (FA) values in the CC and performance on the Stroop Colour Word Interference task in both premanifest and early HD participants. The same has been demonstrated in Verbal Fluency and Symbol Digit tests (Rosas *et al.* 2010), the motor component of the UHDRS, and the Mini Mental State Examination in HD participants (Bohanna *et al.* 2011). Importantly, premanifest HD participants show an association with functionality in motor, oculomotor and cognitive tasks (Dumas *et al.* 2012). These relationships suggest that changes in the CC might reflect the pathological changes in the cerebral cortex in HD.

Having developed a novel CC segmentation technique (chapter 3), the present study aimed to validate and expand previous findings using multiple time-points and a large cohort. This study was published in *The Journal of Huntington's Disease* (Crawford *et al.* 2013).

### **7.1 Aims**

To investigate cross-sectional and longitudinal group differences in CC volume and hypothesis-driven associations with three cognitive tasks. The current study investigated whether premanifest and symptomatic HD participants had reduced CC volume at baseline and elevated atrophy rates over 24 months compared with healthy controls. An

interval of 24 months was chosen in order to increase the likelihood of observing group difference in the premanifest stage as well as early HD. The association between CC volume and performance in three specific cognitive measures, implicated in the function of the CC and known to be impaired in HD was also examined. Three tasks from the Track-HD battery were selected (Tabrizi *et al.* 2009):

1. The Circle Tracing Indirect task (Lemay *et al.* 2005) requires visuomotor transformation and integration, in which the CC has a well-established role (Schulte & Muller-Oehring 2010). The task is sensitive in revealing deficits in the premanifest period (Hobbs *et al.* 2011), as well as being able to detect significant change over one year in premanifest participants compared with controls (Tabrizi *et al.* 2011).
2. The Stroop Word Reading task is associated with degeneration of the CC in premanifest and early HD participants (Dumas *et al.* 2012; Rosas *et al.* 2006; 2010), as well as in other populations (Jokinen *et al.* 2012; Sullivan *et al.* 2002). Tabrizi *et al.* (2009) found that this task was a sensitive outcome measure for cross-sectional group comparison even in the premanifest stages of HD.
3. The Trail Making B task has been shown to significantly correlate with the apparent diffusion coefficient (ADC) in the CC of both premanifest and symptomatic HD participants (Dumas *et al.* 2012). This task is also sensitive enough to detect cross-sectional group differences across all stages of HD (Tabrizi *et al.* 2009).

It was hypothesised that CC volume would be reduced in premanifest and early HD participants and rates of CC atrophy over 24 months would be increased compared with healthy controls. Additionally, it was hypothesised that CC volume would be associated with performance in three cognitive tasks in the premanifest and early HD participants.

## 7.2 Materials and Methods

### 7.2.1 Participants

Participants who had good quality baseline and 24-month 3T MRI (n=291) were selected from the Track-HD study (Tabrizi *et al.* 2009); full cohort information is provided in section 2.1.1. These particular visits were chosen because they produced the largest amount of MRI data. Premanifest gene-carriers (n=106) were divided into those further from predicted onset (preHD-A, n=59), and those closer to onset (preHD-B, n=47) and early HD patients (n=84) were separated into Stage 1 (HD1, n=53) and Stage 2 (HD2, n=31). There was also a matched control group of 101 participants. See Table 7-1 for full demographic details.

**Table 7-1. Demographic, Clinical and Cognitive Characteristics of Participants**

	Control	PreHD-A	PreHD-B	All PreHD	HD1	HD2	All HD
N	101	59	47	106	53	31	84
Age, years*	45.89 (10.18)	41.14 (8.83)	40.77 (8.98)	40.98 (8.86)	46.97 (10.05)	52.35 (7.54)	48.96 (9.52)
Gender M/F	60/41	32/27	25/22	57/49	31/22	14/17	45/39
Education (ISCED)**	3.82 (1.09)	4.12 (0.98)	3.87 (0.99)	4.01 (0.99)	3.75 (1.05)	3.55 (1.21)	3.68 (1.11)
CAG repeat length	-	42.15 (1.86)	44.15 (2.37)	43.04 (2.31)	43.75 (3.49)	43.23 (2.11)	43.57 (3.06)
Disease Burden Score*±	-	259.49 (30.69)	333.94 (29.33)	292.50 (47.73)	361.18 (82.65)	395.72 (63.30)	373.93 (77.52)
Total Motor Score*	1.47 (1.58)	2.24 (1.43)	2.96 (1.86)	2.56 (1.67)	19.09 (9.16)	30.23 (9.83)	23.20 (10.80)
Total Functional Capacity*	12.98 (0.14)	12.92 (0.34)	12.85 (0.51)	12.89 (0.42)	12.21 (0.86)	8.77 (1.12)	10.94 (1.92)
Circle Tracing Indirect (log-transformed annulus length, cm)*	5.58 (0.42)	5.60 (0.45)	5.46 (0.39)	5.54 (0.43)	5.26 (0.48)	5.02 (0.50)	5.17 (0.50)

Stroop Word Reading (no. of correct words)*	107.41 (16.01)	101.97 (15.40)	96.34 (17.61)	99.47 (16.58)	83.42 (16.25)	68.42 (24.69)	77.88 (20.95)
Trail Making Task B (time to complete in secs)*	59.59 (25.66)	60.90 (21.25)	75.81 (34.93)	67.51 (28.98)	112.43 (61.44)	164.84 (87.30)	131.77 (75.94)

Values are represented as mean (SD), except gender where the numbers of males/females are given. \*As measured at baseline. \*\* International Standard Classification of Education measured at participants 36 month visit of the Track-HD study.  $\pm$ Disease Burden Score = (CAG length – 35.5)  $\times$  age (Penney *et al.* 1997).

### 7.2.2 Image Analysis

3T MRI data from the Track-HD study were analysed. Scans were pre-processed according to the steps outlined in section 2.3.1 and registered into standard MNI 305 atlas space (Mazziotta *et al.* 1995). This was done in order to ensure consistent orientation and landmark-defined cut-offs over time and in line with the CC segmentation protocol (described in chapter 3 and provided in full in Appendix 1: Volumetric Analysis).

The CC segmentation protocol was applied to the T1-weighted MRI data of all participants at baseline and 24 months. All segmentations were performed by myself in same-participant batches, blinded to year in order to use consistent mid-sagittal slices within participant.

### 7.2.3 Cognitive Measures

In line with previous research, three predefined cognitive tasks thought to utilise CC function (see Aims, 7.1) and known to be particularly sensitive in HD were selected from the Track-HD battery (Tabrizi *et al.* 2009):

#### 1. Circle Tracing Test –Indirect Condition

The Circle Tracing test (Lemay *et al.* 2005) comprises visuomotor integration, motor planning and performance monitoring. Each participant had to trace a circle presented on a horizontally-positioned monitor as quickly and accurately as possible for 45 seconds. In the Indirect condition the participant's hand was obscured by a screen and they received indirect visual feedback from a second screen. The participant was



required to use this feedback to guide their performance. The outcome measure for performance was the log-transformed score for the annulus length (length of line drawn in the time permitted in cm). A longer line indicated better performance. The indirect condition was chosen for this study because there was a more significant between-group difference between HD participants and controls ( $p < 0.0001$ ) and premanifest participants and controls ( $p = 0.022$ ) compared with the direct condition (Tabrizi *et al.* 2011), plus the indirect condition had slightly larger effect sizes over 24 months (Tabrizi *et al.* 2012).

## 2. Stroop Test – Word Reading Condition

The Stroop test normally has three conditions that require visual scanning, cognitive control and processing speed. In premanifest HD the Word Reading condition has been found to be sensitive (Tabrizi *et al.* 2011). Participants were given a card on which the names of colours were printed in black ink. Participants were required to read as many words as they were able in 45 seconds. The outcome measure for performance therefore, was the number of correct words in 45 seconds.

## 3. Trail Making Test – B

The Trail Making test assesses visual search, working memory and psychomotor speed and consists of two parts (trails A and B). The stimuli consist of randomly placed numbers (A) and numbers and letters (B) that the participant must connect in sequence by drawing a continuous line with a pencil. Participants had a maximum of four minutes to complete each part. The outcome measures were the time it took to complete each trail (seconds) and the number of errors on each trail. For this study, it was decided that the time taken for participants to complete trail B would be used because it was thought to be more difficult than trail A.

### 7.2.4 Statistical Analysis

Differences in head size were accounted for by expressing CC volume as a percentage of TIV. TIV had been previously manually delineated as described in section 2.3.1: Total-Intracranial Volume (Whitwell *et al.* 2001). All subsequent cross-sectional analyses were performed on these standardised volumes.

In order to compare cross-sectional CC volumes at baseline, a generalised least squares (GLS) regression model was fitted with baseline CC volume as the outcome variable and disease group as the categorical explanatory variable, with the control group as the reference category. GLS regression was used to allow for the increasing variability in baseline CC volume with increasing disease stage. Two models were fitted, one for main group (controls, premanifest and early HD) and one for subgroup (controls, preHD-A, preHD-B, HD1 and HD2). These models adjusted for age, gender and site by including them as explanatory variables.

GLS regression models were similarly used to examine differences in longitudinal atrophy rates (% per year) between groups controlling for age, gender and study site. Change was converted to a percentage of the baseline volume and annualised.

Restricting the analysis to the gene-mutation carrier main groups only (premanifest and early HD), linear regression models were used to investigate associations between baseline CC volume and baseline task performance in the three pre-defined tasks, controlling for age, gender, study site and education. Disease-burden score (Penney *et al.* 1997) was also included as an adjustment variable to help ensure associations were not driven by general disease severity.

## **7.3 Results**

### **7.3.1 Group Demographics**

The demographics, clinical characteristics and cognitive scores of all study participants are presented in Table 7-1. Between-group comparisons of these variables have previously been reported in detail (Tabrizi *et al.* 2009). Inevitably the premanifest group was younger than the early HD group. The control group was selected in order to be aged midway between the two gene-mutation carrying groups. After adjusting for the covariates age, gender, study site and education level, there were significant differences in performance on the cognitive tasks between groups (Tabrizi *et al.* 2009).

### 7.3.2 Volumetric Group Differences

#### *Cross-Sectional Differences*

Unadjusted baseline CC volumes by group and subgroup are presented in Table 7-2.

**Table 7-2. Table of Mean (SD) Baseline CC Volumes (% of TIV) and Annualised rates of CC Volume Change (% of baseline) measured over 24 months**

	Control	Pre HD-A	Pre HD-B	All PreHD	HD1	HD2	All HD
CC Baseline Volume (% of TIV)	0.393 (0.051)	0.392 (0.048)	0.366 (0.053)	0.380 (0.051)	0.335 (0.045)	0.307 (0.070)	0.325 (0.057)
CC Volume change (% of baseline per year)*	-0.028 (0.861)	-0.481 (0.996)	-0.763 (1.230)	-0.606 (1.120)	-1.414 (1.079)	-2.029 (1.491)	-1.641 (1.274)

\* ((V1-V2/V1)/scan interval in years) x 100

Significant differences in baseline CC volume, after adjusting for age, gender and study site, were found in all three main groups and all of the subgroups compared with controls (all  $p < 0.001$ ), with the exception of the preHD-A group (see Figure 7-1 and Table 7-3). CC volumes in the preHD-A group were, however, significantly larger than those in the preHD-B group ( $p = 0.002$ , see Table 7-3).

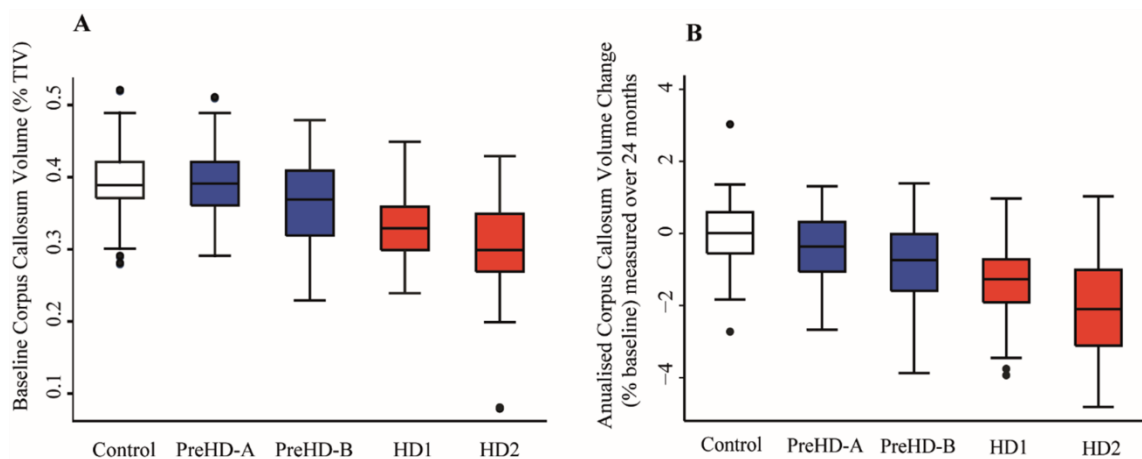


**Figure 7-1. (A) Boxplot of baseline CC volumes (% TIV). (B) Boxplot of annualised CC volume change (% baseline volume per year) measured over 24 months.**

### *Longitudinal Differences*

Unadjusted annualised atrophy rates (% baseline) by main group and subgroup are presented in Table 7-2. After adjustment for age, gender and study site, all gene-mutation carriers showed significantly elevated annualised rates of CC atrophy measured over 24 months compared with controls (all  $p < 0.001$ , see Figure 7-1 and Table 7-3).

**Table 7-3. Table of Adjusted Between-Group differences in Baseline CC Volume (% of TIV) and Annualised CC Volume Change (% of baseline volume) Over 24 months**

	Baseline Volume (% of TIV)			Change in Volume (% of baseline volume/year)**		
	Adjusted Between- Group Difference*	95% CI	P-Value	Adjusted Between- Group Difference*	95% CI	P-Value
<b>Subgroup Analysis</b>						
PreHD-A v Controls	-0.004	-0.019, 0.012	0.643	-0.556	-0.857, - 0.255	<0.001
PreHD-B v Controls	-0.031	-0.049, - 0.014	<0.001	-0.850	-1.243, - 0.458	<0.001
HD1 v Controls	-0.057	-0.072, - 0.042	<0.001	-1.359	-1.703, - 1.015	<0.001
HD2 v Controls	-0.076	-0.101, - 0.050	<0.001	-1.840	-2.405, - 1.276	<0.001
PreHD-B v PreHD-A	-0.028	-0.046, - 0.010	0.002	-0.295	-0.719, 0.130	0.174
HD2 v HD1	-0.019	-0.045, 0.007	0.153	-0.481	-1.095, 0.133	0.124
<b>Main Group Analysis</b>						
All PreHD v Controls	-0.016	-0.030, - 0.003	0.020	-0.690	-0.962, - 0.417	<0.001
All HD v Controls	-0.064	-0.079, - 0.049	<0.001	-1.526	-1.853, - 1.200	<0.001
All HD v all preHD	-0.048	-0.063, - 0.033	<0.001	-0.837	-1.194, - 0.479	<0.001

\*Adjusted for age, gender and study site. \*\*  $((V1-V2/V1)/\text{scan interval in years}) \times 100$ .

Atrophy rates increased with increasing disease stage (preHD-A, preHD-B, HD1, HD2) although differences between preHD-A and preHD-B ( $p=0.174$ ), and HD1 and HD2 ( $p=0.124$ ) did not reach statistical significance.

### *Structure-Function Associations*

A significant relationship was found between impaired performance in the Circle Tracing Indirect task and reduced baseline CC volume in early HD ( $p=0.044$ , see Table 7-4). Additionally, suggestion of some relationship in the premanifest group can be seen in Figure 7-2, although not reaching statistical significance. The same is true for both groups in the Stroop Word Reading task where there is a suggestion of a positive relationship, although not statistically significant (see Figure 7-2).

**Table 7-4. Relationship between Baseline CC Volume (% TIV) and Baseline Task Performance**

Change in task performance per 0.1% TIV change in baseline CC volume* (95% CI), p-value		
Task	All PreHD	All Early HD
Circle Tracing Indirect (log-transformed annulus length, cm)	0.054 (-0.132, 0.240) 0.565	0.179 (0.005, 0.354) 0.044
Stroop Word Reading (no. of correct words)	0.424 (-6.531, 7.378) 0.904	3.535 (-4.937, 12.006) 0.408
Trail Making Task B (time to complete in secs)	-0.964 (-12.918, 10.990) 0.873	-24.598 (-55.323, 5.926) 0.112

\*Adjusting for age, gender, study site, education and disease-burden score.

No significant associations were found between baseline CC volume and performance on the Trail Making B task (premanifest HD  $p=0.873$ , early HD  $p=0.112$ ). Figure 7-2 shows that the early HD group showed much greater variability compared with the premanifest group in performance.

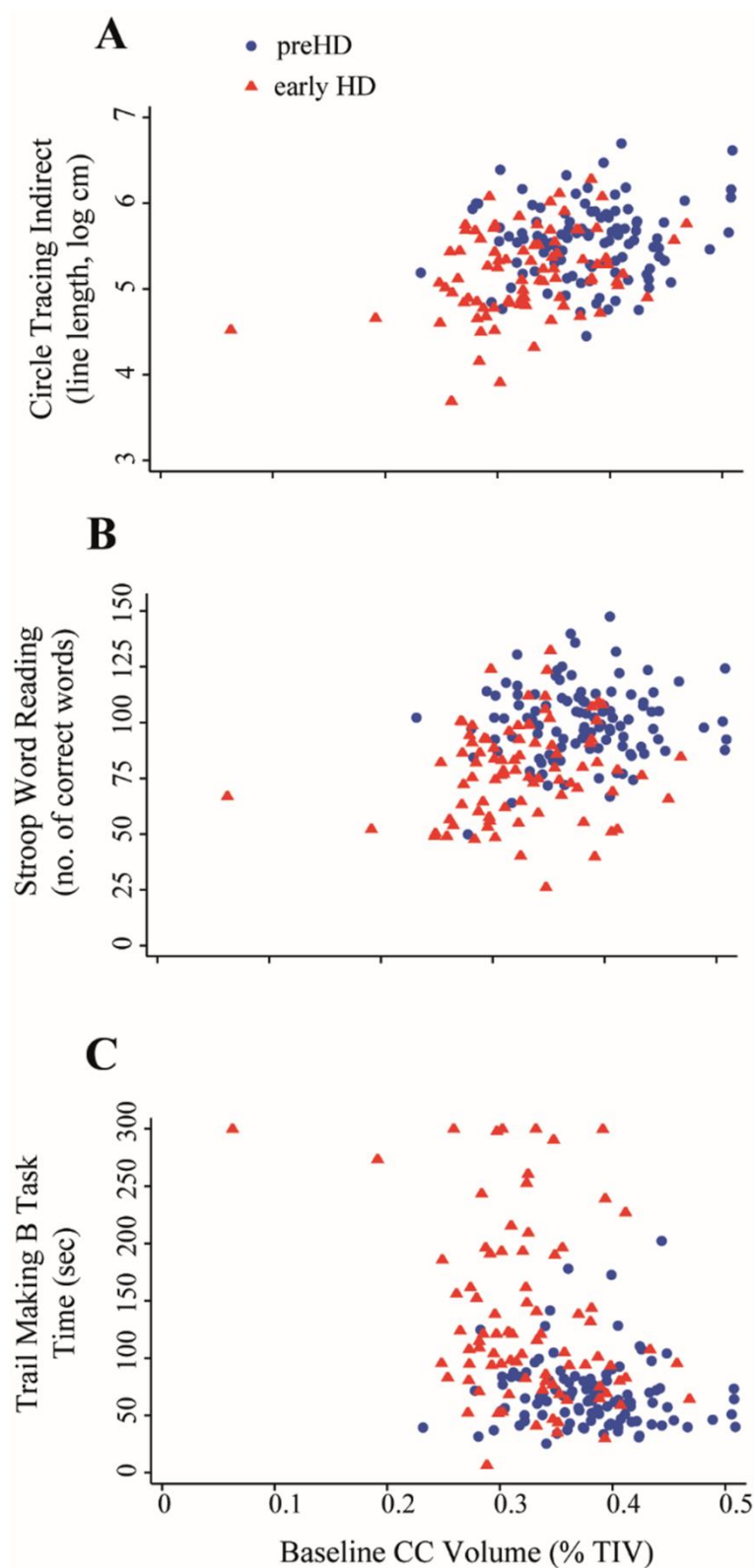


*Figure 7-2. Scatter graphs depicting the association between baseline CC volume (% TIV) and performance on the three pre-defined cognitive measures. (A) Circle Tracing Indirect task, (B) Stroop Word Reading task, (C) Trail Making B task.*

## 7.4 Discussion

Using a sensitive segmentation technique, multiple time-points and a large well-characterised cohort this study found that HD gene-carriers had significantly reduced CC volume at baseline compared with controls and elevated rates of CC atrophy over 24 months, even in those many years prior to estimated disease onset. There was evidence that reduced CC volume was associated with poorer performance on the Circle Tracing Indirect task, significantly so in early HD participants.

Reduced CC volume at baseline in premanifest and early HD is in line with the literature (Bohanna *et al.* 2011; Di Paola *et al.* 2012; Rosas *et al.* 2006; 2010). Most interestingly, when examining the subgroups separately, the preHD-B subgroup, who were on average eight years from predicted onset, had CC volumes significantly smaller than controls, evidence of subtle volume difference in participants well before the onset of overt motor symptoms. PreHD-A volumes were not significantly different from controls, but they were significantly larger than the PreHD-B group, suggesting that accumulated volume loss is not evident more than 10 years before disease onset.

Healthy control participants were found to have a CC baseline volume of 0.39, slightly larger than was observed in the PADDINGTON Study (Hobbs *et al.* 2013), which, using the same segmentation technique found controls to have a CC volume of 0.37. This is most likely explained by differences in age of the two control cohorts, the PADDINGTON cohort being on average five years older than the controls studied here. Also the cohort used in PADDINGTON was much smaller with 40 participants compared with the 101 in the current study.

The longitudinal analysis revealed that all gene-mutation carriers displayed elevated rates of CC atrophy measured over 24 months with premanifest participants losing on average 0.61% of their baseline volume per year and early HD participants losing 1.64% per year, compared with just 0.03% in healthy controls, consistent with previous research (Hobbs *et al.* 2010; Tabrizi *et al.* 2012; 2013). It is interesting to note that in those furthest from expected disease onset, although overall volume was not significantly reduced, rates of CC atrophy were already deviating from the normal control range.

The CC segmentation technique revealed disease-related differences, however, it is still unclear as to what underlying neuropathological factors are causing this observed change in CC volume. Two theories are commonly postulated in the literature. Firstly, that WM is affected by the demyelination of axons, and secondly, that it suffers from associated cortical GM degeneration (Reisberg *et al.* 1999). Equally, variation in CC volume could be attributed to variation in the number or density of axons. Callosal size has been reported to be directly related to the number of interhemispheric connections (Bloom & Hynd 2005), prompting the question of whether a smaller CC represents fewer interhemispheric connections? Further research into the microstructural properties of the callosal tracts is needed using other imaging modalities.

A significant positive relationship was reported between impaired performance on the Circle Tracing Indirect task and reduced CC volume in early HD. This finding is in line with the literature (Hobbs *et al.* 2011; Tabrizi *et al.* 2011) and highlights the disrupted interhemispheric information transfer during early stages of HD. The pathological changes and cognitive dysfunction may not be pronounced enough for this task to detect a relationship in premanifest stages.

Evidence of a positive, non-statistically significant association between performance on the Stroop Word Reading task and CC volume was seen in both premanifest and early HD participants, in agreement with previous research (Dumas *et al.* 2012; Rosas *et al.* 2006; 2010). However this finding is not statistically-significant, therefore it cannot be presumed that this positive correlation demonstrates a close association. There was no association between CC volume and the time taken to complete the Trail Making B task in either group. Both of these tasks have previously been associated with cortico-striatal circuitry (Verny *et al.* 2007) and, as the findings here suggest, may not be directly associated with the whole of the CC measured using the current technique.

In addition to the analyses outlined above, the relationship between CC volume change and change in cognitive score over 24 months was examined, however, no evidence of any associations were found. This could be due to the large amount of individual variability in cognitive performance over time (Tabrizi *et al.* 2012). Furthermore premanifest participants showed little change over 24 months in all of the Track-HD cognitive battery and did not differ statistically from controls (Tabrizi *et al.* 2012). Tabrizi *et al.* (2012) found that performance in the Circle Tracing task actually



improved in both premanifest and early HD groups as well as controls over 24 months, suggesting a practice effect. Therefore a longer time interval may be needed to identify correlations with changing cognition.

One of the limitations of this study was the application of the segmentation technique. The application – one rater and multiple time-points for each participant segmented simultaneously – results in measures of change which are very precise. Whilst useful for understanding the disease, the approach may not be appropriate for use in clinical trials where large numbers of scans need to be processed in real time by several raters. This type of application is likely to increase the variability of measures and possibly decrease the sensitivity.

Secondly, it is well-known that each region of the CC projects to distinct cortical areas. The smaller, more frontal fibres connect prefrontal higher-order processing areas and larger, mid and posterior fibres connect the visual, motor and somatosensory areas and are believed to be involved in mid-line fusion (Aboitiz *et al.* 1992a, 1992b). Therefore subdivision of the CC prior to correlational analysis may provide more specific information regarding cognitive associations. However, this is most reliably achieved using DWI and tractography, which was not available for this current cohort. Subdivision of the CC into the structure's three main regions using the T1 scans was attempted, but proved an unreliable measure (see section 3.4 for a discussion).

Another limitation of the study is that the use of medication in early HD participants was not taken into account, which may have had an effect on task performance (see Tabrizi *et al.* 2009 for details on medication use). Participants' hand dominance was also not accounted for, which has been found to be associated with varying sub-region CC volume (Tuncer *et al.* 2005). If hand dominance can affect CC volume then it may also have an effect on underlying connectivity. In addition, concurrent structural changes were not considered. The distribution of atrophy is widespread in HD (Hobbs *et al.* 2010; Tabrizi *et al.* 2011; 2012; 2013) and will no doubt influence, or be related to rates of CC atrophy. The lateral ventricles expand significantly over the course of HD (Tabrizi *et al.* 2009; 2011; 2012) and may impact the changing morphology of the CC due to its proximate location. There is evidence of a correlation between stretching of the ventricles and arching and thinning of the CC (Peterson *et al.* 2001). Changes in cognitive performance are more likely to be driven by a changing network, rather than

structure, nonetheless it is still important to consider the changing of nearby structures within the context of longitudinal callosal measurement.

The main strength of the study was the large, well-characterised cohort taken from the Track-HD study (Tabrizi *et al.* 2009). This study provides evidence that the CC segmentation technique is sensitive to inter- and intra-individual changes in CC volume over time, revealing how atrophy begins very early on in the preclinical stages. The semi-automated technique was optimised for anatomical precision using structures which are clearly visible in T1-weighted scans. The semi-automated nature gives it an advantage over fully automated techniques because the thresholds can be overridden and manual edits made where necessary. ROI measures like this one may be more sensitive to longitudinal change compared with automated whole-brain analyses, however, are much more time intensive, both in terms of analyst training and administration.

## **7.5 Conclusion**

This study revealed disease-related reduction in baseline CC volume and elevated rates of change over 24 months, even many years prior to disease onset. Associations between callosal volume and performance in the Circle Tracing Indirect task, and a suggestion of a relationship in the Stroop Word Reading task were also evident. These relationships, although small, may reflect the degeneration of interhemispheric information transfer in HD, with evidence that this decline begins well before symptoms, prompting further investigation (chapter 10). Further research into the structural and functional topology of the CC using diffusion imaging and fibre tracking will provide more information about neuropathology underlying the macrostructural changes reported here.

## **8. Association between Brain Volume and White Matter**

### **Microstructure in Healthy Controls and HD Gene-Carriers**

Macrostructural and microstructural neuroimaging metrics are potential biomarkers for both disease status and progression in HD and could also prove useful in assessing the effects of therapeutic intervention in future clinical trials. Macrostructural measures are generally derived from structural T1-weighted MRI scans, while microstructure can be measured using DTI, which indexes the properties of water movement within WM tissue.

WM degeneration is a robust marker of disease progression in early symptomatic stages of the disease and acts as a predictor of onset in premanifest stages (Tabrizi *et al.* 2013). Studies show that both loss of WM volume (Tabrizi *et al.* 2011; 2012) and microstructural degeneration, evidenced by lowered FA and elevated mean diffusivity (MD; Novak *et al.* 2013) are associated with HD pathogenesis but exactly how these two measures interact is not fully understood. Both measures were recently compared in terms of their relative sensitivity to HD pathology (Hobbs *et al.* 2013). All measures were sensitive to pathology, determined by between-group differences, however, statistical comparison of effect sizes showed no significant advantages between the highest performing measures; putamen volume, caudate volume and putamen diffusivity metrics.

Novak *et al.* (2013) examined the relationship between diffusion metrics, FA and MD in the core of WM tracts and structural measures of disease burden, WM and caudate volume. The authors found that across all participants, FA and MD were respectively positively and negatively correlated with caudate volume throughout the WM skeleton. Furthermore, there were widespread positive and negative correlations between FA and MD respectively and WM volume in the combined premanifest and manifest HD group. The authors suggest that change in WM microstructure in HD is related to change in caudate volume, and in those WM tracts directly related to the caudate, it is possible that WM degeneration occurs as a direct result of caudate atrophy.

GM degeneration in premanifest and early stage HD is also well documented, with evidence of both regional volume loss (Tabrizi *et al.* 2009; 2011; 2012; 2013) and

cortical thinning (Rosas *et al.* 2008). However, it is still unclear whether WM changes occur before, after, or concurrently with GM degeneration, and to what extent they are independent. The integrity of WM tracts is likely influenced by changes in associated GM regions and as such it is important to try and understand the possible relationship between changes in GM and WM in HD to further our understanding of disease progression.

There is evidence that cortical thickness correlates with connectivity properties in WM regions and one particular study indicates that GM thickness and changes in FA may be partly driven by the same changes in cerebral myelination (Kochunov *et al.* 2011). Recent research has also shown that superficial WM, located directly below cortical GM, is damaged in both premanifest and manifest HD patients (Phillips *et al.* 2016).

Investigating the associations between DTI metrics, namely FA, radial diffusivity (RD) and axial diffusivity (AD) and MRI volumetrics, including whole WM and whole GM can show the potential influence of macrostructural changes on diffusivity in HD. Using a large cohort of healthy, premanifest and early HD participants, this study builds on previous findings by explicitly examining the relationship between changes in diffusion and brain volume in HD and assessing to what extent this relationship changes with disease progression; plus how known cortical and subcortical GM atrophy might affect the WM microstructure. Studying this relationship in healthy adults in addition to HD gene-carriers could also further our understanding of the role of natural variability in volume and diffusion in the population and the way in which macro- and microstructural imaging measures can influence and complement each other.

## **8.1 Aims**

This study aimed to investigate the relationship between diffusion metrics and structural volume in healthy controls, premanifest and early HD participants. Specifically, TBSS was used to assess the relationships between diffusion metrics and, whole-brain WM and GM.

Due to the exploratory nature of the study it was difficult to state exact hypotheses, however it was predicted that structural GM and WM volume would be associated with diffusion properties in the premanifest and early HD participants.

## 8.2 Methods

### 8.2.1 Participants

T1-MRI and DTI data from healthy controls, premanifest and early HD participants aged  $\leq 55$  years of age from the Track-HD study at 36 months (visit 4, 2011) and from the PADDINGTON study at baseline (visit 1, 2011) were analysed. As mentioned previously, these particular visits were chosen from each of the studies because they produced the largest amount of diffusion data (cohorts have previously been described in full in section 2.1).

For full details regarding demographic and clinical information of participants included in the current study, please see chapters 4 and 9. Only participants up to and including 55 years of age were included to control for possible effects of age-related decline estimated to begin from around 55 years onwards (Raz *et al.* 2005).

### 8.2.2 Image Analysis

Diffusion data were visually checked for gross artefacts, motion and signal dropout and then eddy current corrected. Brain extraction was performed on each participant's B0 image. The diffusion tensor model was fitted at each voxel according to the pre-processing pipeline (described in section 2.3.2: Fitting the Tensors) and TBSS analysis was performed for the control, premanifest and early HD groups independently incorporating the default FSL registration protocol (described in section 2.3.2: Default TBSS Pipeline).

Whole WM and GM regions were segmented in SPM and processed according to the ROI analysis pipeline (section 2.3.2: Region of Interest Analysis). Differences in head size were accounted for by expressing each volume as a percentage of TIV, which was calculated using the WM, GM and CSF regions output using SPM (for a description of tissue segmentation using SPM see section 2.3.1: Segmentation). All subsequent analyses were performed on these standardised volumes.

Whole-brain voxelwise TBSS analysis was conducted separately for each participant group and the correlation between diffusion metrics FA, AD and RD and structural markers, WM and GM volume (corrected for TIV) were examined.

Anatomical labels of significant voxels were obtained using the JHU ICBM-DTI-81 White-Matter Labels atlas (Mori et al., 2005) and for cortical regions that this did not cover, the Harvard-Oxford Cortical Structural atlas (<http://www.cma.mgh.harvard.edu/>) was used (Figure 8-1). Both atlases are freely available as part of FSL.

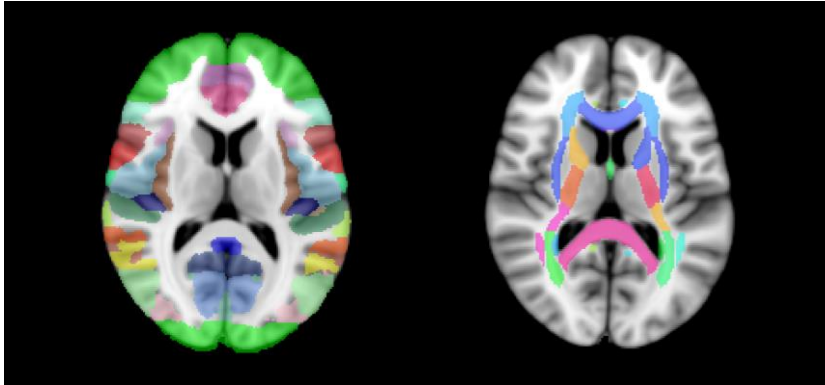


*Figure 8-1. Harvard-Oxford Cortical Structural atlas (left) and JHU ICBM-DTI-81 White-Matter Labels atlas (right).*

### 8.2.3 Statistical Analysis

Between-participant voxelwise analyses were performed to identify those voxels where there were correlations between diffusion metrics and structural markers using the GLM as part of the FSL randomise tool. Correlation analysis between diffusion metrics and GM and WM volume (% TIV) were performed on all voxels within the FA skeleton mask for each participant group using non-parametric permutation tests ( $n=500$ ). Age, gender and study site were included in the model as regressors of no interest. All results were FWE-corrected for multiple comparisons using the TFCE method. Significant clusters ( $p<0.05$ ) of 20 voxels or more were identified using FSL's *cluster* tool. In order to present the skeletonised results more clearly results were 'thickened' to 'fill out' local tracts using the *tbss\_fill* tool.

## 8.3 Results

### 8.3.1 TBSS Analysis

#### *Associations with White Matter Volume*

TBSS analysis revealed a positive correlation between WM volume and FA in the genu, body and splenium of the CC and bilateral superior corona radiata in the premanifest HD group (Figure 8-2, A). A positive association was similarly found in the early HD group in the genu, body and splenium of the CC and several other parts of the WM skeleton, including bilateral anterior and superior corona radiata, frontal regions including the frontal pole and superior frontal gyrus, plus occipital regions including the occipital fusiform gyrus and parts of the temporal occipital fusiform cortex and right posterior thalamic radiation (Figure 8-2, B). No negative relationship was found between WM volume and FA for either group.

Several regions of the WM skeleton showed a negative correlation between WM volume and AD in the premanifest HD group, including, but not limited to the genu, body and splenium of the CC, fornix, bilateral internal capsule, bilateral corona radiata, bilateral external capsule, and parts of the occipital cortex, including the occipital pole and occipital fusiform gyrus, left posterior thalamic radiation and left sagittal stratum (Figure 8-3, A). The early HD group, however, only showed a negative correlation between WM volume and AD in the body and splenium of the CC (Figure 8-3, B). In order to see whether any further correlations were present in the WM skeleton that may not have survived the p-value threshold, it was lowered slightly to  $p < 0.06$ . Further voxels within the callosal body and splenium displayed a negative correlation with AD, but no other regions. No positive relationship was found between WM volume and AD for either group.

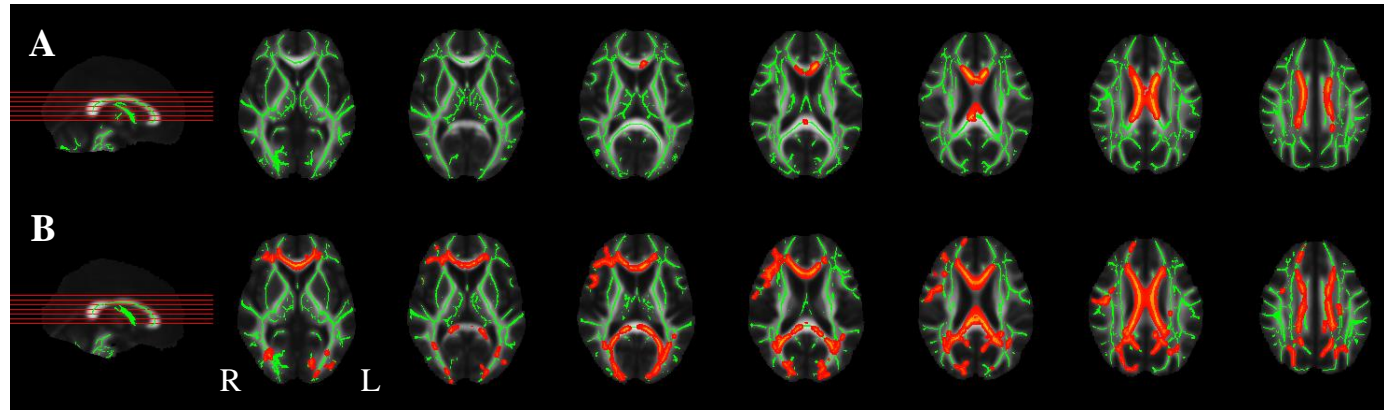


*Figure 8-2. TBSS results (FWE-corrected,  $p < 0.05$ ) showing the positive correlation between WM volume (% TIV) and FA (red) in the premanifest HD group (A) and the early HD group (B). Skeletonised results are overlaid on the mean FA skeleton mask (green) on the mean FA image.*



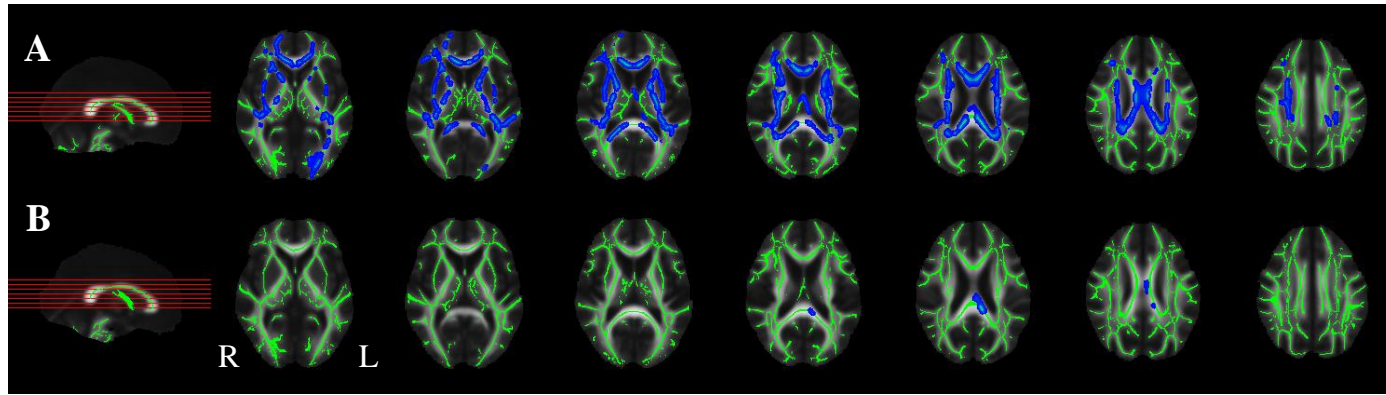


*Figure 8-3. TBSS results (FWE-corrected,  $p < 0.05$ ) showing the negative correlation between WM volume (% TIV) and AD (blue) in the premanifest HD group (A) and the early HD group (B). Skeletonised results are overlaid on the mean FA skeleton mask (green) on the mean FA image.*

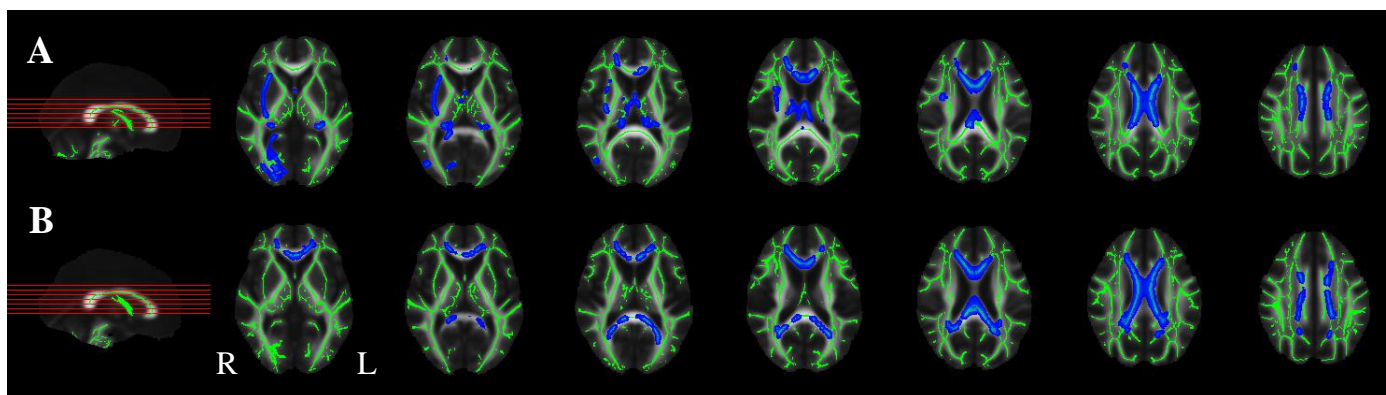


*Figure 8-4. TBSS results (FWE-corrected,  $p < 0.05$ ) showing the negative correlation between WM volume (% TIV) and RD (blue) in the premanifest HD group (A) and the early HD group (B). Skeletonised results are overlaid on the mean FA skeleton mask (green) on the mean FA image.*

**Table 8-1. Peak Voxel Information for Associations with White Matter Volume**

Group	Maximum Intensity Voxels*			Voxels	p-value	White Matter
	x	y	z			
FA						
Controls	-	-	-	-	-	No correlation found
Premanifest HD	84	139	93	3437	0.016	Body of Corpus Callosum
Early HD	73	156	59	16, 718	0.004	Right Anterior Corona Radiata
	73	162	106	232	0.048	Right cortex, superior to Right Anterior Corona Radiata
	59	65	61	149	0.048	Right Inferior Longitudinal Fasciculus
	59	55	71	110	0.048	Right Posterior Thalamic Radiation
AD <sup>Δ</sup>						
Controls	-	-	-	-	-	No correlation found
Premanifest HD	84	155	76	10,504	0.004	Genu of Corpus Callosum
	101	38	68	434	0.040	Left Occipital Pole
	56	127	76	391	0.034	Right External Capsule
	126	74	67	301	0.036	Left Inferior Longitudinal Fasciculus/Inferior Fronto-Occipital Fasciculus
	92	120	83	214	0.036	Fornix
Early HD	99	91	94	142	0.028	Splenium of Corpus Callosum
RD <sup>Δ</sup>						
Controls	-	-	-	-	-	No correlation found
Premanifest HD	97	139	94	3063	0.016	Body of Corpus Callosum
	99	98	86	2476	0.036	Left Anterior Thalamic Radiation
	64	40	69	733	0.036	Right Inferior Longitudinal Fasciculus
	63	103	48	468	0.044	Right Cingulum
	43	111	50	232	0.044	Right Inferior/Superior Longitudinal Fasciculus
	72	45	73	99	0.048	Right Inferior Fronto-Occipital Fasciculus

	132	125	41	45	0.046	Left Inferior/Superior Longitudinal Fasciculus
Early HD	83	94	93	7237	0.018	Splenium of Corpus Callosum

WM volume is adjusted for TIV; \*MNI coordinates; <sup>Δ</sup> (mm<sup>2</sup>/s)×10<sup>-3</sup>

The regional distribution of the negative relationship between WM volume and RD was similar for the premanifest and early HD group (Figure 8-4). Both groups had a significant correlation in the genu, body and splenium of the CC and bilateral anterior and superior corona radiata. The fornix, parts of the bilateral sagittal stratum, right external capsule, some of the right superior longitudinal fasciculus (SLF), part of the left lateral occipital cortex, occipital pole and occipital fusiform gyrus, and the right cingulum also showed a negative relationship between WM volume and RD in premanifest HD group. No positive relationship was found between WM volume and RD for either group.

No positive or negative correlation was found between any of the diffusion metrics and WM volume in the control group. Significant cluster information and the peak voxel locations for associations between the diffusion measures and WM volume (% TIV) are presented in Table 8-1.

### *Associations with Grey Matter Volume*

GM volume was found to positively correlate with FA in parts of the WM skeleton, however, this was only seen in the control group. Regions included the genu, body and splenium of the CC, bilateral anterior, superior and posterior corona radiata, bilateral SLF, and the left posterior thalamic radiation (Figure 8-5, A). No negative relationship was found between GM volume and FA for the control group.

The only group to show a positive correlation between GM volume and AD was the premanifest HD group, with the majority of their WM skeleton exhibiting significant findings. Regions included, but were not limited to the genu, body and splenium of the CC, bilateral anterior and superior corona radiata, bilateral external capsule, left SLF, and frontal regions including part of the inferior frontal gyrus (Figure 8-6, A). No negative association between GM volume and AD in the premanifest HD group was found.

A negative correlation was found between GM volume and RD in the control group in many of the same areas as the positive relationship with FA was found, including the genu and body of the CC, bilateral anterior corona radiata, right superior corona radiata, and part of the right SLF (Figure 8-5, B). No positive association between GM volume and RD was found in the control group.

RD was also found to positively correlate with GM volume in a small part of the WM skeleton in the premanifest HD group, seen in part of the left anterior corona radiata and left external capsule (Figure 8-6, B). Taking into consideration the widespread positive correlation between GM volume and AD, and to examine if further correlations were present with RD at lower statistical thresholds, the p-value was lowered to  $p < 0.06$ . Several further voxels within the left anterior corona radiata and external capsule were identified, as well as part of the left SLF, IFOF, anterior limb of the internal capsule and forceps minor. No negative association was found between GM volume and RD in the premanifest HD group.

No positive or negative correlation was found between any of the diffusion metrics and GM volume in the early HD group, even at a slightly lowered p-value threshold of  $p < 0.06$ . Significant cluster information and the peak voxel locations for associations between the diffusion measures and GM volume (% TIV) are presented in Table 8-2.

As a follow-up investigation to the current study, exploratory regression analyses were conducted using extracted metrics from GM and WM regions from the same participants in a subsequent DTI study (chapter 9). Metrics, however, were extracted from images registered using the DTI-TK method and are not directly comparable with these findings and are therefore not presented here.

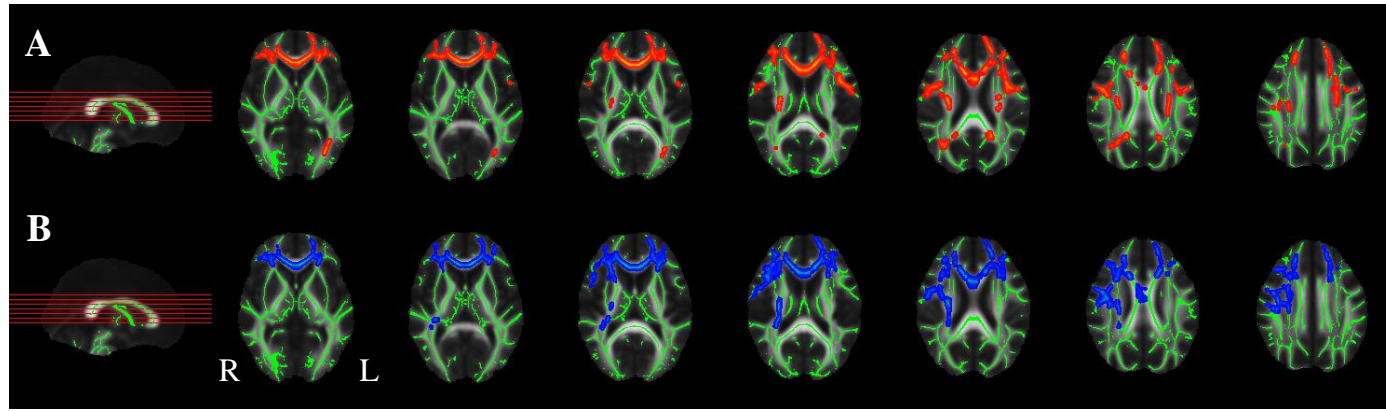


*Figure 8-5. TBSS results (FWE-corrected,  $p < 0.05$ ) in the control group. (A) Positive correlation between GM volume (% TIV) and FA (red). (B) Negative correlation between GM volume (% TIV) and RD (blue). Skeletonised results are overlaid on the mean FA skeleton mask (green) on the mean FA image.*

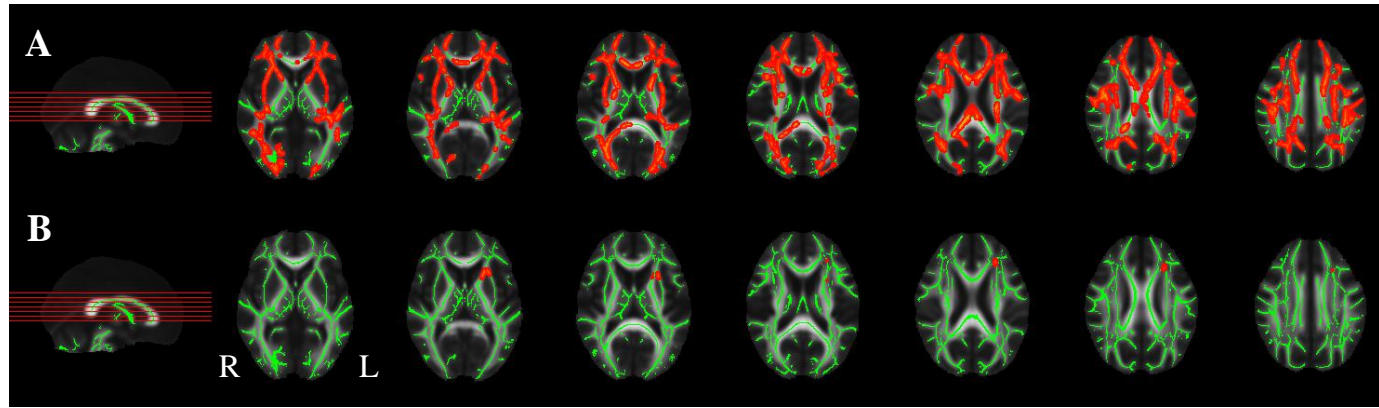


*Figure 8-6. TBSS results (FWE-corrected,  $p < 0.05$ ) in the premanifest HD group. (A) Positive correlation between GM volume (% TIV) and AD (red). (B) Positive correlation between GM volume (% TIV) and RD (red). Skeletonised results are overlaid on the mean FA skeleton mask (green) on the mean FA image.*

**Table 8-2. Peak Voxel Information for Associations with Grey Matter Volume**

Group	Maximum Intensity Voxels*			Voxels	<i>p</i> -value	White Matter
	<i>x</i>	<i>y</i>	<i>z</i>			
FA						
Controls	74	156	58	8139	0.008	Right Anterior Corona Radiata
	68	92	114	1516	0.030	Right Corticospinal Tract
	112	97	113	1028	0.032	Left Corticospinal Tract
	45	130	89	520	0.044	Right Superior Longitudinal Fasciculus
	47	117	42	242	0.042	Right Inferior Longitudinal Fasciculus
	60	74	96	187	0.046	Right Posterior Corona Radiata
	108	75	94	97	0.046	Splenium of Corpus Callosum
Premanifest HD	-	-	-	-	-	No correlation found
Early HD	-	-	-	-	-	No correlation found
AD <sup>Δ</sup>						
Controls	-	-	-	-	-	No correlation found
Premanifest HD	97	166	53	34, 983	0.006	Left Forceps Minor
	42	140	80	114	0.048	Right Superior Longitudinal Fasciculus
Early HD	-	-	-	-	-	No correlation found
RD <sup>Δ</sup>						
Controls	73	154	53	14, 164	0.016	Right Frontal Orbital Cortex
	111	98	114	78	0.048	Left Corticospinal Tract
Premanifest HD	97	142	53	489	0.048	Left Subcallosal Cortex
Early HD	-	-	-	-	-	No correlation found

GM volume is adjusted for TIV; \*MNI coordinates; <sup>Δ</sup> (mm<sup>2</sup>/s)×10<sup>-3</sup>



## 8.4 Discussion

The aim of this study was to investigate the relationship between diffusion metrics and structural volume in healthy controls, premanifest and early HD participants. Localisation of these associations to specific WM tracts can further our understanding of the natural variation in volume and diffusion by examining control groups as well as assessing whether integrity of WM tracts is influenced by the known macrostructural degeneration of GM and WM in HD.

### 8.4.1 Associations with White Matter

There were significant widespread associations between WM volume and diffusion in the premanifest and early HD group. A positive correlation between WM volume and FA was seen in both groups in several regions, suggesting that larger WM volume was associated with higher FA within these WM fibres. The negative correlation present in both groups between WM volume and AD and RD also suggests that smaller WM volume is associated with increased diffusivity both parallel and perpendicular to the WM tracts identified.

The positive correlations between WM volume and FA in both the premanifest and early HD groups, coupled with the lack of associations in the control group would suggest that this relationship is disease-specific and indicative of microstructural degeneration. This finding is supported by Novak *et al.* (2013) and other DTI-HD studies which have shown reduced FA in similar tracts when compared with controls (Bohanna *et al.* 2011; Novak *et al.* 2013; Phillips *et al.* 2013; Steventon *et al.* 2015).

The negative associations between WM volume and diffusivity measures in these patient groups indicate additional disease-related microstructural changes, independent of the normal aging process. The largely similar relationship identified between WM volume and RD in both premanifest and early HD participants is consistent with evidence that these particular tracts, including the CC, bilateral SLF, bilateral corona radiata and cingulum, degenerate during the course of HD (Della Nave *et al.* 2010; Di Paola *et al.* 2014; Phillips *et al.* 2014a). This is further supported by the negative association between WM volume and AD in the premanifest group, which again is consistent with recent findings (Odish *et al.* 2015). AD within whole-WM was found to

be the most sensitive metric to disease pathology, being the only measure to successfully differentiate premanifest participants from both controls and manifest patients (Odish *et al.* 2015). Other studies have also found measures of diffusivity to be more sensitive than anisotropy measures in the premanifest disease stage (Hobbs *et al.* 2013; Novak *et al.* 2013). This may explain the more widespread correlations between WM and measures of diffusion magnitude (AD and RD), compared with FA.

The lack of a larger correlation between AD and WM volume within the WM skeleton in early HD is surprising, especially compared with the widespread associations seen in the premanifest group. WM atrophy is evident from the initial premanifest to early stages of HD, spreading from the subcortical WM throughout the cortex (Tabrizi *et al.* 2012) and so, it would be expected that more WM areas would show significant correlations in the early HD group. This may be related to variability and a lack of power to detect an association within the early HD group. It is possible there is greater variability within the early HD group in terms of WM volume and/or AD and that this, coupled with the smaller sample size, could account for the lack of widespread associations. Conversely, it may be that WM degeneration is at a more advanced stage in early HD and that there is actually a greater range of values in the larger premanifest cohort, making it easier to demonstrate associations earlier on in the disease process.

WM is made up of thousands of axonal fibres surrounded by myelin and is believed to be one of the main effectors in the DTI signal (Assaf & Pasternak 2008). There are, however, many other biological processes which could influence the variation in diffusivity, and therefore, changes in AD and RD must be interpreted with caution (Jones *et al.* 2013). There may also be a disease-specific explanation for the changes in diffusivity reported here, whereby the mutant huntingtin protein causes alterations to oligodendrocytes and axonal membranes, or disrupts axonal transport. The large number of correlations between WM volume and AD throughout the cortex in the premanifest group could reflect a disease-specific biological process which is most prevalent during the early stages prior to disease onset, which is not detectable using whole-brain TBSS in manifest HD.

Overall, the association between smaller WM volume and lower anisotropy and higher diffusivity in the HD gene-carrying groups suggests that these changes could be disease-related. Furthermore, the exploratory regression analyses produced results

which were largely in agreement with the TBSS findings here. In addition, parts of the CC have consistently shown a relationship with WM volume across all metrics for both HD gene-carrying groups and may represent pathological changes both within the interhemispheric tracts and across the cerebral cortex. These findings suggest that changes within the CC are a key feature of HD, even before symptom onset.

#### **8.4.2 Associations with Grey Matter**

In contrast with WM volume findings, GM volume in the control group was found to positively correlate with FA and negatively correlate with RD. These clear associations may be related to normal aging as age-related change in cortical myelin and/or glial cell density has been shown to be a potential underlying factor in the positive relationship between FA and GM thickness (Kochunov *et al.* 2011). The association between these measures was present in the absence of disease-related changes and may also, therefore, reflect natural biological variation in volume and diffusion.

Lifespan DTI studies suggest that in the healthy population, WM follows an inverted U-shaped trajectory and starts to decline after reaching a peak volume at 37 years, whilst GM steadily declines across the lifespan (Lebel *et al.* 2012). Equally, FA has been shown to decrease whilst MD increases near or past the age of 30 in WM tracts such as the CC body, corticospinal tract and SLF (Lebel *et al.* 2012), all of which were identified here. The control group in the current study had a mean age of 44 years, therefore, age-related changes in volume and diffusion are likely to be evident. Changes in perpendicular diffusivity, i.e. RD, has been found to be greater than changes in parallel diffusivity, AD, with increasing age (Lebel *et al.* 2012), which may also explain why associations with RD were detected, but not AD.

It is important to note, however, that all analyses were adjusted for age and participants over the age of 55 were excluded in order to limit the effects of aging as much as possible. Thus, while relationships between volume and diffusivity in controls may be partly driven by the effects of age, they may also reflect natural biological variation in brain matter volume and WM diffusivity in the population.

Unlike the control group, the premanifest HD group did not show any association between GM volume and FA, however, AD within the majority of the WM skeleton and

RD in a small cluster of voxels positively correlated with GM volume. Increases in AD have been purported to reflect axonal injury or degeneration, whereas increases in RD reflect demyelination (Song *et al.* 2002; 2003). Speculatively, therefore, this may be due to more severe axonal degeneration compared to myelin abnormalities during the premanifest stage of the disease leading to more extensive changes in AD compared to RD. This would, however, require further research in a larger cohort.

Diffusion along, or parallel to the WM tracts is greater when GM volume is larger throughout the majority of the WM skeleton in the premanifest group, therefore, it is possible that axon damage, or change in axonal diffusion occurs whilst GM volume is still relatively preserved. GM atrophy rates are much slower compared with WM, initially selectively affecting subcortical structures, like the striatum, before spreading to posterior regions (Tabrizi *et al.* 2012). There is also some evidence that WM damage may precede changes in GM in premanifest HD participants (Phillips *et al.* 2011) and damage to superficial WM may occur before or separately to damage to the cortical GM (Phillips *et al.* 2016). Changes in cell density, cortical myelination or synaptic pruning could be the cause of changes in GM volume (Kochunov *et al.* 2011), which could also be occurring whilst axonal damage is taking place in the premanifest group, causing the unpredicted positive correlation with AD throughout the WM skeleton. Further longitudinal investigation is needed to elucidate this finding and see to what direction the relationship follows with further disease progression.

It is possible that changes in RD are too subtle to detect in the premanifest HD group using a whole-brain technique like TBSS. There may also be insufficient variation in RD levels to identify significant correlations with GM volume; it is possible that associations are present at lower statistical thresholds or prior to correction for multiple comparisons. Further investigation at the slightly lower statistical threshold of  $p < 0.06$  revealed additional positive correlations between RD and GM volume in part of the left SLF, IFOF, anterior limb of the internal capsule and forceps minor, in support of previous studies (Della Nave *et al.* 2010; Poudel *et al.* 2015).

There were no associations between diffusion metrics and GM in the early HD group which was unexpected, given the associations in the premanifest group. As discussed above with regard to the lack of association with AD and WM volume in this group, one

explanation may be a lack of power to detect an association due to differences in variability.

In general the associations found between GM volume and diffusion metrics are more counter-intuitive than those shown with WM. Since these metrics are measured within the WM skeleton and hypothesised to detect processes such as axonal loss and demyelination, it is unsurprising that they show a closer association with WM volume loss than GM. The significance of these GM associations are therefore difficult to interpret.

A whole-brain technique like TBSS may not be sufficiently sensitive to identify the subtle relationships between volume and diffusivity metrics and instead techniques utilising ROI analyses may show improved sensitivity to these associations. Further research using *a priori* selected regions in conjunction with whole-brain methods is needed to investigate whether local volume changes are associated with local diffusion changes. Analysis of metrics from specific WM regions and across a number of time points will also provide more information regarding the relationships between micro- and macrostructural measures and how these change with disease progression.

### **8.4.3 Conclusions**

The current study expands upon previous research by Novak *et al.* (2013) by using a larger, multi-site cohort, examination of the additional diffusion metrics AD and RD, plus an investigation of the association between GM atrophy and diffusion metrics. The associations between WM volume and changes in diffusion in gene-carriers, particularly in the absence of an association in the healthy control group, suggest that this relationship is disease-specific. The relationship found in the controls between FA and RD with GM volume may reflect natural biological variation in brain matter volume and WM diffusivity.

The unexpected findings here, particularly when examining associations with GM, highlight the complexities of interpreting the diffusion signal using DTI analysis. It is not possible to know the true cause of the changes in anisotropy and diffusion within the WM and inferences can only be made indirectly. These unpredicted results may represent a unique pathology, particularly in the premanifest group, however, it is also

not possible to know the direction of the relationships found. It could be that the pathologic processes that alter tissue integrity occur before changes in volume, supported by the association between GM and WM volume seen in the premanifest group, however, further investigation is needed to fully test this hypothesis and to advance our understanding of the underlying pathology and heterogeneity in HD.

## 9. White Matter Degeneration in HD: An Unbiased Tract-Based Spatial Statistics Study

DTI is a widely used technique in HD research, therefore, it is important to understand the relationship between brain volume and WM diffusivity, particularly the variation in healthy controls in order to fully understand disease-related differences. Having established this in the previous chapter, the current chapter further examines group differences in diffusion using optimised TBSS.

DTI studies have demonstrated widespread microstructural WM pathology in premanifest and early stage HD (Bohanna *et al.* 2011; Della Nave *et al.* 2010; Di Paola *et al.* 2014; Dumas *et al.* 2012; Novak *et al.* 2013; Rosas *et al.* 2006). The most common approaches for analysis of DTI data are voxelwise e.g. VBM (Ashburner & Friston 2000), and as used in the current study and previous chapter, TBSS (Smith *et al.* 2006); ROI, often used in conjunction with, and to complement voxel-based techniques (Douaud *et al.* 2006), and tractography (Basser *et al.* 2000).

Voxelwise analysis, in particular VBM, was originally designed to measure morphological differences in GM using structural T1-weighted images, but can also be extended to identify differences in FA across the whole brain (Jones *et al.* 2005). The strengths and limitations of VBM have been previously discussed at length (Ridgway *et al.* 2008), but the main limitations include the effects of variations in smoothing (Jones *et al.* 2005), scanning parameters and software (Henley *et al.* 2010), poor image alignment and the increased possibility of false positives (Bookstein 2001).

ROI analyses and tractography aim to overcome the problems associated with VBM-style analyses by working within individual participant space. Diffusion metrics are extracted from particular regions or tracts and then compared across participants. However, these approaches often require time-consuming manual delineation of anatomy and do not allow whole brain investigation. TBSS was developed as an automated, whole brain analysis technique, designed chiefly to improve image alignment and smoothing (Smith *et al.* 2004; 2006). It has since become widely utilised in voxelwise analysis of diffusion data in HD research (Bohanna *et al.* 2011; Della Nave *et al.* 2010; Di Paola *et al.* 2014; Gregory *et al.* 2015; Kincses *et al.* 2013; Novak *et al.*

2013; Poudel *et al.* 2015). A detailed description of the processing steps utilised in TBSS analysis are outlined in the original paper (Smith *et al.* 2006) and the methodology of this thesis (section 2.3.2: Tract-Based Spatial Statistics).

TBSS, however, does have a number of limitations. Evidence suggests that detection of diffusion changes in voxels furthest from the tract centre, i.e. the mean skeleton is reduced, as is the ability to estimate and interpret statistics at tract junctions or crossings (Smith *et al.* 2006). Since TBSS only makes use of the FA maps and disregards the remaining orientation information within the diffusion data, sub-optimal alignment can arise in areas of merging fibres (Bach *et al.* 2014). The quality of image registration can also greatly affect anatomical specificity. TBSS gives preference to achieving correspondence between FA values over alignment between anatomically concordant voxels and misregistration errors are only reduced by 10% (Zalesky 2011).

The registration of diffusion images is further complicated by the fact that these images contain orientational information that is affected during spatial transformation (Alexander *et al.* 2001). Compared to registering scalar images, diffusion tensor image registration needs to account for not only the size and shape, but also the orientation of the tensor at each voxel (Alexander *et al.* 2001). For example, where WM fibre bundles cross, registration can change the main orientation of the tensor leading to a more pancake-shaped ellipsoid. Registration techniques therefore need to employ algorithms that are capable of aligning WM whilst maintaining consistency with the underlying fibre organisation (Zhang *et al.*, 2006). Many registration techniques utilise scalar images e.g. FA images, but registration using all components of the diffusion tensor could produce more reliable results (Park *et al.*, 2003).

Zhang *et al.* developed a novel, tensor-based registration algorithm that enables explicit optimisation of tensor reorientation for the best matching of diffusion tensor images (Zhang *et al.* 2006). As described in section 2.3.2 (TBSS with DTI-Toolkit), DTI-TK makes use of the whole tensor and in contrast to the nonlinear registration used in the TBSS approach, aligns WM tracts by matching the orientation of the underlying fibre bundle at each voxel. DTI-TK has outperformed other registration algorithms in both human (Keihaninejad *et al.* 2013; Wang *et al.* 2011) and primate research (Adluru *et al.* 2012), yielding more consistent mapping of the scalar DTI measures and tensor orientation compared with intensity based methods. This technique can substantially



improve registration at the individual level and in turn spatial normalisation at the group level (Zhang *et al.* 2006).

Image registration using DTI-TK has been utilised in a wide range of research including studies into Alzheimer's disease (Genc *et al.* 2015; Keihaninejad *et al.* 2013; Ryan *et al.* 2013) and autism (Travers *et al.* 2014; 2015; Walker *et al.* 2012), however, its use in HD research is sparse. At the time of writing, there were only two studies that used DTI-TK to register diffusion images from HD patients. The first sought to establish the reliability of DTI in early HD patients and controls and used DTI-TK to register images for voxelwise and atlas-based ROI analyses (Cole *et al.* 2014). The second study used DTI-TK to register longitudinal DTI data from premanifest HD, manifest HD and control participants as part of a TBSS analysis of WM changes over 18 months (Poudel *et al.* 2015).

As discussed in section 1.2.2 (Whole-Brain Analyses), degeneration of WM in HD measured using standard TBSS analysis of diffusion data has been well documented. Studies reveal consistent findings of decreased FA and increased measures of diffusivity in widespread areas of WM in HD and premanifest HD participants compared with healthy controls. The present study aimed to validate and expand the previous findings using diffusion data from a large and well-characterised cohort of premanifest HD, early HD and control participants and similar to Poudel *et al.* (2015), incorporate DTI-TK's tensor-based registration and study-specific registration. Having already determined the value and consistency of DTI-TK's tensor template creation (chapter 4), the present study applied a modified analysis pipeline using the improved tensor-based registration with DTI-TK instead of the FA-based registration default to TBSS.

## **9.1 Aims**

The main aim of the current project was to assess WM microstructure in premanifest and early HD participants using voxelwise whole-brain analysis. TBSS was used to compare diffusion metrics FA, MD, AD and RD between gene-carriers and healthy controls. Through the application of DTI-TK, an optimised image registration algorithm this study aimed to accurately localise the regional distribution of WM abnormalities in premanifest and early HD participants. ROI analysis was also conducted to investigate between-group differences in diffusion metrics for whole WM regions.

It was hypothesised that all of the diffusion metrics would differ between HD gene-carriers and healthy controls across various tracts in the WM skeleton and within the whole WM regions.

## 9.2 Methods

### 9.2.1 Participants

T1-MRI and DTI data from healthy controls, premanifest and early HD participants aged  $\leq 55$  years of age from the Track-HD study at 36 months (visit 4, 2011) and from the PADDINGTON study at baseline (visit 1, 2011) were analysed (cohorts have been fully described in section 2.1). As mentioned previously, these particular visits were chosen from each of the studies because they produced the largest amount of diffusion data.

The participants analysed in the current study are the same as other projects in this thesis (chapters 4 and 8). In line with these studies, only participants up to and including 55 years of age were included. This was in order to control for some of the effects of age-related decline that begins in the mid-fifties (Raz *et al.* 2005). Demographic and clinical characteristics of the sample are presented in Table 9-1.

**Table 9-1. Demographic and Clinical Characteristics of Participants**

	Control	Premanifest	Early HD
<b>N = 153</b>	50	59	44
<b>Site (total N):</b>			
Leiden (29)	10	13	6
London (53)	17	22	14
Paris (52)	15	24	13
Ulm (19)	8	0	11
<b>Age, years*</b>	44.06 (6.05)	40.93 (6.39)	44.75 (8.18)
<b>Gender F/M</b>	29/21	30/29	23/21
<b>CAG repeat length</b>	-	43.36 (2.12)	44.32 (2.99)
<b>Disease-Burden Score**<math>\pm</math></b>	-	308.73 (66.27)	360.33 (69.12)

Values are represented as mean (SD), except gender where the numbers of males/females are given. \*In 2011 \*\*As measured at baseline  $\pm$ Disease-Burden Score = (CAG length – 35.5) x age (Penney *et al.* 1997).

### 9.2.2 Image Analysis

As described above in chapter 8, diffusion data were visually checked for gross artefacts, motion and signal dropout. Data were then eddy current corrected and brain extraction was performed. The diffusion tensor model was fitted at each voxel according to the pre-processing pipeline (described in section 2.3.2: Pre-Processing). TBSS analysis was then performed following the DTI-TK registration protocol, as described in section 2.3.2: TBSS with DTI-Toolkit.

Previous investigation into the creation of customised tensor templates found good agreement between analyses using three different templates in terms of TBSS between-group comparisons (chapter 4). The findings showed that independent sets of individual tensor data selected for tensor template creation (provided data from each site and group is chosen in a multi-site, multi-group cohort), yielded consistent results. Therefore the reference template in this study was created in the same way.

The customised tensor template was created using the tensor maps from a selection of 24 participants. Eight controls, eight premanifest and eight early HD participants were pseudo-randomly selected from the four sites, i.e. two from each site. No premanifest data was collected from Ulm therefore an additional premanifest participant was chosen from the Paris cohort to reflect the higher number of participants from this site across the whole sample.

Anatomical labels of significant voxels were obtained by warping the labels and tracts from the JHU-ICBM-labels-1mm and JHU-ICBM-tracts-maxprob-thr-0-1mm atlases (Mori *et al.* 2005) to the high resolution mean FA image using the registration tool NiftyReg (<http://cmictig.cs.ucl.ac.uk/wiki/index.php/NiftyReg>). This process was performed using a global affine registration followed by a non-linear registration. This was in order to help identify the anatomic area of any significant findings without having to further register all images and results from DTI-TK space into standard-space.

Whole WM regions for the ROI analysis were segmented in SPM using the T1 images (described in section 2.3.1: Statistical Parametric Mapping). The images were processed according to the ROI analysis pipeline outlined in section 2.3.2 (Region of Interest Analysis). They were eroded in T1 space in order to reduce partial volume effects when warped to diffusion space. The regions were then registered to individual participants' tensor maps using NiftyReg, thresholded to 0.5 and binarised. Thresholding at 0.5 was performed to further reduce partial volume effects in the diffusion metrics (Hobbs *et al.* 2013). All masks were visually inspected and diffusion metrics (FA, MD, RD and AD) were extracted using FSL's *fslstats*.

### 9.2.3 Statistical Analysis

Between-group voxelwise analyses were performed using the GLM as part of the FSL randomise tool. Statistical contrasts between all groups were performed on all voxels within the FA skeleton mask using non-parametric permutation tests (n=500). Age, gender and study site were included in the model as regressors of no interest. All results were FWE-corrected for multiple comparisons using the TFCE method. Significant clusters ( $p < 0.05$ ) of 20 voxels or more were identified using FSL's cluster tool. In order to present the skeletonised results more clearly results were thickened using the *tbss\_fill* tool.

In addition to the whole-brain voxelwise analysis, diffusivity and anisotropy metric measures were output for global WM. This was done for each participant using the *fslstats* utility within FSL. Regression analysis controlling for age, gender and study site was used to examine between-group differences.

Three participants failed registration therefore the final sample for the ROI diffusion-based between-group analysis were 48 controls, 59 premanifest and 43 early HD participants.

## 9.3 Results

Mean diffusion metric maps and the mean FA skeleton derived from the high resolution whole group template can be seen in Figure 9-1.

### 9.3.1 Tract-Based Between-Group Differences

TBSS analysis revealed several regions of the WM skeleton where the premanifest group had significantly reduced FA compared with controls (Figure 9-2, A), including parts of the fornix, genu, body and splenium of the CC, bilateral anterior and superior corona radiata, right posterior corona radiata, right superior longitudinal fasciculi (SLF), right posterior and anterior thalamic radiation and the right tapetum.

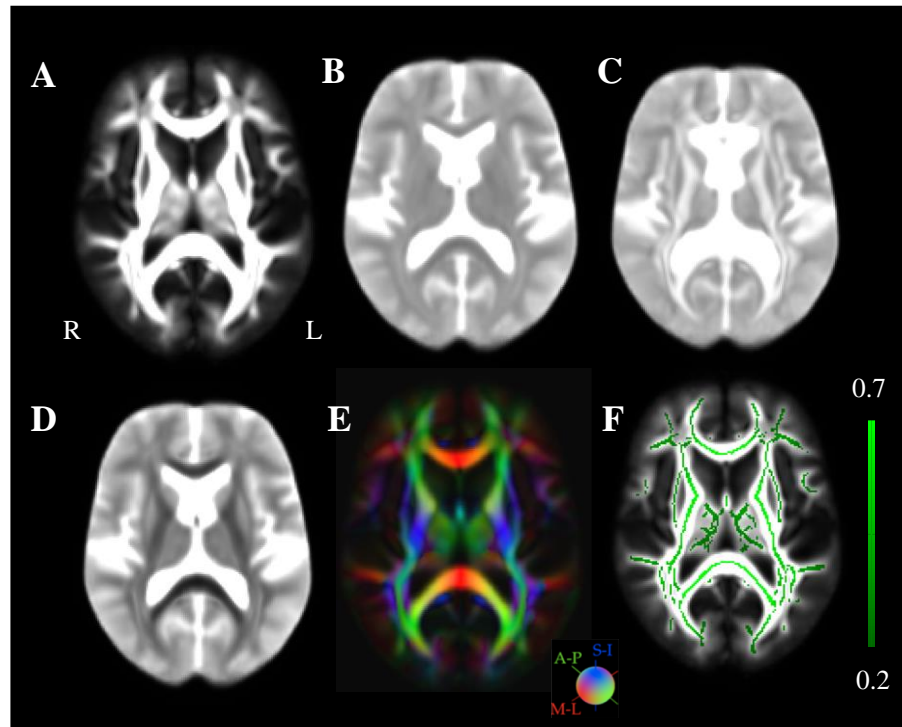


*Figure 9-1. (A) FA. (B) MD. (C) AD. (D) RD. (E) Principle diffusion, directions are encoded in colours where red = right-left; green = anterior-posterior and blue = superior-inferior. (F) Mean FA skeleton overlaid onto the mean FA.*

In the early HD group much more widespread regions were found to have significantly reduced FA compared with controls (Figure 9-2, B). In addition to the areas where the premanifest group had significantly reduced FA compared with controls, regions included bilateral inferior longitudinal fasciculi (ILF), bilateral inferior fronto-occipital fasciculi (IFOF), posterior limb of right internal capsule, bilateral anterior thalamic radiations, left SLF, right corticospinal tract, and the left cingulum. Compared with the premanifest group, however, the early HD group also showed a considerable number of reductions in FA (Figure 9-2, C) in similar regions including the right SLF, bilateral

superior corona radiata, whole of the CC, bilateral corticospinal tracts, left anterior thalamic radiation, left forceps minor, right forceps major and the bilateral IFOF.

Significant cluster information at the peak voxel locations for between-group contrasts in FA is presented in Table 9-2.

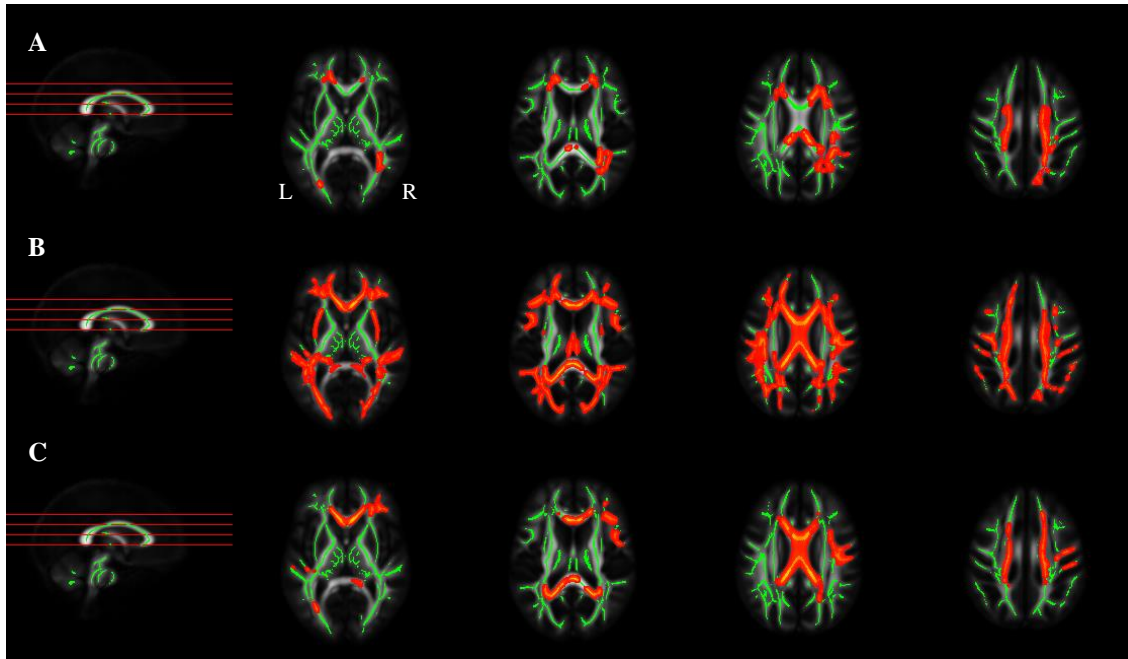


**Figure 9-2. TBSS results (FWE-corrected,  $p < 0.05$ ) for between-group differences in FA. Skeletonised results (red) are overlaid on the mean FA skeleton mask (green) on the mean FA image. (A) Controls > Premanifest HD, (B) Controls > Early HD, (C) Premanifest > Early HD.**

**Table 9-2. Peak Voxel Information for Between-Group Differences in FA**

Group Contrast	Maximum Intensity Voxels			Voxels	$p$ -value	White Matter
	$x$	$y$	$z$			
<b>Controls &gt; Premanifest</b>	126	86	97	5560	0.020	Right Callosal Body
	110	99	86	225	0.026	Fornix
<b>Controls &gt; Early HD</b>	150	107	52	32144	0.002	Right Inferior Longitudinal Fasciculus
<b>Premanifest &gt; Early HD</b>	88	58	77	10717	0.002	Left Splenium

Peak voxel information for clusters > 20 voxels at  $p < 0.05$ . Coordinates are in DTI-TK-registered diffusion space.

No parts of the WM skeleton were found to have any voxels where premanifest participants had higher FA than controls. However, early HD participants were found to have higher FA than controls in small clusters located in the bilateral anterior thalamic radiation, posterior limbs of bilateral internal capsules, and the bilateral superior, posterior and anterior corona radiata (Figure 9-3, A). Similarly, early HD participants showed higher FA than premanifest participants in smaller clusters in the same regions (Figure 9-3, B).

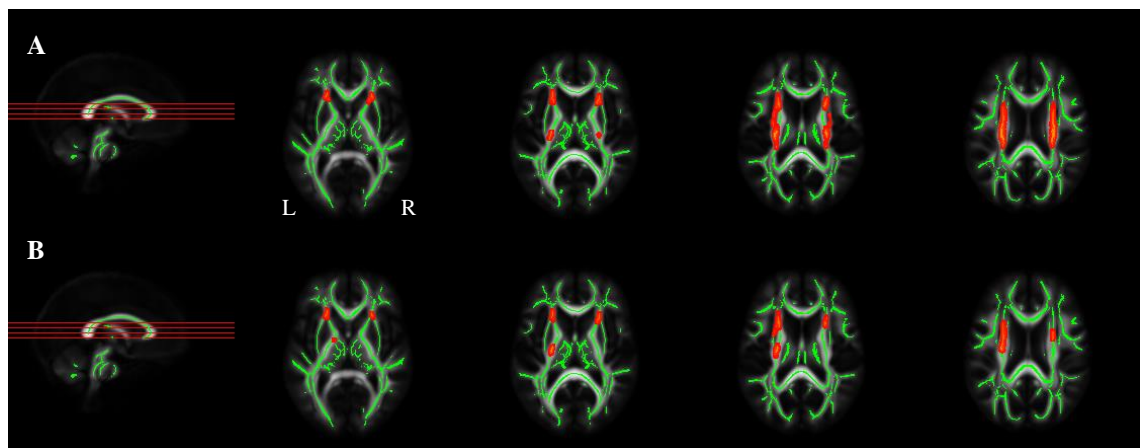


**Figure 9-3. TBSS results (FWE-corrected,  $p < 0.05$ ) for between-group differences in FA. Skeletonised results (red) are overlaid on the mean FA skeleton mask (green) on the mean FA image. (A) Early HD > Controls, (B) Early HD > Premanifest.**

Results for between-group differences in MD can be seen in Figure 9-4. TBSS analysis revealed areas of WM where premanifest participants had increased MD even compared with controls (Figure 9-4, A). These areas were quite fragmented throughout the skeleton and affected tracts included bilateral IFOF, right UF, bilateral ILF, bilateral SLF, bilateral anterior and posterior thalamic radiations, left forceps major, left corticospinal tract, right anterior and posterior corona radiata, and parts of the CC body and splenium.

The analyses found higher MD in early HD participants compared with controls in the majority of tracts throughout the WM skeleton (Figure 9-4, B), including but not limited to the bilateral anterior thalamic radiations, left cingulum, bilateral ILF, bilateral uncinate fasciculi (UF), bilateral SLF, bilateral IFOF, bilateral superior, anterior and posterior corona radiata, whole of the CC, bilateral forceps major, and parts of the bilateral corticospinal tracts. Early HD participants also had widespread areas of increased MD compared with premanifest participants in many of the same regions, except the bilateral anterior thalamic radiations, and some of the more posterior areas including the right IFOF and forceps major, parts of the left and right SLF and the right ILF (Figure 9-4, C).

Unlike with the between-group FA contrasts, no part of the WM skeleton was found to have voxels where MD was greater for controls than gene-carriers, likewise for premanifest participants greater than early HD participants. Significant cluster information at the peak voxel locations for between-group contrasts in MD is presented in Table 9-3.



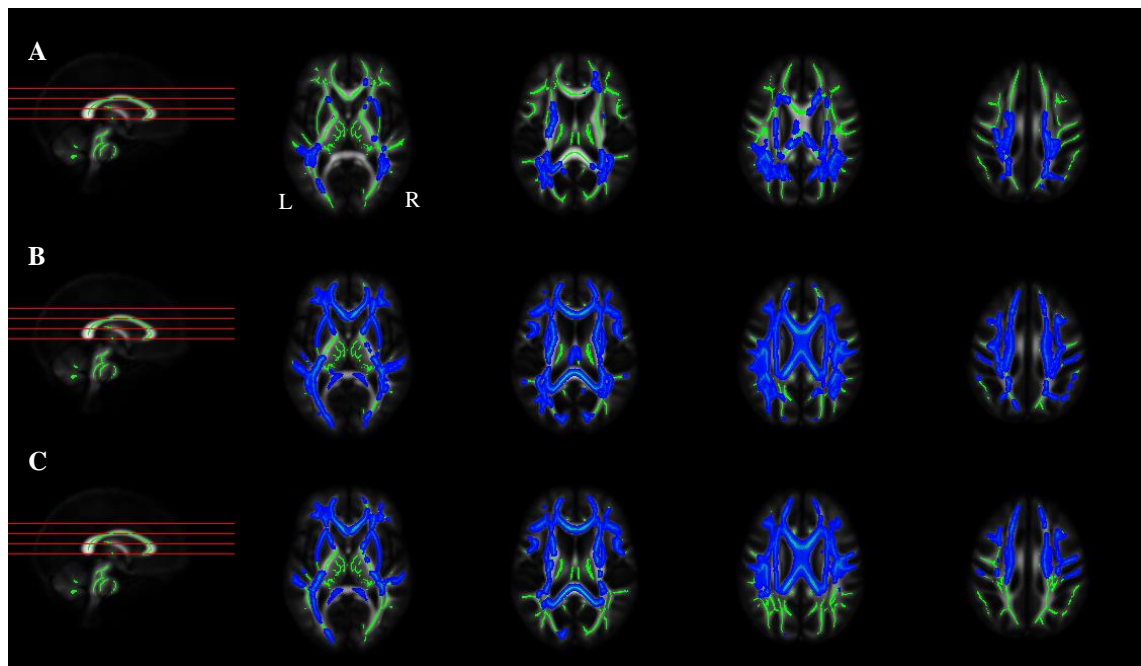


**Figure 9-4. TBSS results (FWE-corrected,  $p < 0.05$ ) for between-group differences in MD. Skeletonised results (dark blue) are overlaid on the mean FA skeleton mask (green) on the mean FA image. (A) Premanifest HD > Controls, (B) Early HD > Controls, (C) Early HD > Premanifest HD.**

Differences in AD between gene-carriers and controls were also found (Figure 9-5). Only two small clusters of WM had significantly higher AD for premanifest participants compared with controls. These were found in the left superior corona radiata and the left corticospinal tract (Figure 9-5, A). Early HD participants had increased AD compared with controls and premanifest participants in numerous WM tracts, similar to the areas affected for MD (Figure 9-5, B, C). These included, but were not limited to corticospinal tracts, UF, ILF, IFOF, forceps minor, anterior thalamic radiations, SLF and the whole of the CC. AD in part of the left forceps major was found to be higher for early HD participants compared with premanifest participants but not controls (Figure 9-5, C). No areas of the WM skeleton were found to have higher AD in controls compared with gene-carriers, similarly in premanifest participants compared with early HD participants.

Significant cluster information at the peak voxel locations for between-group contrasts in AD is displayed in Table 9-4.

**Table 9-3. Peak Voxel Information for Between-Group Differences in MD**

Group Contrast	Maximum Intensity Voxels			Voxels	<i>p</i> -value	White Matter
	<i>x</i>	<i>y</i>	<i>z</i>			
<b>Controls &lt; Premanifest HD</b>	149	63	71	10771	0.036	Right Superior Longitudinal Fasciculus
	138	128	67	388	0.046	Right Inferior Fronto-Occipital Fasciculus
<b>Controls &lt; Early HD</b>	87	102	46	41647	0.002	Left Cingulum
	109	109	78	266	0.012	Left Anterior Thalamic Radiation
<b>Premanifest &lt; Early HD</b>	152	115	49	30368	0.002	Right Inferior Longitudinal Fasciculus

MD units are  $10^{-3}\text{mm}^2\cdot\text{s}^{-1}$ . Peak voxel information for clusters > 20 voxels at  $p<0.05$ . Coordinates are in DTI-TK-registered diffusion space.

TBSS analyses also highlighted differences in RD between gene-carriers and controls (Figure 9-6). Premanifest participants showed higher RD compared with control participants in parts of the bilateral SLF, bilateral IFOF, right anterior corona radiata, left superior corona radiata, right anterior thalamic radiation, right ILF, right UF, bilateral forceps major and minor, body, genu and splenium of CC, and bilateral cingulum (Figure 9-6, A).

Similar to the results for the MD analysis, early HD participants had higher RD compared with controls in the majority of the WM skeleton including bilateral anterior thalamic radiation, fornix, bilateral corticospinal tracts, bilateral SLF, parts of bilateral cingulum, bilateral IFOF, whole CC, bilateral forceps major, bilateral ILF, and parts of the bilateral UF (Figure 9-6, B). Early HD participants also had higher RD compared with premanifest participants in the bilateral SLF, bilateral IFOF, bilateral ILF, left anterior and posterior thalamic radiation, bilateral forceps minor, whole CC, left cingulum, and the bilateral UF (Figure 9-6, C).

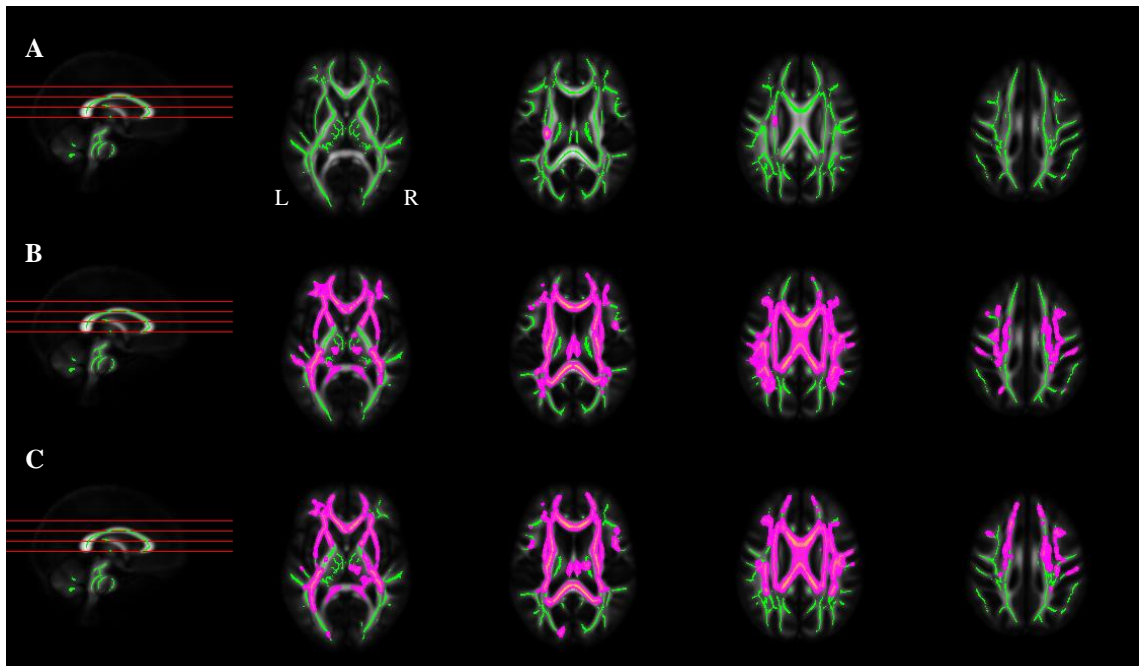


**Figure 9-5.** TBSS results (FWE-corrected,  $p < 0.05$ ) for between-group differences in AD. Skeletonised results (pink) are overlaid on the mean FA skeleton mask (green) on the mean FA image. (A) Premanifest HD > Controls, (B) Early HD > Controls, (C) Early HD > Premanifest HD.

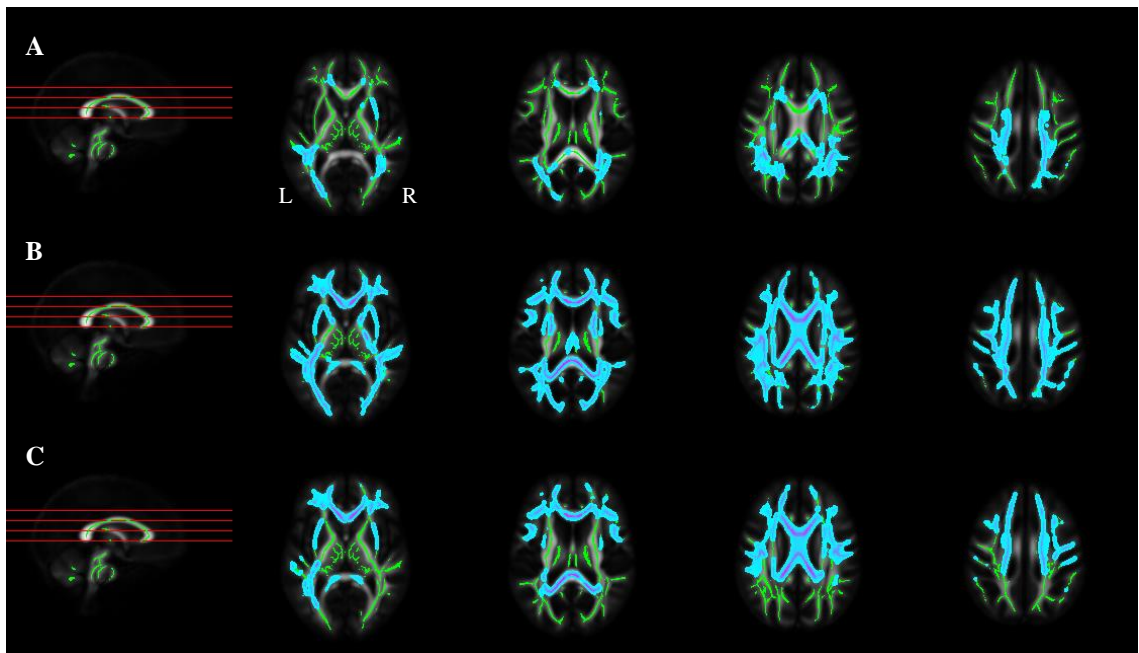


**Figure 9-6.** TBSS results (FWE-corrected,  $p < 0.05$ ) for between-group differences in RD. Skeletonised results (light blue) are overlaid on the mean FA skeleton mask (green) on the mean FA image. (A) Premanifest HD > Controls, (B) Early HD > Controls, (C) Early HD > Premanifest HD.

**Table 9-4. Peak Voxel Information for Between-Group Differences in AD**

Group Contrast	Maximum Intensity Voxels			Voxels	<i>p</i> -value	White Matter
	<i>x</i>	<i>y</i>	<i>z</i>			
<b>Controls &lt; Premanifest HD</b>	87	98	83	50	0.042	Left Corticospinal Tract
	88	110	88	48	0.048	Left Superior Corona Radiata
<b>Controls &lt; Early HD</b>	154	108	49	26766	0.002	Right Inferior Longitudinal Fasciculus
	109	108	78	745	0.002	Left Anterior Thalamic Radiation
<b>Premanifest &lt; Early HD</b>	65	99	49	24893	0.002	Left Superior Longitudinal Fasciculus
	77	93	96	302	0.028	Left Superior Longitudinal Fasciculus
	118	95	45	246	0.030	Right Corticospinal Tract
	109	109	78	219	0.016	Left Anterior Thalamic Radiation
	96	102	62	36	0.046	Left Corticospinal Tract

AD units are  $10^{-3}\text{mm}^2\cdot\text{s}^{-1}$ . Peak voxel information for clusters > 20 voxels at  $p<0.05$ . Coordinates are in DTI-TK-registered diffusion space.

Significant cluster information at the peak voxel locations for between-group contrasts in RD is displayed in Table 9-5. Again, there were no areas of increased RD in controls or premanifest participants compared with HD participants.

**Table 9-5. Peak Voxel Information for Between-Group Differences in RD**

Group Contrast	Maximum Intensity Voxels			Voxels	<i>p</i> -value	White Matter
	<i>x</i>	<i>y</i>	<i>z</i>			
<b>Controls &lt; Premanifest HD</b>	138	70	96	8705	0.024	Right Superior Longitudinal Fasciculus
	141	124	72	1357	0.042	Right Inferior Fronto-Occipital Fasciculus
	128	149	68	421	0.050	Right Anterior Corona Radiata
	160	71	56	204	0.050	Right Superior Longitudinal Fasciculus
	120	63	83	35	0.050	Right Cingulum
<b>Controls &lt; Early HD</b>	87	100	47	42261	0.002	Left Cingulum
	109	108	78	305	0.01	Left Anterior Thalamic Radiation
<b>Premanifest &lt; Early HD</b>	126	145	68	21915	0.002	Right Anterior Corona Radiata
	150	106	55	731	0.012	Right Inferior Longitudinal Fasciculus
	142	119	75	410	0.006	Right Superior Longitudinal Fasciculus

RD units are  $10^{-3}\text{mm}^2\cdot\text{s}^{-1}$ . Peak voxel information for clusters > 20 voxels at  $p<0.05$ . Coordinates are in DTI-TK-registered diffusion space.

### 9.3.2 Diffusion-Based Between-Group Differences

Diffusion metrics were output from the masked global WM in order to examine microstructural differences. Mean values for each group are presented in Table 9-6 and median values in Figure 9-7. Between-group differences in diffusion can be seen in Table 9-7. Results are adjusted for age, gender and study site.

**Table 9-6. Mean Diffusion Metrics in White Matter by Group**

Metric	Control		Premanifest		Early HD	
	Mean	SD	Mean	SD	Mean	SD
<b>FA</b>	0.401	0.020	0.401	0.018	0.390	0.020
<b>MD*</b>	2.151	0.076	2.150	0.067	2.245	0.089
<b>AD*</b>	1.047	0.026	1.048	0.024	1.080	0.030
<b>RD*</b>	0.552	0.028	0.551	0.024	0.583	0.032

\* $10^{-3}\text{mm}^2.\text{s}^{-1}$ . SD = standard deviation; FA = fractional anisotropy; MD = mean diffusivity; AD = axial diffusivity; RD = radial diffusivity.

**Table 9-7. Adjusted Between-Group Differences in White Matter Diffusion**

Metric	Premanifest v Controls	Early HD v Controls	Early HD v Premanifest
<b>FA</b>	-0.003 (-0.011, 0.004) 0.353	-0.012 (-0.020, -0.005) <b>0.002</b>	-0.009 (-0.016, -0.001) <b>0.024</b>
<b>MD*</b>	0.016 (-0.011, 0.042) 0.237	0.088 (0.060, 0.116) <b>0.000</b>	0.072 (0.044, 0.100) <b>0.000</b>
<b>AD*</b>	0.005 (-0.004, 0.014) 0.253	0.029 (0.020, 0.038) <b>0.000</b>	0.024 (0.015, 0.033) <b>0.000</b>
<b>RD*</b>	0.005 (-0.004, 0.015) 0.278	0.029 (0.019, 0.040) <b>0.000</b>	0.024 (0.013, 0.034) <b>0.000</b>

Adjusted for age, gender and study site. \* $10^{-3}\text{mm}^2.\text{s}^{-1}$ . FA = fractional anisotropy; MD = mean diffusivity; AD = axial diffusivity; RD = radial diffusivity. Dark grey highlights the adjusted between-group differences significant at  $p < 0.001$  and the light grey highlights the significant differences at  $p < 0.05$ .

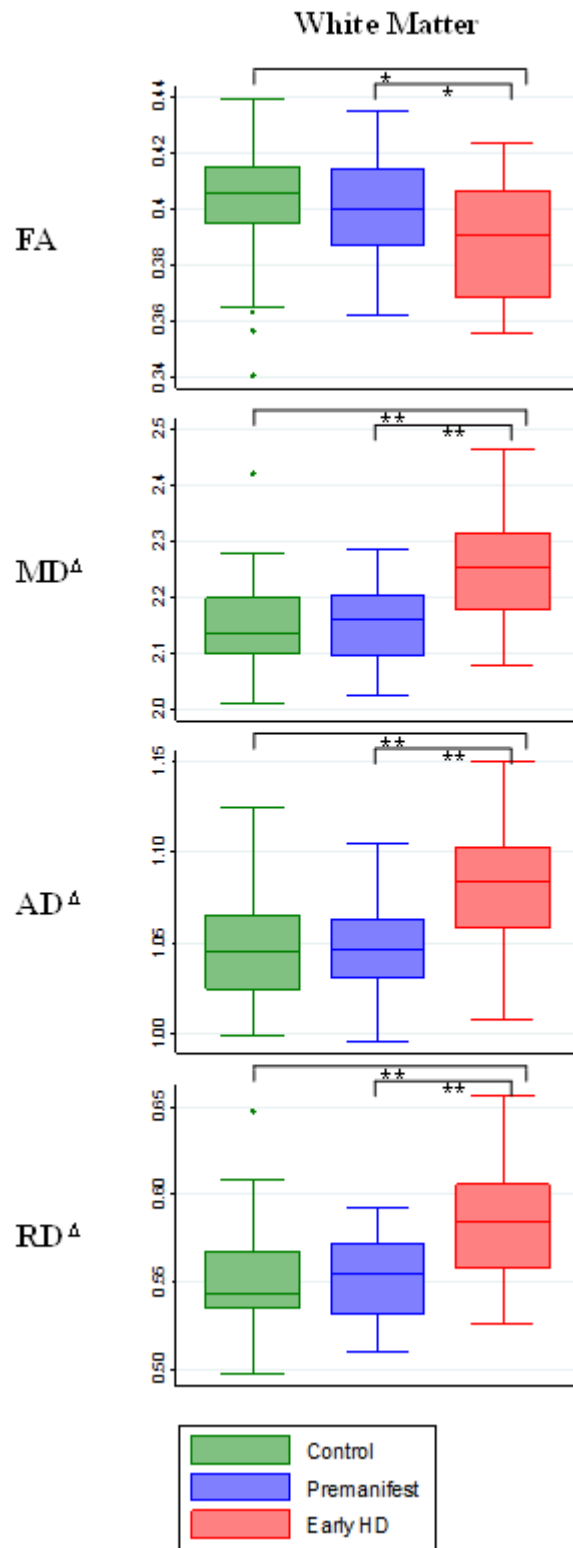


Figure 9-7. Boxplots of WM diffusion metrics for each group.  $\Delta 10^{-3} \text{mm}^2 \cdot \text{s}^{-1}$ . \* $p < 0.001$ ; \*\* $p < 0.05$ .

## 9.4 Discussion

TBSS analysis of diffusion data with an improved registration technique has shown that the diffusion properties of WM are significantly altered throughout widespread parts of the WM skeleton in HD gene-carriers when compared with controls. Regression analysis has also shown significant differences in the magnitude of diffusion in WM between early HD participants and both controls and premanifest HD participants.

### 9.4.1 Tract-Based Between-Group Differences

#### *Fractional Anisotropy*

TBSS analysis was sensitive to differences in FA many years prior to symptom onset. The premanifest HD group had significantly lower FA compared with the control group in several WM regions, compatible with much of the literature (Di Paola *et al.* 2014; Poudel *et al.* 2014; 2015; Rosas *et al.* 2010). Similar regions also displayed lower FA when compared with early HD participants, also consistent with previous findings (Di Paola *et al.* 2014). The early HD group showed much more widespread reductions in FA, encompassing most of the WM skeleton when compared with controls which are also supported by existing evidence (Della Nave *et al.* 2010; Di Paola *et al.* 2014; Novak *et al.* 2013). These findings in both participants groups are indicative of microstructural degeneration and suggest that the integrity, or coherence of the WM fibres decrease with disease progression.

There were, however, some unexpected findings in the analysis of FA. Early HD participants were found to have higher FA than controls and premanifest participants in small clusters within the WM skeleton, including parts of the anterior thalamic radiations, internal capsules, and corona radiata. Similar increases in FA in these areas have been shown previously in a group of early to moderate stage HD patients and were associated with increased AD in the absence of any change in RD (Della Nave *et al.* 2010). The increases found here may have been caused by selective damage to fibres running perpendicular to the tracts showing increased FA, causing an overall increase in the anisotropy at the voxel level. Despite utilising an improved tensor-based registration technique, crossing or interleaving axons can still have an unwanted influence on FA.



Disease-related fibre changes, such as one fibre bundle degenerating more than another, can cause anisotropy to be increased or decreased within a voxel (Jbabdi *et al.* 2010).

A previous study into the reliability of voxelwise DTI measures found that, although reliability was generally high across the brain, the areas surrounding the lateral ventricles were less reliable and more variable, particularly in FA metrics (Cole *et al.* 2014). Reasons for this could be residual registration error between voxels, and/or the selective damage to adjacent fibres in these areas of WM as other evidence has shown (Della Nave *et al.* 2010). It is possible that the microstructural degeneration of neighbouring tracts, evidenced by lower FA in these same regions in both the premanifest and early HD groups has caused elevated FA in these areas of merging or crossing fibres.

### ***Mean Diffusivity***

Significantly increased MD was found in premanifest participants in several WM tracts compared with controls, including those found to also have decreased FA, consistent with other TBSS analysis (Novak *et al.* 2013). Several other WM tracts also showed elevated MD including the CC, which is in contrast to previous studies where no differences in MD were found between premanifest HD and controls using TBSS (Di Paola *et al.* 2014). It is possible, therefore, that this finding suggests tensor-based registration is more sensitive to subtle microstructural changes during the premanifest stage of HD. Further research, however, replicating these results is needed to verify this.

MD was lower in the premanifest HD group in widespread areas compared with the early HD group including many of the same tract regions where MD was elevated compared with controls. Differences in the callosal body are consistent with previous analyses (Di Paola *et al.* 2014), while MD values have not been compared between premanifest and early HD using whole-brain voxelwise techniques. Instead, much of the literature describes changes in AD and RD as discussed below. Areas of increased MD in early HD participants compared with controls was also bilaterally extensive, including the majority of the WM skeleton, consistent with previous reports (Della Nave *et al.* 2010; Di Paola *et al.* 2014; Novak *et al.* 2013). MD represents the average diffusion in all three axes directions, therefore, examination of the individual parallel

( $\lambda_1$ ) and perpendicular axes ( $\lambda_2, \lambda_3$ ) will reveal the extent to which it is axial or radial increases in diffusion that are increasing with disease progression.

### ***Axial Diffusivity***

The premanifest HD group had significantly higher AD compared with the control group in two small WM clusters. AD has not previously been examined using whole-brain TBSS in a sample of premanifest HD gene-carriers, however, has been examined in the CC using ROI analysis (Rosas *et al.* 2010) and ROI TBSS analysis (Di Paola *et al.* 2014) and no differences were found compared with controls. These findings may, therefore, provide additional support to the argument that tensor-based registration is more sensitive to subtle microstructural changes during the premanifest stage of HD, but further research is required to confirm this.

Premanifest HD participants showed few differences in AD when compared with the control group and extensive bilateral differences in AD when compared with the early HD group, suggesting WM microstructure is not overly dissimilar from controls prior to disease onset and axonal damage may not become more pronounced until symptoms manifest. The areas where the early HD group had increased AD compared with the premanifest and control groups were analogous to the regions showing elevated MD, suggesting that increased diffusion along the main WM fibre could be driving the widespread areas of increased MD. Many of these tracts have previously been found to have abnormal AD in manifest HD patients compared with controls (Della Nave *et al.* 2010; Di Paola *et al.* 2014).

### ***Radial Diffusivity***

TBSS analysis was sensitive to differences in RD in the premanifest HD group in a few areas of the WM skeleton when compared with controls, including clusters in the CC and fronto-parietal tracts which have previously been demonstrated (Di Paola *et al.* 2014; Poudel *et al.* 2014; Rosas *et al.* 2010). Additional areas showing raised RD may represent novel findings using the optimised registration technique but need replicating to be certain.

Premanifest HD participants also had lower RD than early HD participants in extensive bilateral tracts, consistent with previous research (Di Paola *et al.* 2014), and suggesting

that increases in RD, indicative of demyelination (Song *et al.* 2002; 2003), becomes much more pronounced with symptom onset.

Similar to the results for the MD analysis, early HD participants had higher RD compared with controls symmetrically across the majority of the WM skeleton in agreement with numerous studies (Della Nave *et al.* 2010; Di Paola *et al.* 2014; Poudel *et al.* 2014; 2015; Rosas *et al.* 2010). Changes in RD apparent in both the premanifest and early manifest group compared with controls were, again, similar to the regions showing elevated MD. This suggests that increased diffusion perpendicular to the axons oriented in the principal diffusion direction could also be driving the increased MD in these same tracts at the same time as increases in axial diffusion.

### ***Key Findings***

TBSS has several advantages over other whole-brain methods, including the investigation of the core of WM tracts to avoid problems arising from misregistration, particularly at the boundary between WM and GM, which can often occur in advanced atrophied brains (Della Nave *et al.* 2010) as well as healthy individuals due to the highly variable arrangement of WM fibres (Phillips *et al.* 2016). Despite overall improvements in image alignment (Smith *et al.* 2006), poor alignment has been demonstrated in areas of merging fibres (Bach *et al.* 2014) and tensor-based registration such as DTI-TK (Zhang *et al.* 2006) has been shown to outperform other registration algorithms (Keihaninejad *et al.* 2013; Wang *et al.* 2011).

Compared to previous TBSS analyses (Novak *et al.* 2013), the incorporation of tensor-based registration in the current study increased the ability of TBSS to identify differences in FA many years before symptom onset. This indicates the superiority of tensor-based over FA-based registration, however, current findings also demonstrate that this technique is not immune to the influence of crossing or interleaving axons.

Overall, the present study demonstrated sensitivity to changes in all diffusion measures, even in individuals many years prior to disease onset. One of the main regions to show consistent, substantial microstructural damage was the CC, suggesting that degeneration of this structure is a key feature of the disease, even in presymptomatic stages. Degradation of callosal tracts has substantial implications for HD gene-carriers because

of its connection to numerous widespread areas of the cortex, as well as the integral role the CC has in interhemispheric communication. Further investigation into how the microstructural abnormalities found here, particularly in the premanifest HD group relate to interhemispheric transfer is needed to assess the functional role of these tracts (chapter 10).

#### **9.4.2 Diffusion-Based Between-Group Differences**

ROI analysis is often included in DTI studies to complement the TBSS analysis (Douaud *et al.* 2006; Novak *et al.* 2013; Rosas *et al.* 2006). Correspondingly, the current study conducted ROI analysis of diffusion metrics extracted from whole WM regions to further investigate between-group differences. Regression analysis revealed highly significant differences in all diffusion measures in WM between early HD participants and both controls and premanifest HD participants, consistent with previous research (Hobbs *et al.* 2013; Odish *et al.* 2015). No differences were found between the premanifest HD group and the control group in any of the metrics, however. This suggests that ROI analysis of whole-WM is perhaps not as sensitive as whole-brain TBSS analysis to microstructural degeneration in the premanifest stage of HD but is useful for confirming findings from the TBSS analyses in the early manifest stages.

### **9.5 Conclusions**

This study has replicated previous findings of microstructural degeneration in premanifest and manifest HD using TBSS and an improved registration technique. Evidence has been found in support of the superiority of tensor-based registration over FA-based registration, demonstrated by the discovery of previously undetected changes in WM microstructure in premanifest HD.

Despite this, however, whole-brain voxelwise analysis using optimised registration such as DTI-TK is still vulnerable to potential artefacts in areas of crossing WM fibres. The findings here of increased FA in selected WM regions highlight the importance of interpreting DTI results with caution and to always consider how crossing or interleaving axons may influence FA.

## **Clinical Application: Cognitive Tools**

Previous chapters have consistently highlighted the CC as a region with pronounced atrophy and microstructural abnormalities (chapters 7 and 9). To explore the functional impact of these neuropathological changes in the premanifest stage of HD, the specially developed interhemispheric transfer task (chapter 5) was applied to a sample of healthy controls and premanifest HD participants at two time points. Similarly, the functional impact of the degeneration of the striatum and cortico-striatal network (Marrakchi-Kacem *et al.* 2013; Novak *et al.* 2015) was explored using the specially designed interference task (chapter 6), which was also applied to the same sample of healthy controls and premanifest HD participants at two time points.

## **10. Interhemispheric Information Transfer Degeneration in Premanifest HD**

### **10.1 Introduction**

Pathology and degeneration of the CC will undoubtedly have an effect on interhemispheric communication. The CC, the largest WM fibre bundle within the brain, plays a significant role in interhemispheric information transfer and is involved in many cognitive processes by way of its connectivity to numerous brain areas. Research has found evidence of increases in interhemispheric information transfer time in split-brain patients (Ouimet *et al.* 2010), Multiple Sclerosis (MS) patients (Brown *et al.* 2010), and in normal aging (Jeeves & Moes 1996; Reuter-Lorenz & Stanczak 2000). Research into interhemispheric communication in MS patients in particular has been useful in showing how reduced CC volume, compared with controls, compromises interhemispheric transfer (Brown *et al.* 2010).

Recent research has found evidence of significant CC atrophy in HD, even many years prior to disease onset (Crawford *et al.* 2013; chapter 7) and numerous studies have shown microstructural degeneration of the CC across all disease stages (Di Paola *et al.* 2014; Dumas *et al.* 2012; Novak *et al.* 2013; Phillips *et al.* 2013; Phillips *et al.* 2014a; Poudel *et al.* 2014; Rosas *et al.* 2010; Steventon *et al.* 2015; and chapter 9). Abnormalities within the CC have also been associated with cumulative probability to

onset (CPO), disease burden and CAG repeat length (Gregory *et al.* 2015; Phillips *et al.* 2013), and significant volume loss and changes in CC microstructure have been demonstrated over time (Crawford *et al.* 2013; Poudel *et al.* 2015, and chapter 7).

Functional MRI (fMRI) studies confirm the CC's involvement in interhemispheric communication (Pellicano *et al.* 2013; Tettamanti *et al.* 2002) and have demonstrated the topographical organisation of callosal fibres (Fabri *et al.* 2011). The CC is organised in an orbital-frontal-parietal-occipital pattern (Phillips *et al.* 2013), with anterior fibres connecting prefrontal cortical areas; fibres in the central body connecting premotor and motor cortical areas; posterior fibres connecting parietal cortical areas and splenium fibres connecting occipital areas (Fabri & Polonara 2013). Similarly, the degeneration of the CC in HD has been shown to have a topographical pattern, degenerating in a posterior – anterior direction with disease progression (Di Paola *et al.* 2014; Phillips *et al.* 2013). Compromised interhemispheric transfer, therefore, may be due to the topographical pattern of CC degeneration and the concurrent degeneration of the cortical areas with which it is connected.

Evidence of CC integrity loss has additionally been measured using tasks that require interhemispheric transfer, such as indirect circle tracing (Crawford *et al.* 2013; chapter 7), Stroop Colour Word Interference (Rosas *et al.* 2006) and Verbal Fluency and Symbol Digit tests (Rosas *et al.* 2010). However, research into explicit interhemispheric processing in HD has been limited. A recent transcranial magnetic stimulation study using finger muscle stimulation found impaired transcallosal conduction in early stage HD, which correlated with clinical and genetic data (Bocci *et al.* 2015). Findings from this study, however, cannot be generalised to other HD or premanifest participants; inferences regarding wider cognitive function are difficult due to both the nature of the study and the very small sample, comprising only seven HD participants and seven controls.

The Poffenberger Paradigm (Poffenberger 1912; chapter 5) is a simple reaction task designed to directly measure interhemispheric transfer time (ITT) and has been applied to various cohorts e.g. healthy participants (Chaumillon *et al.* 2014; Pellicano *et al.* 2013; Westerhausen *et al.* 2006), elderly participants (Schulte *et al.* 2013), sportsmen (Semprini *et al.* 2012), and individuals with Down syndrome (Heath *et al.* 2007). Typically, healthy participants are slower to respond to crossed stimuli, where

interhemispheric transfer occurs via the CC, than uncrossed stimuli (Chaumillon *et al.* 2014; Cherbuin & Brinkman 2006; Marzi *et al.* 1991; Pellicano *et al.* 2013; Schulte *et al.* 2013; Semprini *et al.* 2012). Individuals with CC pathology, e.g. alcoholics, similarly demonstrate the same prolonged RT during crossed stimuli but also show an association between ITT and microstructural properties of the CC (Schulte *et al.* 2005). At the time of writing, no other studies had investigated this paradigm in a sample of premanifest HD participants over 12 months.

Having successfully developed an interhemispheric transfer task (chapter 5), the aim of the present study was to investigate cross-sectional and longitudinal group differences in interhemispheric transfer in a group of premanifest HD participants and healthy controls, and hypothesis-driven associations with clinically relevant variables and imaging metrics of interest. Specifically, ROI analysis of structural MRI data, and both tractography and TBSS analysis of diffusion MRI data was used to investigate the associations between interhemispheric transfer and:

1. CC volume – CC volume is significantly reduced in premanifest HD (Crawford *et al.* 2013; chapter 7) and volume loss has been associated with compromised interhemispheric transfer (Brown *et al.* 2010; Schulte *et al.* 2004).
2. CC diffusion properties – Significant microstructural abnormalities have consistently been reported in premanifest HD using ROI analysis, evidenced by reduced FA and increased measures of diffusivity (Dumas *et al.* 2012; Rosas *et al.* 2010). Microstructural tissue properties of the CC have also been found to be related to ITT (Schulte *et al.* 2005; Westerhausen *et al.* 2006).
3. TBSS analysis within the CC – TBSS analysis has revealed significant reductions in FA and increases in RD and MD in the CC of premanifest HD participants (Di Paola *et al.* 2014; Novak *et al.* 2013).
4. Diffusion properties of CC tracts; genu, body and splenium – DTI Tractography analysis of the CC has consistently found decreased FA (Phillips *et al.* 2013; Steventon *et al.* 2015) and increased MD (Steventon *et al.* 2015) and RD (Phillips *et al.* 2013), particularly in tracts connecting parietal and occipital regions, in premanifest HD patients compared with controls (Phillips *et al.*

2013). Regional microstructural integrity of the CC has also been found to be associated with ITT in the genu and splenium (Schulte *et al.* 2005; Westerhausen *et al.* 2006).

## **10.2 Aims**

Firstly, this study aimed to better understand how known degeneration of the CC in HD affects interhemispheric information transfer, particularly in the premanifest stage, and whether this simple task was sensitive to differences between premanifest participants and healthy controls, both cross-sectionally and longitudinally. Secondly, the study aimed to investigate whether there is an association between disease-related interhemispheric transfer and clinical measures, as well as CC volume and microstructural integrity using various techniques.

Due to the exploratory nature of the study it was difficult to state exact hypotheses, however it was predicted that interhemispheric information transfer time would be increased in premanifest HD participants compared with healthy controls and would be associated with CC volume and microstructural measures.

## **10.3 Methods**

### **10.3.1 Participants**

A total of 26 participants were recruited at baseline, the majority of which (24/26) were taken from the TrackOn-HD cohort. The participants were chosen from this study because they were in the premanifest stage of HD and had recently received T1-weighted and diffusion-weighted MRI scans as part of the third study visit. Details of the TrackOn-HD study are provided in section 2.1.2 and in Kloppel *et al.* (2015). One of the additional premanifest participants was recruited during their routine visit to the HD clinic at The National Hospital for Neurology and Neurosurgery. The final control participant was recruited through a connection to the HD Research Centre.

Inclusion and exclusion criteria in this study were the same criteria used in the TrackOn-HD and Track-HD studies (see section 2.1), with the additional requirement that these study participants needed to have expressed an interest in taking part in future HD studies, or consented via existing studies in order to be contacted. Left-handed



participants were included as well as right-handed participants in order to increase the sample size, as well as examine the interhemispheric transfer of information in both left and right directions across the CC. Participants, therefore, were required to use both hands in this study.

Twenty two participants (11 controls and 11 premanifest HD) completed the one year follow-up visit. Attrition was due to three of the participants not responding to messages at the second visit and one participant sadly died due to a brain haemorrhage. All participants provided written informed consent before participation at both time points. Please see Table 10-1 for demographic and clinical characteristics of the participants.

Ethical approval was gained for the study from the Queen Square Research Ethics Committee (REC number: 14/LO/0588).

**Table 10-1. Demographic and Clinical Characteristics of Participants**

	<b>Control</b>	<b>Premanifest HD</b>
<b>N (26)</b>	14	12
<b>Age, years*</b>	46.66 (10.64)	45.65 (9.03)
<b>Gender F/M</b>	11/3	7/5
<b>ISCED**</b>	4.29 (0.73)	4.83 (0.58)
<b>Handedness R/L</b>	13/1	11/1
<b>CAG repeat length**</b>	-	42.83 (1.80)
<b>Disease-Burden Score*±</b>	-	323.11 (47.31)
<b>Total Motor Score</b>	0.29 (0.73)	6.67 (4.33)
<b>CPO</b>	-	0.30 (0.17)

Values are represented as mean (standard deviation), except gender where the numbers are of females/males; \*At time of baseline testing; \*\*As measured during TrackOn-HD baseline; ±Disease-Burden Score = (CAG length – 35.5) x age (Penney *et al.* 1997); <sup>Δ</sup> As measured during TrackOn-HD visit three; ISCED = International Standard Classification of Education; CPO = Cumulative Probability to Onset (Langbehn *et al.* 2004).

### **10.3.2 Task Administration**

A full description of how the task was developed and piloted is given in chapter 5. To summarise, this simple reaction task involved participants responding to lateralised

stimuli as quickly as possible. Participants were tested using both their left and right hands. There were four conditions in total: left visual field (LVF) and left hand (LH); right visual field (RVF) and right hand (RH); LVF and RH; RVF and LH. The first two conditions were the uncrossed conditions and the latter two were the crossed conditions.

Participants were positioned at arms-length from the computer screen and were instructed to wear their glasses or contact lenses if necessary. This task and the interference task (chapter 11) were administered one after another, in a counterbalanced order. Full written and oral instructions were given to participants before beginning the task. 10 practice trials using the left hand and 10 practice trials using the right hand were completed before beginning the main experiment in order for participants to become familiar with the task.

Responding hand was alternated between blocks with the starting hand inter-individually balanced. The task was completed on a laptop in a dimly lit room and lasted approximately 15-20 minutes. Administration of the task was the same at visit two.

### **10.3.3 Behavioural Data Analysis**

All statistical analyses were performed using STATA (StataCorp LP). Responses were excluded due to anticipation (<150 ms) or attentional lapses (>750 ms) and the median was calculated in each individual condition for each participant. The between-group difference in number of responses was then assessed using linear regression with robust estimate of variance, whilst controlling for gender, age and education (measured using the International Standard Classification of Education; ISCED). The variables age and education were centred around their respective means in order to help balance any difference in these variables. This allows the estimation of the number of responses in each group at the average age and education level, without affecting any of the between-group estimates.

The average of the uncrossed responses (LVF, LH and RVF, RH) was then subtracted from the crossed responses (LVF, RH and RVF, LH) to calculate the crossed-uncrossed difference (CUD). This is also known as the ITT.

### ***Cross-sectional Analysis***

A linear regression model (ordinary least squares) tested for within- and between-group differences in reaction time (RT) due to hand dominance and the crossing of stimulus presentation and hand response, as well as the between-group difference in ITTs. An interaction term to describe the interaction between hand (non-dominant; dominant), condition (uncrossed; crossed) and group (controls; premanifest HD) was included in the model.

Robust estimate of variance was used to help control for the effects of outliers and differing variance between the groups. All regression models controlled for age and gender. RTs were weighted in the regression model by the number of individual responses used to calculate the mean described above. This was to limit the effects of unequal responses between participants and groups. In order to be consistent with the Track-HD study (Tabrizi *et al.* 2009), education was also controlled for. The variables age and education were centred around their respective means in order to help balance any difference in these variables, and allow the estimation of experimental effects at the average level without affecting any of the between-group estimates.

At visit two the same cross-sectional regression as above was carried out with participants' age and number of responses adjusted accordingly. This was to help ascertain the consistency of the task over time. Due to the exploratory nature of this study, p-value thresholds ( $p < 0.05$ ) were not adjusted for multiple comparisons in any of the regression analyses.

### ***Longitudinal Analysis***

In order to analyse any possible change in results over one year a linear regression model was used to test for within- and between-group change in RTs, whilst taking into account the time interval between visits and the number of responses.

Firstly, the annual change in RTs was calculated for each participant by subtracting the baseline RT (V1) from the visit two RT (V2), and then multiplying this by 365.25 divided by the actual time interval between visits:  $(V2 - V1) \times 365.25 / \text{interval}$ . Secondly, the number of responses at baseline and the number of responses at visit two were

averaged for each participant in order to control for number responses at both time points within the longitudinal analysis.

The cross-sectional statistical model was also used here, however the outcome variable of RT was altered to the change value and the number of responses were adjusted as mentioned above (and included in the model using weighted means). Similar to the cross-sectional regression model, mean-centred baseline age and education were included as covariates, as was gender. Due to the exploratory nature of this study, p-value thresholds ( $p < 0.05$ ) were not adjusted for multiple comparisons.

#### **10.3.4 Clinical Correlations**

Spearman's correlation analysis was used in order to assess the relationship between ITT and disease status in the premanifest HD participants. Non-dominant and dominant hand CUD was analysed with disease burden and CPO.

#### **10.3.5 Image Analysis**

T1-MRI and DTI data from visit three of the TrackOn-HD study (Kloppel *et al.* 2015) were analysed. Images were acquired according to the acquisition protocols of the London site described in detail in section 2.2.2.

Of the two participants not part of the TrackOn-HD study, one had a structural MRI scan taken as part of another research study, details of which are provided in section 2.1.4. Imaging data for 25 participants (14 controls and 11 premanifest HD) therefore was available for structural analysis and 24 participants (13 controls and 11 premanifest HD) had data for the diffusion analysis.

T1 images were processed according to the steps described in section 2.3.1, with the exception of the additional non-TrackOn-HD scan that required re-orienting and converting to MIDAS format before bias correction and standard space registration. Diffusion images were also processed according to the pipeline outlined in section 2.3.2.

### 10.3.6 Volumetric Analysis

TIV was calculated for all participants using SPM8 by adding together the WM, GM and CSF regions created using the *segment* tool (as described in section 2.3.1: Segmentation). All images were visually checked at each stage. CC segmentations were performed according to the protocol described in chapter 3 and Appendix 1: Volumetric Analysis. In order for the CC regions to be transformed into native space for further registration to diffusion space, they first had to be resliced and parameters from the original native to standard space transformations were applied.

Linear regression models examined the association between dominant and non-dominant hand CUDs and CC volume. Volumes were adjusted for TIV in order to account for variation in head size. The covariates age, education (both mean-centred) and gender were included. The time interval between scanning and cognitive testing (mean = 196.24 days) was also controlled for.

### 10.3.7 Regional Diffusion Analysis

Analysis of regional diffusion metrics was done in line with the ROI processing pipeline (section 2.3.2: Region of Interest Analysis). Firstly, T1 images were registered to each participant's FA map using NiftyReg. Whole CC regions were transformed from standard space (where they were originally segmented in MIDAS) back into native T1 space. The CC regions were eroded in T1 space in order to reduce partial volume effects when warping to diffusion space. They were then registered to individual participant's tensor maps using the parameters from the initial T1 to FA registration in NiftyReg, then thresholded to 0.5 and binarised.

Diffusivity and anisotropy metrics FA, AD and RD were outputted from the regions using *fslstats* and linear regression models analysed the association with dominant and non-dominant hand CUD for each group. Covariates were the same as those stated above.

### 10.3.8 ROI Tract-Based Spatial Statistics

The TBSS with DTI-TK registration pipeline was followed (see section 2.3.2: TBSS with DTI-Toolkit). DTI-TK was used to create a separate customised group tensor

template for each participant group. Due to the small sample size it was computationally possible to use all tensor maps to create the respective templates (see chapter 4 for more information regarding tensor template choice).

In order to create a CC mask for the ROI TBSS, the JHU-ICBM-labels atlas was firstly registered to the mean FA image of each group using NiftyReg. The atlas was then thresholded in FSL so that just the genu, body and splenium of the CC were selected. These three regions were then binarised to create one whole CC mask. The mask was visually checked to verify its position over the CC and to see if it successfully included the FA skeleton when overlaid onto the mean FA and FA skeleton images (see Figure 10-1).

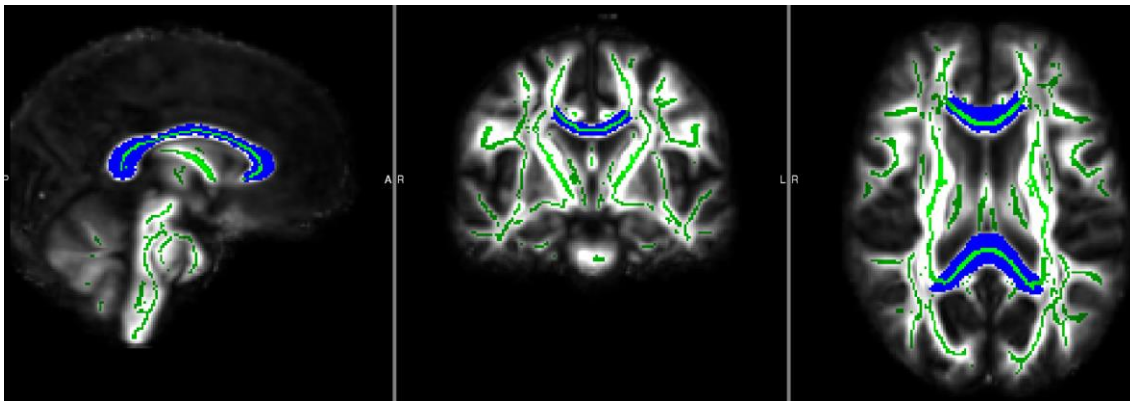


*Figure 10-1. The CC mask (blue) overlaid on the control groups' mean FA and mean FA skeleton (green).*

Voxelwise statistics were performed using the FSL Randomise tool, with the CC mask used in place of the FA skeleton mask. Statistical contrasts to identify positively or negatively correlating voxels were performed just within the CC using non-parametric permutation tests (n=500). Age, gender and education were included in the model as regressors of no interest. Analyses were repeated using AD and RD data.

Statistics were run separately for each participant group to examine the correlations between diffusion properties of the CC and the behavioural variables of interest: non-dominant and dominant hand CUD. All results were FWE-corrected for multiple comparisons using the TFCE method. Significant clusters ( $p < 0.05$ ) of 20 voxels or more were identified using FSL's *cluster* tool. In order to present the skeletonised results more clearly, results were 'thickened' using the *tbss\_fill* tool.

A between-group comparison of FA, AD and RD values within the CC was also conducted using this ROI TBSS method. Contrasts were run in both directions and the variables age and gender were controlled for.

### **10.3.9 Tractography of the Corpus Callosum**

Tractography of the genu, body and splenium was carried out in order to further examine the association between interhemispheric transfer and microstructural properties of the CC tracts. Tractography was performed in FSL using the probabilistic tractography tool PROBTRACKX2. A detailed description of the analysis steps are provided in section 2.3.2: Tractography.

Each participant's structural T1 image was registered to their B0 image using FSL's *flirt* registration tool. This linear registration was visually checked for each participant by overlaying the T1 on the B0 and checking the alignment of key structures such as the CC and the frontal region.

CC regions for the tractography were taken from SPM's Anatomy Toolbox. The genu, body and splenium were warped to T1 space for each individual using SPM's *Apply Deformation* tool. Exclusion masks to prevent wayward fibre tracking were created in standard space using the MNI template (Mazziotta *et al.* 1995) and then similarly warped to T1 space with SPM. See Figure 10-2 for an example of the CC ROIs and the positioning of the exclusion masks. A WM termination mask was also used to ensure tracts did not extend beyond the WM into GM, CSF or dura. All regions and masks were visually inspected to check if their warped location was sensible by overlaying them onto each participant's T1 image.

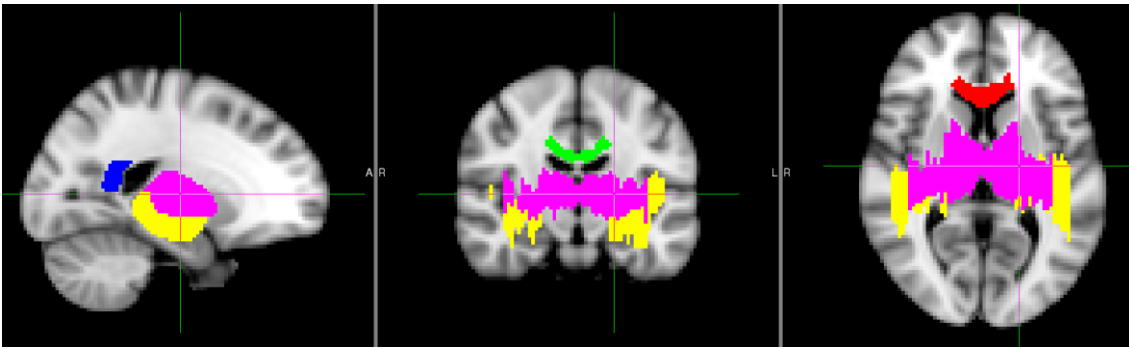


*Figure 10-2. The genu (red), body (green) and splenium (blue) of the CC overlaid on the MNI brain. The exclusion mask to prevent wayward fibre tracking for the genu and body is shown in pink. The exclusion mask for the splenium is shown in yellow.*

PROBTRACKX2 was run using the Legion cluster (UCL Legion High Performance Computing facility) in network mode whereby paths are only tracked through at least one of the seed points and applying waypoint conditions to each half tract separately. Default parameters were used (full details are given in section 2.3.2: Tractography).

Each resulting tract was visually checked by overlaying it on the T1 image along with the ROIs (see Figure 10-3, top row). These tracts were then warped from structural space into diffusion space using FSL's flirt and the previously obtained transformation parameters. Warping of the tracts was again visually checked by overlaying them onto each participant's FA image (see Figure 10-3, bottom row). Finally, diffusion metrics (AD, RD and FA) were output for each of the tracts using a script that takes a mask of the warped pathways and then gives each streamline a weighting based on the weighted mean of the FA within that mask (as described in section 2.3.2: Output Diffusion Metrics).



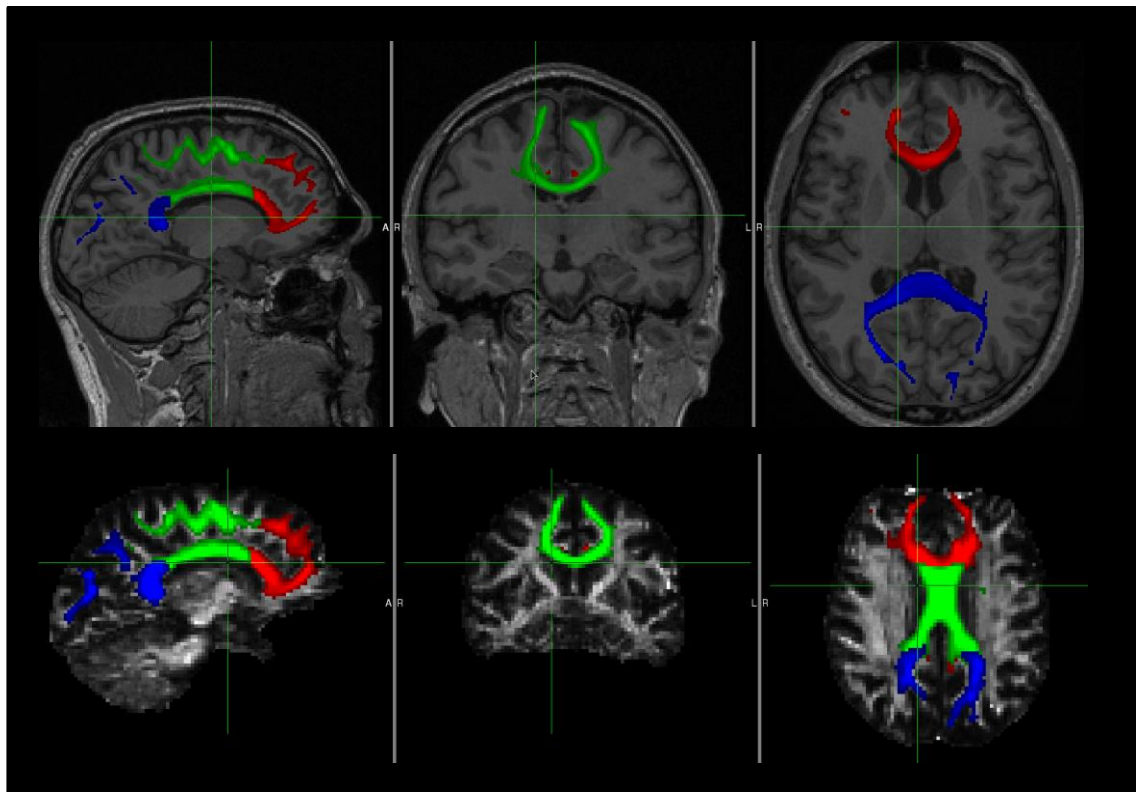


*Figure 10-3. Top row: Fibre tracts of the genu (red), body (green) and splenium (blue) overlaid on a T1 image. Bottom row: Fibre tracts of the genu (red), body (green) and splenium (blue) warped into diffusion space and overlaid on a FA image.*

In addition to the analyses of the association between CUD and CC imaging metrics outlined above, a between-group comparison of CC imaging metrics was conducted to examine differences unrelated to the task. Linear regression models were used whilst covarying for age and gender.

## 10.4 Results

### 10.4.1 Baseline Results

On average, control participants had five (out of 320) trials removed (1.566%) and premanifest HD participants had 11 removed (3.438%) due to anticipation or lapses in attention. This was a significant difference of 5.23 responses (95% C.I. -8.390, -2.060;  $p=0.001$ ). Raw mean RTs and between-group differences adjusted for age, gender and education for all conditions are provided in Table 10-2.

### ***Within-Group Analysis Results***

Overall, both groups had faster RTs in the uncrossed conditions compared with the crossed conditions, however there was no significant effect of responding hand or stimulus crossing for either group (see Table 10-3).

There was no significant difference in RTs between crossed and uncrossed responses in the control group when using their non-dominant (5.825ms; 95% C.I. -20.283, 31.933;  $p=0.659$ ) or dominant hand (1.607ms; 95% C.I. -26.022, 29.236;  $p=0.908$ ). The dominant hand CUD was 4.218ms quicker than the non-dominant hand CUD, however, this was not significant (95% C.I. -42.231, 33.796;  $p=0.826$ ).

For premanifest HD participants, there was also no significant difference in RTs between crossed and uncrossed responses when using their non-dominant (0.935ms; 95% C.I. -47.407, 49.277;  $p=0.969$ ) or dominant hand (9.703ms; 95% C.I. -65.730, 85.136;  $p=0.799$ ). The dominant hand CUD was 4.551ms slower than the non-dominant hand CUD in the premanifest HD group, however this was also not significant (95% C.I. -76.579, 85.681;  $p=0.912$ ).

Controls were slowest to react to crossed stimuli when using their non-dominant hand and stimulus was presented to the dominant visual field (345.571ms), whereas, premanifest HD participants were slowest in the crossed condition when using their dominant hand and stimulus was presented to the non-dominant visual field (386.667ms). Figure 10-4 presents the raw mean RTs for each group as a function of responding hand and demonstrates the asymmetry in CUDs.

### ***Between-Group Analysis Results***

Premanifest HD participants had slower RTs in all conditions compared with controls, significantly so when using their non-dominant hand to both crossed and uncrossed stimuli and when using their dominant hand with uncrossed stimuli (Table 10-2). This meant that compared with the controls, premanifest HD participants were, on average, 48.082ms (95% C.I. 13.987, 82.178;  $p=0.006$ ) slower for the overall uncrossed conditions and 47.577ms slower for the overall crossed conditions (95% C.I. 12.511, 82.642;  $p=0.008$ ).

Despite the variation in the CUDs, (between the dominant and non-dominant responding hands, as well as between the groups) the two groups did not significantly differ for either hand (Table 10-2). The between-group difference in the CUD asymmetry was not significant at 8.768ms (95% C.I. -80.826, 98.362;  $p=0.846$ ).

#### **10.4.2 Clinical Correlations**

There was no significant ( $p<0.05$ ) correlation between non-dominant hand CUD and disease burden (Spearman's  $Rho=0.078$ ;  $p=0.811$ ) or CPO (Spearman's  $Rho=0.473$ ;  $p=0.121$ ) in the premanifest HD group. Similarly, there was no evidence of a correlation between dominant hand CUD and disease burden (Spearman's  $Rho=0.140$ ;  $p=0.664$ ) or CPO (Spearman's  $Rho=-0.354$ ;  $p=0.259$ ).

**Table 10-2. Mean (SD) RT (ms) and Adjusted Between-Group Differences at Baseline**

Responding Hand	Visual Field	Condition	Control	Premanifest HD	Premanifest HD vs. Control**
Non-Dominant	Non-Dominant	Uncrossed	339.750 (42.160)	370.833 (63.733)	44.401 (2.025, 86.777) 0.040
	Dominant	Crossed	345.571 (35.245)	371.792 (62.827)	39.511 (-0.106, 79.128) 0.051
		CUD*	5.821 (17.542)	0.958 (16.975)	-4.890 (-59.832, 50.052) 0.860
Dominant	Dominant	Uncrossed	342.214 (34.358)	381.167 (81.794)	51.764 (2.105, 101.423) 0.041
	Non-Dominant	Crossed	343.786 (37.094)	386.667 (89.528)	48.279 (-34.436, 130.995) 0.249
		CUD*	1.571 (10.599)	5.500 (13.886)	3.879 (-66.892, 74.649) 0.914
		<b>Overall Uncrossed</b>	340.982 (36.423)	376 (71.743)	48.082 (13.987, 82.178) 0.006
		<b>Overall Crossed</b>	344.679 (33.893)	379.229 (75.867)	47.577 (12.511, 82.642) 0.008
		<b>Overall CUD*</b>	3.696 (9.069)	3.229 (12.342)	-0.506 (-45.303, 44.291) 0.982

\*crossed – uncrossed difference i.e. Interhemispheric transfer time (ms); \*\* Regression Coefficient (95% C.I.) and p-value; Dark grey highlights the significant (p<0.05) adjusted between-group differences in RT and the light grey highlights the borderline significant differences (p<0.06). Adjustment is for age, gender and education; SD = standard deviation; SEM = standard error of the mean.

**Table 10-3. Adjusted Within-Group Analysis of the Effects of Hand Dominance and Crossing on RT (ms) at Baseline**

Interactions		Control*	Premanifest HD*
Non-Dominant Hand	Uncrossed	5.825	0.935
	vs. Crossed	(-20.283, 31.933) 0.659	(-47.407, 49.277) 0.969
Dominant Hand	Uncrossed	1.607	9.703
	vs. Crossed	(-26.022, 29.236) 0.908	(-65.730, 85.136) 0.799
Uncrossed Condition	Non-Dominant	2.552	9.915
	vs. Dominant	(-24.857, 29.961) 0.854	(-45.962, 65.792) 0.725
Crossed Condition	Non-Dominant	-1.666	18.683
	vs. Dominant	(-28.005, 24.674) 0.900	(-51.351, 88.718) 0.598

\*Regression Coefficient (95% C.I.) and p-value, adjusted for age, gender and education.

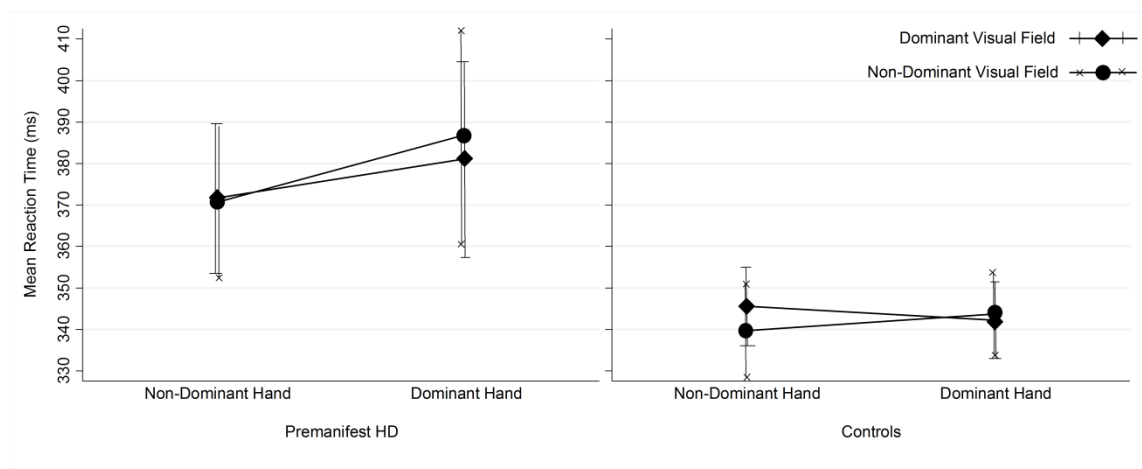


**Figure 10-4. Mean RT (ms) for the premanifest HD group (left) and control group (right) as a function of responding hand at baseline.**

In addition to the above, the same within-group analyses were run but with data from the two left-handed participants removed. All findings in purely right-handed participants were the same.

### 10.4.3 Association between Whole CC Volume and CUD

Results from the regression analysis with CC volumes and CUDs for each group can be seen in Table 10-4. No association was found between CC volume and either CUD in the control group.

Non-dominant hand CUD was found to be significantly associated with CC volume (% TIV) in the premanifest HD group (-318.397ms; 95% C.I. -628.883, -7.912;  $p=0.046$ ; see Figure 10-5); larger CUD (i.e. the bigger the difference between crossed and uncrossed RT) was associated with smaller CC volume. The same trend was seen for the dominant hand CUD, however, was only bordering on significance (-364.224ms; 95% C.I. -743.57, 15.12;  $p=0.057$ ).

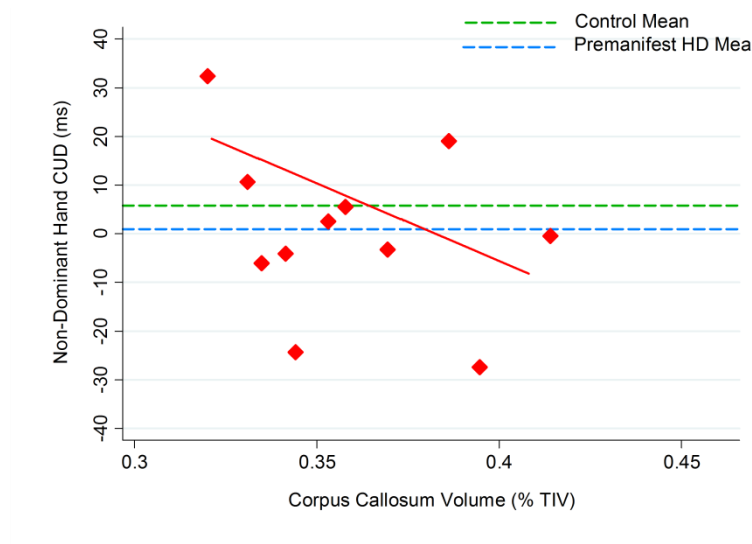


*Figure 10-5. Association between non-dominant hand CUD (ms) and CC volume (% TIV) in the premanifest HD group with adjusted regression line (red).*

### 10.4.4 Association between Whole CC Diffusion and CUD

Results from the regression analyses with whole CC diffusion metrics and CUDs for each group can be seen in Table 10-4. In the premanifest HD group, non-dominant hand CUD was found to be positively associated with AD in the CC (3.343ms; 95% C.I. 1.647, 5.039;  $p=0.004$ ; see Figure 10-6); larger CUD (i.e. the bigger the difference between crossed and uncrossed RT) was associated with higher AD in the CC.

**Table 10-4. Association Between CC Volume and Diffusion Metrics and Interhemispheric Transfer Time (ms)**

Metric	Brain Region	Control CUD <sup>+Δ</sup>		Premanifest HD CUD <sup>+Δ</sup>	
		Non-Dominant Hand	Dominant Hand	Non-Dominant Hand	Dominant Hand
Volume					
	Corpus Callosum *	-108.906 (-376.994, 159.181) 0.376	-83.909 (-268.793, 100.975) 0.326	-318.397 (-628.883, -7.912) 0.046	-364.224 (-743.571, 15.124) 0.057
Diffusion					
FA	Corpus Callosum	47.107 (-382.408, 476.621) 0.803	301.325 (72.789, 529.861) 0.017	-34.201 (-592.614, 524.212) 0.881	-181.510 (-530.267, 167.248) 0.239
	Genu (Tract)	-227.037 (-582.411, 128.337) 0.175	16.639 (-435.760, 469.039) 0.933	-340.421 (-593.137, -87.706) 0.018	-185.007 (-512.983, 142.969) 0.207
	Body (Tract)	-212.228 (-535.791, 111.336) 0.165	39.388 (-327.950, 406.727) 0.807	-492.993 (-1144.323, 158.337) 0.109	-400.691 (-995.788, 194.405) 0.144
	Splenium (Tract)	-216.345 (-524.504, 91.814) 0.141	41.782 (-355.166, 438.729) 0.811	-262.832 (-947.597, 421.934) 0.369	-199.512 (-614.113, 215.088) 0.271
AD** <sup>‡</sup>	Corpus Callosum	1.663 (-4.047, 7.373) 0.513	0.316 (-5.028, 5.661) 0.893	3.343 (1.647, 5.039) 0.004	1.979 (-1.349, 5.308) 0.187
	Genu (Tract)	-0.451 (-2.944, 2.043) 0.682	-0.857 (-2.758, 1.044) 0.322	-0.831 (-3.764, 2.102) 0.499	0.078 (-2.132, 2.287) 0.932
	Body (Tract)	-0.731 (-3.020, 1.559) 0.475	-0.453 (-2.848, 1.942) 0.668	-0.850 (-2.748, 1.048) 0.302	0.158 (-1.939, 2.255) 0.854
	Splenium (Tract)	0.558 (-1.301, 2.418) 0.501	-0.688 (-1.819, 0.444) 0.194	-1.220 (-4.985, 2.545) 0.443	0.396 (-3.563, 4.356) 0.807

RD** <sup>#</sup>	Corpus Callosum	-0.074 (-3.701, 3.553) 0.963	-2.556 (-4.608, -0.505) 0.022	0.814 (-3.095, 4.722) 0.615	1.679 (-0.667, 4.025) 0.125
	Genu (Tract)	1.432 (-1.408, 4.273) 0.272	-0.647 (-4.206, 2.912) 0.680	1.534 (-1.020, 4.088) 0.183	1.166 (-0.729, 3.062) 0.174
	Body (Tract)	1.538 (-1.889, 4.965) 0.324	-0.631 (-3.744, 2.482) 0.646	-0.015 (-4.666, 4.635) 0.994	1.450 (-0.978, 3.879) 0.185
	Splenium (Tract)	2.510 (-0.424, 5.443) 0.083	-1.392 (-3.936, 1.152) 0.237	0.336 (-4.943, 5.616) 0.876	1.184 (-0.196, 2.564) 0.079

+crossed – uncrossed difference i.e. Interhemispheric transfer time (ms); \*% TIV; <sup>#</sup>Estimates have been multiplied by 10<sup>^5</sup> for readability; \*\*( $\text{mm}^2/\text{s}$ ) $\times 10^{-3}$ ; <sup>^</sup>Regression coefficients (95%C.I.), p-value; FA = fractional anisotropy; AD = axial diffusivity; RD = radial diffusivity; Dark grey highlights the significant (p<0.05) association between imaging metrics and CUD, and the light grey highlights the borderline significant differences (p<0.06), adjusted for age, gender and education.



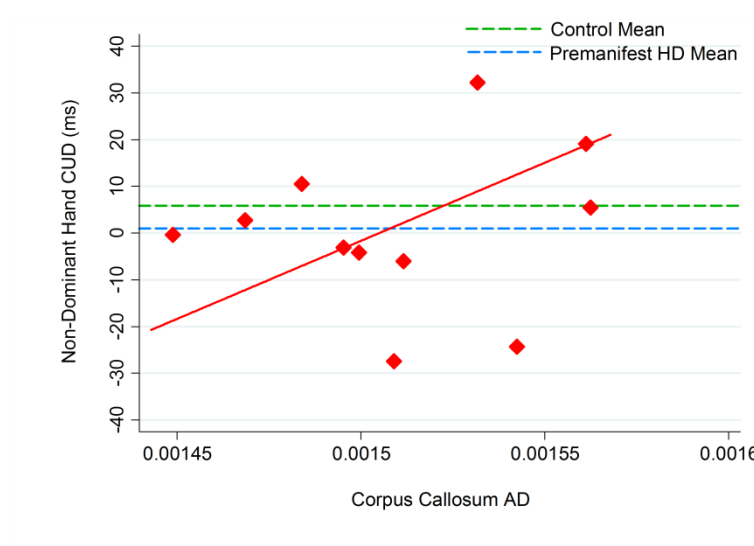


*Figure 10-6. Association between non-dominant hand CUD (ms) and AD ( $(\text{mm}^2/\text{s}) \times 10^{-3}$ ) in the CC in the premanifest HD group, with adjusted regression line (red).*

#### 10.4.5 ROI Tract-Based Spatial Statistics of the CC

##### *Between-Group Analysis*

ROI TBSS of the CC revealed no between-group differences in FA, AD or RD in any part of the CC, even at lower p-value thresholds ( $p < 0.06$ , FWE-corrected for multiple comparisons).

##### *Within-Group Analysis*

TBSS analysis found no significant positive or negative correlations between non-dominant or dominant hand CUD and diffusivity properties within the WM tracts of the CC in the control group.

Similarly, no relationship between any of the diffusion metrics in the CC skeleton and dominant hand CUD was found in the premanifest HD group. The TBSS analysis, however, did reveal an association with non-dominant hand CUD. A significant, positive correlation was found with AD in the CC splenium and a few voxels in the medial CC body ( $p < 0.05$ , FWE-corrected for multiple comparisons; see Figure 10-7). Significant cluster information at the peak voxel locations for this association is presented in Table 10-5. There was no evidence of any other associations.

**Table 10-5. Peak Voxel Information for the Correlation Between AD and Non-Dominant Hand CUD in the Premanifest HD Group**

Maximum Intensity Voxels			Voxels	p-value	CC Region
X	Y	Z			
118	77	82	67	0.020	Splenium
103	77	82	44	0.024	Splenium
118	76	76	26	0.044	Splenium

Peak voxel information for clusters > 20 voxels significant at  $p < 0.05$ . Coordinates are in DTI-TK-registered diffusion space. CC = corpus callosum.

#### 10.4.6 Association between CC Tract Diffusion and CUD

Results from the regression analysis with diffusion metrics extracted from the regional CC fibre tracts can be seen in Table 10-4. No significant findings were revealed in the control group.

Premanifest HD participants, however, were found to have a negative association between the CUD in their non-dominant hand and FA within tracts of the genu (-340.421; 95% C.I. -593.137, -87.706;  $p = 0.018$ ; see Figure 10-8); larger CUD (i.e. the bigger the difference between crossed and uncrossed RT) was associated with lower FA in the CC genu.

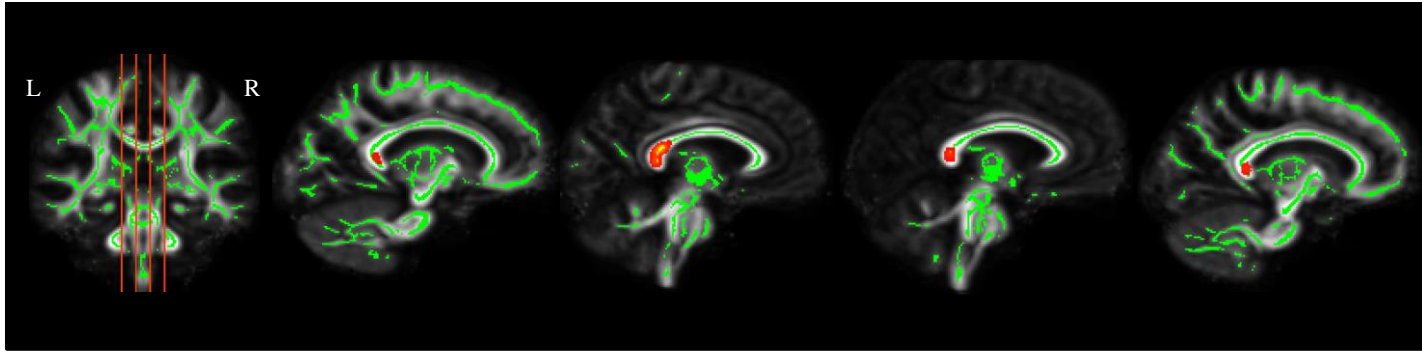


*Figure 10-7. TBSS results for the positive association between AD and non-dominant hand CUD in the premanifest HD group. Skeletonised results are overlaid on the mean FA skeleton mask (green) on the mean FA image. Red-yellow voxels are thresholded at  $p < 0.05$  (FWE-corrected).*

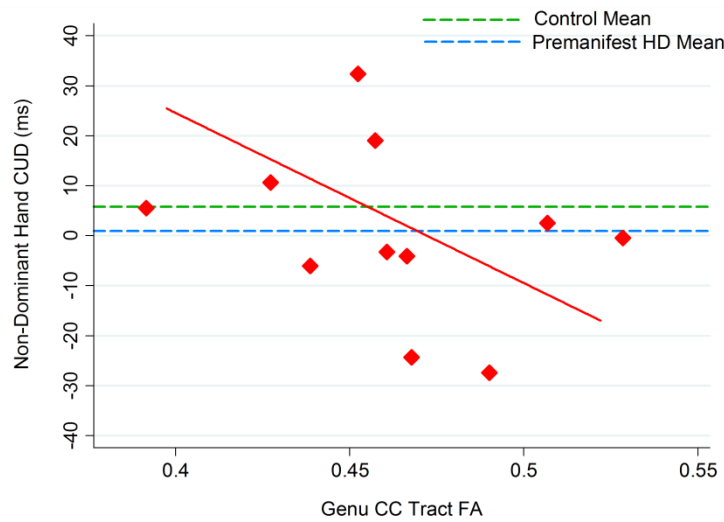


**Figure 10-8.** Association between non-dominant hand CUD (ms) and FA within the genu of the CC in the premanifest HD group with adjusted regression line (red).

In order to further investigate the significant associations found in the premanifest HD group, CC volume, and CC AD and FA in the genu were correlated with CPO using Spearman's correlation analysis. CC volume did not correlate with CPO (Spearman's  $Rho=0.046$ ;  $p=0.894$ ), nor did CC AD (Spearman's  $Rho=0.436$ ;  $p=0.180$ ). Genu FA, however, did significantly correlate with CPO (Spearman's  $Rho=-0.664$ ;  $p=0.026$ ; see Figure 10-9); lower FA in the genu was associated with closer proximity to onset.

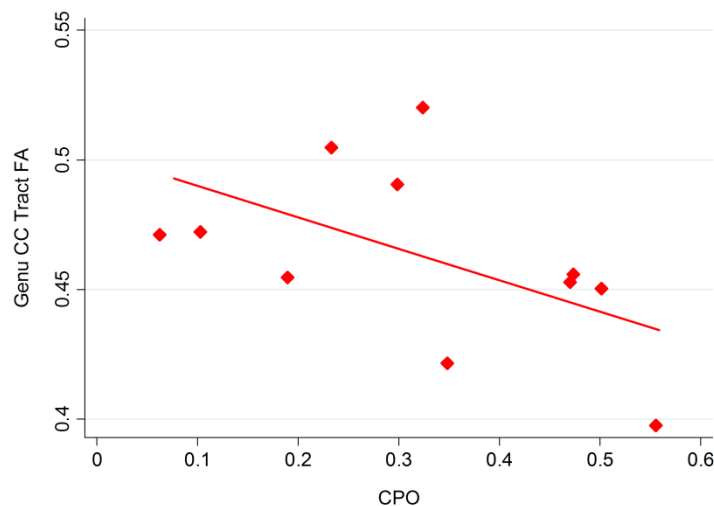


**Figure 10-9.** Association between genu tract FA and CPO in the premanifest HD group with the unadjusted fitted line (red).

#### **10.4.7 Between-Group Differences in Imaging Metrics**

The two groups did not significantly differ in CC volume (% TIV) or any of the diffusion metrics extracted from the whole CC or sub-region tracts.

#### **10.4.8 Visit Two Results**

On average, control participants had six (out of 320) trials removed (1.847%) and premanifest HD participants had seven removed (2.131%) due to anticipation or lapses in attention. This difference of -0.584 responses was not significant (95% C.I. -8.090, 6.921;  $p=0.871$ ).

Raw mean RTs and between-group differences adjusted for age, gender and education for all conditions at visit two are provided in Table 10-6. Overall, results at visit two were consistent with the findings at baseline and there was no significant within-group effect of responding hand or crossing, or any significant between-group difference in CUD or CUD asymmetry for each hand.

#### ***Within-Group Analysis Results***

The same CUD asymmetry was seen in the control participants at visit two, i.e. the CUD was slightly smaller when responding with their dominant hand than their non-dominant hand. This difference of 1.500ms, however, was not significant (95% C.I. -38.878, 35.877;  $p= 0.936$ ). Similarly, CUD asymmetry in the premanifest HD group was also in the same direction at visit two; their CUD was smaller when using their non-dominant hand. This difference of 5.743ms was also not significant (95% C.I. -36.559, 48.046;  $p= 0.788$ ).

**Table 10-6. Mean (SD) RT (ms) and Adjusted Between-Group Differences at Visit Two**

Responding Hand	Visual Field	Condition	Control	Premanifest HD	Premanifest HD vs. Control**
Non-Dominant	Non-Dominant	Uncrossed	333.727 (33.972)	350.000 (37.961)	19.797 (-10.839, 50.433) 0.202
	Dominant	Crossed	335.955 (34.287)	352.955 (34.104)	20.477 (-8.073, 49.028) 0.157
		CUD*	2.227 (10.771)	2.955 (9.234)	0.680 (-40.883, 42.243) 0.974
Dominant	Dominant	Uncrossed	331.182 (28.069)	355.000 (38.619)	27.339 (-1.342, 56.019) 0.061
	Non-Dominant	Crossed	331.773 (24.333)	363.682 (35.703)	27.721 (-21.236, 76.679) 0.263
		CUD*	0.591 (12.280)	8.682 (7.107)	7.924 (-30.274, 46.123) 0.681
		<b>Overall Uncrossed</b>	332.455 (29.363)	352.500 (36.239)	23.568 (2.272, 44.864) 0.031
		<b>Overall Crossed</b>	333.864 (27.876)	358.318 (33.452)	27.870 (8.435, 47.305) 0.006
		<b>Overall CUD*</b>	1.409 (4.545)	5.818 (4.960)	4.302 (-23.923, 32.527) 0.762

\*crossed – uncrossed difference i.e. Interhemispheric transfer time (ms); \*\* Regression Coefficient (95% C.I.) and p–value; Dark grey highlights the significant (p<0.01) between-group differences in RT and the light grey highlights the significant differences (p<0.05), adjusted for age, gender and education.

### ***Between-Group Analysis Results***

The between-group difference in the dominant and non-dominant hand CUD was slightly smaller at visit two. Similar to baseline, the largest difference was when participants were using their dominant hands, although not significantly so (7.924ms; 95% C.I. -30.274, 46.123;  $p=0.68$ ). The between-group difference in the overall CUD averaged across responding hand was larger than at baseline but still not significant (see Table 10-6).

There was a non-significant between-group difference of 7.244ms in the difference between non-dominant and dominant hand CUDs (95% C.I. -49.206, 63.694;  $p=0.799$ ). The premanifest HD group was still significantly slower than the control group in the overall crossed and overall uncrossed conditions (27.870ms; 95% C.I. 8.435, 47.305;  $p=0.006$  and 23.568ms; 95% C.I. 2.272, 44.864;  $p=0.031$  respectively).

Figure 10-10 displays the mean RTs as a function of responding hand at visit two. It demonstrates the similarity between findings at visit two and at baseline and also effectively presents the difference (non-significant) in CUD asymmetry. Although an observed difference in the data, it is not evidence of a true difference between the participant groups.

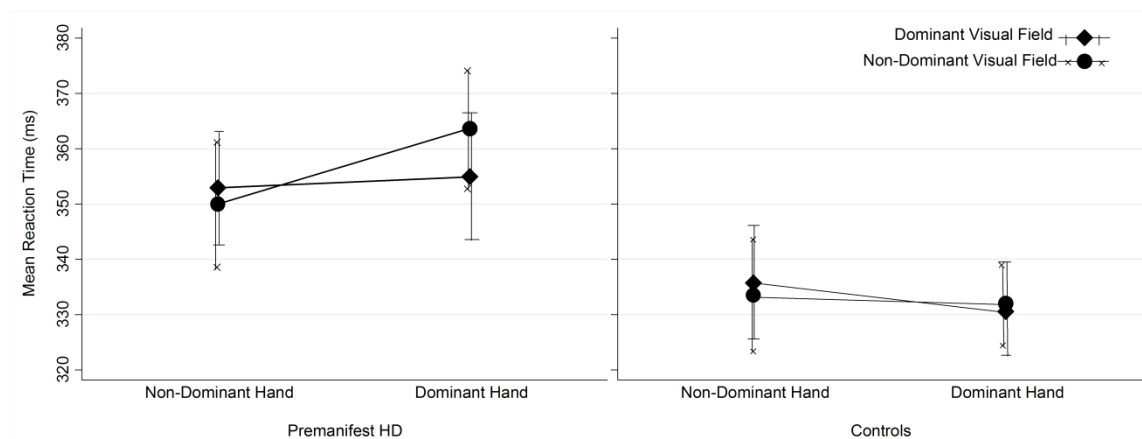


***Figure 10-10. Mean RT (ms) for the premanifest HD group (left) and control group (right) as a function of responding hand at visit two.***

#### **10.4.9 Longitudinal Results**

Mean annualised change in RTs and adjusted between-group differences in annualised change for all conditions are provided in Table 10-7.

##### ***Within-Group Analysis Results***

Within-group analysis of change for each condition is shown in Table 10-8 and the effects of responding hand and crossing on change in RTs is presented in Table 10-9.

There was no significant change in RTs from baseline to visit two for any condition in both groups (see Table 10-8). The coefficients represent annualised change whereby positive coefficients reflect a slower RT at visit two compared with baseline, and negative coefficients indicate that RTs were faster at visit two compared with baseline.

There was no significant effect of responding hand or the crossing of hand and stimulus on the change in RTs within-group (see Table 10-9). In controls, the difference in change between the non-dominant and dominant hand CUDs was not significant at 0.328ms (95% C.I. -35.655, 36.310;  $p = 0.986$ ). In the premanifest HD group the difference in change between the non-dominant and dominant hand CUDs was also not significant at 1.048ms (95% C.I. -64.596, 66.692;  $p = 0.975$ ).

##### ***Between-Group Analysis Results***

There were no significant differences in change in RTs over one year between the two groups (see Table 10-7). There was a non-significant between-group difference of 0.720ms in the change in difference between non-dominant and dominant hand CUDs (95% C.I. -74.139, 75.579;  $p = 0.985$ ).



**Table 10-7. Mean (SD) Annualised Change in RT (ms) and Adjusted Between-Group Differences in Annualised Change**

<b>Responding Hand</b>	<b>Visual Field</b>	<b>Condition</b>	<b>Control</b>	<b>Premanifest HD</b>	<b>Premanifest HD vs. Control**</b>
Non-Dominant	Non-Dominant	Uncrossed	1.298 (26.238)	-22.167 (42.797)	-26.912(-59.595, 5.771) 0.105
	Dominant	Crossed	-1.157 (30.539)	-20.321 (40.700)	-22.567 (-54.278, 9.144) 0.160
		CUD*	-2.455 (18.976)	1.846 (18.234)	4.345 (-39.460, 48.150) 0.844
Dominant	Dominant	Uncrossed	-8.611 (28.017)	-28.794 (60.865)	-23.441 (-64.408, 17.525) 0.258
	Non-Dominant	Crossed	-10.961 (26.277)	-25.896 (74.327)	-21.847 (-90.908, 47.214) 0.531
		CUD*	-2.350 (18.892)	2.898 (15.825)	5.065 (-55.639, 65.769) 0.868
		<b>Overall Uncrossed</b>	-3.657 (24.347)	-25.480 (48.875)	-25.177 (-52.339, 1.985) 0.069
		<b>Overall Crossed</b>	-6.059 (24.745)	-23.108 (56.199)	-20.472 (-49.909, 8.965) 0.170
		<b>Overall CUD*</b>	-2.402 (7.945)	2.372 (14.130)	4.705 (-32.724, 42.135) 0.803

\*crossed – uncrossed difference i.e. Interhemispheric transfer time (ms); \*\* Regression Coefficient (95% C.I.) and p–value, adjusted for age, gender and education.

**Table 10-8. Adjusted Within-Group Analysis of Change in RT (ms)**

Responding Hand	Condition	Control*	Premanifest HD*
Non-Dominant	Uncrossed	0.940 (-29.385, 31.266) 0.951	-25.972 (-66.346, 14.402) 0.204
		-1.582 (-33.242, 30.078) 0.921	-24.149 (-59.849, 11.551) 0.182
	CUD**	-2.522 (-28.743, 23.698) 0.849	1.823 (-33.268, 36.914) 0.918
Dominant	Uncrossed	-9.011 (-38.885, 20.862) 0.550	-32.453 (-76.262, 11.356) 0.144
		-11.206 (-40.468, 18.056) 0.448	-33.927 (-101.597, 33.743) 0.321
	CUD**	-2.195 (-26.837, 22.447) 0.860	2.871 (-52.607, 58.348) 0.918

\*Regression Coefficient (95% C.I.) and p-value, adjusted for age, gender and education; \*\*crossed – uncrossed difference i.e. Interhemispheric transfer time (ms).

**Table 10-9. Adjusted Within-Group Analysis of the Effects of Hand Dominance and Crossing on Annualised Change in RT (ms)**

Interactions		Control*	Premanifest HD*
Non-Dominant Hand	Uncrossed	-2.522 (-28.743, 23.698) 0.849	1.823 (-33.268, 36.914) 0.918
	vs. Crossed		
Dominant Hand	Uncrossed	-2.195 (-26.837, 22.447) 0.860	2.543 (-63.582, 68.667) 0.939
	vs. Crossed		
Uncrossed Condition	Non-Dominant	-9.952 (-35.067, 15.164) 0.433	-6.481 (-50.195, 37.233) 0.769
	vs. Dominant		
Crossed Condition	Non-Dominant	-9.624 (-35.391, 16.144) 0.459	-5.761 (-66.530, 55.008) 0.851
	vs. Dominant		

\*Regression Coefficient (95% C.I.) and p-value, adjusted for age, gender and education.

## 10.5 Discussion

Using a specially designed Poffenberger paradigm (Poffenberger 1912), this study investigated interhemispheric transfer in premanifest HD participants and healthy controls over 12 months and examined the extent to which disease-related cognitive performance was related to clinical measures and macro- and microstructural properties of the CC. This study found that premanifest HD participants' speed difference value between crossed and uncrossed conditions, the so-called CUD, which is thought to be a behavioural estimate of ITT, did not significantly differ from controls and, although, both groups were slower to react to crossed stimuli than uncrossed, there was no statistically significant effect of crossing or responding hand, or significant change in performance over time.

Overall, premanifest HD participants were significantly slower to respond than controls at both visits, and in contrast to controls, displayed a larger CUD when responding with their dominant hand, although this was not significant. Several possible explanations for the observed differences between the groups are discussed below, including specific interhemispheric disruption from the non-dominant to the dominant hemisphere. Large variance in CUDs and the lack of significant effects, however, make interpretation of the findings difficult. Despite the absence of between-group differences, there was a strong association between non-dominant hand CUD and disease-related degeneration of the CC in premanifest HD participants.

### *Interhemispheric Transfer*

The Poffenberger paradigm (Poffenberger 1912) predicts that responses take slightly longer when the responding hand is on the opposite side to the hemifield of visual stimulation, than when both responding hand and the visual stimulation are on the same side. If the responding hand and visual stimulus are on the same side (referred to as the uncrossed condition) then processing of the sensory input and initiation of motor execution are performed within the same hemisphere, whereas in the crossed condition, an interhemispheric transfer of information, from the hemisphere receiving the input to the hemisphere controlling the motor response is required (Marzi *et al.* 1991). Interhemispheric transfer via the CC, therefore, should lead to longer RT in the crossed than in the uncrossed condition, which has been reported in numerous publications

investigating interhemispheric processing in healthy participants (Chaumillon *et al.* 2014; Cherbuin & Brinkman 2006; Marzi *et al.* 1991; Pellicano *et al.* 2013; Schulte *et al.* 2013; Semprini *et al.* 2012).

This study found that both premanifest HD and control participants took slightly longer to respond in the crossed conditions than the uncrossed conditions, when using both their dominant and non-dominant hand, however this was not statistically significant. When averaged over the responding side, overall CUDs for both groups were between 3-4ms, consistent with previous studies (Cherbuin & Brinkman 2006; Corballis 2002; Semprini *et al.* 2012).

Against expectations, the overall CUD did not significantly differ between premanifest HD participants and controls, nor was there a significant difference when examining the CUDs according to responding hand. The observed difference in CUD asymmetry between the groups, i.e. control CUD was greater when responding with their non-dominant hand and premanifest CUD was greater with their dominant hand, however, was an interesting finding and raises several possible explanations.

Consistent with previous studies, the control group demonstrated an overall non-dominant visual field advantage over the dominant visual field (Chaumillon *et al.* 2014; Marzi *et al.* 1991; Pellicano *et al.* 2013; Schulte *et al.* 2013; Semprini *et al.* 2012; Tettamanti *et al.* 2002). RTs were longest in the crossed condition; dominant visual field/non-dominant hand (345.571ms), confirming evidence that interhemispheric transfer is slower from left to right hemispheres in healthy participants (Marzi *et al.* 1991), or in this case, dominant to non-dominant hemispheres. In other words, faster transfer occurred when visual stimulus was presented to the non-dominant visual field and channelled to the non-dominant hemisphere and the motor response was then initiated by the dominant hemisphere, than in the reverse direction. This phenomenon is demonstrated by a smaller CUD when responding with the right, or dominant hand, as replicated in the control group in the current study.

The premanifest HD group, however, did not demonstrate the same speed advantage of information transfer from the non-dominant to the dominant hemisphere. RTs were longest in the crossed condition; non-dominant visual field/dominant hand (386.667ms) and the CUD was greater when responding with the dominant hand than the non-

dominant hand. Similar dysfunctional inhibition processes in the left/dominant hemisphere have been demonstrated in early manifest and premanifest HD patients using event-related potentials (Beste *et al.* 2009). Premanifest participants lacked the faster RTs seen when using the dominant hand compared with controls, indicating that altered intra- and interhemispheric processes are restricted to the dominant motor system (Beste *et al.* 2009). The current findings, therefore, potentially indicate that neural mechanisms involved in converting visual inputs into motor commands when using the dominant hand are disrupted in premanifest HD.

A possible explanation for the asymmetry in CUDs in both groups is the effect of eye dominance. Eye dominance refers to the unconscious preference individuals have when performing a monocular task (Chaumillon *et al.* 2014). Among right-handed people (representing 90% of the population), 66% are believed to have a right dominant eye and 34% a left dominant eye, whereas 40% of left-handed people have a right dominant eye and 60% have a left dominant one (Bourassa *et al.* 1996). Chaumillon *et al.* (2014) found that right-handers with right eye dominance show a left visual field speed advantage, similar to that seen in the control group in the current study, whereas right-handers with left eye dominance show a right visual field advantage. In left-handers, however, RTs were only shorter with the left hand responses for individuals with right eye dominance, irrespective of the stimulated visual field. These findings, therefore, suggest that the larger CUD from dominant to non-dominant than non-dominant to dominant hemispheres seen in the controls in the current study could reflect right eye dominance, and correspondingly, the opposite pattern seen in the premanifest group could reflect left eye dominance.

Consequently, one limitation of the current study was that individuals with atypical patterns of asymmetry, i.e. left-handers, were included in the sample and may have confounded the results. There were, however, only two left-handed participants in the study and additional analyses with these individuals excluded produced very similar results to the main findings. This also suggests that the dominant/non-dominant CUD asymmetry found here can be related to the left/right CUD asymmetry described in earlier studies examining only right-handed participants (Chaumillon *et al.* 2014; Marzi *et al.* 1991; Pellicano *et al.* 2013; Semprini *et al.* 2012; Tettamanti *et al.* 2002).

An alternative explanation for the CUD asymmetry could be that increases in CUD are driven by disproportionately faster information processing in the uncrossed conditions. In other words, a longer CUD does not necessarily reflect longer interhemispheric transfer, rather, it shows that within-hemisphere processing is more efficient at the expense of between-hemisphere communication (Semprini *et al.* 2012). In the current study, therefore, it is possible that the control group have more efficient within-hemisphere processing in the non-dominant hemisphere, whereas the premanifest HD group do not. On the other hand, individuals with premanifest HD may have more efficient processing within the dominant hemisphere. Further research is required to elucidate whether it is altered intra- or interhemispheric processes, in the dominant or non-dominant hemisphere that are driving the abnormal CUD asymmetry evident in the premanifest HD group.

Findings at visit two, however, support the argument for altered interhemispheric processing in the dominant hemisphere in premanifest HD. Abnormal CUD asymmetry was much more pronounced in the premanifest HD group at visit two, demonstrated by the larger CUD in the dominant hand compared with controls, although not a statistically significant difference. CUDs using the non-dominant hand, however, were very similar in both groups. The non-dominant visual field advantage representing faster interhemispheric transfer from the non-dominant to dominant hemisphere was replicated in controls at visit two. Likewise, the dominant visual field advantage indicating disrupted interhemispheric transfer from the non-dominant to dominant hemisphere was reproduced in premanifest HD participants at visit two.

It is worth noting that although, overall, CUDs were positive, reflecting a larger RT for crossed compared with uncrossed responses, some individuals had negative CUDs, indicating uncrossed responses were larger. Negative CUDs are not uncommon (Schulte *et al.* 2013; Semprini *et al.* 2012), and often large inter-individual variability in CUDs, also seen in the present study, can cause this (Schulte *et al.* 2013). There are several other possible explanations for negative CUDs, including dominant ipsilateral control (Semprini *et al.* 2012), dichotomous laterality of motor control (Derakhshan 2006), and non-anatomical components such as arm crossing (Mooshagian *et al.* 2009), although the latter was controlled as much as possible by instructing participants to keep their non-responding hand by their side. The lack of a statistically significant between-group difference in mean CUD scores, therefore, may partly reflect the variation in individual

mean RTs. Further testing with a larger sample may reduce the potentially confounding effects of large inter-individual variability and increase the likelihood of detecting group differences.

There was no significant change in RTs or CUDs in either group over 12 months, suggesting that subtle changes in interhemispheric transfer cannot be captured with this particular task over a one year interval. It is important to emphasise that this study was an exploratory study and at the time of writing the study proposal there were no other studies that had explicitly investigated behavioural estimates of interhemispheric transfer longitudinally in a premanifest HD cohort. Although the task was not sensitive to change over 12 months, findings were consistent at baseline and visit two, suggesting that this task is reliable, however, this was not statistically tested. Further investigation with a larger time interval may be required to detect significant within-group alterations and between-group differences in change in interhemispheric processing.

### ***Clinical Correlations***

The lack of a statistically significant association between the CUDs and CPO or disease burden in the premanifest HD group indicates that either these disease-related measures are not the primary driver of interhemispheric communication, or that a relationship between these variables exists but was not able to be detected by the current analysis. CPO and disease burden are models designed to predict disease onset and disease stage, and although CPO in particular is a strong predictor of many HD phenomena before and after HD diagnosis (Langbehn *et al.* 2004), there may still be a lot of variance in disease stage and onset that is not captured by them. Caudate atrophy may have been a more accurate estimate of disease pathology in the premanifest stages of HD and has previously been used as a structural marker of disease burden (Kloppel *et al.* 2015; Novak *et al.* 2013). Future research into interhemispheric information transfer should, therefore, consider using caudate volume in the analyses. Furthermore, the large variability in CUDs, combined with the small sample may also explain why no associations between CUD and the clinical measures were found.

## ***Between-Group Differences and Disease-Related Associations with Imaging Measures***

There was no significant between-group difference in CC volume (adjusted for TIV) or any of the diffusion metrics extracted from the whole CC or sub-region tracts. This is in contrast to previous research that has found both reduced CC volume (Crawford *et al.* 2013; chapter 7) and microstructural CC abnormalities in premanifest HD participants compared with controls (Di Paola *et al.* 2014; Dumas *et al.* 2012; Novak *et al.* 2013; Phillips *et al.* 2013). The current study, however, is much smaller in size than these previous studies, which may explain this discrepancy. Additionally, it may be that microstructural abnormalities within callosal tracts are not sufficient in these premanifest participants to detect between-group differences with the current technique. A larger sample, closer to disease onset may prove more sensitive to between-group differences in diffusion magnitude within the CC.

A recent study demonstrated that partial volume effects near the CC can alter diffusion MR indices in HD using both ROI and tractography analysis (Steventon *et al.* 2015). Free water contamination was found to suppress FA values and inflate MD values, whilst also increasing within-group variance changing the statistical outcome and interpretation of HD-related changes (Steventon *et al.* 2015). It is possible, therefore, that partial volume effects in the current study may have had the same effect and in premanifest individuals, who exhibit more subtle pathology, it was more difficult to detect group differences. In order to minimise these potential volume effects, the ventricles could have been masked out. Additionally, the application of a tractography algorithm capable of resolving multiple fibre orientations, e.g. spherical deconvolution, may have produced a more complete reconstruction of the CC (Steventon *et al.* 2015), improving the anatomical validity of the results and increasing the sensitivity to detect group differences.

Despite no significant group difference in the metrics, there were, however, significant associations between the CUD when responding with the non-dominant hand and various CC metrics in the premanifest HD group. A significant, negative relationship between non-dominant hand CUD and CC volume was found, as well as a trend towards the same relationship with dominant hand CUD. The latter correlation indicates that smaller CC volume is associated with a larger dominant hand CUD, indicating



interhemispheric speed is less like the control group with reduced CC size. This is consistent with the behavioural results demonstrating longer interhemispheric transfer from the non-dominant to dominant hemisphere, in opposition to the control group who showed facilitated transfer in this direction. It is also in line with previous studies that have found reduced CC size to be related to longer interhemispheric transfer, albeit in MS patients (Brown *et al.* 2010).

The negative association between non-dominant hand CUD and CC volume, however, is more difficult to explain and suggests that a larger CUD, which when responding with the non-dominant hand is more like that seen in the controls, is actually associated with smaller CC volume. When viewing the scatter plot (Figure 10-5), it is clear that there is large variation in non-dominant CUD values, ranging from -25.5ms to 36ms. The individual with the highest CUD (36ms) has the smallest CC volume. However the CUD value is much higher than that of the controls (mean=5.821ms; SD =17.542ms), likewise the individual with the largest CC volume has a CUD value closer to that of the control mean (-2ms). The participant with a CUD value closest to the control mean (8.5ms), also has an average CC size. One possible explanation is that participants with similar CUD scores to the controls, or smaller CUD scores, tend to have larger CC volume. However, it is only once CC atrophy becomes more pronounced that the CUD becomes very large, indicating a prolonged interhemispheric transfer, greater than normal values when using the non-dominant hand.

Without further investigation in a larger sample it is not possible to confirm the above explanation, or know exactly what it is about these individuals that causes their negative CUD. Equally, it is not possible to know what particular changes in CC microarchitecture are causing the decreases in volume, i.e. a loss in the number or size of WM axons, or which of these changes may be driving the volume reduction associated with ITT.

Evidence of a link between CC pathology and non-dominant hand CUD was also identified using ROI analysis of the whole CC. Increased AD within the CC was found to be significantly associated with larger non-dominant hand CUD. Although this relationship with CUD in premanifest HD has not been reported before, increased AD is analogous to results from previous studies which found increased ADC and MD in the CC (Dumas *et al.* 2012; Novak *et al.* 2013) in premanifest HD and increases in AD in

early manifest patients (Phillips *et al.* 2013). Results from the TBSS analysis provide evidence to confirm the result and localised the association with CUD to tracts within the splenium and posterior CC body. This finding is consistent with a previous study that showed ITT to be directly related to microstructural integrity of the posterior CC evidenced by increased MD (Westerhausen *et al.* 2006), as well as reports of reduced FA in the isthmus in premanifest HD compared with controls (Di Paola *et al.* 2014). No such association between AD and CUD was evident in the control group, suggesting that this relationship is disease-specific.

Similar to the negative association with CC volume, the positive association between AD and non-dominant CUD is difficult to interpret. Turning to the scatter plots again (Figure 10-5 and Figure 10-6), the same individual with the largest CC volume and CUD value close to the control mean was found to have the lowest AD, however, the individual with the CUD value closest to the control mean has the highest AD value. It is possible that, like above, participants with similar CUD scores to the controls, or smaller CUD scores, tend to have lower AD and it is only once AD increases more substantially that the CUD becomes very large, indicating prolonged interhemispheric transfer. Once more, it is not possible to confirm this assumption and further analysis with more participants is needed to identify the true pattern of results.

Further investigation of diffusion properties within callosal tracts of CC sub-regions using tractography revealed that FA in anterior tracts was negatively associated with increasing non-dominant hand CUD. This is also consistent with previous studies that demonstrated a similar relationship between lower FA in the genu and longer interhemispheric transfer time in healthy adults (Schulte *et al.* 2005; 2013), and is understandable given the known degeneration of prefrontal cortices in HD with which the anterior CC tracts connect (Aylward *et al.* 2011; Tabrizi *et al.* 2009). Reduced FA in the anterior CC in premanifest HD participants has also previously been reported (Di Paola *et al.* 2014; Rosas *et al.* 2010).

Additional analysis of the significant associations found in the premanifest HD group revealed a significant, negative correlation between FA in the genu and CPO, indicating that microstructural integrity of the anterior CC tracts decreases with disease proximity. It is important to remember, however, that FA is an indirect measure of axonal integrity and only represents the degree of anisotropy in the principal diffusion direction.

Individual examination of the data points seen in Figure 10-8 and Figure 10-9 has found that individuals closest to disease onset tend to have lower FA, and are the same individuals with smaller CC volume and higher AD. The previous argument, therefore, could also be applied here, postulating that participants with similar CUD scores to the controls, or smaller CUD scores tend to have higher FA and it is only once FA decreases more substantially (in those individuals closer to onset) that the CUD becomes very large, indicating prolonged interhemispheric transfer. However, a few participants conflict with this interpretation, such as the individual with low FA and a non-dominant CUD score close to the control mean, therefore, more research is required to elucidate this.

The link between CC pathology in anterior and posterior tracts and non-dominant hand CUD, although not fully understood was consistently found and supported by the negative correlation between FA in the genu and CPO. This finding reveals that disease-related alterations in the CUD estimate of interhemispheric transfer is related to degradation of both posterior and anterior callosal fibres, connecting to visual and prefrontal regions respectively. These tracts show abnormal structural connectivity in premanifest HD and correlate with motor and visual impairments (Phillips *et al.* 2013), which highlights the important functional role of these tracts in HD.

No association was found between CUD for either responding hand and RD within any of the CC regions or tracts, suggesting that pathological changes in diffusion perpendicular to the main callosal fibres may not be pronounced enough to detect a relationship with ITT in these premanifest participants. Changes in AD have been purported to reflect axonal injury or degeneration, whilst changes in RD possibly reflect demyelination (Song *et al.* 2002; 2003). It is possible, therefore, that the integrity of the axons is changing, reflected by increasing AD in the CC, but demyelination is relatively unchanged, reflected by the absence of an association with RD.

It is possible that the correlation analysis described above has identified a disease-related process not apparent in the behavioural results; variation in interhemispheric transfer from the dominant to the non-dominant hemisphere is associated with changes in CC volume and microstructure. Without histological analysis it is impossible to be certain which changes in callosal microarchitecture are the underlying cause of the observed associations. The current findings do, however, suggest that altered

microstructural properties of the CC are directly associated with interhemispheric transfer and, in the absence of the same associations in the control group, imply that these relationships are disease-specific and may contribute to the cognitive phenotype in premanifest HD.

### ***Strengths and Limitations***

One of this study's main strengths is the well characterised cohort of premanifest and healthy control participants and the good retention rate over one year. Task administration is another key strength; it was administered by the same individual for every participant and for every visit, ensuring the standardisation of key factors such as instruction delivery and monitoring. The task was also always completed using the same equipment, however not always in the same testing room. Due to room relocation at visit two, some participants were tested in a different room from baseline, however conditions were replicated as much as possible by ensuring participants sat the same distance from the laptop and the room was dimly lit.

The choice of paradigm is also one of this study's strengths. The Poffenberger paradigm (Poffenberger 1912), also known as the divided visual field paradigm (Bourne 2006) has been used to examine a variety of lateralised processes and has been frequently utilised to assess interhemispheric transfer, as outlined above. When conducting the task, however, it is very important to employ strict controls to ensure the effectiveness of the paradigm (Bourne 2006). Where possible, these controls were implemented, including using a central fixation point to control participants' gaze. There were a few controls, however, that were not in place. A backward visual mask was not displayed immediately following stimulus presentation, therefore participants may have experienced afterimage effects. Participants' head position was also not strictly controlled, therefore, the visual angle of presentation may have not been maintained. Future administration of this task would need to ensure that these controls were followed.

The small sample size is also a substantial limitation. There were several factors that could not be controlled for at the time of recruitment, including, many of the potential participants from the Track-HD and TrackOn-HD studies had progressed from premanifest to manifest disease status, therefore no longer met the inclusion criteria for

the current study, plus several participants had been recruited into clinical drug trials and again, this compromised the inclusion criteria. Further research with a larger study is required to fully explore the current findings and increase the power with which to detect the potentially significant interhemispheric deficits in premanifest HD.

Sample size calculations were carefully conducted for this study (please see Appendix 2: Sample Size Calculations: Interhemispheric Transfer Task). It is important to emphasise that this study was a pilot study and at the time of writing the study proposal there were no other studies that had investigated this task in a HD cohort. Previous studies had looked at this task in other populations, plus many different cognitive tasks have been investigated in HD. Therefore inferences were drawn from the evidence available using similar tasks but in different cohorts, and in a similar cohort but with different tasks. Despite the fact that the sample recruited was smaller than the estimated calculations, there were many repetitions per experimental condition which was thought to hopefully counterbalance this.

Finally, it is important to note that many hypotheses were tested in the analyses but no correction was made for multiple testing due to the small sample and exploratory nature of the study. The results from the current study, therefore, should be considered exploratory and informative for the design of larger studies in the future.

## **10.6 Conclusion**

Using a specially designed interhemispheric transfer task, this study found no significant difference in ITT between premanifest HD participants and healthy controls, or any significant change in ITT over 12 months. The premanifest HD group, however, showed consistently slower RTs for both crossed and uncrossed conditions, as well as opposite CUD asymmetry to the control group, indicating abnormal interhemispheric transfer from the non-dominant to dominant hemisphere. Non-dominant CUD was also associated with macro- and microstructural properties of the CC, although further analysis is required to ascertain the underlying causes of impaired ITT and to better elucidate the link between CC structure and function. This was an exploratory study and further research with a larger cohort over a longer time interval may help explain the current findings.

## 11. Susceptibility to Interference in Premanifest HD

### 11.1 Introduction

There is much variability in both the cognitive domain affected and the detection of deficits in individuals with less pathology (Papp *et al.* 2011), resulting in inconsistent evidence of cognitive dysfunction in the premanifest stages of HD. Cognitive tests, therefore, not only need to target specific cognitive abilities, but also the underlying structure-functional relationships in order to increase their sensitivity.

One cognitive domain that has, however, consistently been found to be sensitive in premanifest HD is psychomotor speed (Stout *et al.* 2011; Unmack Larsen *et al.* 2015; Verny *et al.* 2007). Premanifest HD participants have demonstrated significant impairment compared with healthy controls on interference tasks, such as the Eriksen flanker (Beste *et al.* 2008a; see chapter 6) and Stroop interference test (Beste *et al.* 2012), as well as tasks involving making attentional shifts and inhibiting inappropriate responses (Beste *et al.* 2012; Georgiou *et al.* 1995; Unmack Larsen *et al.* 2015).

Anatomically, susceptibility to interference in people with HD may be explained by disruption in basal ganglia connectivity. The striatum, the most severely affected structure in HD, forms the centre of the cortico-striatal-thalamic loop, receiving input from the thalamus and cerebral cortex which is then modulated and fed back to the cortex via a complex network of connections with other regions, including the substantia nigra and globus pallidus (Papoutsis *et al.* 2014). Input and output between the striatum and cerebral cortex is topographically organised (e.g., dorsolateral prefrontal cortex, motor cortex), and influences cognitive function and sensory and motor control (DeLong & Wichmann 2007; Mazzoni & Wexler 2009).

Degeneration of the striatum and cortico-striatal network has recently been shown in premanifest and manifest HD patients (Marrakchi-Kacem *et al.* 2013; Novak *et al.* 2015). Differential patterns of basal ganglia-cortical structural connectivity were associated with SDMT score and Stroop word-reading score in the early manifest group, suggesting that altered structural connectivity directly contributes to clinical phenotype. Compromised performance on inhibition and interference tasks may, therefore, be due

to striatal degeneration in HD and/or erroneous distribution of signals from divergent brain areas affecting implicit and explicit control (Mazzoni & Wexler 2009).

Beste *et al.* (2012) investigated the fronto-striatal circuitry in premanifest HD using a Stroop interference task. Response times were longer in the premanifest HD group compared with the controls and were associated with the ACC–basal ganglia networks. Increased activation measured using fMRI in anterior cingulate–frontal–motor–parietal cortex has also been demonstrated in both premanifest and manifest HD patients during inhibitory attentional control tasks (Georgiou-Karistianis *et al.* 2007; Gray *et al.* 2013).

Having successfully developed an interference task (see chapter 6), the aim of the current study was to investigate cross-sectional and longitudinal group differences in susceptibility to interference in a group of premanifest HD participants and healthy controls, and hypothesis-driven associations with clinically relevant variables and imaging metrics of interest. Specifically, tract and ROI analysis of T1- and diffusion-weighted MRI data was used to investigate the associations between cognitive impairment measured using the interference task and:

1. Caudate volume - Atrophy of the caudate has been shown in premanifest individuals many years before disease onset (Tabrizi *et al.* 2009) and is implicated in dysfunctional fronto-striatal circuitry during interference tasks (Beste *et al.* 2012). Caudate volume has also been used as a structural measure of disease burden (Novak *et al.* 2013).
2. Microstructural properties of the ACC and caudate and thalamic connections to the dorsolateral-prefrontal cortex (DLPFC) – Microstructural degeneration of these WM tracts is apparent in premanifest HD (Dumas *et al.* 2012; Matsui *et al.* 2015), and these tracts have been shown to be associated with conflict and interference tasks (Beste *et al.* 2012; Georgiou-Karistianis *et al.* 2007; Gray *et al.* 2013).

## **11.2 Aims**

This study aimed to investigate susceptibility to interference in premanifest HD participants compared with healthy controls using a specially developed interference task. This study also aimed to assess whether there was a disease-related association between cognitive performance and *a priori* selected imaging and clinical measures, as well as examine change in cognitive performance over one year.

It was predicted that interference effects would be greater in premanifest HD participants compared with controls and would be associated with caudate volume and microstructural properties of specific WM tracts.

## **11.3 Methods**

### **11.3.1 Participants**

The same 26 participants that participated in the interhemispheric transfer task were recruited at baseline, details of which have been provided in chapter 10. The same inclusion and exclusion criteria applied. The table of demographic and clinical characteristics has been included again for easier reference (Table 11-1).



**Table 11-1. Demographic and Clinical Characteristics of Participants**

	<b>Control</b>	<b>Premanifest HD</b>
<b>N (26)</b>	14	12
<b>Age, years*</b>	46.66 (10.64)	45.65 (9.03)
<b>Gender F/M</b>	11/3	7/5
<b>ISCED**</b>	4.29 (0.73)	4.83 (0.58)
<b>Handedness R/L</b>	13/1	11/1
<b>CAG repeat length**</b>	-	42.83 (1.80)
<b>Disease-Burden Score*±</b>	-	323.11 (47.31)
<b>Total Motor Score</b>	0.29 (0.73)	6.67 (4.33)
<b>CPO</b>	-	0.30 (0.17)

Values are represented as mean (standard deviation), except gender where the numbers are of females/males; \*At time of baseline testing; \*\*As measured during TrackOn-HD baseline; ±Disease-Burden Score = (CAG length – 35.5) x age (Penney *et al.* 1997); <sup>Δ</sup> As measured during TrackOn-HD visit three; ISCED = International Standard Classification of Education; CPO = Cumulative Probability to Onset (Langbehn *et al.* 2004).

The same 22 participants that completed the interhemispheric transfer task at visit two also completed the follow-up for the current task (details provided in chapter 10). All participants provided written informed consent before participation at both time points. Ethical approval was gained for the study from the Queen Square Research Ethics Committee (REC number: 14/LO/0588).

### **11.3.2 Task Administration**

A full description of how the task was developed and piloted is given in chapter 6. To briefly summarise, the task involved participants responding as quickly as possible to the direction of a centrally presented arrow (target), whilst ignoring the direction of surrounding arrows (flankers). Participants used their right hand to respond to left and right arrows with the left and right mouse buttons, whilst for upwards and downwards facing arrows the left and right mouse buttons were randomly assigned. It was hypothesised that by including conditions that varied in difficulty, e.g. the memory

component to arrows facing upwards and downwards, it would increase the cognitive load and might prove more sensitive to between-group differences.

There were two main conditions: congruent (all arrows in the same direction) and incongruent (flanking arrows in opposite direction to the central target arrow). There were therefore eight conditions in total incorporating both left/right and up/down congruent and incongruent trials. Table 11-2 presents each arrow combination for all of the conditions.

Participants were positioned at arms-length from the computer screen and were instructed to wear their glasses or contact lenses if necessary. This task and the interhemispheric transfer task (see chapter 10) were administered one after another, in a counterbalanced order. Full written and oral instructions were given to participants before beginning the task. Participants completed a practice experiment first which included all eight of the conditions in order to familiarise themselves with the task.

The task was completed on a laptop in a dimly lit room and lasted approximately 20 minutes. Administration of the task was the same at visit two.

**Table 11-2. Task Conditions**

Condition	Congruency	Arrow direction
1	Congruent	<<<<<
2	Congruent	>>>>>
3	Congruent	^^^
4	Congruent	vvv
5	Incongruent	<<><<
6	Incongruent	>><>>
7	Incongruent	^^v^^
8	Incongruent	v^v^v

### 11.3.3 Behavioural Data Analysis

All statistical analyses were performed using STATA (StataCorp LP). Each participant's mean RT was calculated by firstly, excluding responses that were due to anticipation (<150ms) or lapses in attention (>1500ms) and secondly, excluding incorrect responses. The median was then calculated in each individual condition and used in the RT analysis. The number of errors for each condition was also obtained and used in the error analysis.

The between-group difference in number of responses was assessed using linear regression with robust estimate of variance, whilst controlling for gender, age and education (measured using the ISCED). The variables age and education were centred around their respective means in order to help balance any difference in these variables. This allows the estimation of the number of responses in each group at the average age and education level, without affecting any of the between-group estimates.

For each participant and visit the average of the congruent conditions and incongruent conditions was calculated and subtracted from one another to find the time difference (ms), also referred to as the interference or congruency effect.

#### *Cross-Sectional Analysis*

A linear regression model examined the effects of condition (congruent or incongruent), direction (left/right or up/down) and group (control or premanifest HD) on RTs. Robust estimate of variance was used to help control for the effects of outliers and differing variance between the groups. All regression models controlled for age and gender. RTs were weighted in the regression model by the number of correct responses used to calculate the mean described above. This was to limit the effects of unequal responses between participants and groups. In order to be consistent with the Track-HD study (Tabrizi *et al.* 2009) education (measured using the ISCED) was also controlled for. The variables age and education were centred around their respective means in order to help balance any difference in these variables, and allow the estimation of experimental effects at the average level without affecting any of the between-group estimates.

A second regression analysis using the same model as above examined the within- and between-group effects of congruence and arrow direction on the number of errors. The

same cross-sectional regressions with RT and accuracy results as above were carried out on the data collected at visit two with participants' age and number of responses adjusted accordingly. This was to help ascertain the consistency of the task over time. Due to the exploratory nature of this study, p-value thresholds ( $p < 0.05$ ) were not adjusted for multiple comparisons in any of the regression analyses.

### ***Longitudinal analysis***

In order to analyse any possible change in results over one year a linear regression model was used to test for within- and between-group change in RTs, whilst taking into account the time interval between visits and the number of responses.

Firstly, the annual change in RTs was calculated for each participant by subtracting the baseline RT (V1) from the visit two RT (V2), and then multiplying this by 365.25 divided by the actual time interval between visits:  $(V2 - V1) \times 365.25 / \text{interval}$ . Secondly, the number of responses at baseline and the number of responses at visit two were averaged for each participant in order to control for number responses at both time points within the longitudinal analysis.

The same statistical model that was used in the cross-sectional analysis was used here, however the outcome variable of RT was altered to the change value and the number of responses were adjusted as mentioned above (and included in the model using weighted means). Similar to the cross-sectional regression model, mean-centred baseline age and education were included as covariates, as was gender. Due to the exploratory nature of this study, p-value thresholds ( $p < 0.05$ ) were not adjusted for multiple comparisons.

#### **11.3.4 Clinical Correlations**

Spearman's correlation analysis was used in order to assess the relationship between the interference effect and disease status in the premanifest HD participants. The interference effect for left and right targets as well as up and down targets were analysed with disease burden and CPO.

### 11.3.5 Image Analysis

The structural and diffusion imaging data were processed according to the steps outlined in chapter 10.

In addition to the analyses of the association between task variables and imaging metrics outlined below, a between-group comparison of all imaging metrics (caudate volume, and FA, AD and RD of the ACC, DLPFC to caudate and DLPFC to thalamus tracts) was conducted to examine differences unrelated to the task. Linear regression models were used whilst covarying for age and gender.

### 11.3.6 Caudate Volume Analysis

Linear regression models examined the association between left/right and up/down interference effects and caudate volumes. Caudate volumes were acquired using FreeSurfer (version 5.3.0) - an open source software suite for processing and analysing brain MRI images, available freely at <http://surfer.nmr.mgh.harvard.edu/>. It provides an automated pipeline for the segmentation and analysis of cortical thickness (as well as cortical curvature and volume) and numerous subcortical volumes (Fischl & Dale 2000; Fischl *et al.* 2004a).

To output caudate volume, FreeSurfer generates subcortical regions and labels them in several stages (Fischl *et al.* 2002; Fischl *et al.* 2004b). T1 scans firstly undergo skull stripping using a deformable template model (Segonne *et al.* 2004) in order to create a mask of the brain in which the region labelling is performed. This is followed by an affine registration to MNI305 standard space (Mazziotta *et al.* 1995) and initial volumetric labelling. The images are then bias corrected (Sled *et al.* 1998) and aligned to the MNI305 atlas using a high dimensional nonlinear volumetric registration. The final segmentations are based upon a probabilistic atlas from a training dataset, as well as participant-specific measured values. The region labels are mapped into the common MNI305 space to achieve accurate voxel-to-voxel correspondence for all participants. Left and right caudate volumes were output, summed and divided by 1000 to give a total volume measurement in millilitres.

Caudate volume was adjusted for TIV in order to account for variation in head size. TIV was calculated using the GM, WM and CSF segmentations acquired in SPM (described

in section 2.3.1: Statistical Parametric Mapping). The covariates age, education (both mean-centred) and gender were included in the model. The time interval between scanning and cognitive testing (mean=196.24, SD=102.583 days) was also controlled for.

### **11.3.7 Tractography Analysis**

Tractography of the ACC, DLPFC to caudate and DLPFC to thalamus was performed in the left and right hemisphere in order to examine if diffusion properties within these tracts were associated with the interference RTs. The processing steps were the same as described in the interhemispheric task (chapter 10) but with different ROIs and exclusion masks.

The ACC, DLPFC, caudate and thalamus (prefrontal) regions (left and right) were acquired from SPM's Anatomy Toolbox. Each one was warped to T1 space for each individual using SPM's *Apply Deformation* tool (see Figure 11-1 for an example of the ROIs). Exclusion masks to prevent wayward fibre tracking were created in standard space using the MNI template (Mazziotta *et al.* 1995) and then similarly warped to T1 space with SPM. Midbrain and hemisphere exclusion masks were used for the ACC, DLPFC-thalamus and DLPFC-caudate tracts, but the latter also had a thalamic mask to prevent wayward fibres tracking through the thalamus (see Figure 11-2). This was drawn manually in FSL and flipped to the alternate hemisphere using *fsxswapdim*.

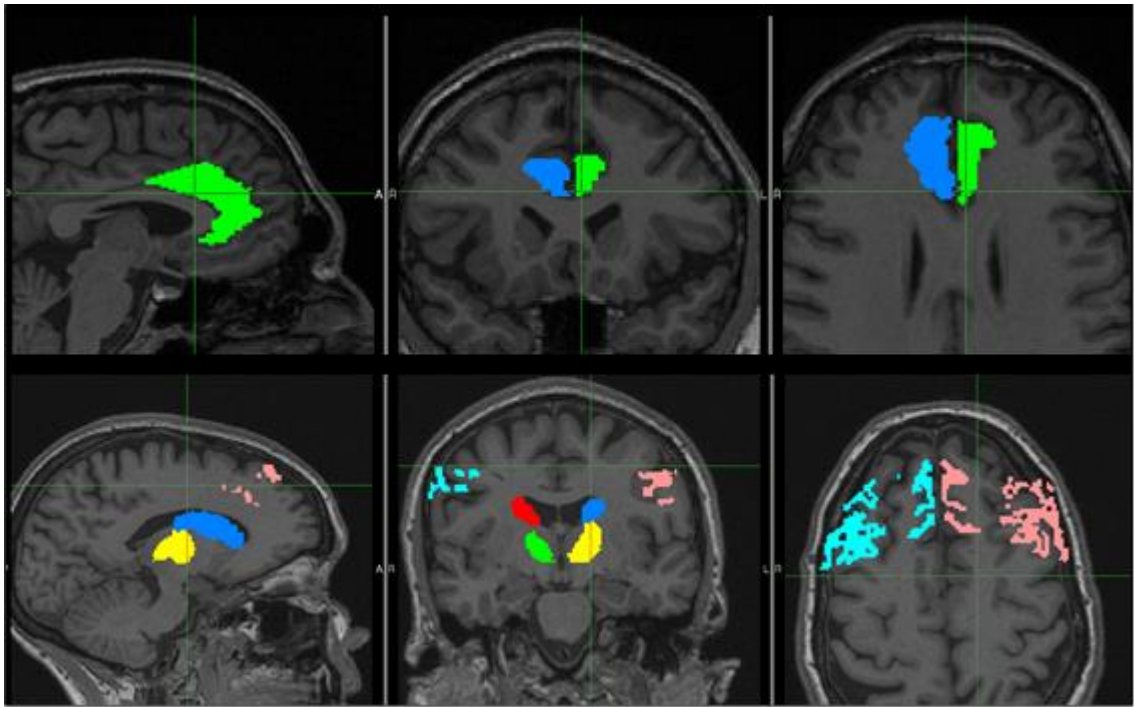


*Figure 11-1. Top row: Left ACC (green) and right ACC (blue). Bottom row: Left DLPFC (pink), right DLPFC (light blue), left caudate (dark blue), right caudate (red), left prefrontal thalamus (yellow) and right prefrontal thalamus (green). All regions are overlaid on an individual T1-weighted image.*

On visual inspection of the ACC tracts, wayward fibres were found to be tracking round the ACC laterally, mainly in the right hemisphere, therefore an exclusion ROI was also placed inferiorly and laterally to the ACC to prevent this (see Figure 11-2). A WM termination mask was also used to ensure tracts did not extend beyond the WM into GM, CSF or dura. All regions and masks were visually inspected to check if their warped location was sensible by overlaying them onto each participant's T1 image.

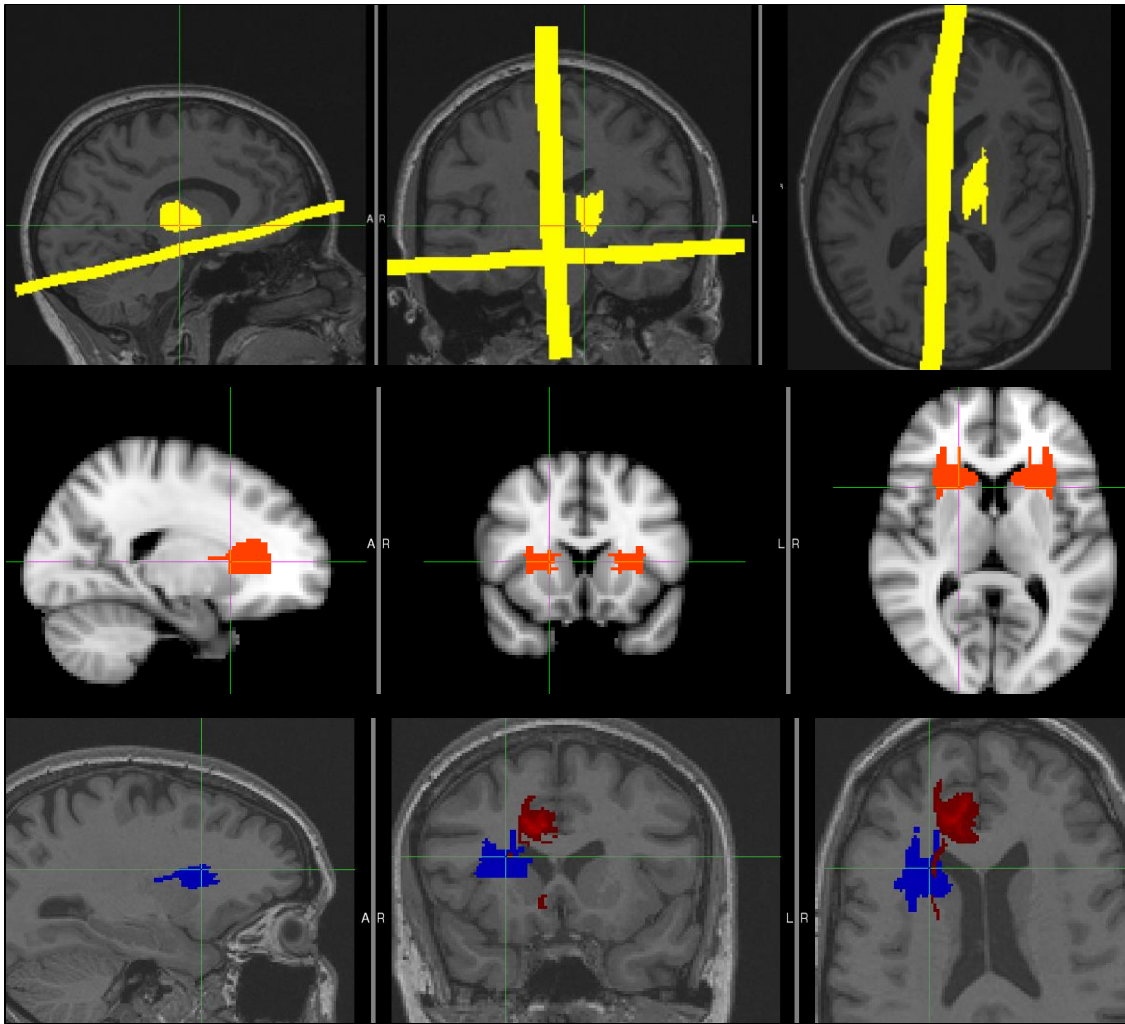


*Figure 11-2. Top row: Midbrain, hemisphere and thalamic exclusion masks for tracts within the left hemisphere (yellow). Middle row: exclusion masks for ACC fibre tracking overlaid on the MNI brain. Bottom row: Example of wayward fibres from the right ACC (red) and the placement of the exclusion mask (blue) to prevent it.*

Tractography was performed in FSL using the probabilistic tractography tool PROBTRACKX2 and run using the Legion cluster (UCL Legion High Performance Computing facility). The same steps outlined in section 2.3.2: Output Diffusion Metrics were also used here to output FA, AD and RD metrics for each tract. Linear regression models then analysed the association with interference effects for each arrow direction and each group. Covariates were the same as those stated above. Due to the exploratory nature of this study, p-value thresholds ( $p < 0.05$ ) were not adjusted for multiple comparisons.



## 11.4 Results

### 11.4.1 Baseline Results

On average, control participants had five out of 416 trials removed (1.305%) and premanifest HD participants had 15 trials removed (3.646%) due to anticipation or lapses in attention. This was not a significant difference (coefficient 9.800; 95% C.I. -2.915, 22.514;  $p=0.124$ ). Premanifest HD participants also had on average three more errors (95% C.I. -3.733, 9.025;  $p=0.398$ ; between-group differences in errors are discussed in more detail below) overall compared with controls, meaning that in total (after adjustments for gender, age and education), premanifest HD participants had on average 12 less responses (95% C.I. -30.756, 5.865;  $p=0.172$ ) compared with controls.

Raw mean RTs and adjusted between-group differences (adjusted for age, gender and education) for all conditions are provided in Figure 11-3, Table 11-3 and Table 11-4. Overall, when the arrows were facing left and right both the control and premanifest HD groups were slower in the incongruent trials compared with the congruent ones, which was significant for the controls (57.356ms; 95% C.I. 15.256, 99.456;  $p=0.008$ ) and bordering on significance in the premanifest group (52.106ms; 95% C.I. -1.222, 105.433;  $p=0.055$ ), successfully demonstrating the phenomenon of the interference effect (see Table 11-5 for within-group RT regression results). There was no significant difference between congruent and incongruent trials in controls or premanifest participants, when the arrows were facing up and down ( $p=0.394$  and  $p=0.190$  respectively).

Both groups demonstrated a larger interference effect for the left and right facing arrows compared with the up and down arrows, although not reaching statistical significance. In controls, the difference between the two was -31.337ms (95% C.I. -104.866, 42.193;  $p=0.400$ ), meaning that the control participants' interference RT was 31.34ms longer when the target arrows were facing left and right compared with up and down. However the difference between directions was much smaller for the premanifest HD group, whose interference RT was only 10.11ms longer when the target arrows were facing left and right (95% C.I. -108.096, 87.877;  $p=0.838$ ). In other words, the interference RTs for left/right and up/down arrows were more similar in the premanifest group compared with the control group. The between-group difference in this difference between the two

interference effects, however, was not significant (21.227ms; 95% C.I. -101.280, 143.734;  $p=0.732$ ), and although an observed difference in the data, it is not evidence of a true difference between the participant groups.

The premanifest HD group were slower at responding than controls in all conditions, which reached statistical significance when the arrows were facing left and right and were congruent in nature (54.892ms; 95% C.I. 7.075, 102.708;  $p=0.025$ ), and also when congruent and incongruent conditions were averaged over direction (54.352ms; 95% C.I. 7.191, 101.512;  $p=0.024$  and 59.715ms; 95% C.I. 8.739, 110.691;  $p=0.022$  respectively; Table 11-3).

Regarding accuracy, there was a significant effect of arrow direction. Both groups made more errors when the arrows were pointing up/down versus left/right (see Table 11-5). Overall, the premanifest group made more errors than the control group, however, the difference was not significant (Table 11-4) and there was also no significant effect of congruency (Table 11-5).

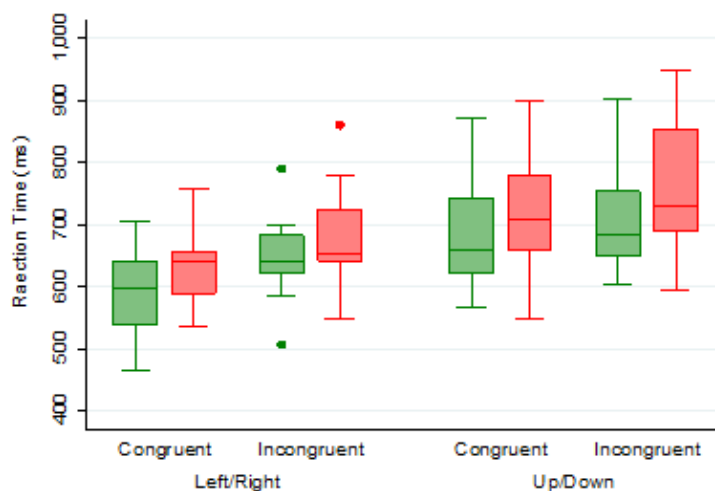


**Figure 11-3.** Box plot of median RTs (ms) for the control group (green) and the premanifest HD group (red) at baseline.

**Table 11-3. Mean (SD) RT (ms) and Adjusted Between-Group Differences at Baseline**

<b>Direction</b>	<b>Condition</b>	<b>Control</b>	<b>Premanifest HD</b>	<b>Premanifest HD vs. Control*</b>
Left/Right	Congruent	588.964 (64.731)	630.083 (62.166)	54.892 (7.075, 102.708) 0.025
	Incongruent	646.429 (66.359)	682.875 (80.625)	49.641 (-6.556222, 105.838) 0.083
	Difference^	57.464 (27.403)	52.792 (30.918)	-5.250 (-73.194, 62.693) 0.878
Up/Down	Congruent	682.321 (87.421)	722.083 (96.257)	53.812 (-21.113, 128.737) 0.157
	Incongruent	708.321 (82.254)	765.833 (110.112)	70.868 (-41.659, 183.396) 0.214
	Difference^	26.000 (22.068)	43.750 (56.758)	15.977 (-85.963, 117.916) 0.756
<b>Overall</b>	<b>Congruent</b>	635.643 (72.687)	676.083 (76.532)	54.352 (7.191, 101.512) 0.024
	<b>Incongruent</b>	677.375 (69.921)	724.354 (91.665)	59.715 (8.739, 110.691) 0.022
	<b>Difference^</b>	41.732 (19.691)	48.271 (32.935)	5.363 (-55.890, 66.617) 0.862

\*Regression Coefficient (95% C.I.) and p-value; ^also known as the interference effect; Dark grey highlights the significant (p<0.05) between-group differences in RT, adjusted for age, gender and education.

Table 11-4. Mean (SD) Number of Errors and Adjusted Between-Group Differences at Baseline

Direction	Condition	Control	Premanifest HD	Premanifest HD vs. Control*
Left/Right	Congruent	0.286 (1.069)	0.500 (0.905)	-0.059 (-1.147, 1.030) 0.915
	Incongruent	0.357 (0.633)	0.333 (0.492)	-0.300 (-1.236, 0.636) 0.526
Up/Down	Congruent	3.643 (3.775)	5.417 (3.777)	1.424 (-1.229, 4.078) 0.289
	Incongruent	3.929 (3.222)	5.500 (5.436)	-0.332 (-4.493, 3.830) 0.875
Overall	Congruent	3.929 (3.792)	5.917 (4.295)	0.683 (-0.792, 2.158) 0.360
	Incongruent	4.286 (3.384)	5.750 (5.610)	0.425 (-1.181, 2.032) 0.600
	Left/Right	0.643 (1.598)	0.833 (0.835)	-0.179 (-0.985, 0.626) 0.659
	Up/Down	7.571 (6.513)	10.833 (8.737)	1.288 (-0.739, 3.314) 0.210

\*Regression Coefficient (95% C.I.) and p-value, adjusted for age, gender and education.

**Table 11-5. Adjusted Within-Group Analysis of the Effects of Arrow Direction and Congruence on RT (ms) and Number of Errors at Baseline**

		Reaction Times (ms)		Number of Errors	
Interactions		Control*	Premanifest HD*	Control*	Premanifest HD*
Congruent Condition	Up/Down vs. Left/Right	92.688 (39.630, 145.746) 0.001	91.609 (27.665, 155.552) 0.005	3.268 (1.471, 5.064) 0.000	4.750 (2.624, 6.877) 0.000
Incongruent Condition	Up/Down vs. Left/Right	61.352 (10.446, 112.257) 0.019	112.836 (8.341, 217.331) 0.035	3.488 (1.972, 5.003) 0.000	4.719 (1.020, 8.417) 0.013
Left/Right Direction	Incongruent vs. Congruent	57.35603 (15.256, 99.456) 0.008	52.106 (-1.222, 105.433) 0.055	0.076 (-0.671, 0.822) 0.841	-0.166 (-1.150, 0.818) 0.739
Up/Down Direction	Incongruent vs. Congruent	26.020 (-34.264, 86.303) 0.394	73.333 (-36.958, 183.624) 0.190	0.296 (-1.933, 2.524) 0.793	-0.198 (-4.349, 3.954) 0.925

\*Regression Coefficient (95% C.I.) and p-value. Dark grey highlights the significant (p<0.05) differences and the light grey highlights the differences approaching significance (p<0.06), adjusted for age, gender and education.

### ***Clinical Correlations***

There were no significant correlations ( $p < 0.05$ ) between the left/right interference effect and CPO (Spearman's  $Rho = 0.518$ ;  $p = 0.0842$ ) or disease burden score (Spearman's  $Rho = 0.445$ ;  $p = 0.147$ ). Similarly, no significant correlations were found between the interference time in the upward and downward facing arrows trials and CPO (Spearman's  $Rho = -0.175$ ;  $p = 0.587$ ) or disease burden score (Spearman's  $Rho = 0.231$ ;  $p = 0.471$ ).

### ***Between-Group Differences in Imaging Metrics***

The premanifest HD group had significantly smaller caudate volume (% TIV) compared with the control group ( $-0.088$ ; 95% C.I.  $-0.119, -0.056$ ;  $p < 0.001$ ). The two groups did not significantly differ in any of the other diffusion metrics extracted from the WM tracts.

### ***Caudate Volume Associations***

Results from the regression analysis between caudate volume (% TIV) and interference RTs for each group can be seen in Table 11-6.

Caudate volume was found to negatively correlate with the up/down interference RT in the premanifest HD group (Table 11-6, Figure 11-4); smaller caudate volume was associated with a larger interference RT. There was one outlier in the group with a very low interference RT. In order to check whether this participant may be skewing the results, the regression was run again with this participant removed. The correlation remained significant ( $-1040.882$ ; 95% C.I.  $-1934.13, -147.633$ ;  $p = 0.030$ ).

Caudate volume was the only imaging metric that significantly differed between the two groups, therefore, as a further examination of variation in response speed, the congruent and incongruent RTs were also analysed with caudate volume (% TIV). Caudate volume was found to be significantly negatively associated with both left/right and up/down congruent and incongruent RTs. Figure 11-5, Figure 11-6 and Table 11-7 presents all of these relationships as well as the non-significant relationships found in controls.

Table 11-6. Association Between Interference RT (ms) and Imaging Measures

Metric	Region	Control		Premanifest HD	
		Left/Right <sup>±</sup>	Up/Down <sup>±</sup>	Left/Right <sup>±</sup>	Up/Down <sup>±</sup>
Volume					
	Caudate*	-242.744 (-694.336, 208.848) 0.244	-371.674 (-827.161, 83.813) 0.095	-899.686 (-1935.805, 136.433) 0.076	-968.537 (-1567.197, -369.877) 0.009
WM Tract Diffusion					
FA	Left ACC	436.655 (-53.770, 927.080) 0.073	-8.300 (-694.264, 677.665) 0.978	-171.241 (-1131.771, 789.290) 0.666	-172.202 (-1789.045, 1444.641) 0.795
		222.399 (-501.790, 946.588) 0.491	-223.501 (-810.502, 363.499) 0.398	-204.483 (-616.352, 207.386) 0.258	-416.247 (-1561.915, 729.421) 0.393
	Right ACC	284.030 (-397.016, 965.076) 0.357	-340.797 (-931.111, 249.516) 0.214	-329.350 (-1511.684, 852.984) 0.506	-421.661 (-2884.787, 2041.464) 0.678
		193.089 (-984.910, 1371.088) 0.710	-443.014 (-1053.086, 167.058) 0.130	-993.375 (-2039.096, 52.345) 0.059	-1148.635 (-2146.315, -150.954) 0.032
	Left DLPFC – Caudate	478.188 (-143.912, 1100.288) 0.112	-242.551 (-731.914, 246.812) 0.280	-800.620 (-1752.051, 150.812) 0.083	-857.699 (-1950.265, 234.867) 0.100
		480.768 (-270.318, 1231.854) 0.174	-377.154 (-927.321, 173.014) 0.149	-946.473 (-2000.572, 107.627) 0.069	-965.306 (-2332.800, 402.189) 0.129
	Right DLPFC – Caudate				

AD**	Left ACC	3.848 (0.117, 7.579) 0.045	-0.545 (-4.152, 3.062) 0.731	-2.346 (-6.830, 2.139) 0.237	3.545 (-2.042, 9.139) 0.164
	Right ACC	1.542 (-4.789, 7.873) 0.583	-0.657 (-6.291, 4.977) 0.791	-6.587 (-14.815, 1.641) 0.095	5.686 (-7.466, 18.838) 0.317
	Left DLPFC – Caudate	1.516 (-4.508, 7.540) 0.571	-0.745 (-4.356, 2.865) 0.640	-3.920 (-10.492, 2.651) 0.186	3.175 (-6.257, 12.607) 0.426
	Right DLPFC – Caudate	1.710 (-4.545, 7.964) 0.539	0.025 (-4.869, 4.919) 0.991	-3.465 (-9.703, 2.772) 0.213	2.977 (-4.801, 10.755) 0.370
	Left DLPFC – Thalamus	2.716 (-2.419, 7.851) 0.251	-0.584 (-3.959, 2.791) 0.695	-4.389 (-10.855, 2.077) 0.141	2.295 (-8.402, 12.991) 0.605
	Right DLPFC – Thalamus	3.268 (-2.775, 9.312) 0.242	0.501 (-3.573, 4.574) 0.780	-4.858 (-12.223, 2.507) 0.151	3.029 (-7.107, 13.165) 0.477
RD**	Left ACC	-2.149 (-6.492, 2.194) 0.280	-0.329 (-6.803, 6.145) 0.908	-0.160 (-7.442, 7.123) 0.957	3.869 (-6.508, 14.246) 0.382
	Right ACC	0.042 (-5.723, 5.807) 0.987	0.944 (-4.845, 6.733) 0.711	0.774 (-2.041, 3.588) 0.511	4.187 (-2.981, 11.355) 0.194
	Left DLPFC – Caudate	-0.545 (-6.534, 5.445) 0.836	3.329 (0.294, 6.363) 0.036	-1.447 (-7.619, 4.726) 0.573	4.133 (-6.061, 14.327) 0.345



Right DLPFC – Caudate	0.825 (-4.898, 6.547) 0.743	2.503 (-2.881, 7.886) 0.308	0.347 (-5.009, 5.704) 0.874	6.244 (0.679, 11.809) 0.034
Left DLPFC – Thalamus	-2.202 (-10.156, 5.752) 0.534	2.672 (-4.631, 9.974) 0.416	2.653 (-7.216, 12.523) 0.520	8.629 (1.066, 16.193) 0.033
Right DLPFC – Thalamus	-1.602 (-8.098, 4.894) 0.578	4.250 (-0.148, 8.648) 0.056	1.527 (-5.508, 8.563) 0.601	7.853 (0.084, 15.622) 0.048

\*% TIV; \*\* $(\text{mm}^2/\text{s}) \times 10^{-3}$ , Estimates have been multiplied by  $10^{45}$  for readability; <sup>‡</sup>Regression coefficient, 95% C.I., p-value; ACC=anterior cingulate cortex; DLPFC=dorsolateral prefrontal cortex. Dark grey highlights the significant associations ( $p < 0.05$ ) and the light grey highlights the associations approaching significance ( $p < 0.06$ ), adjusted for age, gender and education.

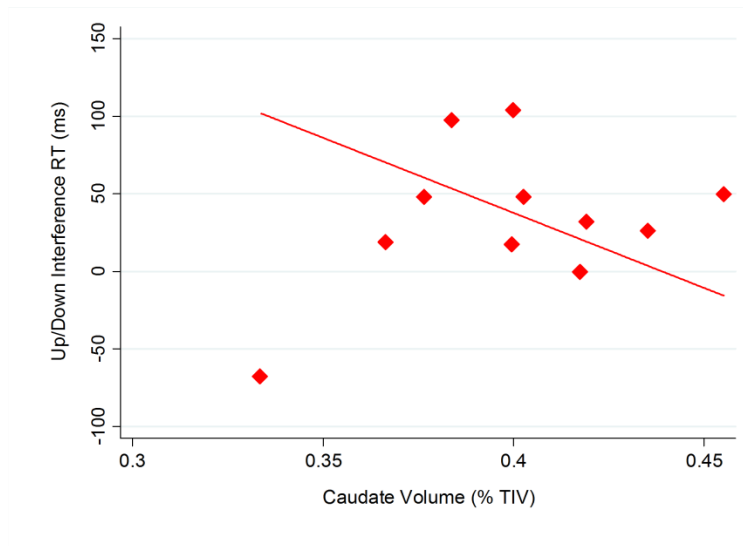


**Figure 11-4.** Association between the up/down interference effect and caudate volume (%TIV) in the premanifest HD group with adjusted regression line.

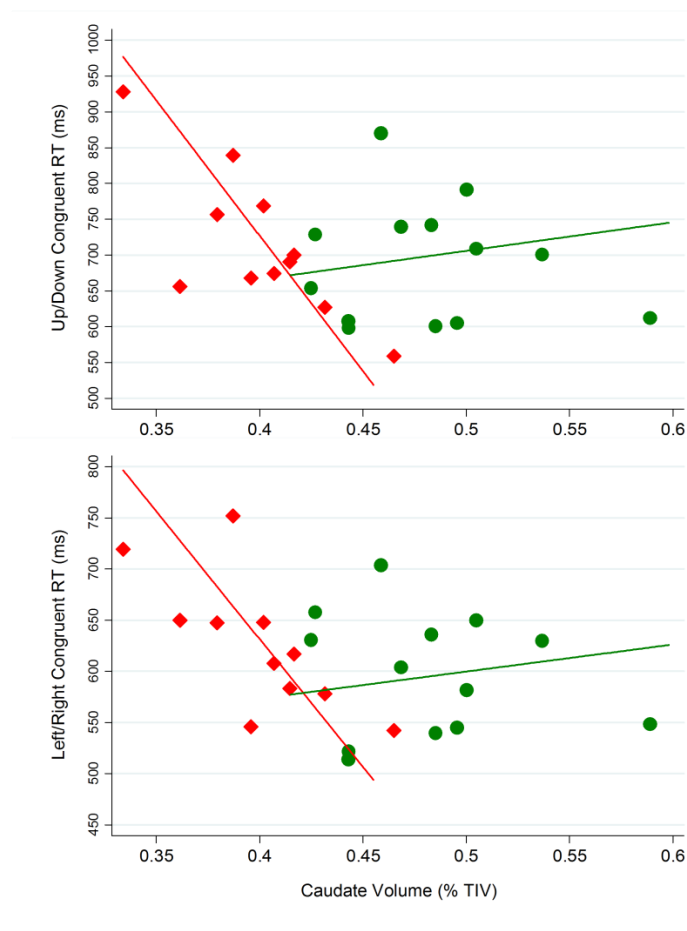


**Figure 11-5.** Association between the up/down congruent RT and caudate volume (% TIV) (top), and between the left/right congruent RT and caudate volume (%TIV) (bottom) in the premanifest HD group (red) and controls (green), along with adjusted regression lines.

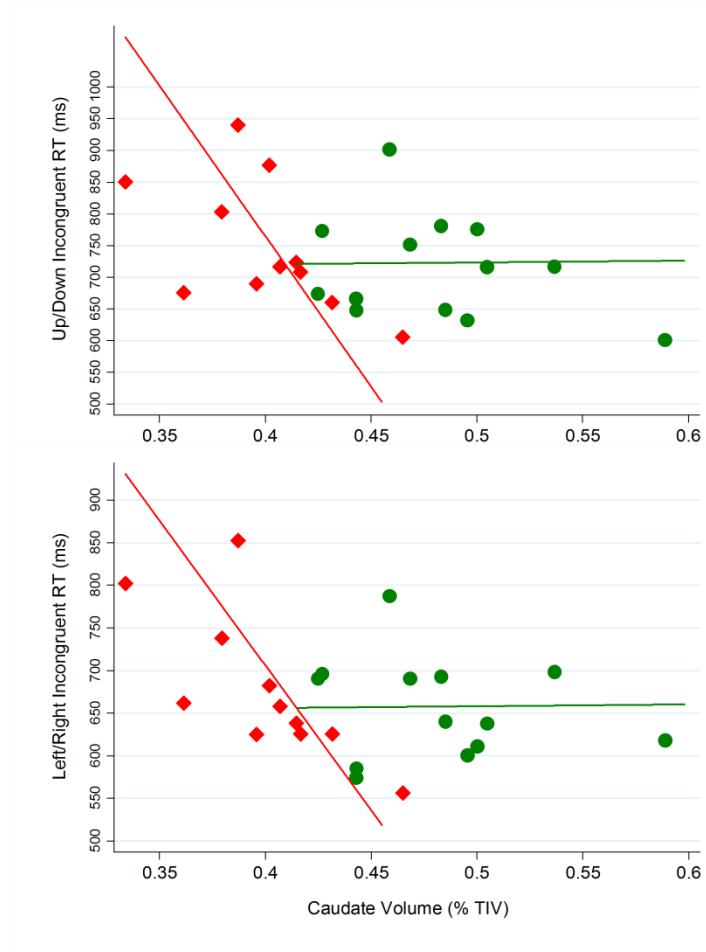


**Figure 11-6.** Association between the up/down incongruent RT and caudate volume (% TIV) (top), and between the left/right incongruent RT and caudate volume (%TIV) (bottom) in the premanifest HD group (red) and controls (green), along with adjusted regression lines.

Table 11-7. Adjusted Associations Between RT and Caudate Volume (% TIV)

Caudate Volume*	Control		Premanifest HD	
	Left/Right <sup>±</sup>	Up/Down <sup>±</sup>	Left/Right <sup>±</sup>	Up/Down <sup>±</sup>
Incongruent RT	21.551 (-907.621, 950.723) 0.958	27.920 (-1293.631, 1349.471) 0.962	-3396.233 (-5904.487, -887.980) 0.018	-4745.716 (-7041.544, -2449.888) 0.003
Congruent RT	264.295 (-705.884, 1234.474) 0.540	-399.594 (-1165.913, 1965.101) 0.565	-2496.540 (-4387.685, -605.409) 0.019	-3777.179 (-5942.306, -1612.052) 0.006

\*% TIV; <sup>±</sup> Regression coefficient, 95% C.I., p-value; Dark grey highlights the significant associations (p<0.05), adjusted for age, gender and education.

### *White Matter Tract Associations*

Results from the regression analyses with WM tract diffusion metrics and interference RTs for each group can be seen in Table 11-6. Figure 11-7 provides examples of each of the tracts overlaid on one participant's FA image.

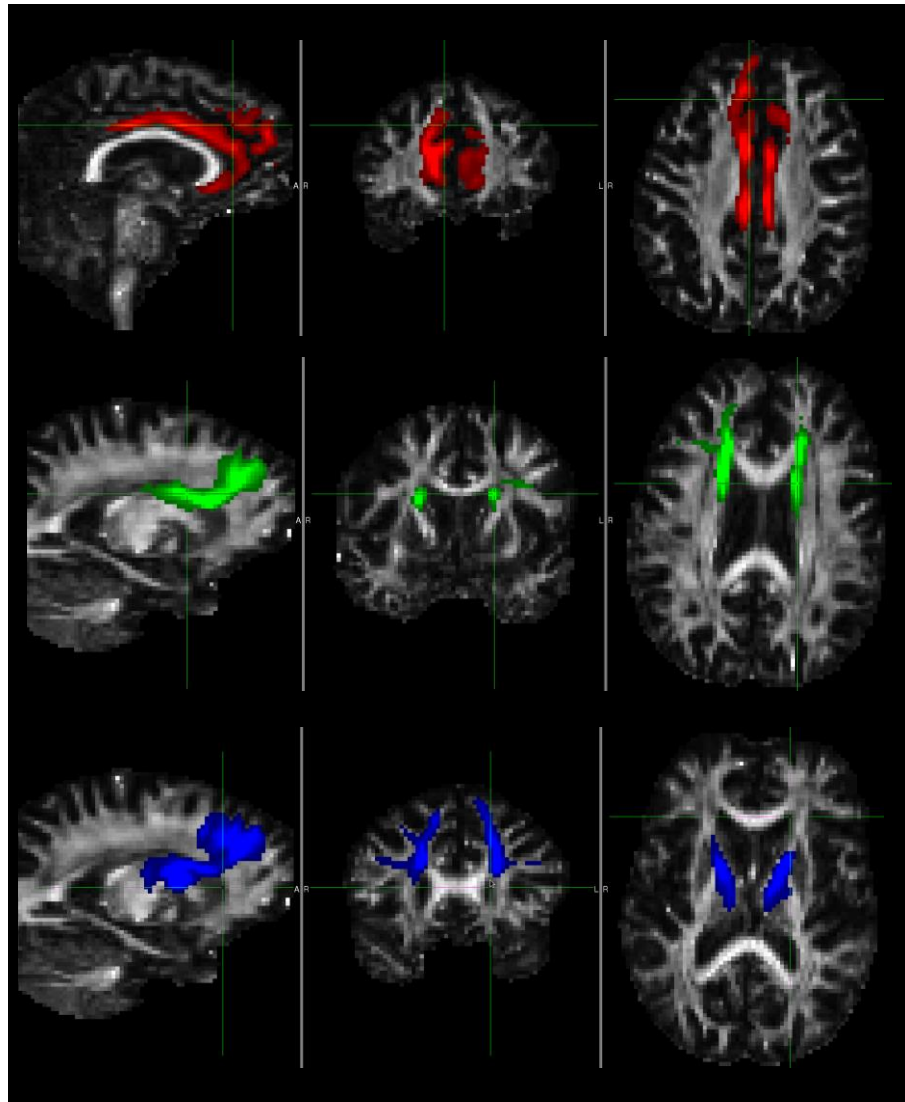


*Figure 11-7. Top row: Left and right ACC tracts (red). Middle row: Left and right DLPFC – caudate tracts (green). Bottom row: Left and right DLPFC - thalamus tracts (blue). All tracts are overlaid on the FA image.*

FA in the right DLPFC-caudate tract in the premanifest HD group was found to negatively correlate with both interference RTs (Figure 11-8), significantly so with up/down facing arrows (-1148.635; 95% C.I. -2146.315, -150.954;  $p=0.0320$ ), however was only bordering on statistical significance with left/right arrows (-993.375; 95% C.I.

-2039.096, 52.345;  $p=0.059$ ). When viewing the scatter plots (Figure 11-8), however, the relationships do not appear very strong.

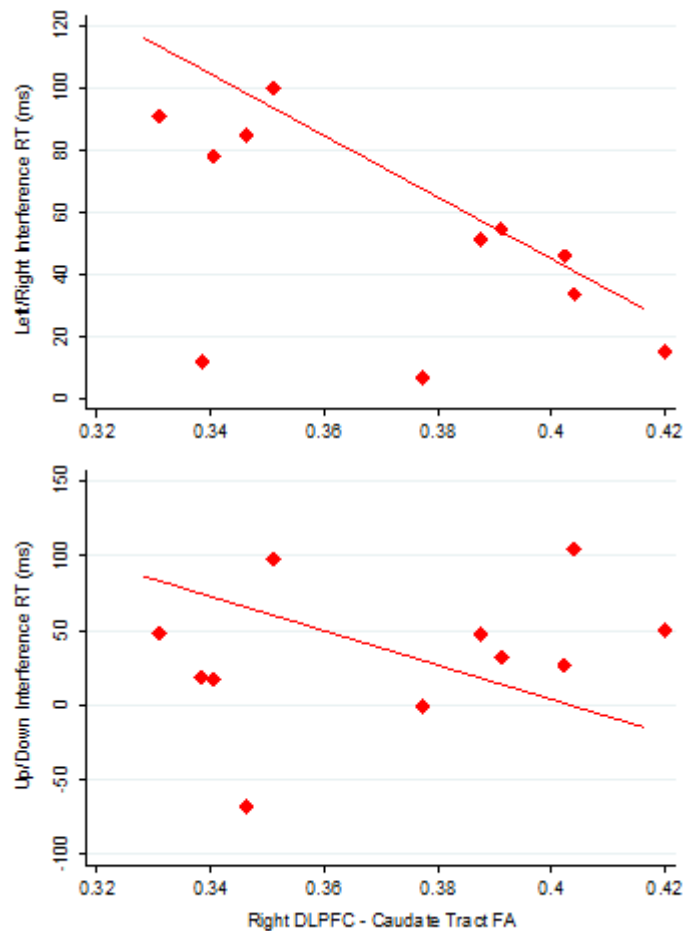


**Figure 11-8.** Association between the left/right (top) and the up/down (bottom) interference effect and FA in the right DLPFC–caudate tract in the premanifest HD group. Displayed with adjusted regression lines.

Premanifest HD participants were also found to have a significantly positive relationship between up/down interference RT and RD in left DLPFC-thalamus tract (8.629ms; 95% C.I. 1.066, 16.193;  $p=0.033$ ; Figure 11-9); larger interference RT was associated with higher RD. Similarly, they showed a positive correlation between up/down interference RT and RD in the right DLPFC-thalamus tract and right DLPFC-caudate tract (7.853ms; 95% C.I. 0.084, 15.622;  $p=0.048$  and 6.244ms; 95% C.I. 0.679, 11.809;  $p=0.034$  respectively; Figure 11-9).

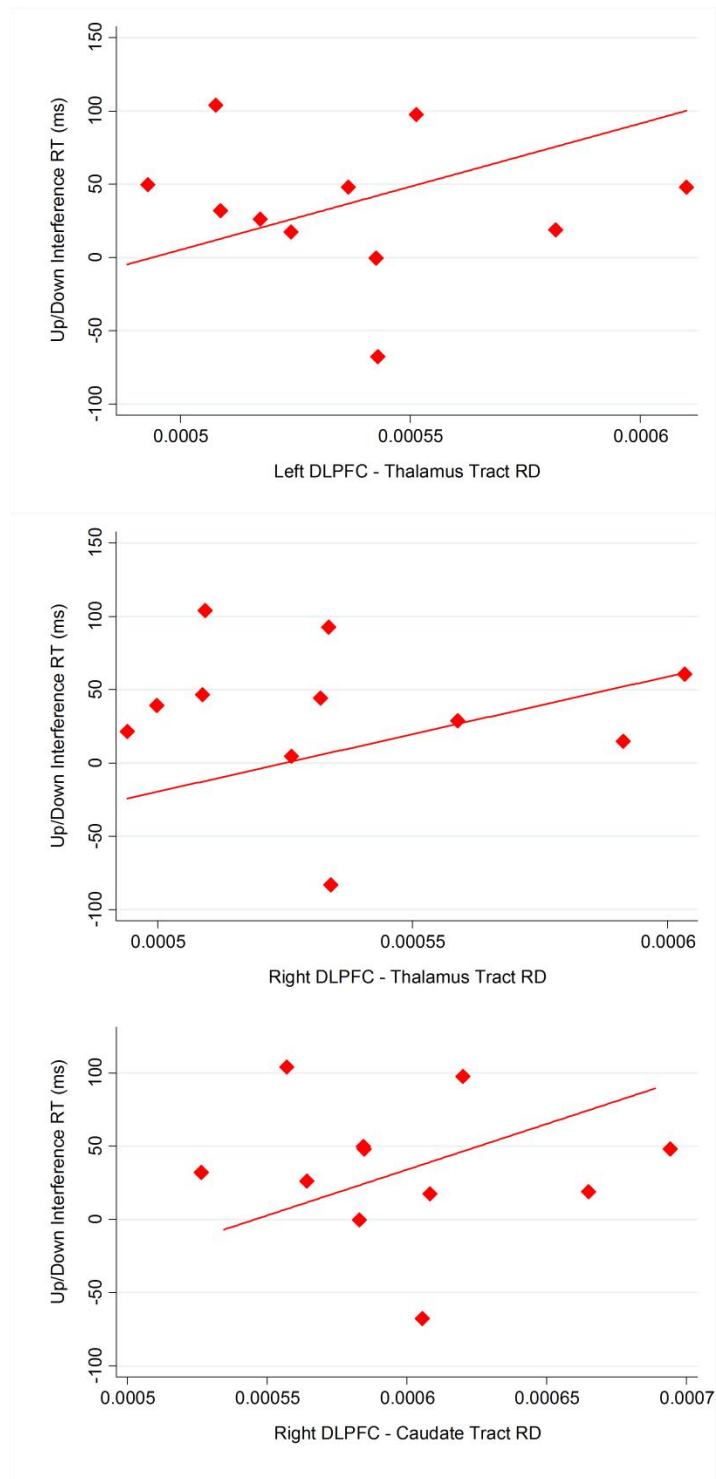


**Figure 11-9.** Association between the up/down interference effect and RD in the left DLPFC-thalamus tract (top), the right DLPFC – thalamus tract (middle) and the right DLPFC – caudate tract (bottom) in the premanifest HD group. Displayed with the adjusted regression lines. RD units are  $(\text{mm}^2/\text{s}) \times 10^{-3}$ .

In order to further examine some of the associations found within the premanifest HD group, Spearman's correlations were also conducted between the imaging metrics that significantly correlated ( $p < 0.05$ ) with the interference RTs and the clinical measures CPO and disease burden. CPO did not correlate with TIV-adjusted caudate volume (Spearman's  $Rho = -0.555$ ;  $p = 0.077$ ), however, did significantly correlate with FA in the right DLPFC-caudate tract (Spearman's  $Rho = -0.636$ ;  $p = 0.035$ ; Figure 11-10); lower FA was associated with closer proximity to onset.

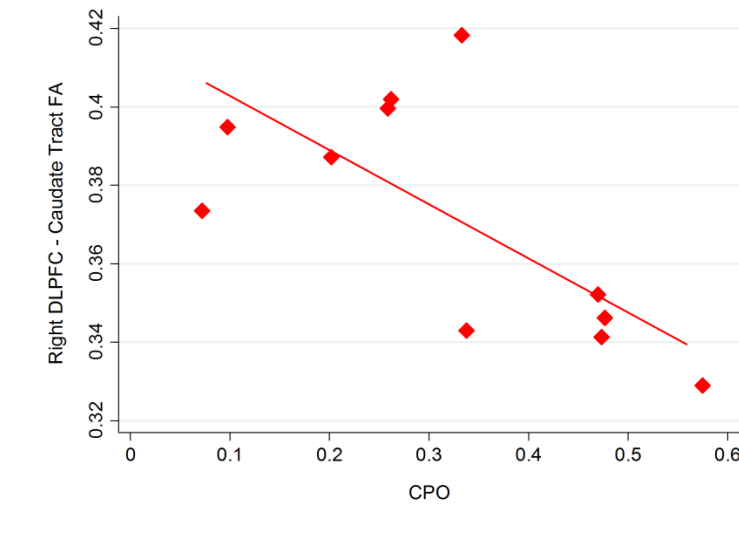


**Figure 11-10. Correlation between FA in the right DLPFC–caudate tract and CPO in the premanifest HD group, along with the unadjusted fitted line.**

CPO was also found to positively correlate with RD in the right DLPFC-caudate tract (Spearman's  $Rho = 0.773$ ;  $p = 0.005$ ) and RD in the right DLPFC-thalamus tract (Spearman's  $Rho = 0.782$ ;  $p = 0.005$ ; Figure 11-11); higher RD was associated with closer proximity to onset. No significant correlation was found between CPO and RD in the left DLPFC-thalamus tract (Spearman's  $Rho = 0.418$ ;  $p = 0.201$ ). Disease burden did not significantly correlate ( $p < 0.05$ ) with any of the imaging metrics.



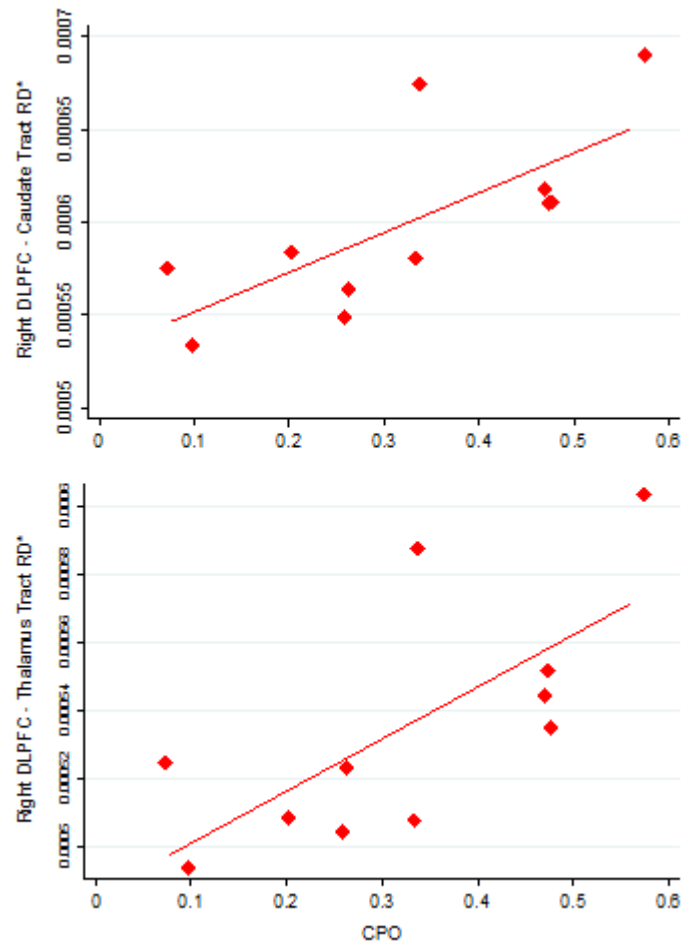


*Figure 11-11. Top: Correlation between RD ( $\text{mm}^2/\text{s}) \times 10^{-3}$ ) in the right DLPFC-caudate tract and CPO in premanifest HD. Bottom: Correlation between RD ( $\text{mm}^2/\text{s}) \times 10^{-3}$ ) in the right DLPFC-thalamus tract and CPO in premanifest HD. Both are shown with the unadjusted fitted lines.*

#### 11.4.2 Visit Two Results

One participant's data had to be excluded at visit two due to a large number of errors (>100), therefore there were 10 controls and 11 premanifest HD participants included in the visit two analyses. Overall, findings at visit two were consistent with those at baseline.

To summarise, both premanifest HD and control participants were slower in the incongruent trials compared with the congruent ones (45.727ms and 41.525ms respectively). This effect of congruence was only found to be significant in the premanifest HD group at visit two and only with arrows pointed left or right (54.862ms; 95% C.I. 7.784, 101.939;  $p=0.023$ ). Equally, both groups demonstrated a larger

interference effect for the left and right facing arrows compared with the up and down arrows, consistent with the baseline findings, however, was also not significant.

There was a significant effect of arrow direction on the RTs and number of errors made (all at least  $p < 0.05$ ), consistent with the baseline results, with the exception of RTs in the incongruent condition. Congruence, similarly had no significant effect on the number of errors made by either group.

#### **11.4.3 Longitudinal Results**

There was no significant change in RT or number of errors made for any condition or trial type from baseline to visit two. This meant there was also no between-group differences in change in RTs or number of errors. Within-group analysis revealed no significant effects of direction and congruence on change in RTs or number of errors made for either group.

Observationally, both groups were slightly faster at reacting at visit two compared with baseline overall, but not significantly so. The premanifest HD group, however, were 3.335ms and 2.399ms slower when arrows faced up and down (congruent and incongruent respectively), but again this was not significant (Table 11-8).

The left/right interference effect in the control group was 16.386ms smaller at visit two compared with baseline (95% C.I. -83.271, 50.499;  $p = 0.627$ ) and 2.996ms larger for the up/down interference effect (95% C.I. -115.781, 121.773;  $p = 0.960$ ; Table 11-8). This meant that in the controls, the difference between the change in the left/right interference RT and the change in the up/down interference RT was 19.382ms (95% C.I. -116.932, 155.696;  $p = 0.778$ ). These are just observations, however, there is no evidence of any statistically significant effects.

The left/right interference effect in the premanifest HD group, however, was 1.316ms larger at visit two compared with baseline (95% C.I. 52.965, 55.598;  $p = 0.962$ ) and 0.936ms smaller for the up/down interference effect (95% C.I. -88.217, 86.345;  $p = 0.983$ ; Table 11-8). Therefore there was no real change in either effects and the difference between the change in the left/right interference RT and the change in the up/down interference RT was just -2.253ms (95% C.I. -105.037, 100.531;  $p = 0.965$ ).

Again, it is important to note that these are just observations in the data and there is no evidence of any statistically significant effects.

The between-group difference in the difference between the change in left/right and up/down interference effects is -21.635ms (95% C.I. -192.357, 149.087;  $p=0.801$ ). Again, this is not a significant finding but does indicate that the control's interference effects changed more at visit two, i.e. got quicker on the whole, compared with the premanifest group, who did not noticeably change.

**Table 11-8. Adjusted Within-Group Analysis of Change in RT (ms)**

Direction	Condition	Control*	Premanifest HD*
Left/Right	Congruent	-7.820 (-51.843, 36.203) 0.724	-18.978 (-52.843, 14.889) 0.268
	Incongruent	-24.206 (-76.440, 28.028) 0.359	-17.661 (-58.736, 23.413) 0.394
	Difference^	-16.386 (-83.271, 50.499) 0.627	1.316 (-52.965, 55.598) 0.962
Up/Down	Congruent	-25.917 (-108.755, 56.921) 0.535	3.335 (-56.244, 62.915) 0.911
	Incongruent	-22.921 (-110.189, 64.348) 0.602	2.399 (-59.543, 64.341) 0.939
	Difference^	2.996 (-115.781, 121.773) 0.960	-0.936 (-88.217, 86.345) 0.983

\*Regression Coefficient (95% C.I.) and  $p$ -value, adjusted for age, gender and education; ^also known as the interference effect.

## 11.5 Discussion

Using a specially designed interference task, this study investigated susceptibility to interference in premanifest HD participants and healthy controls over 12 months and examined the extent to which disease-related cognitive performance was related to clinical measures and macro- and microstructural properties of the caudate and hypothesis-driven selected WM tracts.

In summary, the interference effect was successfully demonstrated in the control participants for the left/right arrow direction, and a similar trend was seen in the premanifest HD participants. The significant effect of congruency on RTs and accuracy in both groups meant that participants were slower and made more errors during incongruent trials. The premanifest HD group were significantly slower to respond than the control group in overall congruent and incongruent conditions. There was, however, no between-group difference in the interference effects and no change in cognitive performance over 12 months. Despite this, there was a strong association between the interference effects and disease-related degeneration in the caudate and selected WM tracts in premanifest participants.

### ***Interference Effects***

Participants were slower to react in trials when the flanking arrows were incongruent to the target arrow, which is consistent with previous studies using similar Eriksen flanker tasks with arrowhead stimuli in both healthy controls (Mansfield *et al.* 2013) and premanifest HD participants (Beste *et al.* 2008a). In the trials where the effect of congruence was significant, i.e. the left/right facing arrows, the effect of incompatible versus compatible conditions was 57.356ms in the control group, which is very similar to the 60ms congruency effect demonstrated in controls previously (Mansfield *et al.* 2013). The interference RTs in the premanifest group, however, were much smaller in the current study; the effect of incompatible versus compatible conditions was 52.106ms, which is in contrast to the 114ms found in Beste *et al.* (2008a). Sample size was comparable to the current study; 14 premanifest participants and 12 respectively, however, the premanifest participants in Beste *et al.* (2008a) had a duration until estimated age of onset ranging from -3.4 – 23.8, indicating that some participants had actually already passed estimated onset by 3.4 years. This could be driving the larger interference effect than the one seen in the present study.

Another explanation for this inconsistency with the previous research is methodological. Beste *et al.* (2008a) do not provide any information regarding the apparatus with which the task was administered or how they recorded the behavioural responses. It is possible that with such small samples variation in equipment and recording devices may explain the discrepancy in RTs.

Congruency effects were only found in the left/right facing arrow trials meaning that the difference between congruent and incongruent trials was larger in the left/right arrow trials compared with the up/down trials. This difference between arrow directions was not significant for either participant group but does suggest that the incongruent left and right facing arrows caused more of an interference than the up and down arrows, despite all participants being slower to respond to up and down facing arrows. A possible explanation for this is the strong, automated response that humans display to left and right stimuli, which may be more easily hindered by interfering stimuli than a less familiar or novel response like to that of the up and down arrows.

Against expectations, the interference effect in the control group in the left/right arrow trials was larger than the premanifest HD group, and although this was not a statistically significant finding, it is interesting and provides support to the impaired automaticity hypothesis (Vaportzis *et al.* 2014). The fact that the left/right interference effect was larger could be due to the premanifest HD group responding slower overall, therefore, the advantage of congruent stimuli was not as pronounced as that demonstrated in the controls, or it could be due to alterations in attentional processing.

Simple tasks have been shown to place greater attentional demands on HD participants compared with controls and they do not demonstrate any change in RT from simple to complex tasks, whereas the speed of controls significantly declines from simple to complex tasks (Vaportzis *et al.* 2014). Equally in the current study, unlike the control group, the premanifest group responded at more similar speeds in the compatible and incompatible conditions and demonstrated a similar interference effect in both left/right and up/down arrow facing trials. Premanifest participants, therefore, did not demonstrate the same detrimental effects of incongruency that the controls did during the left/right arrow trials and correspondingly did not display a disproportionately smaller interference effect in the up/down arrow trials. It could be argued, therefore, that the flanker interference task places greater attentional demands on premanifest HD participants compared with controls, and attentional deficits are present even before symptom onset caused by impaired automaticity.

An alternative explanation for this observed difference between the groups could be that they used different motor control systems. The controls used an automatic response system producing a greater interference effect for automatic left/right responses,

whereas the premanifest participants used a more cognitive control system producing less of an interference effect. This could also explain why the control group did not show as much of an interference effect for the up/down trials, because like the premanifest HD participants, they too were not using the automatic response mechanism for these trials.

Overall, accuracy was high and there was no difference between the groups with regards to the number of errors made. There was, however, a significant effect of arrow direction on the number of errors and RT, consistent with the argument of up/down arrows increasing cognitive load. One explanation for the poorer accuracy is that participants had to actively remember which button was assigned to which direction and the response was less automatic compared with responding to left and right facing stimuli. It could be argued, therefore, that this task also has a strong memory component which may impede the effects of interference. Nevertheless, the additional cognitive load was included to help better differentiate the groups and, although there was no significant between-group difference in speed or accuracy with the upward and downward facing arrows, it has highlighted the possibility that premanifest HD participants suffer impaired automaticity, which is an interesting discovery.

Overall, findings were consistent at baseline and visit two. Premanifest HD participants showed a borderline significant interference effect for left and right facing arrows at baseline but demonstrated a significant interference effect at visit two. This is in contrast to the control group who did not show a significant effect at visit two, and who were slightly faster in all trials, suggesting that the control group have improved. Whereas the premanifest group, who were more significantly affected by the left/right incongruent arrows at visit two, arguably have not improved. This was not a significant change but is interesting to observe and potentially indicates a detrimental disease-related effect on performance.

The failure to detect significant change in cognitive performance over one year may have been due to test-retest effects. All cognitive tasks are subject to practice effects whereby second exposure to a task can cause unexpected improvements in performance. The test-retest effect may also impede detection of cognitive decline in HD, particularly with a short interval. Pronounced retest effects over one year in premanifest and manifest HD patients have previously been seen in the Stroop interference task (Schramm

*et al.* 2015) and indirect circle tracing task (Tabrizi *et al.* 2011). Practice effects are equally seen in cognitively normal people (Tabrizi *et al.* 2011) and need to be taken into account when designing cognitive experiments. Practice effects can be minimised through pre-testing exposure or implementing a second baseline prior to taking initial measurements (Stout *et al.* 2015). The current study included a practice task before the experimental task at both time points in order to prevent these effects, however, it is possible that test-retest effects may still have confounded the longitudinal results and prevented the detection of change in the premanifest HD group.

It is important to emphasise that this study was an exploratory study and at the time of writing the study proposal there were no other studies that had investigated this type of interference task longitudinally in a premanifest HD cohort. Although the task was not sensitive to change over 12 months, findings were consistent at baseline and visit two, suggesting that this task is reliable, however, this has not been statistically tested. Further investigation with a larger time interval may be required to detect significant within-group decline and between-group differences in change in performance.

### ***Clinical Correlations***

The lack of a statistically significant association between the interference effects and CPO or disease burden in the premanifest HD group indicates that either these disease-related measures are not the primary driver of susceptibility to interference, or that a relationship between these variables exists but was not captured by the current technique. The Spearman correlation analysis was chosen for the current study because it is more robust than other analyses such as the Pearson correlation analysis and is not overly influenced by outliers in the data, making it more appropriate for small sample sizes. However, the large variability in interference RTs, combined with the small sample may explain why no associations were found.

Alternatively, it may be that there is still a lot variance in disease stage and onset that is not captured by the models CPO and disease burden. Caudate atrophy may have been a more accurate estimate of disease pathology in the premanifest stages of HD and has previously been used as a structural marker of disease burden (Kloppel *et al.* 2015; Novak *et al.* 2013). Future research into susceptibility to interference should, therefore, consider using caudate volume in the analyses.

### ***Between-Group Differences and Disease-Related Associations with Imaging Measures***

Caudate volume was the only imaging measure to show significant pathology in the premanifest HD group compared with controls. Caudate volume is a robust structural marker of disease progression and evidence of atrophy is apparent many years before disease onset (Tabrizi *et al.* 2009), consistent with the current finding. Caudate volume also significantly correlated with the interference effect for upwards and downwards facing arrows in the premanifest group, indicating that smaller caudate volume was associated with greater susceptibility to interference in this condition. This association, along with the lack of correlation in the left/right condition supports the argument that premanifest participants suffer from impaired automaticity causing them to display similar interference effects in both arrow direction conditions and not show the marked increase in interference for the left/right facing arrows, as seen in controls. This correlation between the abnormal up/down interference effect and caudate volume indicates that this is a disease-specific association.

Further examination of caudate volume and RTs in the premanifest group found that smaller caudate volume was also significantly associated with slower RTs in all conditions. This strong association suggests degeneration of the caudate is having a direct impact on premanifest participants' ability to respond in this task in an automatic way. It is not possible, however, to know the causation of this relationship, only that it is disease-specific.

The lack of significant between-group differences in diffusion measures within the selected WM tracts is not surprising given the small sample and higher signal to noise ratio present in diffusion imaging, caused by both physical and physiological factors (Alexander *et al.* 2007). Alternatively, it may be that microstructural abnormalities within these tracts may not be sufficient in these participants to detect between-group differences with the current technique. A larger sample, closer to disease onset may prove more sensitive to between-group differences in diffusion magnitude within these tracts.

Despite no significant group difference in the metrics, there were, however, significant associations between the interference effects and microstructural properties of some of



the WM tracts in the premanifest HD group. Evidence of a positive, significant association between the up/down interference effect and RD within bilateral tracts connecting the thalamus and the DLPFC were found. This suggests that changes in diffusion perpendicular to the main WM fibre, possibly caused by demyelination (Song *et al.* 2002; 2003) within thalamic-prefrontal-cortical tracts is related to impaired attention processing and/or cognitive control in premanifest HD.

These findings are in agreement with previous research examining these tracts but with a different psychomotor speed task in a group of early manifest HD patients (Novak *et al.* 2015). Altered basal ganglia-cortical structural connectivity, of which the thalamus was particularly affected, correlated with SDMT score. Similarly, increased RD has been found in these tracts in early manifest HD (Poudel *et al.* 2015) and shown associations with SDMT and Stroop performance in analogous prefrontal tracts in premanifest HD compared with controls (Poudel *et al.* 2014).

Evidence of a negative association between the up/down interference effect and FA, and a positive association between the up/down interference effect and RD within tracts connecting the right caudate with the DLPFC was also found. These relationships suggest that these right tracts may be degenerating more than those connecting the same regions in the left hemisphere, and in the absence of an association with the left tracts, also suggests that these relationships may be specific to the tracts in the right hemisphere. However, no asymmetry in degeneration of the caudate has previously been found (Mascalchi *et al.* 2004) and basal-ganglia cortical connections are bilaterally affected (Novak *et al.* 2015). Further investigation into caudal-prefrontal-cortical between-hemisphere differences is required.

The simultaneous associations between the interference effect and FA and RD is potentially due to the fact that FA is a summary index of diffusivity along both the parallel and perpendicular axes, therefore the increases in RD within fibres connecting the right caudate with the DLPFC could also be causing a decrease in the anisotropy within these fibres. FA can also be influenced by underlying biological causes, such as changes in neuronal fibre density, intracellular structures and myelin (Beaulieu 2002). In the absence of any associations with AD, it is possible that increases in demyelination, causing an increase in RD explain the concurrent increase in FA (Song *et al.* 2002; 2003).

When viewing these associations in the scatter plots, the correlations do not appear that strong and the data points are quite dispersed. The Spearman's analysis will have limited the influence of any outliers, however, to be fully confident in the results, further analysis is required with a larger sample. Nonetheless, the additional correlations between the metrics in the significantly associated tracts and CPO confirm the disease-specificity of the relationships with the interference effects and suggest that subtle microstructural changes are increasing with proximity to disease onset.

No association was found between the interference effects and any of the diffusion metrics in the ACC tracts, which is in contrast to earlier studies. The ACC has previously been shown to be associated with interference-related cognitive function and inhibitory attentional control in premanifest HD (Beste *et al.* 2012; Gray *et al.* 2013). One explanation for this discrepancy are the techniques used. Firstly, Beste *et al.* (2012) investigated event-related potentials using electroencephalography and Gray *et al.* (2013) measured brain activation using fMRI, therefore, the techniques cannot be directly compared to the DTI tractography used in the current study. Secondly, it is possible that anatomical inaccuracies in the placement of the ACC seed ROI may have caused inaccuracies in the generated streamlines and connectivity-based segmentation of the tracts, i.e. seeding every voxel within the ROI mask (Behrens *et al.* 2003) may have proved more sensitive. Likewise, a manual segmentation method may have proved more accurate than the ACC atlas masks selected from SPM. These automated ROIs may have included partial volume from neighbouring regions causing spurious streamlines. All ROIs and image registrations, however, passed visual quality checks at every step. Further research with manually segmented ACC regions may prove more sensitive to changes and associations in premanifest HD participants' susceptibility to interference.

There was no evidence of an association between AD in any of the tracts and interference effects. Pathological changes along the axonal fibres may not be pronounced enough to detect a relationship with cognitive dysfunction in these premanifest participants. Changes in AD have been purported to reflect axonal injury or degeneration, whilst changes in RD possibly reflect demyelination (Song *et al.* 2002; 2003). It is possible, therefore, that demyelination is occurring in these tracts, reflected by increasing RD, but the integrity of the axon is relatively unchanged, reflected by the absence of an association with AD.

### ***Strengths and Limitations***

One of this study's main strengths is the well characterised cohort of premanifest and healthy control participants and the standardised task administration, as discussed in chapter 10. Similarly, the small sample size is also a substantial limitation for this study, which is also discussed in chapter 10.

It is important to note that many hypotheses were tested in the analyses but no correction was made for multiple testing due to the small sample and exploratory nature of the study. The results from the current study, therefore, should be considered exploratory and informative for the design of larger studies in the future.

### **11.6 Conclusions**

Using a specially designed interference task, this study successfully demonstrated the interference effect in premanifest HD and healthy control participants, however, there was no significant between-group difference and no significant change in susceptibility to interference over 12 months. Premanifest HD participants were found to display similar interference effects in both arrow direction conditions and did not show the same marked increase in interference for the left and right facing arrows as the controls, indicating abnormal attentional processing and impaired automaticity. Disease-related cognitive performance was related to clinical measures and macro- and microstructural properties of the caudate and thalamic-prefrontal-cortical WM tracts. These findings indicate that early functional changes in these tracts implicated with inhibitory and attentional control occur in the absence of significant microstructural or cognitive decline. This was an exploratory study and further research is required with a larger cohort over a longer time interval to elucidate the current findings.

## Conclusions

The important role of WM pathology in the manifestation and progression of HD is well established and structural and diffusion MRI studies have already yielded significant insights in this regard. However, further assessment and improvement of current imaging techniques is needed to better ascertain structural brain changes and optimise technique sensitivity, particularly in individuals with less pathology. Similarly, the development of hypothesis-driven, pathology-targeted neuropsychological tasks will help measure the functional effects of WM degeneration in premanifest individuals who show greater variability in cognitive deficits. Application of these optimised techniques to a large cohort of HD gene-carriers and healthy controls will help characterise WM abnormalities and their relation to clinically relevant behaviour.

Studies in this thesis have sought to address the challenges above and have revealed several novel findings. Firstly, a novel segmentation technique for the CC, a key WM structure linking the left and right hemispheres of the brain was successfully developed; when applied to a large clinical cohort this methodology revealed disease-related reduction in baseline CC volume and elevated rates of change over 24 months, even many years prior to disease onset. Associations between CC volume and cognitive performance on tasks requiring interhemispheric communication may reflect degeneration of interhemispheric information transfer in HD, prompting further investigation into evidence that this decline begins well before symptoms. This original work was published in the *Journal of Huntington's Disease*. In addition, the CC segmentation tool was subsequently applied in the EU-funded PADDINGTON study, a large multi-site investigation into potential biomarkers in early HD, resulting in a publication in *NeuroImage*.

One issue which has previously had a negative effect on the investigation of WM microstructure using DTI is that of registration inaccuracy, thereby potentially reducing sensitivity to disease effects. DTI-TK (Zhang *et al.* 2006), a tensor-based registration tool, was developed to improve alignment by matching the orientation of the underlying fibres at each voxel. An investigation into the application of DTI-TK revealed that, overall, there was good agreement between analyses using each of three customised tensor templates, both in terms of extracted diffusion metrics and tract-based between-

group comparisons. Tensor-based registration using DTI-TK was used in further diffusion imaging analysis in this thesis to replicate previous findings of microstructural degeneration in premanifest and manifest HD using TBSS (Smith *et al.* 2006). Evidence was found in support of the superiority of tensor-based registration over scalar-based registration, demonstrated by the discovery of previously undetected changes in WM microstructure in premanifest HD. Findings of increased FA in selected WM regions in HD gene-carriers, however, highlight the importance of interpreting DTI results with caution and to be wary of crossing or interleaving axons.

Investigation into the relationship between diffusion metrics and structural volume revealed associations between WM volume and changes in diffusion in HD gene-carriers, particularly in the absence of an association in the healthy control group, suggest that this relationship is disease-specific. The relationship found in the controls between FA and RD with GM volume may reflect natural biological variation in brain matter volume and WM diffusivity. The unexpected findings however, particularly when examining associations with GM, highlight the complexities of interpreting the diffusion signal using DTI analysis.

In parallel to elucidating WM pathology in HD, this thesis sought to investigate the impact of this pathology on patient function. In particular, the influence of atrophy of the CC was of interest. Having successfully developed an interhemispheric transfer task based upon the Poffenberger paradigm (Poffenberger 1912) and applied it to a cohort of premanifest HD and control participants, results revealed no significant between-group differences in ITT. The premanifest HD group, however, demonstrated an opposite visual field/responding hand asymmetry to the control group, indicating abnormal interhemispheric transfer from the non-dominant to dominant hemisphere. Disease-related non-dominant ITT was also associated with macro- and microstructural properties of the CC, however this was an exploratory study and further research with a larger cohort over a longer time interval will help verify the current findings.

Lastly, using a specially designed interference task, the interference effect (Eriksen & Eriksen 1974) was successfully demonstrated in premanifest HD and healthy control participants, however, there was no significant between-group difference and no significant change in susceptibility to interference over 12 months. Premanifest HD participants, however, displayed similar interference effects in both arrow direction

conditions and did not show the same marked increase in interference for the left and right facing arrows as the controls, indicating abnormal attentional processing and impaired automaticity. Disease-related cognitive performance was related to clinical measures and macro- and microstructural properties of the caudate and thalamic-prefrontal-cortical WM tracts, suggesting that degeneration of these tracts is directly associated with alterations in attention processing and automaticity deficits in HD.

Using multi-modal image analysis and development of novel neuropsychological tests, this thesis has helped characterise WM abnormalities present in premanifest and early HD and their relation to clinically relevant behaviour. The work presented here has led to several advancements in understanding of underlying WM pathology in HD as well as some of the functional effects of degeneration in this tissue in the premanifest stage.

## **Publications**

Published peer-reviewed papers associated with results described in this thesis are detailed below, together with individual contributions. Following the publications is a list of abstracts and accompanying poster titles also associated with results in this thesis.

### **Journal Articles**

#### Chapter 7 - Corpus Callosal Atrophy in Premanifest and Early HD

**Crawford H.E., Hobbs N.Z., Keogh R., Langbehn D.R., Frost C., Johnson H., Landwehrmeyer B., Reilmann R., Craufurd D., Stout J.C., Durr A., Leavitt B.R., Roos R.A., Tabrizi S.J., & Scahill R.I. 2013. Corpus callosal atrophy in premanifest and early Huntington's disease. *Journal of Huntington's Disease*, 2 (4): 517-526.**

For this study I led on the study concept and design, with guidance from Nicola Hobbs and Rachael Scahill. I developed a novel method for volumetric analysis of the CC with input from Nicola Hobbs, Rachael Scahill, Elin Rees and James Cole with regards to the final procedure. I analysed all the data and had statistical supervision from Ruth Keogh, with final statistical revisions from Chris Frost. I compiled the first draft of the manuscript and received input from all authors for the final submitted article.

#### Chapter 3 - Development of a Novel Segmentation Tool

**Hobbs, N. Z., Cole, J.H., Farmer, R. E., Rees, E. M., Crawford, H.E. , Malone, I. B., Roos, R. A. C., Sprengelmeyer, R., Durr, A., Landwehrmeyer, B., Scahill, R. I., Tabrizi, S. J., & Frost, C. (2013). Evaluation of multi-modal, multi-site neuroimaging measures in Huntington's disease: Baseline results from the PADDINGTON study. *NeuroImage: Clinical*, 2, 204-211.**

This publication reports the baseline results from the PADDINGTON study. My main responsibility was volumetric image analysis and the contribution of my CC segmentation technique, which was applied to the data and used in the analysis. I also contacted participants and accompanied them to the scanner when necessary, plus I

provided input for the final manuscript. Specific contributions from the other authors are listed below.

Obtained funding: SJT, BL

Study concept and design: NH, SJT, BL, CF

Acquisition of data: NH, ER, JC

Analysis and interpretation of data: NH, JC, RF, ER, RS, SJT, CF

Statistical analysis: RF, CF

Drafting of the manuscript: NH

Critical revision of the manuscript for important intellectual content: NH, JC, RF, ER, HC, IM, RR, RS, AD, BL, RS, SJT, CF

#### Throughout - The Track-HD Cohort

**Tabrizi, S. J., Scahill, R. I., Owen, G., Durr, A., Leavitt, B. R., Roos, R., Borowsky, B., Landwehrmeyer, B., Frost, C., Johnson, H., Craufurd, D., Reilmann, R., Stout, J. C., & Langbehn, D. (2013). Predictors of phenotypic progression and disease onset in premanifest and early-stage Huntington's disease in the TRACK-HD study: analysis of 36 month observational data. *Lancet Neurology*, 12, 637-649.**

The Track-HD cohort used in this thesis is characterised in a series of four *Lancet Neurology* publications. This publication reports the 36 month results from the study, for which I am listed as an investigator. I was responsible for centralised QC and analysis of the T1-weighted scans from all assessment sites. Specific contributions from the authors are listed below.

Obtained funding: SJT, BL

Study concept and design: SJT, BL, RS, CF



Acquisition of data: Track-HD investigators across the four sites

Analysis and interpretation of data: SJT, RS, CF

Statistical analysis: CF, DL

Drafting of the manuscript: SJT, RS

Critical revision of the manuscript for important intellectual content: All authors

## **Abstracts for Poster Presentations**

### Chapter 8 - Association between Brain Volume and White Matter Microstructure in Healthy Controls and HD Gene-Carriers

**Crawford, H. E., Gregory, S., Hobbs, N.Z., Johnson, H., Cole, J. H., Rees, E. M., Malone, I. B., Sprengelmeyer, R., Durr, A., Leavitt, B. R., Roos, R. A. C., Langbehn, D. R., Landwehrmeyer, G. B., Tabrizi, S., J., & Scahill, R. I. (2014). Association between brain volume and white matter microstructure in healthy controls. *Journal of Neurology Neurosurgery & Psychiatry* 85(Suppl 1):A39-A40.**

This abstract was accepted for a poster presentation at the European Huntington's Disease Network plenary meeting in Barcelona in 2014. I led on the study concept and design, with guidance from Rachael Scahill, Sarah Gregory and Nicola Hobbs. I analysed the data with support from Sarah Gregory. I had help from Rachael Scahill, Sarah Gregory and Nicola Hobbs with drafting of the abstract and creation of the poster. Comments on the final abstract came from all authors.

### Chapter 10 - Interhemispheric Information Transfer Degeneration in Premanifest HD

**Crawford, H. E., Cassidy, A. M., Tabrizi, S. J., Scahill, R. I., & the TrackOn-HD Investigators. (2016). Association between abnormal interhemispheric information transfer and corpus callosal structure in premanifest Huntington's disease.**

This abstract has been submitted and accepted for poster presentation at the Society for Neuroscience conference 'Neuroscience 2016' in San Diego, November 2016. I led on

the study concept and design, with guidance from Rachael Scahill and Marina Papoutsis. I gained ethical approval, recruited all study participants and collected data for the cognitive task component of the study. I also analysed the imaging data that had been collected previously. Statistical analysis was conducted with generous and patient supervision from Amy Cassidy. Comments on the final abstract came from all authors.

## Acknowledgements

Firstly, I would like to thank the participants who generously gave their time to be part of HD research and without whom none of this work would be possible, as well as the European Union and CHDI for funding the PADDINGTON, Track-HD and TrackOn-HD studies and making this research happen in the first place.

I am very grateful to the Brain Research Trust who have funded my four year PhD programme and given me the opportunity to continue to work at such a renowned institution as UCL's Institute of Neurology. I also want to thank the Trust for reminding me why this work is so important.

To all those who have worked and currently work in the HD Research Centre; I could not have done it without you. In particular I must give special thanks to the following: Sarah Tabrizi for the opportunity to work in an amazing research group, there is no better motivation to work hard; Sarah Gregory for all her help with the diffusion analysis, for always making time for me and for always telling it like it is; Eli Johnson for helping with all the image analysis over the years and understanding the highs and lows, and most of all for being my buddy; Amy Cassidy for her generous statistical help and limitless patience; Marina Papoutsis for aiding with my cognitive tasks and her extremely valuable suggestions; and to Elin Rees for simply being such a good act to follow.

Finally, I want to mention Rachael Scahill, one of the most supportive, kind and selfless supervisors there are. Huge thanks to Rach for her constant encouragement, her wealth of knowledge, and her endless drive. A fantastic supervisor but even more an inspirational woman.

Thank you.

# Appendix 1: Volumetric Analysis

## Corpus Callosum Segmentation: Standard Operational Procedure

Chapter 3 describes the development of a manual segmentation protocol for volumetric analysis of the CC. The full protocol is provided below.

### Introduction

This standard operational procedure describes how to manually segment the CC, primarily for use as a ROI over which to compute diffusion metrics. The aim of the segmentation is to include all WM voxels whilst excluding any CSF or blood vessels surrounding the structure. This process should mainly rely upon the thresholds applied with minimum manual editing. Segmentation is to be performed on scans in standard space to ensure consistent orientation and application of landmark-defined cut-offs. Scans are registered to standard space once the whole-brain region has been segmented.

### Procedure

#### Image setup

1. Start MIDAS with the command **wp2-midas -morph 100 150** (this automatically calculates the 100% and 150% of the mean brain intensity (MBI) required later).
2. Load the standard space image by selecting **Regions->Show Database... ->Register-Template-9dof6**
3. Highlight the whole-brain region and select **Measure -> Simple Mean**
4. Read the 100% and 150% of the MBI from the log window and make a note of them.
5. Select **Regions -> Remove** to remove the region.
6. Select **Regions -> Edit -> Irregular volume -> 2 Views**
7. Select sagittal view in the main window, magnified by approximately 6.
8. Select coronal view in the edit window, magnified by approximately 2.

9. Move the position bar in the sagittal view to be in line with the anterior commissure (see Figure Appendix 1- 1), where the yellow circle highlights the location of the anterior commissure.
10. Check in the coronal view that the position bar is located in the centre of the two ventricles where they are at their closest point. **It may be necessary to move the position bar in the coronal view to the left or right to locate the mid-sagittal slice. Always chose the slice in the sagittal view where there is the least brain evident surrounding the corpus callosum.** This is to be the starting mid-sagittal slice for the segmentation (see Figure Appendix 1- 1). Make a note of this slice.
  - a. Rarely some participants have cavum septum pellucidum, which means that there is a space between the two leaflets of their septum pellucidum. In these cases the mid-sagittal slice should be selected the same but you should firstly place the position bar in the centre of the space between the two ventricles (see Figure Appendix 1- 1). Continue as normal.
11. Set the upper and lower thresholds to be 100% and 150% of the MBI.

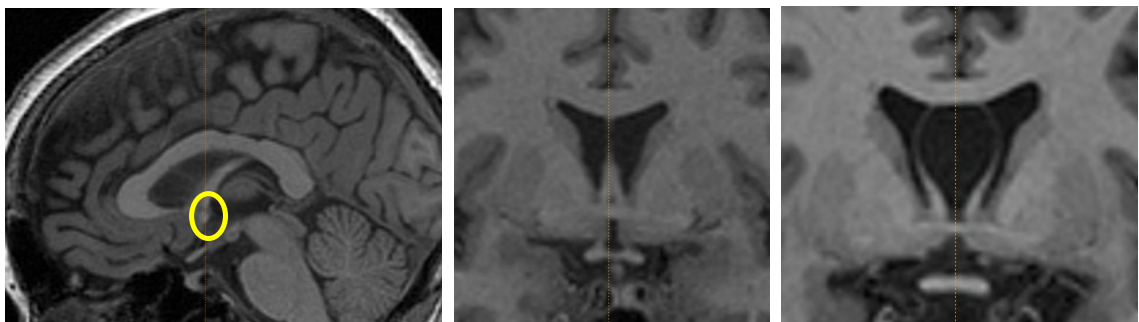


*Figure Appendix 1- 1. Left: Typical starting slice. Sagittal view with anterior commissure. The mid-sagittal slice is easily seen by brain beginning to disappear, as in the top-left of the scan. Middle: Coronal view showing the centre of the two ventricles. Right: Coronal view showing the centre in an example of cavum septum pellucidum.*

### **Sagittal segmentation**

12. Begin by placing a seed in the corpus callosum on the mid-sagittal slice.
13. Using the draw tool edit the borders where the region might be spilling out. Most commonly the rostrum needs to be edited and the fornix removed (see Figure Appendix 1- 2).

- a. As the rostrum curves round and extends, edit where it is obvious that the corpus callosum stops, otherwise go with the thresholds and don't make any minor edits (see Figure Appendix 1- 3).
- b. Remove any other obvious protrusions that could occur above or underneath the structure (see Figure Appendix 1- 4).
- c. **Flick between view (V) and draw (D) mode to keep the borders in mind as you do this.**
- d. **Let the thresholds do the majority of the work.**
- e. In some cases blood vessels appear as areas of hyper-intensity. These should be cut out where they run adjacent to the structure (Figure Appendix 1- 4) and when it is clear that it is a vessel and it is moving away from the corpus callosum (Figure Appendix 1- 5, in pink). Areas of hyperintensity that remain bright when leaving the structure should be removed but areas that become dark once outside the region should be left in.
- f. **If the vessels or regions of hyper-intensity run solely within the body of the structure they should not be edited out. i.e if you cannot see a vessel moving away from the boundaries of the corpus callosum on that particular slice do not edit out the hyper-intensity, instead follow the line of the structure (see Figure Appendix 1- 5). This is most commonly seen in the body of the corpus callosum and usually only involves a couple of voxels. To reiterate never cut into the body of the corpus callosum, instead follow the line of the structure and only remove bits that you are certain are not corpus callosal matter.**
- g. Sometimes internal holes occur within the segmentation that are biologically implausible. These should be filled in manually once the threshold has been applied (**App.Thresh.**) by placing a seed within the hole (see Figure Appendix 1- 6).
- h. If any area within the segmentation is brighter than the 150% threshold but is clearly not a blood vessel then this too should be manually filled in regardless of whether it is on the edge of the structure or not (see Figure Appendix 1- 6). However **do not fill** if the area is on the edge and is darker than the 100% threshold (see Figure Appendix 1- 6).

- i. Finally **if you are certain** that there is an area included in the thresholds that is **definitely not** part of the corpus callosum then **remove**.
14. Move up a slice in the sagittal view (i.e. move right one slice across the brain) and repeat the segmentation. Continue for four slices then stop (i.e. four slices in addition to the mid-sagittal slice).
15. Go back to the starting mid-sagittal slice and move down a slice in the sagittal view (i.e. move left across the brain) and segment. Again, continue until four slices have been segmented.
16. The whole segmentation should contain **9 slices** of the brain i.e. the mid-sagittal slice, plus four slices either side.
17. Finally press **App. Thresh.** to apply the threshold.

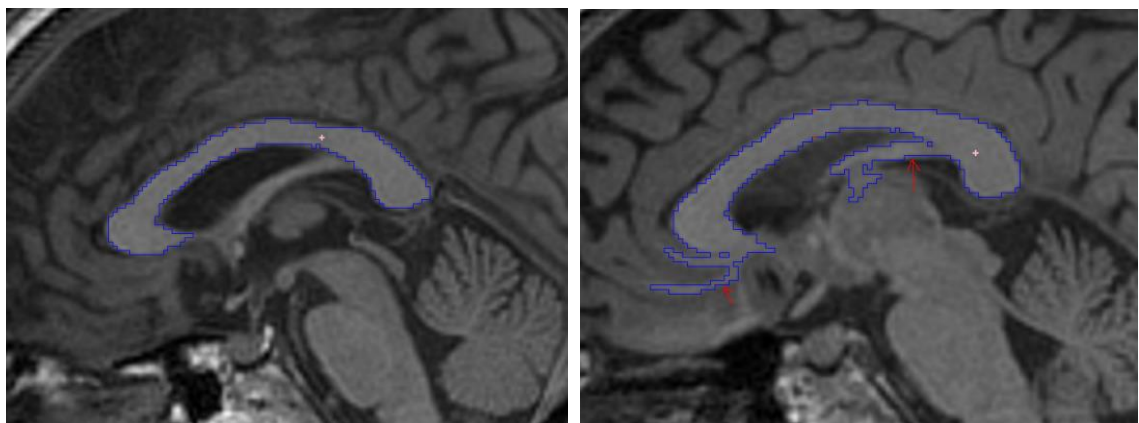


*Figure Appendix 1- 2. Left: Seeded region where threshold has successfully segmented the structure with no over-spill. Right: Editing is necessary to remove the fornix and rostral seepage (red arrows).*

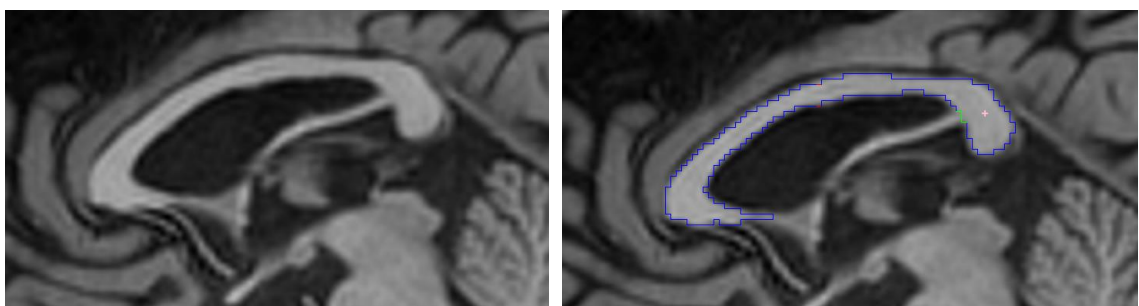


*Figure Appendix 1- 3. Example of an ambiguous edit to the rostrum. Left image shows the corpus callosum and the right shows the ROI segmentation over the top. In this case do not edit and trust the thresholds.*

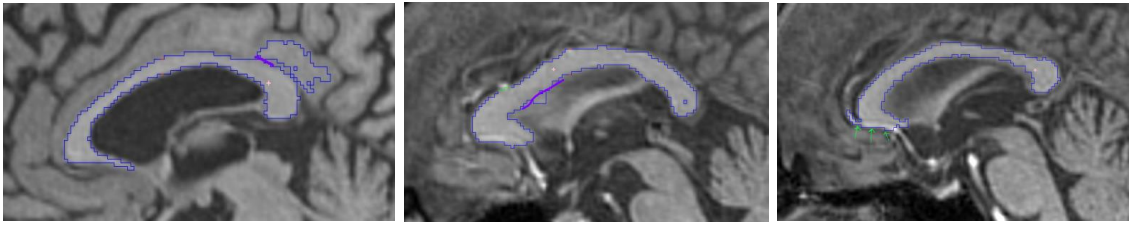


**Figure Appendix 1- 4.** Left and middle: Examples of obvious edits, delineated by the purple line. Right: Example of a blood vessel that needs removing, highlighted by the green arrows.

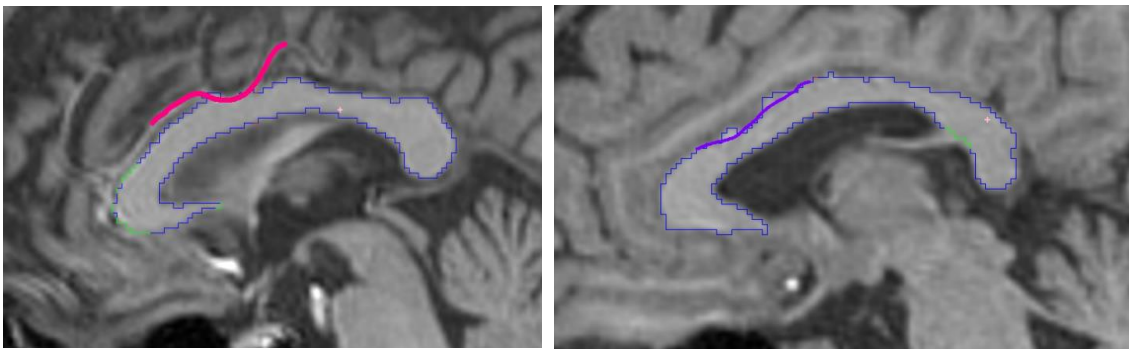


**Figure Appendix 1- 5.** Left: Blood vessel, shown in pink, which needs to be removed from the top of corpus callosum in this example. Right: Purple line delineating how to edit the segmentation. In this case no vessels can be seen moving away from the corpus callosum therefore follow the line of the structure and do not cut in.

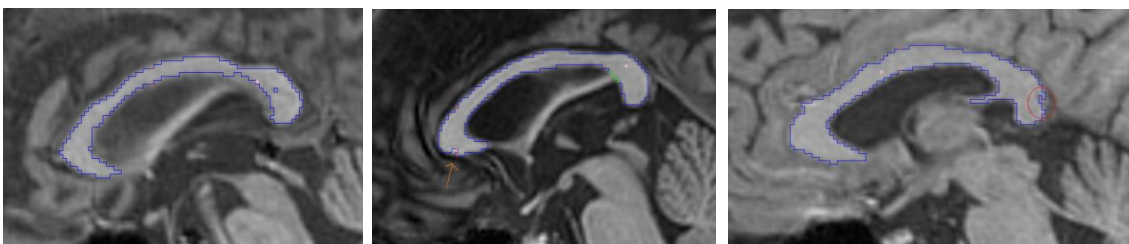


**Figure Appendix 1- 6.** Left: Showing hole within the body of the structure that should be filled in. Middle: Orange arrow indicating area of hyper-intensity that is not a vessel and therefore should be filled in. Right: Example of area that is darker than the 100% threshold and should not be filled in, highlighted in red circle.



## Sanity Check

18. Check that you have segmented **9 slices** in total, i.e the mid-sagittal slice plus four slices either side.

## Saving the region

19. Click OK in the dual edit window.
20. In sagittal view highlight the region, turning the outline from blue to red.
21. Save in the appropriate database by selecting **Regions-> Database In...**  
-> **Projects-> Corpus\_Callosum**, noting down the quality, the thresholds and the mid-sagittal slice number  
(e.g. OK\_lowerthreshold\_upperthreshold\_midsagslice).

## Appendix 2: Sample Size Calculations

The sample size estimates below for the two cognitive tasks (chapters 10 and 11) are imprecise and are unadjusted for potential confounders (apart from the estimates using the Track-HD study). Firstly, it is not clear to what extent the studies, other than Track-HD, are directly applicable to HD. The studies were also very small in terms of sample size, so estimates of effect sizes would likely have large confidence intervals. However, these studies were included in the sample size calculation due to the literature using these tasks being very limited.

Despite the fact that the sample recruited for the tasks was smaller than the estimated calculations below, there were many repetitions per experimental condition in each task, which was hoped to counterbalance this.

### Interhemispheric Transfer Task

The main outcomes were:

1. Reaction time (RT) in milliseconds under ‘crossed’ (stimulus and responding hand on opposite sides) and ‘uncrossed’ (same sides) conditions.
2. Crossed-Uncrossed Difference (CUD): difference in milliseconds between RTs under the crossed and uncrossed conditions (also referred to as interhemispheric transfer time; ITT).

Sample size calculations were given for the null hypothesis, testing the aim ‘premanifest HD participants have increased ITT compared with healthy controls’, which was thought to be the most difficult to detect. The hypothesis was a general group comparison  $H_0: CUD_{premanifest} = CUD_{controls}$ , which was a two-sample t-test on whether the mean CUDs were equal in controls and premanifest individuals. The regression model used to test the hypothesis looked for a group difference in RTs after adjusting for disease burden and other confounders.

Main assumptions:

1. The outcomes would be assessed using ordinary least squares (OLS) regression.
2. Residual variability in the outcome would be equal in both groups. (This may not be the case in reality, and if ultimately a generalised least squares (GLS) approach was determined to be more appropriate, sample size requirements could vary in either direction).
3. The parameter estimates would be adjusted for a predefined set of potential confounders.

Although effect sizes were unknown, possible values were estimated using comparable tasks from the Track-HD study (Tabrizi *et al.* 2009) and results from the Poffenberger Paradigm, an ITT task first developed by Poffenberger (1912) in studies of other diseases.

4. Adjusted cross-sectional effect sizes of 0.22 (Indirect Circle Tracing), 0.23 (Symbol Digit Modalities Test; SDMT), and 0.44 (Speeded Tapping mean inter-tap interval) were reported after visit 1 of Track-HD (Tabrizi *et al.* 2009). Further approximate unadjusted cross-sectional effect sizes were hand-calculated using results published in aging research; 0.63 (Jeeves & Moes 1996), split-brain individuals; 0.17 (Ouimet *et al.* 2010) and sport physiology; 0.38 (Semprini *et al.* 2012). These were imprecise since it was unclear to what extent these effect sizes were directly applicable to analyses using HD groups. Furthermore, effects were unadjusted for potential confounders, which could create bias in either direction. Estimates in this entire interval were included for comparison.
5. The power for the range of potential effect sizes and participant numbers based on London recruitment databases was also calculated.
6. Controls and premanifest HD participants were to be recruited into the study in a 1:1 ratio.

**Table Appendix 2 - 1. Total number of participants required (i.e. half of the reported number for each group) to test the hypothesis that CUDpremanifest = CUDcontrols for a range of potential effect sizes and statistical power. All alpha=0.05.**

<b>Effect Size</b>	<b>Study (year) effect size seen in Task</b>	<b>70% Power</b>	<b>80% Power</b>	<b>90% Power</b>
<b>0.10</b>	<i>low estimate</i>	2472	3142	4206
<b>0.22</b>	Tabrizi <i>et al.</i> (2009) Indirect Circle Tracing	514	652	872
<b>0.23</b>	Tabrizi <i>et al.</i> (2009) SDMT*	470	596	798
<b>0.38</b>	Semprini <i>et al.</i> (2012) Poffenberger Paradigm	174	220	294
<b>0.44</b>	Tabrizi <i>et al.</i> (2009) Speeded Tapping	130	166	220
<b>0.63</b>	Jeeves & Moes (1996) CUD Paradigm** <i>high estimate</i>	66	82	108

\*Symbol Digit Modalities Test; \*\*Crossed-Uncrossed Difference

**Table Appendix 2 - 2. Power achievable to test the hypothesis that CUDpremanifest = CUDcontrols for a range of potential effect sizes and total N (N to be split in 1:1 ratio between controls and premanifest individuals). All alpha=0.05.**

<b>Effect Size</b>	<b>Study (year) effect size seen in Task</b>	<b>50 Participants</b>	<b>60 Participants</b>	<b>70 Participants</b>
<b>0.10</b>	<i>low estimate</i>	6.4	6.7	7.0
<b>0.22</b>	Tabrizi <i>et al.</i> (2009) Indirect circle tracing	11.9	13.4	14.8
<b>0.23</b>	Tabrizi <i>et al.</i> (2009) SDMT*	12.5	14.1	15.8
<b>0.38</b>	Semprini <i>et al.</i> (2012) Poffenberger Paradigm	26.1	30.4	34.7
<b>0.44</b>	Tabrizi <i>et al.</i> (2009) Speeded Tapping	33.2	38.9	44.2
<b>0.63</b>	Jeeves & Moes (1996) CUD Paradigm** <i>high estimate</i>	58.8	67.0	73.8

\*Symbol Digit Modalities Test; \*\*Crossed-Uncrossed Difference

## **Interference Task**

The main outcome was:

1. RT in milliseconds under ‘congruent’ (target and flankers pointing in same direction) and ‘incongruent’ (different directions) trials.

Sample size calculations were given for the null hypothesis testing the aim ‘premanifest HD participants will have longer RTs in the incongruent trials, i.e. a larger flanker effect compared with controls’, which was thought to be the most difficult to detect. This hypothesis was a general group comparison  $H_0: RT_{premanifest} = RT_{controls}$ , which was a two-sample t-test on whether the mean RTs were equal in controls and premanifest individuals.

A regression model was to test for a group difference in RTs after adjusting for disease burden and other confounders.

Main assumptions:

1. The outcomes would be assessed using OLS regression.
2. Residual variability in the outcome would be equal in both groups. (This may not be the case in reality, and if ultimately a GLS approach was determined to be more appropriate, sample size requirements could vary in either direction).
3. The parameter estimates would be adjusted for a predefined set of potential confounders.

Although effect sizes were unknown, possible values were estimated using comparable tasks from the Track-HD study (Tabrizi *et al.* 2009) and results from the Flanker task in one, a study in premanifest HD participants of conflict monitoring and task switching using Stroop interference (Beste *et al.* 2012) and two, a study of mild cognitive impairment (Wang *et al.* 2013).

4. Adjusted cross-sectional effect sizes of 0.23 (SDMT) were reported after visit 1 in the Track-HD study (Tabrizi *et al.* 2009), an unadjusted cross-sectional effect size of 0.92 was hand-calculated from results published in Beste *et al.* (2012), and an age- and Mini Mental State Examination-adjusted cross-sectional effect size of 0.34 was hand-calculated from results published in Wang *et al.* (2013). Estimates in this interval were included for comparison.
5. The power for the range of potential effect sizes and participant numbers based on London recruitment databases was also calculated.
6. Controls and premanifest HD participants were to be recruited into the study in a 1:1 ratio.

**Table Appendix 2 - 3. Total number of participants required to test the hypothesis  $RT_{premanifest} = RT_{controls}$  for a range of potential effect sizes and statistical power. All  $\alpha=0.05$ .**

<b>Effect size</b>	<b>Study (year) effect size seen in Task</b>	<b>70% power</b>	<b>80% power</b>	<b>90% power</b>
<b>0.10</b>	<i>low estimate</i>	2472	3142	4206
<b>0.23</b>	Tabrizi <i>et al.</i> (2009) SDMT*	470	596	798
<b>0.34</b>	Wang <i>et al.</i> (2013) Eriksen Flanker Task	216	274	366
<b>0.44</b>	<i>intermediate estimate</i>	130	166	220
<b>0.63</b>	<i>intermediate estimate</i>	66	82	108
<b>0.92</b>	Beste <i>et al.</i> (2012) Stroop and Task Switching	32	40	52

\*Symbol Digit Modalities Test

**Table Appendix 2 - 4. Power achievable to test the hypothesis RTpremanifest = RTcontrols for a range of potential effect sizes and total N (N to be split in 1:1 ratio between controls and premanifest individuals). All alpha=0.05.**

<b>Effect size</b>	<b>Study (year) effect size seen in Task</b>	<b>50 subjeсs</b>	<b>60 participants</b>	<b>70 participants</b>
<b>0.10</b>	<i>low estimate</i>	6.4	6.7	7.0
<b>0.23</b>	(Tabrizi <i>et al.</i> 2009) SDMT*	12.5	14.1	15.8
<b>0.34</b>	(Wang <i>et al.</i> 2013) Eriksen Flanker Task	21.8	25.4	28.9
<b>0.44</b>	<i>intermediate estimate</i>	33.2	38.8	44.2
<b>0.63</b>	<i>intermediate estimate</i>	58.8	67.0	73.8
<b>0.92</b>	(Beste <i>et al.</i> 2012) Stroop and Task Switching	89.0	93.9	96.7

\*Symbol Digit Modalities Test

It is important to emphasise that the sample size calculations above are not exact estimates and are based on indirectly related literature. There was a strong rationale for conducting these tasks in premanifest HD participants and due to the exploratory nature of the study it was necessary to choose a sample size that was feasible for pilot data.



## References

- Aboitiz F., Scheibel A.B., Fisher R.S., & Zaidel E. 1992a. Fiber composition of the human corpus callosum. *Brain Res*, 598 (1-2): 143-153.
- Aboitiz F., Scheibel A.B., Fisher R.S., & Zaidel E. 1992b. Individual differences in brain asymmetries and fiber composition in the human corpus callosum. *Brain Res*, 598 (1-2): 154-161.
- Adluru N., Zhang H., Fox A.S., Shelton S.E., Ennis C.M., Bartosic A.M., Oler J.A., Tromp D.P.M., Zakszewski E., Gee J.C., Kalin N.H., & Alexander A.L. 2012. A diffusion tensor brain template for rhesus macaques. *Neuroimage*, 59 (1): 306-318.
- Alexander A.L., Lee J.E., Lazar M., & Field A.S. 2007. Diffusion tensor imaging of the brain. *Neurotherapeutics*, 4 (3): 316-329.
- Alexander D.C., Pierpaoli C., Basser P.J., & Gee J.C. 2001. Spatial transformations of diffusion tensor magnetic resonance images. *IEEE Trans Med Imaging*, 20 (11): 1131-1139.
- Andersson J.L., Jenkinson M., & Smith S. 2007a. Non-linear optimisation. *FMRIB technical report TR07JA1*.
- Andersson J.L., Jenkinson M., & Smith S. 2007b. Non-linear registration, aka spatial normalisation. *FMRIB technical report TR07JA2*.
- Arnold J.B., Liow J.S., Schaper K.A., Stern J.J., Sled J.G., Shattuck D.W., Worth A.J., Cohen M.S., Leahy R.M., Mazziotta J.C., & Rottenberg D.A. 2001. Qualitative and quantitative evaluation of six algorithms for correcting intensity nonuniformity effects. *Neuroimage*, 13 (5): 931-943.
- Ashburner J., & Friston K.J. 2000. Voxel-based morphometry—the methods. *Neuroimage*, 11 (6): 805-821.
- Ashburner J., & Friston K.J. 2005. Unified segmentation. *Neuroimage*, 26 (3): 839-851.

- Ashburner J. 2007. A fast diffeomorphic image registration algorithm. *Neuroimage*, 38 (1): 95-113.
- Assaf Y., & Pasternak O. 2008. Diffusion tensor imaging (DTI)-based white matter mapping in brain research: A review. *J Mol Neurosci*, 34 (1): 51-61.
- Avants B.B., Tustison N.J., Stauffer M., Song G., Wu B., & Gee J.C. 2014. The insight toolkit image registration framework. *Front Neuroinform*, 8: 44.
- Aylward E.H., Codori A.M., Barta P.E., Pearlson G.D., Harris G.J., & Brandt J. 1996. Basal ganglia volume and proximity to onset in presymptomatic Huntington disease. *Arch Neurol*, 53 (12): 1293-1296.
- Aylward E.H., Nopoulos P.C., Ross C.A., Langbehn D.R., Pierson R.K., Mills J.A., Johnson H.J., Magnotta V.A., Juhl A.R., & Paulsen J.S. 2011. Longitudinal change in regional brain volumes in prodromal Huntington disease. *J Neurol Neurosurg Psychiatry*, 82 (4): 405-410.
- Bach M., Laun F.B., Leemans A., Tax C.M.W., Biessels G.J., Stieltjes B., & Maier-Hein K.H. 2014. Methodological considerations on tract-based spatial statistics (tbss). *Neuroimage*, 100: 358-369.
- Barnes J., Ridgway G.R., Bartlett J., Henley S.M., Lehmann M., Hobbs N., Clarkson M.J., MacManus D.G., Ourselin S., & Fox N.C. 2010. Head size, age and gender adjustment in MRI studies: A necessary nuisance? *Neuroimage*, 53 (4): 1244-1255.
- Basser P.J., Mattiello J., & LeBihan D. 1994. MR diffusion tensor spectroscopy and imaging. *Biophys J*, 66 (1): 259-267.
- Basser P.J., Pajevic S., Pierpaoli C., Duda J., & Aldroubi A. 2000. In vivo fiber tractography using DT-MRI data. *Magn Reson Med*, 44 (4): 625-632.
- Bates G.P., Dorsey R., Gusella J.F., Hayden M.R., Kay C., Leavitt B.R., Nance M., Ross C.A., Scahill R.I., Wetzel R., Wild E.J., & Tabrizi S.J. 2015. Huntington disease. *Nat Rev Dis Primers*, 1: 15005.
- Beaulieu C. 2002. The basis of anisotropic water diffusion in the nervous system - a technical review. *NMR Biomed*, 15 (7-8): 435-455.

Behrens T.E., Woolrich M.W., Jenkinson M., Johansen-Berg H., Nunes R.G., Clare S., Matthews P.M., Brady J.M., & Smith S.M. 2003. Characterization and propagation of uncertainty in diffusion-weighted MR imaging. *Magn Reson Med*, 50 (5): 1077-1088.

Behrens T.E., Berg H.J., Jbabdi S., Rushworth M.F., & Woolrich M.W. 2007. Probabilistic diffusion tractography with multiple fibre orientations: What can we gain? *Neuroimage*, 34 (1): 144-155.

Beste C., Saft C., Andrich J., Gold R., & Falkenstein M. 2008a. Stimulus-response compatibility in Huntington's disease: A cognitive-neurophysiological analysis. *J Neurophysiol*, 99 (3): 1213-1223.

Beste C., Saft C., Konrad C., Andrich J., Habbel A., Schepers I., Jansen A., Pfeleiderer B., & Falkenstein M. 2008b. Levels of error processing in Huntington's disease: A combined study using event-related potentials and voxel-based morphometry. *Hum Brain Mapp*, 29 (2): 121-130.

Beste C., Konrad C., Saft C., Ukas T., Andrich J., Pfeleiderer B., Hausmann M., & Falkenstein M. 2009. Alterations in voluntary movement execution in Huntington's disease are related to the dominant motor system: Evidence from event-related potentials. *Exp Neurol*, 216 (1): 148-157.

Beste C., Ness V., Lukas C., Hoffmann R., Stuwe S., Falkenstein M., & Saft C. 2012. Mechanisms mediating parallel action monitoring in fronto-striatal circuits. *Neuroimage*, 62 (1): 137-146.

Bloom J.S., & Hynd G.W. 2005. The role of the corpus callosum in interhemispheric transfer of information: Excitation or inhibition? *Neuropsychol Rev*, 15 (2): 59-71.

Bocci T., Hensghens M.J., Di Rollo A., Parenti L., Barloscio D., Rossi S., & Sartucci F. 2015. Impaired interhemispheric processing in early Huntington's disease: A transcranial magnetic stimulation study. *Clin Neurophysiol*: 1750-1752.

Bohanna I., Georgiou-Karistianis N., Sritharan A., Asadi H., Johnston L., Churchyard A., & Egan G. 2011. Diffusion tensor imaging in Huntington's disease reveals distinct patterns of white matter degeneration associated with motor and cognitive deficits. *Brain Imaging Behav*, 5 (3): 171-180.

Bookstein F.L. 2001. "Voxel-based morphometry" should not be used with imperfectly registered images. *Neuroimage*, 14 (6): 1454-1462.

Bora E., Velakoulis D., & Walterfang M. 2015. Social cognition in Huntington's disease: A meta-analysis. *Behav Brain Res*, 297: 131-140.

Botvinick M.M., Cohen J.D., & Carter C.S. 2004. Conflict monitoring and anterior cingulate cortex: An update. *Trends Cogn Sci*, 8 (12): 539-546.

Bourassa D.C., McManus I.C., & Bryden M.P. 1996. Handedness and eye-dominance: A meta-analysis of their relationship. *Laterality*, 1 (1): 5-34.

Bourne V.J. 2006. The divided visual field paradigm: Methodological considerations. *Laterality*, 11 (4): 373-393.

Boyes R.G., Gunter J.L., Frost C., Janke A.L., Yeatman T., Hill D.L.G., Bernstein M.A., Thompson P.M., Weiner M.W., Schuff N., Alexander G.E., Killiany R.J., DeCarli C., Jack C.R., & Fox N.C. 2008. Intensity non-uniformity correction using n3 on 3-t scanners with multichannel phased array coils. *Neuroimage*, 39 (4): 1752-1762.

Brown L.N., Zhang Y., Mitchell J.R., Zabad R., & Metz L.M. 2010. Corpus callosum volume and interhemispheric transfer in multiple sclerosis. *Can J Neurol Sci*, 37 (5): 615-619.

Cagigas X.E., Filoteo J.V., Stricker J.L., Rilling L.M., & Friedrich F.J. 2007. Flanker compatibility effects in patients with parkinson's disease: Impact of target onset delay and trial-by-trial stimulus variation. *Brain Cogn*, 63 (3): 247-259.

Catani M., Howard R.J., Pajevic S., & Jones D.K. 2002. Virtual in vivo interactive dissection of white matter fasciculi in the human brain. *Neuroimage*, 17 (1): 77-94.

Chaumillon R., Blouin J., & Guillaume A. 2014. Eye dominance influences triggering action: The Poffenberger paradigm revisited. *Cortex*, 58: 86-98.

Cherbuin N., & Brinkman C. 2006. Efficiency of callosal transfer and hemispheric interaction. *Neuropsychology*, 20 (2): 178-184.

Cicchetti D.V. 1994. Guidelines, criteria, and rules of thumb for evaluating normed and standardized assessment instruments in psychology. *Psychological assessment*, 6 (4): 284.

Cole J.H., Farmer R.E., Rees E.M., Johnson H.J., Frost C., Scahill R.I., & Hobbs N.Z. 2014. Test-retest reliability of diffusion tensor imaging in Huntington's disease. *PLoS Curr*, 6.

Corballis M.C. 2002. Hemispheric interactions in simple reaction time. *Neuropsychologia*, 40 (4): 423-434.

Crawford H.E., Hobbs N.Z., Keogh R., Langbehn D.R., Frost C., Johnson H., Landwehrmeyer B., Reilmann R., Craufurd D., Stout J.C., Durr A., Leavitt B.R., Roos R.A., Tabrizi S.J., & Scahill R.I. 2013. Corpus callosal atrophy in premanifest and early Huntington's disease. *J Huntingtons Dis*, 2 (4): 517-526.

Davies S.W., Turmaine M., Cozens B.A., DiFiglia M., Sharp A.H., Ross C.A., Scherzinger E., Wanker E.E., Mangiarini L., & Bates G.P. 1997. Formation of neuronal intranuclear inclusions underlies the neurological dysfunction in mice transgenic for the hd mutation. *Cell*, 90 (3): 537-548.

Della Nave R., Ginestroni A., Tessa C., Giannelli M., Piacentini S., Filippi M., & Mascalchi M. 2010. Regional distribution and clinical correlates of white matter structural damage in Huntington disease: A tract-based spatial statistics study. *AJNR Am J Neuroradiol*, 31 (9): 1675-1681.

Delmaire C., Dumas E.M., Sharman M.A., van den Bogaard S.J., Valabregue R., Jauffret C., Justo D., Reilmann R., Stout J.C., Craufurd D., Tabrizi S.J., Roos R.A., Durr A., & Lehericy S. 2013. The structural correlates of functional deficits in early Huntington's disease. *Hum Brain Mapp*, 34 (9): 2141-2153.

DeLong M.R., & Wichmann T. 2007. Circuits and circuit disorders of the basal ganglia. *Arch Neurol*, 64 (1): 20-24.

Derakhshan I. 2006. Crossed-uncrossed difference (cud) in a new light: Anatomy of the negative cud in Poffenberger's paradigm. *Acta Neurol Scand*, 113 (3): 203-208.

Di Paola M., Luders E., Cherubini A., Sanchez-Castaneda C., Thompson P.M., Toga A.W., Caltagirone C., Orobello S., Elifani F., Squitieri F., & Sabatini U. 2012.

Multimodal MRI analysis of the corpus callosum reveals white matter differences in presymptomatic and early Huntington's disease. *Cereb Cortex*, 22 (12): 2858-2866.

Di Paola M., Phillips O.R., Sanchez-Castaneda C., Di Pardo A., Maglione V., Caltagirone C., Sabatini U., & Squitieri F. 2014. MRI measures of corpus callosum iron and myelin in early Huntington's disease. *Hum Brain Mapp*, 35 (7): 3143-3151.

DiFiglia M., Sapp E., Chase K.O., Davies S.W., Bates G.P., Vonsattel J.P., & Aronin N. 1997. Aggregation of Huntingtin in neuronal intranuclear inclusions and dystrophic neurites in brain. *Science*, 277 (5334): 1990-1993.

Douaud G., Gaura V., Ribeiro M.J., Lethimonnier F., Maroy R., Verny C., Krystkowiak P., Damier P., Bachoud-Levi A.C., Hantraye P., & Remy P. 2006. Distribution of grey matter atrophy in Huntington's disease patients: A combined roi-based and voxel-based morphometric study. *Neuroimage*, 32 (4): 1562-1575.

Douaud G., Behrens T.E., Poupon C., Cointepas Y., Jbabdi S., Gaura V., Golestani N., Krystkowiak P., Verny C., Damier P., Bachoud-Lévi A.-C., Hantraye P., & Remy P. 2009. In vivo evidence for the selective subcortical degeneration in Huntington's disease. *Neuroimage*, 46 (4): 958-966.

Dumas E.M., van den Bogaard S.J., Ruber M.E., Reilman R.R., Stout J.C., Craufurd D., Hicks S.L., Kennard C., Tabrizi S.J., van Buchem M.A., van der Grond J., & Roos R.A. 2012. Early changes in white matter pathways of the sensorimotor cortex in premanifest Huntington's disease. *Hum Brain Mapp*, 33 (1): 203-212.

Dumas E.M., van den Bogaard S.J., Middelkoop H.A., & Roos R.A. 2013. A review of cognition in Huntington's disease. *Front Biosci (Schol Ed)*, 5: 1-18.

Dyhring T., Nielsen E.Ø., Sonesson C., Pettersson F., Karlsson J., Svensson P., Christophersen P., & Waters N. 2010. The dopaminergic stabilizers pridopidine (acr16) and (–)-osu6162 display dopamine d2 receptor antagonism and fast receptor dissociation properties. *European Journal of Pharmacology*, 628 (1–3): 19-26.

Eickhoff S.B., Stephan K.E., Mohlberg H., Grefkes C., Fink G.R., Amunts K., & Zilles K. 2005. A new spm toolbox for combining probabilistic cytoarchitectonic maps and functional imaging data. *Neuroimage*, 25 (4): 1325-1335.

Eriksen B., & Eriksen C. 1974. Effects of noise letters upon the identification of a target letter in a nonsearch task. *Perception & Psychophysics*, 16 (1): 143-149.

Estrada Sanchez A.M., Mejia-Toiber J., & Massieu L. 2008. Excitotoxic neuronal death and the pathogenesis of Huntington's disease. *Arch Med Res*, 39 (3): 265-276.

Fabri M., Polonara G., Mascioli G., Salvolini U., & Manzoni T. 2011. Topographical organization of human corpus callosum: An fMRI mapping study. *Brain Res*, 1370: 99-111.

Fabri M., & Polonara G. 2013. Functional topography of human corpus callosum: An fMRI mapping study. *Neural Plast*, 2013: 251308.

Fabri M., Pierpaoli C., Barbaresi P., & Polonara G. 2014. Functional topography of the corpus callosum investigated by DTI and fMRI. *World J Radiol*, 6 (12): 895-906.

Fischl B., & Dale A.M. 2000. Measuring the thickness of the human cerebral cortex from magnetic resonance images. *Proc Natl Acad Sci U S A*, 97 (20): 11050-11055.

Fischl B., Salat D.H., Busa E., Albert M., Dieterich M., Haselgrove C., van der Kouwe A., Killiany R., Kennedy D., Klaveness S., Montillo A., Makris N., Rosen B., & Dale A.M. 2002. Whole brain segmentation: Automated labeling of neuroanatomical structures in the human brain. *Neuron*, 33 (3): 341-355.

Fischl B., Salat D.H., van der Kouwe A.J., Makris N., Segonne F., Quinn B.T., & Dale A.M. 2004a. Sequence-independent segmentation of magnetic resonance images. *Neuroimage*, 23 Suppl 1: S69-84.

Fischl B., van der Kouwe A., Destrieux C., Halgren E., Segonne F., Salat D.H., Busa E., Seidman L.J., Goldstein J., Kennedy D., Caviness V., Makris N., Rosen B., & Dale A.M. 2004b. Automatically parcellating the human cerebral cortex. *Cereb Cortex*, 14 (1): 11-22.

Freeborough P.A., Fox N.C., & Kitney R.I. 1997. Interactive algorithms for the segmentation and quantitation of 3-d MRI brain scans. *Comput Methods Programs Biomed*, 53 (1): 15-25.

Genc S., Steward C.E., Malpas C.B., Velakoulis D., O'Brien T.J., & Desmond P.M. 2015. Short-term white matter alterations in alzheimer's disease characterized by diffusion tensor imaging. *J Magn Reson Imaging*:

Georgiou-Karistianis N., Sritharan A., Farrow M., Cunnington R., Stout J., Bradshaw J., Churchyard A., Brawn T.L., Chua P., Chiu E., Thiruvady D., & Egan G. 2007. Increased cortical recruitment in Huntington's disease using a simon task. *Neuropsychologia*, 45 (8): 1791-1800.

Georgiou N., Bradshaw J.L., Phillips J.G., Bradshaw J.A., & Chiu E. 1995. The simon effect and attention deficits in gilles de la tourette's syndrome and Huntington's disease. *Brain*, 118 ( Pt 5): 1305-1318.

Gispert J.D., Reig S., Pascau J., Vaquero J.J., Garcia-Barreno P., & Desco M. 2004. Method for bias field correction of brain t1-weighted magnetic resonance images minimizing segmentation error. *Hum Brain Mapp*, 22 (2): 133-144.

Goto M., Abe O., Miyati T., Kabasawa H., Takao H., Hayashi N., Kurosu T., Iwatsubo T., Yamashita F., Matsuda H., Mori H., Kunitatsu A., Aoki S., Ino K., Yano K., & Ohtomo K. 2012. Influence of signal intensity non-uniformity on brain volumetry using an atlas-based method. *Korean J Radiol*, 13 (4): 391-402.

Gray M.A., Egan G.F., Ando A., Churchyard A., Chua P., Stout J.C., & Georgiou-Karistianis N. 2013. Prefrontal activity in Huntington's disease reflects cognitive and neuropsychiatric disturbances: The IMAGE-HD study. *Exp Neurol*, 239: 218-228.

Gregory S., Scahill R.I., Seunarine K.K., Stopford C., Zhang H., Zhang J., Orth M., Durr A., Roos R.A., Langbehn D.R., Long J.D., Johnson H., Rees G., Tabrizi S.J., & Craufurd D. 2015. Neuropsychiatry and white matter microstructure in Huntington's disease. *J Huntingtons Dis*: 239-249.

Greve D.N., & Fischl B. 2009. Accurate and robust brain image alignment using boundary-based registration. *Neuroimage*, 48 (1): 63-72.

Gusella J.F., MacDonald M.E., & Lee J.M. 2014. Genetic modifiers of Huntington's disease. *Mov Disord*, 29 (11): 1359-1365.

Harper S.Q., Staber P.D., He X., Eliason S.L., Martins I.H., Mao Q., Yang L., Kotin R.M., Paulson H.L., & Davidson B.L. 2005. Rna interference improves motor and neuropathological abnormalities in a Huntington's disease mouse model. *Proc Natl Acad Sci U S A*, 102 (16): 5820-5825.



Harrington D.L., Smith M.M., Zhang Y., Carlozzi N.E., & Paulsen J.S. 2012. Cognitive domains that predict time to diagnosis in prodromal Huntington disease. *J Neurol Neurosurg Psychiatry*, 83 (6): 612-619.

Hart E.P., Dumas E.M., van Zwet E.W., van der Hiele K., Jurgens C.K., Middelkoop H.A., van Dijk J.G., & Roos R.A. 2013. Longitudinal pilot-study of sustained attention to response task and p300 in manifest and pre-manifest Huntington's disease. *J Neuropsychol*:

Heath M., Grierson L., Binsted G., & Elliott D. 2007. Interhemispheric transmission time in persons with Down Syndrome. *J Intellect Disabil Res*, 51 (Pt 12): 972-981.

Henley S.M., Wild E.J., Hobbs N.Z., Scahill R.I., Ridgway G.R., Macmanus D.G., Barker R.A., Fox N.C., & Tabrizi S.J. 2009. Relationship between cag repeat length and brain volume in premanifest and early Huntington's disease. *J Neurol*, 256 (2): 203-212.

Henley S.M., Ridgway G.R., Scahill R.I., Kloppel S., Tabrizi S.J., Fox N.C., & Kassubek J. 2010. Pitfalls in the use of voxel-based morphometry as a biomarker: Examples from Huntington disease. *AJNR Am J Neuroradiol*, 31 (4): 711-719.

Hobbs N.Z., Henley S.M., Ridgway G.R., Wild E.J., Barker R.A., Scahill R.I., Barnes J., Fox N.C., & Tabrizi S.J. 2010. The progression of regional atrophy in premanifest and early Huntington's disease: A longitudinal voxel-based morphometry study. *J Neurol Neurosurg Psychiatry*, 81 (7): 756-763.

Hobbs N.Z., Pedrick A.V., Say M.J., Frost C., Dar Santos R., Coleman A., Sturrock A., Craufurd D., Stout J.C., Leavitt B.R., Barnes J., Tabrizi S.J., & Scahill R.I. 2011. The structural involvement of the cingulate cortex in premanifest and early Huntington's disease. *Mov Disord*, 26 (9): 1684-1690.

Hobbs N.Z., Cole J.H., Farmer R.E., Rees E.M., Crawford H.E., Malone I.B., Roos R.A.C., Sprengelmeyer R., Durr A., Landwehrmeyer B., Scahill R.I., Tabrizi S.J., & Frost C. 2013. Evaluation of multi-modal, multi-site neuroimaging measures in Huntington's disease: Baseline results from the PADDINGTON study. *NeuroImage: Clinical*, 2 (1): 204-211.

Hobbs N.Z., Farmer R.E., Rees E.M., Cole J.H., Haider S., Malone I.B., Sprengelmeyer R., Johnson H., Mueller H.P., Sussmuth S.D., Roos R.A., Durr A., Frost C., Scahill R.I., Landwehrmeyer B., & Tabrizi S.J. 2015. Short-interval observational data to inform clinical trial design in Huntington's disease. *J Neurol Neurosurg Psychiatry*: 1-8.

Hofer S., & Frahm J. 2006. Topography of the human corpus callosum revisited--comprehensive fiber tractography using diffusion tensor magnetic resonance imaging. *Neuroimage*, 32 (3): 989-994.

Huntington Study Group 1996. Unified Huntington's Disease Rating Scale: Reliability and consistency. *Mov Disord*, 11 (2): 136-142.

Jbabdi S., Behrens T.E., & Smith S.M. 2010. Crossing fibres in tract-based spatial statistics. *Neuroimage*, 49 (1): 249-256.

Jeeves M.A., & Moes P. 1996. Interhemispheric transfer time differences related to aging and gender. *Neuropsychologia*, 34 (7): 627-636.

Jenkinson M., & Smith S. 2001. A global optimisation method for robust affine registration of brain images. *Med Image Anal*, 5 (2): 143-156.

Jenkinson M., Bannister P., Brady M., & Smith S. 2002. Improved optimization for the robust and accurate linear registration and motion correction of brain images. *Neuroimage*, 17 (2): 825-841.

Jokinen H., Frederiksen K.S., Garde E., Skimminge A., Siebner H., Waldemar G., Ylikoski R., Madureira S., Verdelho A., van Straaten E.C., Barkhof F., Fazekas F., Schmidt R., Pantoni L., Inzitari D., & Erkinjuntti T. 2012. Callosal tissue loss parallels subtle decline in psychomotor speed. A longitudinal quantitative MRI study. The ladis study. *Neuropsychologia*, 50 (7): 1650-1655.

Jones D.K., Symms M.R., Cercignani M., & Howard R.J. 2005. The effect of filter size on vbm analyses of DT-MRI data. *Neuroimage*, 26 (2): 546-554.

Jones D.K., Knosche T.R., & Turner R. 2013. White matter integrity, fiber count, and other fallacies: The do's and don'ts of diffusion MRI. *Neuroimage*, 73: 239-254.

Karakas P., Koc Z., Koc F., & Gulhal Bozkir M. 2011. Morphometric MRI evaluation of corpus callosum and ventricles in normal adults. *Neurol Res*, 33 (10): 1044-1049.

Keihaninejad S., Ryan N.S., Malone I.B., Modat M., Cash D., Ridgway G.R., Zhang H., Fox N.C., & Ourselin S. 2012. The importance of group-wise registration in tract based

spatial statistics study of neurodegeneration: A simulation study in Alzheimer's disease. *PLoS One*, 7 (11): e45996.

Keihaninejad S., Zhang H., Ryan N.S., Malone I.B., Modat M., Cardoso M.J., Cash D.M., Fox N.C., & Ourselin S. 2013. An unbiased longitudinal analysis framework for tracking white matter changes using diffusion tensor imaging with application to alzheimer's disease. *Neuroimage*, 72: 153-163.

Kerns J.G. 2006. Anterior cingulate and prefrontal cortex activity in an fMRI study of trial-to-trial adjustments on the simon task. *Neuroimage*, 33 (1): 399-405.

Kincses Z.T., Szabo N., Toth E., Zadori D., Farago P., Nemeth D., Janacsek K., Babos M., Klivenyi P., & Vecsei L. 2013. Diffusion MRI measured white matter microstructure as a biomarker of neurodegeneration in preclinical Huntington's disease. *Ideggyogy Sz*, 66 (11-12): 399-405.

Kipps C.M., Duggins A.J., Mahant N., Gomes L., Ashburner J., & McCusker E.A. 2005. Progression of structural neuropathology in preclinical Huntington's disease: A tensor based morphometry study. *J Neurol Neurosurg Psychiatry*, 76 (5): 650-655.

Klein A., Andersson J., Ardekani B.A., Ashburner J., Avants B., Chiang M.C., Christensen G.E., Collins D.L., Gee J., Hellier P., Song J.H., Jenkinson M., Lepage C., Rueckert D., Thompson P., Vercauteren T., Woods R.P., Mann J.J., & Parsey R.V. 2009. Evaluation of 14 nonlinear deformation algorithms applied to human brain MRI registration. *Neuroimage*, 46 (3): 786-802.

Kloppel S., Draganski B., Golding C.V., Chu C., Nagy Z., Cook P.A., Hicks S.L., Kennard C., Alexander D.C., Parker G.J., Tabrizi S.J., & Frackowiak R.S. 2008. White matter connections reflect changes in voluntary-guided saccades in pre-symptomatic Huntington's disease. *Brain*, 131 (Pt 1): 196-204.

Kloppel S., Henley S.M., Hobbs N.Z., Wolf R.C., Kassubek J., Tabrizi S.J., & Frackowiak R.S. 2009. Magnetic resonance imaging of Huntington's disease: Preparing for clinical trials. *Neuroscience*, 164 (1): 205-219.

Kloppel S., Gregory S., Scheller E., Minkova L., Razi A., Durr A., Roos R.A., Leavitt B.R., Papoutsis M., Landwehrmeyer G.B., Reilmann R., Borowsky B., Johnson H., Mills J.A., Owen G., Stout J., Scahill R.I., Long J.D., Rees G., & Tabrizi S.J. 2015. Compensation in preclinical Huntington's disease: Evidence from the track-on hd study. *EBioMedicine*, 2 (10): 1420-1429.

Kochunov P., Glahn D.C., Lancaster J., Thompson P.M., Kochunov V., Rogers B., Fox P., Blangero J., & Williamson D.E. 2011. Fractional anisotropy of cerebral white matter and thickness of cortical gray matter across the lifespan. *Neuroimage*, 58 (1): 41-49.

Langbehn D.R., Brinkman R.R., Falush D., Paulsen J.S., & Hayden M.R. 2004. A new model for prediction of the age of onset and penetrance for Huntington's disease based on cag length. *Clin Genet*, 65 (4): 267-277.

Lebel C., Gee M., Camicioli R., Wieler M., Martin W., & Beaulieu C. 2012. Diffusion tensor imaging of white matter tract evolution over the lifespan. *Neuroimage*, 60 (1): 340-352.

Lemay M., Fimbel E., Beuter A., Chouinard S., & Richer F. 2005. Sensorimotor mapping affects movement correction deficits in early Huntington's disease. *Exp Brain Res*, 165 (4): 454-460.

Leow A.D., Klunder A.D., Jack C.R., Jr., Toga A.W., Dale A.M., Bernstein M.A., Britson P.J., Gunter J.L., Ward C.P., Whitwell J.L., Borowski B.J., Fleisher A.S., Fox N.C., Harvey D., Kornak J., Schuff N., Studholme C., Alexander G.E., Weiner M.W., & Thompson P.M. 2006. Longitudinal stability of MRI for mapping brain change using tensor-based morphometry. *Neuroimage*, 31 (2): 627-640.

MacDonald M.E., Ambrose C.M., Duyao M.P., Myers R.H., Lin C., Srinidhi L., Barnes G., Taylor S.A., James M., & Groot N. 1993. A novel gene containing a trinucleotide repeat that is expanded and unstable on Huntington's disease chromosomes. *Cell*, 72 (6): 971-983.

Mansfield K.L., van der Molen M.W., Falkenstein M., & van Boxtel G.J. 2013. Temporal dynamics of interference in Simon and Eriksen tasks considered within the context of a dual-process model. *Brain Cogn*, 82 (3): 353-363.

Marrakchi-Kacem L., Delmaire C., Guevara P., Poupon F., Lecomte S., Tucholka A., Roca P., Yelnik J., Durr A., Mangin J.F., Lehericy S., & Poupon C. 2013. Mapping cortico-striatal connectivity onto the cortical surface: A new tractography-based approach to study Huntington disease. *PLoS One*, 8 (2): e53135.

Marzi C.A., Bisiacchi P., & Nicoletti R. 1991. Is interhemispheric transfer of visuomotor information asymmetric? Evidence from a meta-analysis. *Neuropsychologia*, 29 (12): 1163-1177.

Marzi C.A. 1999. The Poffenberger paradigm: A first, simple, behavioural tool to study interhemispheric transmission in humans. *Brain Res Bull*, 50 (5-6): 421-422.

Mascalchi M., Lolli F., Della Nave R., Tessa C., Petralli R., Gavazzi C., Politi L.S., Macucci M., Filippi M., & Piacentini S. 2004. Huntington disease: Volumetric, diffusion-weighted, and magnetization transfer MR imaging of brain. *Radiology*, 232 (3): 867-873.

Matsui J.T., Vaidya J.G., Wassermann D., Kim R.E., Magnotta V.A., Johnson H.J., & Paulsen J.S. 2015. Prefrontal cortex white matter tracts in prodromal Huntington disease. *Hum Brain Mapp*: 1-16.

Mazziotta J.C., Toga A.W., Evans A., Fox P., & Lancaster J. 1995. A probabilistic atlas of the human brain: Theory and rationale for its development. The International Consortium for Brain Mapping (ICBM). *Neuroimage*, 2 (2): 89-101.

Mazzoni P., & Wexler N.S. 2009. Parallel explicit and implicit control of reaching. *PLoS One*, 4 (10): e7557.

Mestre T., Ferreira J., Coelho M.M., Rosa M., & Sampaio C. 2009. Therapeutic interventions for disease progression in Huntington's disease. *Cochrane Database Syst Rev*, (3): Cd006455.

Modat M., Ridgway G.R., Taylor Z.A., Lehmann M., Barnes J., Hawkes D.J., Fox N.C., & Ourselin S. 2010. Fast free-form deformation using graphics processing units. *Comput Methods Programs Biomed*, 98 (3): 278-284.

Mooshagian E., Iacoboni M., & Zaidel E. 2009. Spatial attention and interhemispheric visuomotor integration in the absence of the corpus callosum. *Neuropsychologia*, 47 (3): 933-937.

Mori S., Wakana S., Van Zijl P.C., & Nague-Poetscher L. MRI atlas of human white matter: Am Soc Neuroradiology; 2005.

Morkl S., Muller N.J., Blesl C., Wilkinson L., Tmava A., Wurm W., Holl A.K., & Painold A. 2016. Problem solving, impulse control and planning in patients with early- and late-stage Huntington's disease. *Eur Arch Psychiatry Clin Neurosci*: In Press.

Muller H.P., Gorges M., Gron G., Kassubek J., Landwehrmeyer G.B., Sussmuth S.D., Wolf R.C., & Orth M. 2016. Motor network structure and function are associated with motor performance in Huntington's disease. *J Neurol*: 539-549.

Niccolini F., & Politis M. 2014. Neuroimaging in Huntington's disease. *World J Radiol*, 6 (6): 301-312.

Noordzij M., Tripepi G., Dekker F.W., Zoccali C., Tanck M.W., & Jager K.J. 2010. Sample size calculations: Basic principles and common pitfalls. *Nephrol Dial Transplant*, 25 (5): 1388-1393.

Nopoulos P.C., Aylward E.H., Ross C.A., Mills J.A., Langbehn D.R., Johnson H.J., Magnotta V.A., Pierson R.K., Beglinger L.J., Nance M.A., Barker R.A., & Paulsen J.S. 2011. Smaller intracranial volume in prodromal Huntington's disease: Evidence for abnormal neurodevelopment. *Brain*, 134 (Pt 1): 137-142.

Novak M.J., Seunarine K.K., Gibbard C.R., Hobbs N.Z., Scahill R.I., Clark C.A., & Tabrizi S.J. 2013. White matter integrity in premanifest and early Huntington's disease is related to caudate loss and disease progression. *Cortex*: 98-112.

Novak M.J., Seunarine K.K., Gibbard C.R., McColgan P., Draganski B., Friston K., Clark C.A., & Tabrizi S.J. 2015. Basal ganglia-cortical structural connectivity in Huntington's disease. *Hum Brain Mapp*, 36 (5): 1728-1740.

Odish O.F., Leemans A., Reijntjes R.H., van den Bogaard S.J., Dumas E.M., Wolterbeek R., Tax C.M., Kuijf H.J., Vincken K.L., van der Grond J., & Roos R.A. 2015. Microstructural brain abnormalities in Huntington's disease: A two-year follow-up. *Hum Brain Mapp*, 36 (6): 2061-2074.

Ouimet C., Jolicoeur P., Lassonde M., Ptito A., Paggi A., Foschi N., Ortenzi A., & Miller J. 2010. Bimanual crossed-uncrossed difference and asynchrony of normal, anterior- and totally-split-brain individuals. *Neuropsychologia*, 48 (13): 3802-3814.

Ourselin S., Roche A., Subsol G., Pennec X., & Ayache N. 2001. Reconstructing a 3d structure from serial histological sections. *Image and Vision Computing*, 19 (1-2): 25-31.

Papoutsis M., Labuschagne I., Tabrizi S.J., & Stout J.C. 2014. The cognitive burden in Huntington's disease: Pathology, phenotype, and mechanisms of compensation. *Mov Disord*, 29 (5): 673-683.

Papp K.V., Kaplan R.F., & Snyder P.J. 2011. Biological markers of cognition in prodromal Huntington's disease: A review. *Brain Cogn*, 77 (2): 280-291.

Park H.-J., Kubicki M., Shenton M.E., Guimond A., McCarley R.W., Maier S.E., Kikinis R., Jolesz F.A., & Westin C.-F. 2003. Spatial normalization of diffusion tensor MRI using multiple channels. *Neuroimage*, 20 (4): 1995-2009.

Paulsen J.S., Hayden M., Stout J.C., Langbehn D.R., Aylward E., Ross C.A., Guttman M., Nance M., Kieburtz K., Oakes D., Shoulson I., Kayson E., Johnson S., & Penziner E. 2006a. Preparing for preventive clinical trials: The PREDICT-HD study. *Arch Neurol*, 63 (6): 883-890.

Paulsen J.S., Magnotta V.A., Mikos A.E., Paulson H.L., Penziner E., Andreasen N.C., & Nopoulos P.C. 2006b. Brain structure in preclinical Huntington's disease. *Biol Psychiatry*, 59 (1): 57-63.

Paulsen J.S., Nopoulos P.C., Aylward E., Ross C.A., Johnson H., Magnotta V.A., Juhl A., Pierson R.K., Mills J., Langbehn D., & Nance M. 2010. Striatal and white matter predictors of estimated diagnosis for Huntington disease. *Brain Res Bull*, 82 (3-4): 201-207.

Paulsen J.S., Long J.D., Johnson H.J., Aylward E.H., Ross C.A., Williams J.K., Nance M.A., Erwin C.J., Westervelt H.J., Harrington D.L., Bockholt H.J., Zhang Y., McCusker E.A., Chiu E.M., & Panegyres P.K. 2014. Clinical and biomarker changes in premanifest Huntington disease show trial feasibility: A decade of the PREDICT-HD study. *Front Aging Neurosci*, 6: 78.

Pellicano A., Barna V., Nicoletti R., Rubichi S., & Marzi C.A. 2013. Interhemispheric vs. Stimulus-response spatial compatibility effects in bimanual reaction times to lateralized visual stimuli. *Front Psychol*, 4: 362.

Penney J.B., Jr., Vonsattel J.P., MacDonald M.E., Gusella J.F., & Myers R.H. 1997. Cag repeat number governs the development rate of pathology in Huntington's disease. *Ann Neurol*, 41 (5): 689-692.

Peterson B.S., Feineigle P.A., Staib L.H., & Gore J.C. 2001. Automated measurement of latent morphological features in the human corpus callosum. *Hum Brain Mapp*, 12 (4): 232-245.

Phillips O., Sanchez-Castaneda C., Elifani F., Maglione V., Di Pardo A., Caltagirone C., Squitieri F., Sabatini U., & Di Paola M. 2013. Tractography of the corpus callosum in Huntington's disease. *PLoS One*, 8 (9): e73280.

Phillips O., Squitieri F., Sanchez-Castaneda C., Elifani F., Caltagirone C., Sabatini U., & Di Paola M. 2014a. Deep white matter in Huntington's disease. *PLoS One*, 9 (10): e109676.

Phillips O., Squitieri F., Sanchez-Castaneda C., Elifani F., Griguoli A., Maglione V., Caltagirone C., Sabatini U., & Di Paola M. 2014b. The corticospinal tract in Huntington's disease. *Cereb Cortex*:

Phillips O.R., Clark K.A., Woods R.P., Subotnik K.L., Asarnow R.F., Nuechterlein K.H., Toga A.W., & Narr K.L. 2011. Topographical relationships between arcuate fasciculus connectivity and cortical thickness. *Hum Brain Mapp*, 32 (11): 1788-1801.

Phillips O.R., Joshi S.H., Squitieri F., Sanchez-Castaneda C., Narr K., Shattuck D.W., Caltagirone C., Sabatini U., & Di Paola M. 2016. Major superficial white matter abnormalities in Huntington's disease. *Front Neurosci*, 10: 197.

Poffenberger A.T. Reaction time to retinal stimulation, with special reference to the time lost in conduction through nerve centers. New York: The Science press; 1912. iii, 73 p. p.

Poudel G.R., Stout J.C., Domínguez D J.F., Salmon L., Churchyard A., Chua P., Georgiou-Karistianis N., & Egan G.F. 2014. White matter connectivity reflects clinical and cognitive status in Huntington's disease. *Neurobiol Dis*, 65 (0): 180-187.

Poudel G.R., Stout J.C., Dominguez D.J., Churchyard A., Chua P., Egan G.F., & Georgiou-Karistianis N. 2015. Longitudinal change in white matter microstructure in Huntington's disease: The image-hd study. *Neurobiol Dis*, 74: 406-412.

Rawlins M.D., Wexler N.S., Wexler A.R., Tabrizi S.J., Douglas I., Evans S.J., & Smeeth L. 2016. The prevalence of Huntington's disease. *Neuroepidemiology*, 46 (2): 144-153.



Raz N., Lindenberger U., Rodrigue K.M., Kennedy K.M., Head D., Williamson A., Dahle C., Gerstorf D., & Acker J.D. 2005. Regional brain changes in aging healthy adults: General trends, individual differences and modifiers. *Cereb Cortex*, 15 (11): 1676-1689.

Rees E.M., Scahill R.I., & Hobbs N.Z. 2013. Longitudinal neuroimaging biomarkers in Huntington's disease. *J Huntingtons Dis*, 2 (1): 21-39.

Reilmann R., Leavitt B.R., & Ross C.A. 2014. Diagnostic criteria for Huntington's disease based on natural history. *Mov Disord*, 29 (11): 1335-1341.

Reisberg B., Franssen E.H., Hasan S.M., Monteiro I., Boksay I., Souren L.E., Kenowsky S., Auer S.R., Elahi S., & Kluger A. 1999. Retrogenesis: Clinical, physiologic, and pathologic mechanisms in brain aging, alzheimer's and other dementing processes. *European Archives of Psychiatry and Clinical Neuroscience*, 249 (3): S28-S36.

Reuter-Lorenz P.A., & Stanczak L. 2000. Differential effects of aging on the functions of the corpus callosum. *Dev Neuropsychol*, 18 (1): 113-137.

Ridgway G., Barnes J., Pepple T., & Fox N. 2011. Estimation of total intracranial volume; a comparison of methods. *Alzheimer's & Dementia*, 7 (4, Supplement): S62-S63.

Ridgway G.R., Henley S.M.D., Rohrer J.D., Scahill R.I., Warren J.D., & Fox N.C. 2008. Ten simple rules for reporting voxel-based morphometry studies. *Neuroimage*, 40 (4): 1429-1435.

Rosas H.D., Goodman J., Chen Y.I., Jenkins B.G., Kennedy D.N., Makris N., Patti M., Seidman L.J., Beal M.F., & Koroshetz W.J. 2001. Striatal volume loss in hd as measured by MRI and the influence of cag repeat. *Neurology*, 57 (6): 1025-1028.

Rosas H.D., Koroshetz W.J., Chen Y.I., Skeuse C., Vangel M., Cudkowicz M.E., Caplan K., Marek K., Seidman L.J., Makris N., Jenkins B.G., & Goldstein J.M. 2003. Evidence for more widespread cerebral pathology in early hd: An MRI-based morphometric analysis. *Neurology*, 60 (10): 1615-1620.

Rosas H.D., Tuch D.S., Hevelone N.D., Zaleta A.K., Vangel M., Hersch S.M., & Salat D.H. 2006. Diffusion tensor imaging in presymptomatic and early Huntington's disease:

Selective white matter pathology and its relationship to clinical measures. *Mov Disord*, 21 (9): 1317-1325.

Rosas H.D., Salat D.H., Lee S.Y., Zaleta A.K., Pappu V., Fischl B., Greve D., Hevelone N., & Hersch S.M. 2008. Cerebral cortex and the clinical expression of Huntington's disease: Complexity and heterogeneity. *Brain*, 131 (Pt 4): 1057-1068.

Rosas H.D., Lee S.Y., Bender A.C., Zaleta A.K., Vangel M., Yu P., Fischl B., Pappu V., Onorato C., Cha J.H., Salat D.H., & Hersch S.M. 2010. Altered white matter microstructure in the corpus callosum in Huntington's disease: Implications for cortical "disconnection". *Neuroimage*, 49 (4): 2995-3004.

Rosas H.D., Reuter M., Doros G., Lee S.Y., Triggs T., Malarick K., Fischl B., Salat D.H., & Hersch S.M. 2011. A tale of two factors: What determines the rate of progression in Huntington's disease? A longitudinal MRI study. *Mov Disord*, 26 (9): 1691-1697.

Ross C.A., & Tabrizi S.J. 2011. Huntington's disease: From molecular pathogenesis to clinical treatment. *Lancet Neurol*, 10 (1): 83-98.

Roze E., Saudou F., & Caboche J. 2008. Pathophysiology of Huntington's disease: From Huntingtin functions to potential treatments. *Curr Opin Neurol*, 21 (4): 497-503.

Rueckert D., Sonoda L.I., Hayes C., Hill D.L., Leach M.O., & Hawkes D.J. 1999. Nonrigid registration using free-form deformations: Application to breast MR images. *IEEE Trans Med Imaging*, 18 (8): 712-721.

Ryan N.S., Keihaninejad S., Shakespeare T.J., Lehmann M., Crutch S.J., Malone I.B., Thornton J.S., Mancini L., Hyare H., Yousry T., Ridgway G.R., Zhang H., Modat M., Alexander D.C., Rossor M.N., Ourselin S., & Fox N.C. 2013. Magnetic resonance imaging evidence for presymptomatic change in thalamus and caudate in familial alzheimer's disease. *Brain*, 136 (Pt 5): 1399-1414.

Sanchez-Castaneda C., Cherubini A., Elifani F., Peran P., Orobello S., Capelli G., Sabatini U., & Squitieri F. 2013. Seeking Huntington disease biomarkers by multimodal, cross-sectional basal ganglia imaging. *Hum Brain Mapp*, 34 (7): 1625-1635.

Scahill R.I., Hobbs N.Z., Say M.J., Bechtel N., Henley S.M., Hyare H., Langbehn D.R., Jones R., Leavitt B.R., Roos R.A., Durr A., Johnson H., Lehericy S., Craufurd D.,

Kennard C., Hicks S.L., Stout J.C., Reilmann R., & Tabrizi S.J. 2013. Clinical impairment in premanifest and early Huntington's disease is associated with regionally specific atrophy. *Hum Brain Mapp*, 34 (3): 519-529.

Schramm C., Katsahian S., Youssov K., Demonet J.F., Krystkowiak P., Supiot F., Verny C., Cleret de Langavant L., & Bachoud-Levi A.C. 2015. How to capitalize on the retest effect in future trials on Huntington's disease. *PLoS One*, 10 (12): e0145842.

Schulte T., Pfefferbaum A., & Sullivan E.V. 2004. Parallel interhemispheric processing in aging and alcoholism: Relation to corpus callosum size. *Neuropsychologia*, 42 (2): 257-271.

Schulte T., Sullivan E.V., Muller-Oehring E.M., Adalsteinsson E., & Pfefferbaum A. 2005. Corpus callosal microstructural integrity influences interhemispheric processing: A diffusion tensor imaging study. *Cereb Cortex*, 15 (9): 1384-1392.

Schulte T., & Muller-Oehring E.M. 2010. Contribution of callosal connections to the interhemispheric integration of visuomotor and cognitive processes. *Neuropsychol Rev*, 20 (2): 174-190.

Schulte T., Maddah M., Muller-Oehring E.M., Rohlfing T., Pfefferbaum A., & Sullivan E.V. 2013. Fiber tract-driven topographical mapping (FTTM) reveals microstructural relevance for interhemispheric visuomotor function in the aging brain. *Neuroimage*, 77: 195-206.

Segonne F., Dale A.M., Busa E., Glessner M., Salat D., Hahn H.K., & Fischl B. 2004. A hybrid approach to the skull stripping problem in MRI. *Neuroimage*, 22 (3): 1060-1075.

Semprini G., Coggi D., & Corballis M.C. 2012. Interhemispheric transfer time in sportsmen. *J Mot Behav*, 44 (5): 373-377.

Shao J., & Diamond M.I. 2007. Polyglutamine diseases: Emerging concepts in pathogenesis and therapy. *Hum Mol Genet*, 16 Spec No. 2: R115-123.

Shen S., Szameitat A.J., & Sterr A. 2007. Vbm lesion detection depends on the normalization template: A study using simulated atrophy. *Magn Reson Imaging*, 25 (10): 1385-1396.

Shoulson I., & Fahn S. 1979. Huntington disease: Clinical care and evaluation. *Neurology*, 29 (1): 1-3.

Sled J.G., & Pike G.B. 1998. Standing-wave and rf penetration artifacts caused by elliptic geometry: An electrodynamic analysis of MRI. *IEEE Trans Med Imaging*, 17 (4): 653-662.

Sled J.G., Zijdenbos A.P., & Evans A.C. 1998. A nonparametric method for automatic correction of intensity nonuniformity in MRI data. *IEEE Trans Med Imaging*, 17 (1): 87-97.

Smith S.M. 2002. Fast robust automated brain extraction. *Hum Brain Mapp*, 17 (3): 143-155.

Smith S.M., Jenkinson M., Woolrich M.W., Beckmann C.F., Behrens T.E., Johansen-Berg H., Bannister P.R., De Luca M., Drobnjak I., & Flitney D.E. 2004. Advances in functional and structural MR image analysis and implementation as FSL. *Neuroimage*, 23: S208-S219.

Smith S.M., Jenkinson M., Johansen-Berg H., Rueckert D., Nichols T.E., Mackay C.E., Watkins K.E., Ciccarelli O., Cader M.Z., & Matthews P.M. 2006. Tract-based spatial statistics: Voxelwise analysis of multi-subject diffusion data. *Neuroimage*, 31 (4): 1487-1505.

Smith S.M., & Nichols T.E. 2009. Threshold-free cluster enhancement: Addressing problems of smoothing, threshold dependence and localisation in cluster inference. *Neuroimage*, 44 (1): 83-98.

Song S.K., Sun S.W., Ramsbottom M.J., Chang C., Russell J., & Cross A.H. 2002. Dysmyelination revealed through MRI as increased radial (but unchanged axial) diffusion of water. *Neuroimage*, 17 (3): 1429-1436.

Song S.K., Sun S.W., Ju W.K., Lin S.J., Cross A.H., & Neufeld A.H. 2003. Diffusion tensor imaging detects and differentiates axon and myelin degeneration in mouse optic nerve after retinal ischemia. *Neuroimage*, 20 (3): 1714-1722.

Sprengelmeyer R., Orth M., Muller H.P., Wolf R.C., Gron G., Depping M.S., Kassubek J., Justo D., Rees E.M., Haider S., Cole J.H., Hobbs N.Z., Roos R.A., Durr A., Tabrizi S.J., Sussmuth S.D., & Landwehrmeyer G.B. 2014. The neuroanatomy of subthreshold

depressive symptoms in Huntington's disease: A combined diffusion tensor imaging (DTI) and voxel-based morphometry (VBM) study. *Psychol Med*, 44 (9): 1867-1878.

Sritharan A., Egan G.F., Johnston L., Horne M., Bradshaw J.L., Bohanna I., Asadi H., Cunnington R., Churchyard A.J., Chua P., Farrow M., & Georgiou-Karistianis N. 2010. A longitudinal diffusion tensor imaging study in symptomatic Huntington's disease. *J Neurol Neurosurg Psychiatry*, 81 (3): 257-262.

Steventon J.J., Trueman R.C., Rosser A.E., & Jones D.K. 2015. Robust MR-based approaches to quantifying white matter structure and structure/function alterations in Huntington's disease. *J Neurosci Methods*:

Stout J.C., Paulsen J.S., Queller S., Solomon A.C., Whitlock K.B., Campbell J.C., Carlozzi N., Duff K., Beglinger L.J., Langbehn D.R., Johnson S.A., Biglan K.M., & Aylward E.H. 2011. Neurocognitive signs in prodromal Huntington disease. *Neuropsychology*, 25 (1): 1-14.

Stout J.C., Glikmann-Johnston Y., & Andrews S. 2015. Cognitive assessment strategies in Huntington's disease research. *J Neurosci Methods*: 19-24.

Sturrock A., & Leavitt B.R. 2010. The clinical and genetic features of Huntington disease. *J Geriatr Psychiatry Neurol*, 23 (4): 243-259.

Sullivan E.V., Pfefferbaum A., Adalsteinsson E., Swan G.E., & Carmelli D. 2002. Differential rates of regional brain change in callosal and ventricular size: A 4-year longitudinal MRI study of elderly men. *Cereb Cortex*, 12 (4): 438-445.

Tabrizi S.J., Langbehn D.R., Leavitt B.R., Roos R.A., Durr A., Craufurd D., Kennard C., Hicks S.L., Fox N.C., Scahill R.I., Borowsky B., Tobin A.J., Rosas H.D., Johnson H., Reilmann R., Landwehrmeyer B., & Stout J.C. 2009. Biological and clinical manifestations of Huntington's disease in the longitudinal TRACK-HD study: Cross-sectional analysis of baseline data. *Lancet Neurol*, 8 (9): 791-801.

Tabrizi S.J., Scahill R.I., Durr A., Roos R.A., Leavitt B.R., Jones R., Landwehrmeyer G.B., Fox N.C., Johnson H., Hicks S.L., Kennard C., Craufurd D., Frost C., Langbehn D.R., Reilmann R., & Stout J.C. 2011. Biological and clinical changes in premanifest and early stage Huntington's disease in the TRACK-HD study: The 12-month longitudinal analysis. *Lancet Neurol*, 10 (1): 31-42.

Tabrizi S.J., Reilmann R., Roos R.A., Durr A., Leavitt B., Owen G., Jones R., Johnson H., Craufurd D., Hicks S.L., Kennard C., Landwehrmeyer B., Stout J.C., Borowsky B., Scahill R.I., Frost C., & Langbehn D.R. 2012. Potential endpoints for clinical trials in premanifest and early Huntington's disease in the TRACK-HD study: Analysis of 24 month observational data. *Lancet Neurol*, 11 (1): 42-53.

Tabrizi S.J., Scahill R.I., Owen G., Durr A., Leavitt B.R., Roos R.A., Borowsky B., Landwehrmeyer B., Frost C., Johnson H., Craufurd D., Reilmann R., Stout J.C., & Langbehn D.R. 2013. Predictors of phenotypic progression and disease onset in premanifest and early-stage Huntington's disease in the TRACK-HD study: Analysis of 36-month observational data. *Lancet Neurol*, 12 (7): 637-649.

Tettamanti M., Paulesu E., Scifo P., Maravita A., Fazio F., Perani D., & Marzi C.A. 2002. Interhemispheric transmission of visuomotor information in humans: FMRI evidence. *J Neurophysiol*, 88 (2): 1051-1058.

Tobin A.J., & Signer E.R. 2000. Huntington's disease: The challenge for cell biologists. *Trends Cell Biol*, 10 (12): 531-536.

Travers B.G., Bigler E.D., Tromp D.P.M., Adluru N., Froehlich A.L., Ennis C., Lange N., Nielsen J.A., Prigge M.B.D., Alexander A.L., & Lainhart J.E. 2014. Longitudinal processing speed impairments in males with autism and the effects of white matter microstructure. *Neuropsychologia*, 53: 137-145.

Travers B.G., Tromp do P.M., Adluru N., Lange N., Destiche D., Ennis C., Nielsen J.A., Froehlich A.L., Prigge M.B., Fletcher P.T., Anderson J.S., Zielinski B.A., Bigler E.D., Lainhart J.E., & Alexander A.L. 2015. Atypical development of white matter microstructure of the corpus callosum in males with autism: A longitudinal investigation. *Mol Autism*, 6: 15.

Tuncer M.C., Hatipoglu E.S., & Ozates M. 2005. Sexual dimorphism and handedness in the human corpus callosum based on magnetic resonance imaging. *Surg Radiol Anat*, 27 (3): 254-259.

Unmack Larsen I., Vinther-Jensen T., Gade A., Nielsen J.E., & Vogel A. 2015. Assessing impairment of executive function and psychomotor speed in premanifest and manifest Huntington's disease gene-expansion carriers. *J Int Neuropsychol Soc*: 1-10.

van den Bogaard S., Dumas E., van der Grond J., van Buchem M., & Roos R. 2012. MRI biomarkers in Huntington's disease. *Front Biosci (Elite Ed)*, 4: 1910-1925.

van der Hiele K., Jurgens C.K., Vein A.A., Reijntjes R.H., Witjes-Ane M.N., Roos R.A., van Dijk G., & Middelkoop H.A. 2007. Memory activation reveals abnormal EEG in preclinical Huntington's disease. *Mov Disord*, 22 (5): 690-695.

Vaportzis E., Georgiou-Karistianis N., Churchyard A., & Stout J.C. 2014. Effects of task difficulty during dual-task circle tracing in Huntington's disease. *J Neurol*:

Verny C., Allain P., Prudean A., Malinge M.C., Gohier B., Scherer C., Bonneau D., Dubas F., & Le Gall D. 2007. Cognitive changes in asymptomatic carriers of the Huntington disease mutation gene. *Eur J Neurol*, 14 (12): 1344-1350.

Vonsattel J.-P., Myers R.H., Stevens T.J., Ferrante R.J., Bird E.D., & Richardson E.P.J. 1985. Neuropathological classification of Huntington's disease. *Journal of Neuropathology & Experimental Neurology*, 44 (6): 559-577.

Vonsattel J.P., Keller C., & Cortes Ramirez E.P. 2011. Huntington's disease - neuropathology. *Handb Clin Neurol*, 100: 83-100.

Walker L., Gozzi M., Lenroot R., Thurm A., Behseta B., Swedo S., & Pierpaoli C. 2012. Diffusion tensor imaging in young children with autism: Biological effects and potential confounds. *Biological Psychiatry*, 72 (12): 1043-1051.

Wang P., Zhang X., Liu Y., Liu S., Zhou B., Zhang Z., Yao H., Zhang X., & Jiang T. 2013. Perceptual and response interference in Alzheimer's disease and Mild Cognitive Impairment. *Clin Neurophysiol*, 124 (12): 2389-2396.

Wang Y., Gupta A., Liu Z., Zhang H., Escolar M.L., Gilmore J.H., Gouttard S., Fillard P., Maltbie E., Gerig G., & Styner M. 2011. DTI registration in atlas based fiber analysis of infantile Krabbe disease. *Neuroimage*, 55 (4): 1577-1586.

Westerhausen R., Kreuder F., Woerner W., Huster R.J., Smit C.M., Schweiger E., & Wittling W. 2006. Interhemispheric transfer time and structural properties of the corpus callosum. *Neurosci Lett*, 409 (2): 140-145.

Wexler N.S., Collett L., Wexler A.R., Rawlins M.D., Tabrizi S.J., Douglas I., Smeeth L., & Evans S.J. 2016. Incidence of adult Huntington's disease in the uk: A uk-based primary care study and a systematic review. *BMJ Open*, 6 (2): e009070.

Whitwell J.L., Crum W.R., Watt H.C., & Fox N.C. 2001. Normalization of cerebral volumes by use of intracranial volume: Implications for longitudinal quantitative MR imaging. *AJNR Am J Neuroradiol*, 22 (8): 1483-1489.

Wild E.J., & Tabrizi S.J. 2014. Targets for future clinical trials in Huntington's disease: What's in the pipeline? *Mov Disord*, 29 (11): 1434-1445.

Wild E.J. 2016. Huntington's disease: The most curable incurable brain disorder? *EBioMedicine*, 8: 3-4.

Winkler A.M., Ridgway G.R., Webster M.A., Smith S.M., & Nichols T.E. 2014. Permutation inference for the general linear model. *Neuroimage*, 92: 381-397.

Witelson S.F. 1989. Hand and sex differences in the isthmus and genu of the human corpus callosum. A postmortem morphological study. *Brain*, 112 ( Pt 3): 799-835.

Witjes-Ane M.N., Mertens B., van Vugt J.P., Bachoud-Levi A.C., van Ommen G.J., & Roos R.A. 2007. Longitudinal evaluation of "presymptomatic" carriers of Huntington's disease. *J Neuropsychiatry Clin Neurosci*, 19 (3): 310-317.

Wolf R.C., Sambataro F., Vasic N., Schonfeldt-Lecuona C., Ecker D., & Landwehrmeyer B. 2008. Altered frontostriatal coupling in pre-manifest Huntington's disease: Effects of increasing cognitive load. *Eur J Neurol*, 15 (11): 1180-1190.

Wolf R.C., Thomann P.A., Thomann A.K., Vasic N., Wolf N.D., Landwehrmeyer G.B., & Orth M. 2013. Brain structure in preclinical Huntington's disease: A multi-method approach. *Neurodegener Dis*, 12 (1): 13-22.

You S.C., Geschwind M.D., Sha S.J., Apple A., Satris G., Wood K.A., Johnson E.T., Gooblar J., Feuerstein J.S., Finkbeiner S., Kang G.A., Miller B.L., Hess C.P., Kramer J.H., & Possin K.L. 2013. Executive functions in premanifest Huntington's disease. *Mov Disord*: 405-409.

Zaidel E., & Iacoboni M. The parallel brain: The cognitive neuroscience of the corpus callosum: MIT press; 2003.



Zalesky A. 2011. Moderating registration misalignment in voxelwise comparisons of DTI data: A performance evaluation of skeleton projection. *Magn Reson Imaging*, 29 (1): 111-125.

Zhang H., Hui Z., Yushkevich P.A., & Gee J.C. 2004. Registration of diffusion tensor images. *Proceedings of the 2004 IEEE Computer Society Conference on Computer Vision and Pattern Recognition, 2004 CVPR 2004*, 1: 842-847.

Zhang H., Yushkevich P.A., Alexander D.C., & Gee J.C. 2006. Deformable registration of diffusion tensor MR images with explicit orientation optimization. *Med Image Anal*, 10 (5): 764-785.

Zielonka D., Mielcarek M., & Landwehrmeyer G.B. 2015. Update on Huntington's disease: Advances in care and emerging therapeutic options. *Parkinsonism Relat Disord*, 21 (3): 169-178.

Zuccato, C. & Cattaneo, E., 2014. Huntington's Disease. Oxford University Press, 243–273.